Synthèse et propriétés de cristaux liquides et magnétiques de 1,8,15,22-tétraalkoxy-phtalocyanines de métaux (II) et (III)

Petru Apostol

université de BORDEAUX

THÈSE PRÉSENTÉE

POUR OBTENIR LE GRADE DE

DOCTEUR DE

L'UNIVERSITÉ DE BORDEAUX

École doctorale des sciences chimiques

SPÉCIALITÉ : Physico-Chimie de la Matière Condensée

par Petru APOSTOL

Synthèse et propriétés de cristaux liquides et magnétiques de 1,8,15,22-tétraalkoxy–phtalocyanines de métaux (II) et (III)

Sous la direction de : Harald BOCK

Soutenue le 6 Septembre 2016

Membres du jury:

Mme. MOINEAU-CHANE CHING Kathleen	Directeur de recherche, CNRS	Rapporteur
M. HIORNS Roger	Chargé de recherche, UPPA	Rapporteur
M. BOCK Harald	Directeur de recherche, CNRS	Directeur de thèse
Mme. ZAKRI Cécile	Professeur, Université de Bordeaux	Examinateur

-2016-

Dedicated to future generations involved in science …

When I had a problem or felt unsafe, I found an endless reserve of unconditional aid in the people around me. Without their help, this thesis work would not be completed; I would like to thank all of them for their valuable contribution.

Firstly, I thank **Dr. Philippe Richetti** for welcoming me at the Centre of Research Paul Pascal. I thank **Dr. Roger Hiorns** and **Dr. Kathleen Moineau-Chane Ching** for their time and consideration to review this thesis; **Prof. Cécile Zakri** for the participation in the thesis defense jury.

Sincere thanks to my supervisor **Dr. Harald Bock,** for having introduced me to a fascinating and an interesting research field, of liquid crystallinity. I thank him for training me into less practiced by me: organic chemistry field. Being in the lab, I felt his kindness, enthusiasm, openness and friendliness that allowed me to quickly adapt. His constructive criticism and collaboration has been great assets throughout my PhD. I thank him for valuable discussion about my work which has been done during three years. I would like to thank **Dr. Fabien Durola** for his inspiring discussions during group meetings. One of the most greater results obtained in this thesis were achieved as the result of collaboration with many generous people from Brazil: **Prof. Ivan H. Bechtold**, **Prof. Hugo Gallardo**, **Prof. Marta E. Dotto** and **Prof. Juliana Eccher.**

I would like to thank **Dr. Rodolphe Clérac**, for having introduced me into an interesting research field, the molecule-based magnetic materials. I also thank **Dr. Pierre Dechambenoit** for his help to figure out the problems with single crystal diffraction experiments and **Dr. Elizabeth Hillard** for her help concerning cyclic voltammetry measurements as well as organization of the group and "after" group meetings.

I also thank the people who gave me scientific and technical support and especially **Mathieu Rouzières** for the SQUID/PPMS, **Stéphanie Exiga** for NMR, Mass Spectroscopies and Elemental Analysis, **Ahmed Bentaleb** for powder diffraction measurements.

Many thanks to postdocs from the team who managed to keep a relaxing atmosphere in our team, which helped a lot to 'evaporate' my pressure: **David Aguilà, Yoann Prado**, **Daniel Rosario-Amorin**, **Jun-Liang Liu**, **Abhishake Mondal, Kasper Steen Pedersen.**

Thanks to my colleagues and friends **Elena Darbinean**, **Vlad Bulicanu**, **Dumitru Samohvalov**, **Anandi Srinivasan, Evangelia Koumousi, Marli Ferreira, Marília Gabriela Cabral** and **Edivandro Girotto** for their friendship, help in my research or simply moral support, well wishes, and nice time that I will always clip in my memory.

Last but not least, many thanks to my **Family** for their encouragement, faith and eternal support throughout all my life.

Thank you all – Merci à tous – Mulțumesc tuturor

Petru APOSTOL
Pessac, September 2016

Table of Contents

General Introduction

Since the discovery of liquid crystals by botanist Friedrich Reinitzer in the late 19th century, these fascinating materials attracted the attention of chemists and physicists, theoreticians and experimentalists. In the last quarter of the 20th century, due to their combination of fluidity, birefringence and polarizability, liquid crystals where found to be efficient materials for the construction of flat panel displays [1]. In the same period, the anisotropic charge carrier mobility in various liquid crystal phases started to be investigated. The often good π-orbital overlap between neighboring molecules recommended liquid crystalline materials as organic semiconductors that are easy processable (due to their good solubility and small molecular mass) and can conveniently deposited on substrates by either spin coating or vacuum deposition. In spite of the rapid development of a large variety of electronic devices, there is still a considerable technological effort under way to optimize these devices in order to save cost, space, energy, and raw materials. Accordingly, a large number of liquid crystals continue to be designed and studied for their mesomorphism and the resulting optoelectronic and anisotropic behavior.

While calamitic (rod-like) liquid crystals have already contributed a lot to the development of large area flat panel displays, the discotic (disk-like) liquid crystals, which are particularly interesting for applications such as solar cells (photovoltaics), light-emitting diodes (LEDs) and field-effect transistors (FETs), are still in the proof-of device-concept state. Stacking of the large conjugated disk-shaped mesogens in columnar assemblies improves the charge carrier mobility via a hopping mechanism along the axis of the columns [2]. In this context, liquid crystalline phthalocyanine derivatives (Pcs) are promising candidates. Their semiconducting properties can be modified to suit a broad range of applications by varying the central metal atom and the peripheral substituents. Rare-earth(III) double-decker complexes are highly desirable materials, because the metal contributes two additional features to the overall properties of the complex: luminescence and magnetism. Double decker phthalocyanines are known also to be mononuclear single molecular magnets (SMMs), with possible applications in data storage, quantum computing [3] and molecule-based spintronic devices [4].

In this thesis, we focused on columnar liquid-crystalline phthalocyanine-based organic semiconductors and new mononuclear Mn(III) and Dy(III) phthalocyanine-based SMMs. The first chapter starts with a general description of liquid crystals, followed by examples of discotic liquid crystals based on phthalocyanine. Chapter II focuses on functionalization and regioselective synthesis of tetrasubstituted phthalocyanines with four branched alkyl chains in α-positions and their transition metal(II) complexes, and their liquid crystalline order. With respect to the branched chain substituents, the compounds are divided in three classes: (a) Pcs with racemic 2-butyloctyloxy chains; (b) Pcs with 2-pentylheptyloxy chains; and (c) Pcs with 2-butylhexyloxy chains. In chapter III we present the electronic behavior in solution-processed organic diodes of metal-free (H_2-) and metalated (Cu- and Ni-) tetrakis-butyloctyloxy-Pcs in order to correlate the optoelectronic properties with molecular organization and film structure. In chapter IV, mononuclear Mn(III) and Dy(III) tetra-α-butylhexyloxy-PCs and a corresponding monoleptic double decker Dy-Pc were synthesized and their structural and magnetic properties studied.

References

[1] a) G. H. Heilmeier, L. A. Zanonii; L. A. Barton; *Appl. Phys. Lett.*, **1968**, 13, 46; b) M. Schadt; W. Helfrich; *Appl. Phys Lett.*, **1971**, 18, 127.

[2] a) A. Bayer; S. Zimmermann; J. H. Wendorff; *Mol. Cryst. Liq. Cryst.*, **2003**, 396, 1; b) K. Kohary; H. Cordes; S. D. Baranovskii; P. Thomas; J.-H. Wendorff; *Phys. Status Solidi B*, **2004**, 241, 76; c) S. Laschat; A. Baro; N. Steinke; F. Giesselmann; C. Hägele; G. Scalia; R. Judele; E. Kapatsina; S. Sauer; A. Schreivogel; M. Tosoni; *Angew Chem Int Ed Engl.*, **2007**; 46, 4832-4887.

[3] M. N. Leuenberger; D. Loss; *Nature*, **2001**, 410, 789–793.

[4] L. Bogan; W. Wernsdorfer; *Nat. Mater.*, **2008**, 7, 179–186.

Chapter I

Generalities and Context

Table of Contents for Chapter I

I.1. Liquid Crystals

In nature a substance can exist in three basic states: solid, liquid and gas. In the crystalline solid state, the arrangement of molecules is ordered, with a regularly repeating pattern in all directions of space. The molecules are held in fixed positions by intermolecular forces such as hydrogen bonding, π-stacking, polar–nonpolar interactions, metal coordination, charge transfer complexation, ionic interactions, etc. In the liquid state, the thermal motion overcomes the intermolecular forces that maintain a crystalline state, and the molecules move into random directions, while still maintaining close contact. Consider that molecular crystal (solid) is subjected to heat: With increasing temperature, the molecular vibrations increase and reach a point where the molecules break away from their fixed positions and lose their specific orientations. Accordingly, the molecules then begin to move more freely, implying rotational motion as well. The solid now changes into the liquid state where the molecules are moving chaotically in all directions. In other words, an anisotropic solid becomes an isotropic liquid. If, however, the molecules of the crystal have pronounced geometric shape anisotropy like a rod or a disk, counterbalanced by the thermal motion of attached flexible alkyl chains, the isotropic liquid state is preceded by another intermediate state in terms of molecular ordering. This state possesses some degree of orientational ordering and sometimes some positional ordering of the anisotropic molecules, that is, the molecules diffuse throughout the sample but while doing so they maintain some *orientational* and *positional* ordering. This is the fascinating liquid crystalline state. Here, the anisotropic solid changes into a stable anisotropic fluid before turning into an isotropic liquid. This has been recognized as a true thermodynamically stable state of matter. Liquid crystals (LCs) combine the fluidity of liquids with the anisotropy of crystals. Since this anisotropic ordered fluid occurs between the temperatures of the crystalline solid state and the isotropic liquid state and possesses properties of both, it has been referred to as an intermediate phase or *mesophase* (*mesos* in Greek means middle). It has also been called as the fourth state of matter. In contrast, if a three-dimensional intermolecular order is maintained in which the molecules are generally fixed at lattice points, but atomic localization is lost because molecules rotate freely on their lattice points, the resulting intermediate state of matter is referred to as a *plastic crystal*.

The macroscopic behavior of the mesophase is defined by the molecular properties of their constituents, the mesogens. The premise for formation of the liquid crystalline phase, which combines long-range order with the mobility of fluids, is the shape anisotropy of these mesogens**.** While a rigid core (which often consists of aromatic rings) induces the structural order, flexible parts (*i.e.* alkyl chains) provide the necessary mobility within the liquid crystalline phase.

I.2. Classification of Liquid Crystals

The most general classification of LCs divides them into two major categories: a) thermotropic LCs (mesophase formation is temperature dependent) and b) lyotropic LCs (mesophase formation is solvent and concentration dependent). If a compound displays both thermotropic and lyotropic liquid crystalline phases,

then it is called an *amphotropic* LC [1]. The thermotropic mesophase can be obtained either by heating the solid or by cooling the isotropic liquid. The transition temperature from the crystal to the mesophase is called the *melting point*, while the transition temperature from the mesophase to the isotropic liquid is called the *clearing point*. Geometric anisotropy, interaction anisotropy and micro-segregation are the driving parameters for mesophase formation. Based on the shape of the mesogenic molecules, thermotropic LCs are classified into two main groups: (a) calamitic (rod-like, including bent-core) LCs [2], and (b) discotic (disk-like)[3] LCs (Scheme **I.1**).

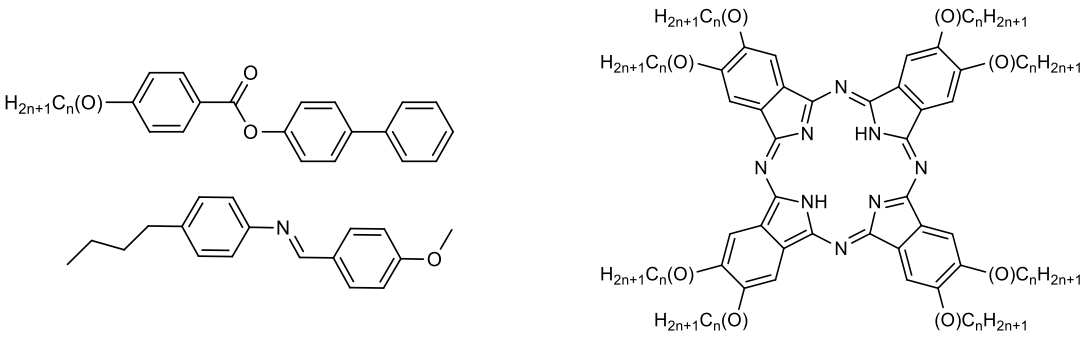

Scheme I.1. Examples of calamitic (left) and discotic (right) molecules.

Most of the calamitic liquid crystalline compounds consist of two or more ring structures, bonded together directly or via linking groups. They usually have terminal hydrocarbon chains and sometimes lateral substituents as well. Calamitic LCs generally exhibit two types of mesophases: (a) *nematic* (from the Greek word *nematos* meaning "thread") and (b) smectic (from the Greek word *smectos* meaning "soap").

Nematic phase

The nematic phase is the least ordered mesophase based only on long-range orientational order of the molecules, meaning their only alignment is along one common axis, called *director*, $\vec{n}$, without positional ordering (periodicity) in any direction. The self-assembled molecules are oriented with their long axis approximately parallel to each other, and the nematic phase is usually found at high temperatures (Figure **I.1**).

Smectic phases

In the *smectic* phase, the rod-shaped molecules are arranged in layers, possessing thus positional order as well, in addition to orientational order. There are several types of smectic mesophases, characterized by a variety of molecular arrangements within and between the layers: $Sm_{A,B,C,E,F,I,J,K}$, with subcategories like Sm_{A1} for monolayer and Sm_{A2} for bilayer etc. [4]. The long axis of the mesogens aligns along the layer normal in the smectic A phase whilst in the smectic C phase it is tilted with respect to the layer normal (Figure **I.1**).The lateral intermolecular forces are stronger than the interlayer interactions and as a consequence, layers are able to slide over one another relatively easily. *Smectic* comes from the Greek word *smectos* meaning "*soap*", because the first

liquid crystals of this type revealed properties similar to soap. In Figure **I.1** the most common Sm_A and Sm_C mesophases are represented.

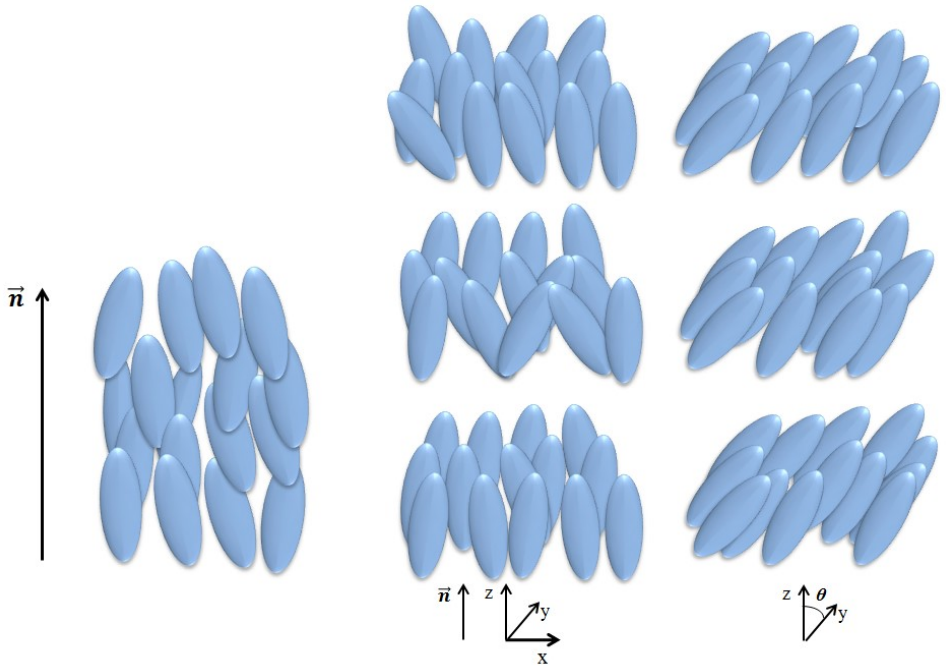

Figure I.1. Schematic representation of a nematic phase formed by calamitic or rod-like molecules (left), a smectic A (SmA) phase (middle), and a smectic C (SmC) phase (right).

Columnar phases

The *columnar* phases are formed by stacking of disk-like mesogens into columns which form a two-dimensional periodic lattice. The columns are in the ideal case of infinite length and the molecules exhibit only short-range positional order along the column axis. The columnar stacking of the molecules appears as a result of the strong interactions between π-conjugated cores and between surrounding dipoles which are counterbalanced by the thermal motion of the alkyl chains, thus inhibiting crystallization into a 3D crystalline structure. Different forms of columnar stacking can be found in the columns: *disordered columns* (with rather irregular stacking of the disks); *ordered columns* (the cores are rather equidistant while the relative positions of the disks in different columns are still ill defined) and *tilted columns* (the normals of the disks are tilted with respect to the column axis). The self-assembling into columns leads to a 2D columnar lattice with the column axes being parallel to each other. Consequently the columnar phase can be considered as 1D fluid (along the columns) and 2D crystalline (along the 2D-lattice vectors) [5]. The structural order and the ways of packing of the columns define hexagonal (Col_h), rectangular (Col_r) and oblique (Col_o) columnar phases (Figure **I.2**). In the Col_h phase the columns are arranged on a 2D-hexagonal lattice, the 3- or 6–fold symmetry of which requires either nontilted columns (c0mm0n), or that the tilts of three or six distinct sets of columns compensate each other (rare). There are three distinguishable Col_r mesophases with the planar space groups $P2_1/a$, P2/a, and C2/m which correspond to the plane groups p2gg, p2mg and c2mm (Figure **I.2**) [6]. The disks in this kind of mesophase are tilted with respect to the column axis, leading to an elliptic cross section of the column. As the

cross section of the tilted columns is elliptical, the symmetries of the Col_r and Col_o phases differ from a proper hexagonal symmetry. The tilt is induced by strong offsetted core-core interactions, which are significantly more pronounced than in the non-tiltedhexagonal columnar mesophase.

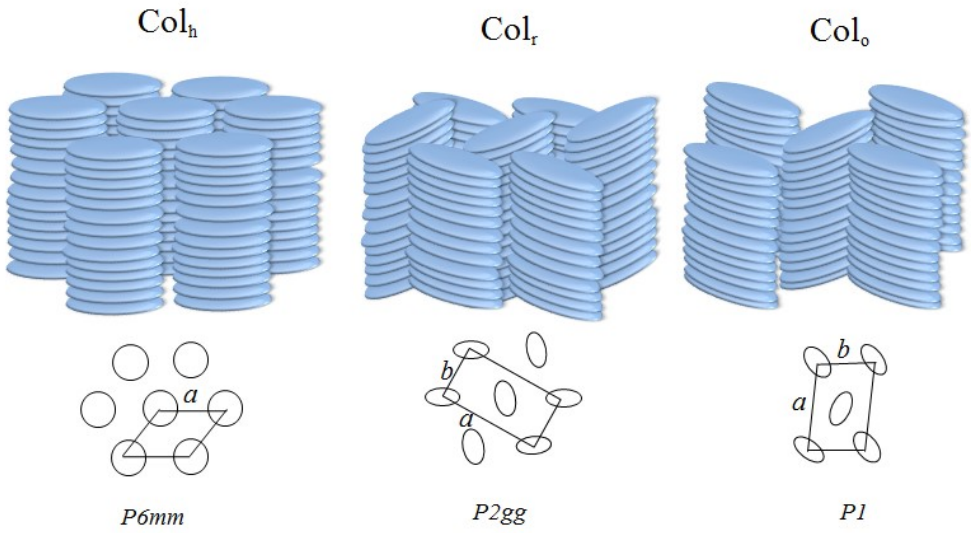

Figure I.2. Schematic representation of (left) columnar hexagonal (Col_h), (center) columnar rectangular (Col_r) and (right) columnar oblique (Col_o) phases; a side view (top) and phase cuts (bottom) are shown.

By increasing the chain length it is often possible to change from Col_h to Col_r. For discotic molecules, two different variations of the nematic phase are known (Figure I.3). In the N_D mesophase, the individual flat molecules have full translational freedom and are oriented parallel to each other. In the columnar nematic phase, N_{col} there is some degree of aggregation with short stacks of molecules acting as mesoscopic rods oriented parallel to each other. Both N_D and N_{col} phases are rare, with only few known examples [7].

Figure I.3. Schematic representation of the N_{col} phase of discotic liquid crystals.

I.3. Identification of Liquid Crystalline Mesophases

In order to distinguish and to identify the mesophase, polarized optical microscopy is one of the simplest and most informative techniques. Because of the birefringent nature of the liquid crystal material, linearly polarized light that passes through it may become elliptically polarized and thus may partially pass through a second orthogonal polarizer. If in some macroscopic region of a sample the transmission axis of the first polarizer is parallel to either the ordinary or extraordinary directions of the material (the components resulting from birefringence), the light is not broken up into components, and no change in the polarization

state occurs. In this case, there is no transmitted component and the region appears dark. The optical texture made of bright and dark regions gives the most immediate and accessible information about a liquid crystalline sample as it visualizes the typical defect patterns of the mesophase. The homeotropic texture of the nematic phase when viewed between crossed polarizers appears uniformly black because the optical axis is perpendicular to the plane of the polarizers, while in planar molecular alignment (optical axis in the plane of the polarizers) the nematic phase shows a characteristic *schlieren* texture as shown in Figure **I.4**, (**left**).

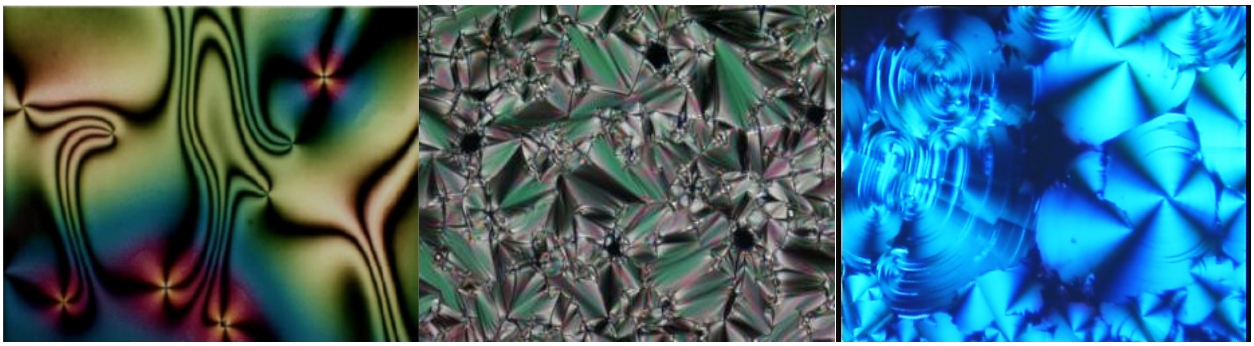

Figure I.4. Characteristic optical textures of the nematic (left)[8], smectic (center)[9] and columnar mesophases (right)[10].

The smectic and columnar mesophases consist of a dense packing of cylindrical micelles. They are often identified by a characteristic planar "fan" shaped texture in the optical microscope, due to the focal conic domains of the layers or columns (Figure **I.4, center** and **right**). Columnar mesophases in planar alignment generally show full circle domains, whilst smectic focal conic textures consist generally of circle segments.

A second means of identification of the type of the mesophase is X-ray scattering studies. Most experimental scattering data are collected in the small-angle regime, characteristic of the longer inter-layer or inter-column spacings in the structure. Because of the remnant crystallinity in the mesophase, some discrete Bragg peaks are seen. In the smectic phase, the characteristic lamellar structure induces long-range ordering resulting in many small-angle diffraction peaks in the ratio 1:2:3:4,… etc. (Figure **I.5, top right**). The x-ray scattering of the columnar hexagonal mesophase reveals a number of Bragg peaks in ratio $1:\sqrt{3}:\sqrt{4}$, etc corresponding to the allowed reflections from the 2D p6mm hexagonal symmetry group. Two strong reflections (resulting from the splitting of the (10) reflection of the hexagonal lattice) in the small angle region of x-ray diffraction pattern are characteristic of a rectangular columnar phase (Figure **I.5, bottom right**), whilst oblique columnar mesophases show generally three main reflections in the small angle regions.

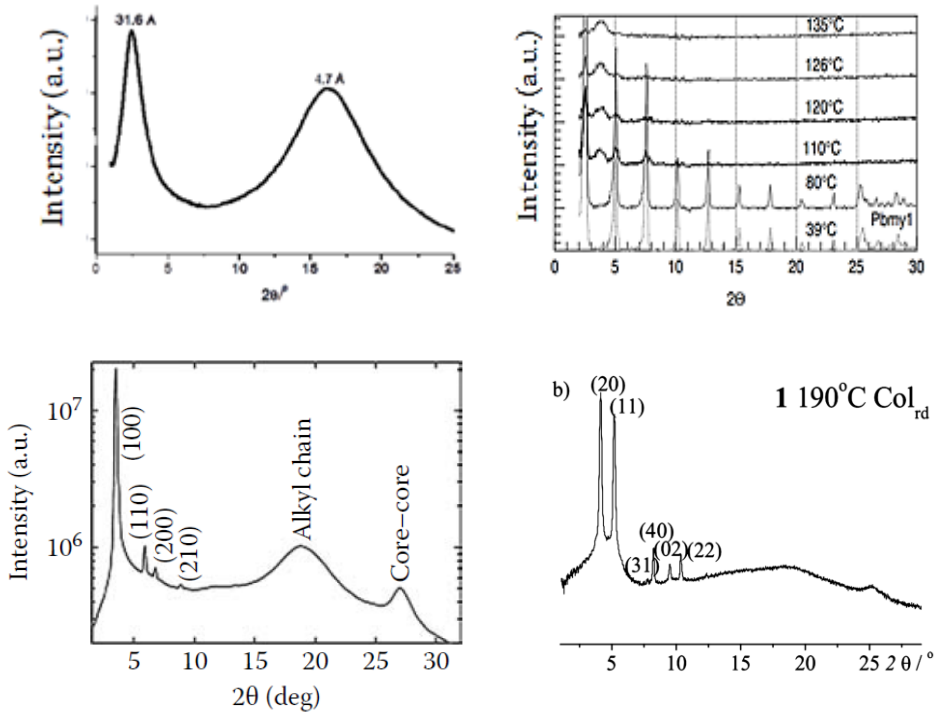

Figure I.5. Typical X-ray powder diffraction pattern of nematic (top, left) [11], smectic (top, right) columnar hexagonal (bottom, left) [12] and columnar rectangular (bottom, right) [12b] mesophases (intensity vs. diffraction angle).

I.4. Charge Transport Properties

I.4.1. Discotic Liquid Crystals as Organic Semiconductors

While calamitic (rod-like) liquid crystals have already contributed a lot to electronic devices, especially in important area of flat panel displays [13], discotic (disk-like) mesogens are still under extensive research in order to understand their structure-property relationship and to create novel compounds with desirable mesomorphic [5] and other physical properties [14]. Mesophases with stacked columns of aromatic cores are attracting particular attention because of their anisotropic electronic properties, with the aromatic stacks transporting electrons or holes and the alkyl chain regions acting as insulators. The transport of charge carriers in an organic semiconductor strongly depends on the packing of the molecules. The stacking of flat aromatic mesogens into columns with a small intra-columnar repeat distance (around 3.5 Å) [15] favors overlapping of π-orbitals of the carbon and/or nitrogen atoms in the plane of the flat aromatic system. Therefore a transfer of the charge carriers (electrons or holes) is enabled preferentially in the direction of the columns, between the aromatic mesogen centers. Because of the insulating chains around the columns, the transfer of charges between columns is much less favored [16] (Figure **I.6**). Another aspect linked to the charge transport along the columns is that the molecules are somewhat mobile along the fluid column, which leads to the destabilization of the π-π stacking. Therefore, weak π-π orbital overlapping leads to unsatisfying charge carrier mobility [17]. Marcus theory (which originally is designed for electron transfer in redox reactions in solution) explains that the charge carrier transport in disordered systems (like columnar LCs) occurs by a hopping mechanism between neighboring molecules [18]. Various molecular parameters were investigated practically and theoretically with respect to their influence on the charge transfer in columnar phases. The charge transport in disordered systems

also strongly depends on lattice vibrations, and the periodic change of the intermolecular distance increases the orbital overlap temporarily followed by a period of less overlap.

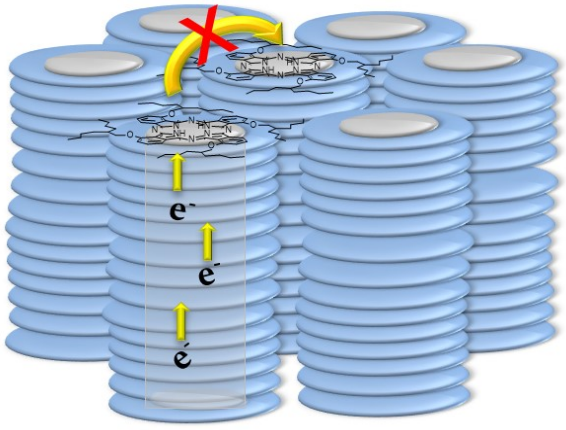

Figure I.6. Schematic representation of the columnar staking of a Pc derivative. Charge carrier transport is favored along the columns, transfer of the charges between columns is suppressed by the insulating chains.

In order to increase the regularity of the stacking, in some cases, hydrogen bonding between molecules is used [19]. An increase of the stacking order can also be achieved by variation of the core mesogens by inserting dipole moments in the aromatic plane or by helical structures with alternation of different side chains around the core of the mesogens [15].

Structural defects can be eliminated partially in liquid crystalline materials by thermal annealing. This technique can also achieve different orientations of the columnar mesophase: homeotropic (face-on) and planar (edge-on) surface alignment. The alignment of the columnar axes of good 1D charge transport is the key objective. Homeotropic alignment of the columnar material is preferred for application in organic light emitting diodes (OLEDs) and organic photovoltaic devices (OPVs) where good charge transport between two metal (top and bottom) electrodes is required. Planar surface alignment is preferred in organic field effect transistors (OFETs) [17, 20] where good transport parallel to the gate surface is required. As a consequence, the alignment of liquid crystalline materials became a challenging issue and different methods like vacuum evaporation, spin coating and deposition of Langmuir-Blodgett films have been extensively used to produce thin films [21].

I.5. Diodes and their Work Principle

In general, an inorganic semiconductor diode, is an electronic device essentially consisting of a junction of two semiconductor materials: one contains an excess of electrons (induced by doping with negatively charged impurity ions), called n-type, and the other has a deficit of electrons (induced by doping with positively charged impurity ions), called p-type. When these two types of semiconductors are in contact, at a so-called *p-n junction*, a momentary diffusion of electrons occurs from the *n* to the *p* side of the junction. As a result, this diffusion of electrons (and, reciprocally, holes) creates a *depletion region*. This special distribution of charges creates an electric field whose electric potential acts as a barrier that prevents displacement of the electrons and holes. Equilibrium occurs when the diffusion current is equal to the drift current. The potential barrier is an obstacle for the diffusion current through the device. It is possible to reduce the height of this potential barrier by

applying an external voltage. When a sufficiently higher electrical potential is applied to the *p* side (the anode) than to the *n* side (the cathode), electrons start to diffuse through the depletion region from the n-type side to the p-type side. Under this condition the p-n junction is set to operate under *forward bias*. If the voltage is reverts, the depletion region becomes larger because the electrons from n type get attracted to the positive terminal, and the positive holes in the p type semiconductor get attracted to the negative terminal. This *reverse bias* increases the potential barrier (Figure I.7).

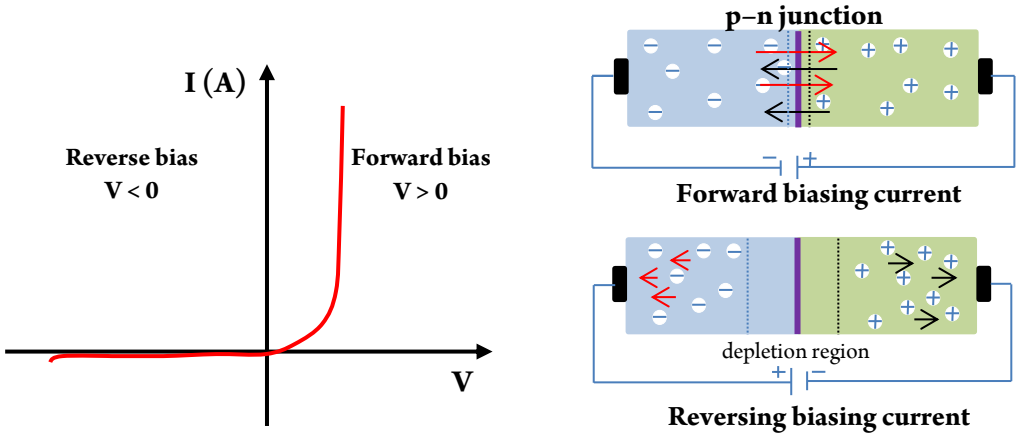

Figure I.7. (left) *I–V* (current vs. voltage) characteristics of a p–n junction diode. (right) Schematic representation of the charge displacement under applied voltage.

Diodes based on organic semiconductor materials follow a similar working mechanism. The materials are selected in accordance with the band gap (HOMO-LUMO) of each type of material. PEDOT:PSS is a very useful conductive polymer in organic electronic devices as it is optically transparent in its conducting state, has a low redox potential and is very stable. It acts as a hole injection layer and improves the interface between the active layer (organic semiconductor) and the electrode, e.g. indium tin oxide (ITO).

The organic diode under forward bias is characterized mainly by two regimes:

I: *Ohmic regime*. Under forward bias at increasing voltage, the current is still minimal until the voltage is enough to cancel the voltage drop over the junction. In this situation, the barrier to the carrier diffusion disappears and the process is "tickness dependent." In the simplest scenario, the semiconductor can be treated as a simple electrical resistance and the electrical current is given by:

$$I = Aqn\mu\frac{V}{d} \qquad \textbf{Eq.I.1}$$

where d is the semiconductor thickness, V is the applied voltage, and A is the contact area. This regime is often only observed at relatively low applied voltages; and if the device is injection-limited, in the most common scenario it is impossible to observe the ohmic regime in the current–voltage plot.

II. *Space-charge-limited current regime* (SCLC). By further increasing the applied voltage, more carriers are injected into the semiconductor. The injected carrier density is higher than that of the thermally activated carriers inside the semiconductor. The current is then only dependent on the mobility and no more on the

charge carrier density, hence, the mobility can be estimated from a simple current-voltage measurement**.** The relationship between electrical current and applied voltage it is described by the Mott-Gurney law:

$$I = \frac{9}{8}\varepsilon\mu_0\frac{V^2}{d^3} \qquad \textbf{Eq.I.2}$$

where μ_0 denotes the mobility of electrons or holes, V is the applied voltage, d is the thickness of the semiconductor, and ε is the permittivity of the material. The current is dominated by charge carriers injected from the contacts and the current-voltage characteristics becomes quadratic ($I \sim V^2$).

I.6. Phthalocyanine Mesogens

Phthalocyanine was for the first time obtained accidentally in 1907 by Braun and Tcherniac in the industrial synthesis of ortho-disubstituted benzene derivatives as a dark and very stable material [22]. In 1927 Disbach and von der Weid obtained a blue compound with an extremely high melting point and poor solubility during the reaction of ortho-dibromobenzene with copper cyanide. The discovery of highly stable innovative compounds with inherent dark green–blue color attracted the interest of the dye industry. One of the challenges was to determine the chemical structure and the reaction mechanism of the reaction. In 1934 Linstead used the combination of elemental analysis, ebullioscopic molecular mass determination and oxidative degradation (which produces phthalamide) to elucidate the structure. The name 'phthalocyanine' was conceived by Linstead as a combination of the prefix phthal which in Greek *naphtha* means rock oil and the second part *cyanine* from the Greek word for blue. He demonstrated that Pc is a symmetrical aromatic macrocycle with 18-π electrons and four iminoisoindoline units with a large enough cavity to accommodate various metal ions [23]. Later this structure was confirmed by X-Ray diffraction [24[a, b, c, d]] (Scheme **I.2**).

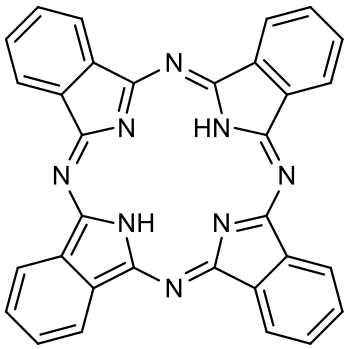

Scheme I.2. The structure of phthalocyanine.

Phthalocyanine is a chemically and thermally very stable π-conjugated macrocycle, and has a number of interesting properties such as: being an organic semiconductor, easily forming compact and smooth thin films, and exhibiting photoconductivity and catalysis [25]. The hydrosoluble dyes based on sulfonated phthalocyanine derivatives discovered in 50's are used in the textile industry. Since 1982, when Piechocki and co-workers [26] synthesized the first mesogenic phthalocyanines, the mesophase structure of a significant number of substituted phthalocyanines and porphyrins were investigated [27]. These include phthalocyanines with eight linear alkyl

[28], alkoxymethyl [29] and alkoxy [30] substituents which exhibit transitions from the crystalline phases to the mesophases at elevated temperatures. Optoelectronic devices based on organic semiconductors are usually used at the ambient temperature. Therefore the self-assembled structure of the organic layer of a mesogenic material should persist at room temperature. Various MPcs with different substituents such as several flexible long alkoxy or alkyl chains as peripheral or non-peripheral substituents were synthesized and studied in terms of structure, LC properties and surface alignment.

The LC properties of MPcs can be varied by introducing alkyl or alkoxy chains either at the peripheral (exo, β) or at the non-peripheral (endo, α) positions of the Pc macrocycle. Tetra-β-substituted MPc differ from their octa-substituted homologues in that they can be obtained as a mixture of four regioisomers formed during the cyclotetramerization reaction [31]. The presence of such a mixture of regioisomers decreases the temperature of the melting transitions, as it hinders crystallization in comparison with the more symmetric octa-substituted analogue. In some cases, the presence of bulky branched side chains destabilizes the packing by steric hindrance and decreases the clearing temperature, making alignment possible by annealing near the clearing temperature [32]. The series of octa-alkoxy peripherally substituted phthalocyanines abbreviated MPc-$(OC_n)_8$ [33] with various central metals as well as with various peripheral chains are characterized by high thermally stability of the mesophase with the temperature range of their mesophases extending over 250 °C. The high thermal stability of these mesophases is ascribed both to the strong van der Waals interactions between the alkyl substituents and to the π interactions between the MPc aromatic cores. Only compounds with long alkyl chains such as hexadecyl exhibit an attainable clearing point, whereas homologs with shorter chains start to decompose before reaching this point. The clearing point did not show a marked dependence on the type of the central metal ion.

The study of the effect of peripheral or non-peripheral substitution with 13, 17-dioxanonacosan-15-yloxy (Scheme **I.3**) to chains was described by Ahsen et. al., [34] who found that peripheral-tetra-substituted metal free, Ni(II) and Zn(II) phthalocyanine derivatives, being stable over a wide temperature including room temperature and exhibiting a ordered hexagonal columnar (Col_h) structure. However, non-peripheral-tetra-substituted metal free, Ni(II) and Zn(II) phthalocyanine derivatives exhibit no mesomorphism and are viscous oils at room temperature.

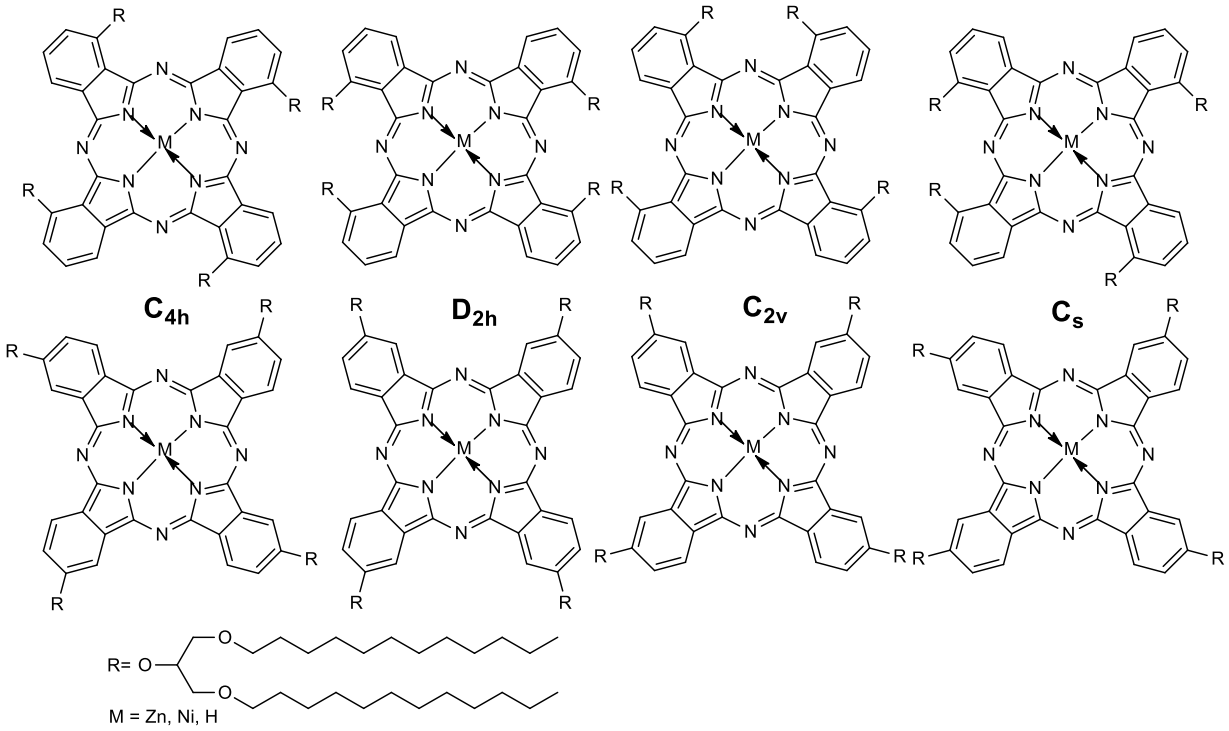

Scheme I.3. Mixed isomeric structures of peripherally and non- peripherally tetra-substituted phthalocyanines with branched chains that show a room temperature mesophase.

This indicates that by introducing somewhat less bulky substituents at the α-position of the Pc core, liquid crystallinity at room temperature may be obtained. Electronic, in addition to steric, factors appear to be very influential in determining the thermal behavior of non-peripherally substituted Pcs. Interaction between non-peripheral substituent chains that are positioned on the neighboring benzo-moieties is the strongest steric constraint with this type of side-chains, and it most likely leads to the displacement of some alkyl chains out of the plane of the phthalocyanine macrocycle. Cook et. al. [35] synthesized 1,4,8,11,15,18,22,25-octaoctylphthalocyanine (**1**) exhibiting an Col_r mesophase between 85 and 101°C, and a Col_h mesophase from 101 to 152 °C. Remarkably high values of hole mobilities of 0.20 $cm^2 V^{-1} s^{-1}$ and 0.10 $cm^2 V^{-1} s^{-1}$ and electron mobilities of 0.30 $cm^2 V^{-1} s^{-1}$ and 0.20 $cm^2 V^{-1} s^{-1}$ were observed in the Col_r phase at 85 °C and in the Col_h phase at 100 °C, respectively [35b, c]. Based on these examples, branched-chain α-alkylated phthalocyanines (Scheme **I.4**, **2** and **3**) were synthesized and, as revealed by DSC and by X-ray diffraction, both compounds show a crystalline phase at temperatures below 112 and 169°C respectively. Compound **2** forms a crystalline phase of unexplained nature at temperatures between 112 and 124 °C, and in the temperature range between 124 and 170°C exhibits a Col_h phase [36]. The shorter chains in **3** lead to the appearance of the Col_h at a higher and lower temperature range, between 169 and 189°C.

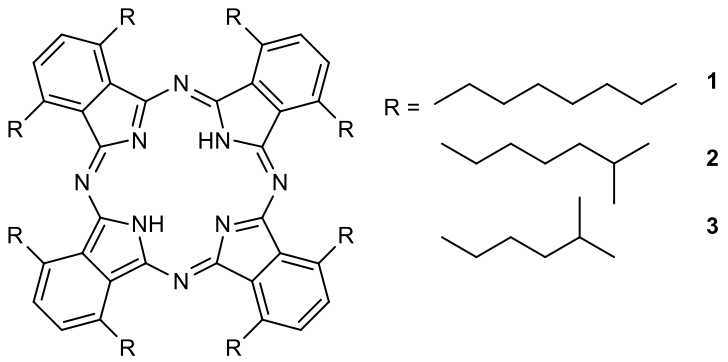

Scheme I.4. Structures of non-peripherally octa-substituted phthalocyanines.

In another work [37], the synthesis of tetrakis-octylthio- and octyloxy-substituted PbPcs with the substituents both in peripheral (Scheme **I.5**, (**4** and **5**)) and nonperipheral (Scheme **I.5**, (**6** and **7**)) positions has been described.

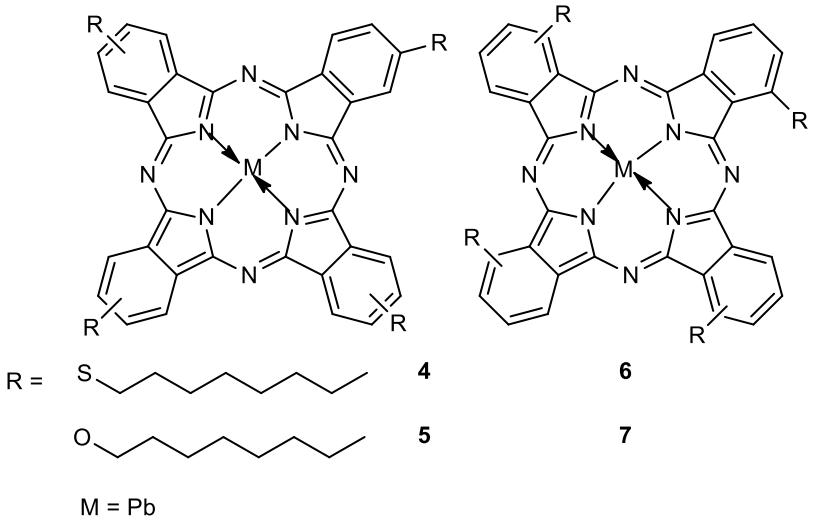

Scheme I.5. The structure of peripherally and nonperipherally tetrakis(octylthio)- and tetrakis(octyloxy)-substituted lead(II) phthalocyanines

The DSC curves of the peripherally substituted PbPc **4** and **5** exhibit two peaks corresponding to phase transition from crystal to LC and LC to isotropic liquid, respectively. In the second cycle, no any enthalpy transition from liquid crystal to crystal is observed in both, indicating that the compounds remain in their liquid crystal phase at room temperature. X-ray analysis has verified the formation of a Col_h mesophase by the peripherally substituted derivatives **4** and **5**, whereas the non-peripherally alkoxy substituted derivative **7** exhibited a columnar tetragonal (Col_t) mesophase. Non-peripherally alkoxy substituted PbPc derivative **6**, according to XRD analysis, does not show any mesophase and melts at 63 ◦C. The cofacial columnar structure is sterically destabilized because the big Pb atoms lie outside the plane of the phthalocyanine macrocycle. This is believed to cause a significant reduction in both melting and clearing points. As expected, non-peripherally substituted derivatives have lower clearing points in comparison with their peripherally substituted analogs. Ohta and co-workers have obtained a series of bis[octakis(alkylthio)phthalocyaninato] rare-earth metal(III) complexes $[(CnS)_8Pc]_2M$ (where M is Eu(III), Tb(III), and Lu(III); n = 8, 10, 12, 14, and 16), and their mesomorphism was studied [38]. A novel unique pseudo-hexagonal mesophase, D_{rh}(P21/a), has been found for

at least two compounds of each rare-earth derivative series, $[(CnS)_8Pc]_2Eu$ (n = 10, 12), $[(CnS)_8Pc]_2Tb$ (n = 10, 12, 14) and $[(CnS)_8Pc]_2Lu$ (n=10, 12). In other works [39], hexylthiosubstituted rare-earth metal bisphthalocyanines {$[(C_6S)_8Pc]_2Lu$, $[(C_6S)_8Pc]_2Gd$, $[(C_6S)_8Pc]_2Dy$, and $[(C_6S)_8Pc]_2Sm$} were synthesized and characterized. These complexes assume similar mesogenic properties as those demonstrated by other alkylthio-substituted bisphthalocyanines. In general, the octakis(alkylthio)-substituted monophthalocyanines are characterized by transition temperatures lower than those of their oxygen analogs [40]; these transition temperatures also decrease with increasing the chain length [41]. Likewise, the alkylthio substitution results in decreasing the melting point in octakis(alkylthio)-substituted bisphthalocyanines [38, 42] in comparison with the analogous alkoxy-substituted derivatives $[(C_6O)_8Pc]_2Gd$, $[(C_6O)_8Pc]_2Dy$, and $[(C_6O)_8Pc]_2Sm$ [43].

In recent years, the elaboration of hybrid magnetic materials via functionalization of organic ligands with various groups to improve thermal or chemical stability and to induce liquid crystalline properties or, simply, to enhance the solubility became an issue. When bearing a paramagnetic central metal ion, phthalocyanines may give rise to original magnetic properties such as single molecule magnet (SMM) behavior [44]. The possibility to induce LC phases in a double-decker terbium phthalocyanine complex (Figure **I.8, left**) with chiral (*S*)-2-(dodecyloxy)propoxy groups was reported [44[a]]. The functionalized complex exhibits a hexagonal columnar mesophase at room temperature, while at low temperature it is an SMM. As a result, this complex showed the possibility to reversibly control its magnetic properties by simple thermal treatment of the studied sample. Thus the thermally trapped disordered phase (prepared by a very rapid cooling from 333 to 150 K) and the ordered crystalline state (slowly cooled from isotropic point) show different temperature dependences of the in-phase (χ') and out-of-phase (χ'') susceptibilities measured at several frequencies (Figure **I.8, right**). The observed differences consisted in different ratios between slowly and quickly relaxing species in the disordered phase and in the crystalline one. This system is one of the first examples of lanthanide double-decker complexes showing two different relaxation processes and it is the only system in which the ratio between these responses has been shown to be reversibly modified by simple thermal treatments.

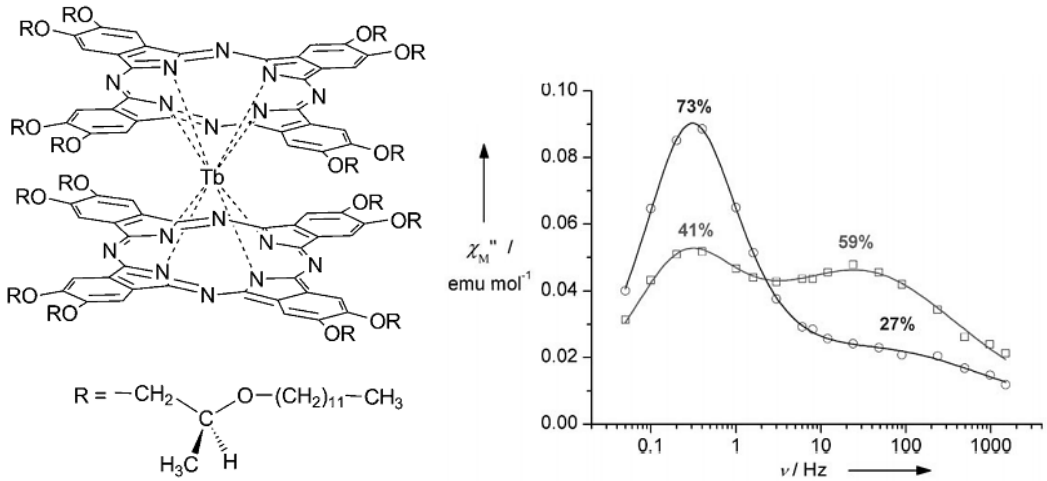

Figure I.8. (left) Structure of a mesogenic functionalized Tb double-decker phthalocyanine complex. (right) Frequency dependence of the out-of-phase (χ'') susceptibility at 25 K for the quenched disordered phase (open squares) and for the crystalline phase (open circles) [40[a]]

I.7. Single-Molecule Magnetism

I.7.1. Generalities

A traditional macroscopic magnet is composed of three-dimensional regions of the material where the individual magnetic moments of the atoms are aligned with one another and point into the same direction. These regions are called magnetic domains, separated by 'domain walls'. A hysteresis is observed in magnetization *vs* field (M *vs* H) plots because altering the magnetization requires the breaking of the domain wall, which consumes certain energy. Thus, the magnetization can be retained for a long time after removal of the field, due to the persisting of the magnetic domains. $SmCo_5$ and $Nd_2Fe_{14}B$ are the most powerful magnets known to date [45]. Magnet-based materials are found in almost every electronic device such as generators, motors, loudspeakers, microphones, switches, sensors and data storage devices. The miniaturization of technological devices has necessitated the exploration of new approaches to design new material which exhibit magnetic behavior at the nano-scale. Therefore, the development of new molecule-based magnetic materials, in order to reduce the size of magnetic units, has grown considerably in recent years. The slow relaxation of magnetization at very low temperature (*i.e.* T < 10 K) in the dodecamanganese coordination complex $[Mn_{12}O_{12}(O_2C_2CH_3)_{16}(H_2O)$, known as '$Mn_{12}$', became an strategic benchmark for further complexes [46]. Such molecules exhibit slow relaxation of their magnetization of purely molecular origin, and thus where called single molecular magnets (SMMs). When a complex exhibits such behavior, but contains only a single metal ion, is called a single-ion magnet (SIM) [46[b]]. In SMMs the magnetic domains do not comprise many molecules, and there are no 'domain walls' between the molecules, as the complexes are completely isolated and are not interacting. When a SMM is magnetized, the unpaired spins of the molecules align with the direction of the applied magnetic field, as that is the most energetically favorable orientation of the magnetization. When the field is removed, at low temperatures, the magnetization can be retained in that direction for some period of time. The larger the energy barrier to spin reversal (U) [47], the longer the magnetization can be retained, and the higher the temperature at which this can be observed. To produce a single molecule magnet, three criteria must be met: the molecule must have a large axial magnetic anisotropy (characterized by the axial zero-field splitting parameter, D) induced by the ligand geometry and the coupling of orbital and spin angular momentums, there must be a high spin ground state, and the magnetic interaction with neighboring molecules must be low [48]. For transition metals ions the comparable ligand field (LF) and electronic repulsion energies are much stronger than spin orbital (SO) coupling energies. For 4f ions, spherical effects (inter-electronic repulsion and SO coupling) strongly dominate over LF effects, which, due to the shielded nature of the 4f orbitals, are much smaller than for 3d ions. Because of the strong angular dependence of the 4f orbitals, the electronic structures of Tb^{III} and Dy^{III} ions possess substantial anisotropy and can show SMM properties even as single ions, for which they are also known as single ion magnets (SIM).

I.7.2. Magnetic Anisotropy

The most fundamental parameter of a SMM is its magnetic anisotropy. The magnetic anisotropy is determined by the interaction between the orbital state of a magnetic ion and the surrounding strong crystal field. This interaction is transferred to the spin moments via the spin–orbit coupling, giving a weaker d-electron coupling of the spins to the crystal lattice. This phenomenon is the preferential alignment of the magnetic moment along a specific direction. For most of the SMMs there is an *energetically most favorable anisotropic axis* in which orientation of magnetization occurs, and a plane perpendicular to that axis which is the least favorable orientation for the magnetization. In this case, the anisotropic axis is known as the 'easy axis' and the plane as the 'hard plane'. The 'easy' direction can be a plane, instead of an axis, if there is a two-dimensional region of space in which it is preferable to find the magnetization [55].

The anisotropy of the magnetization is also a result of zero field splitting phenomena (ZFS). There are two phenomena that can result in the development of ZFS: (I) first order spin–orbit coupling (in-state spin–orbit coupling) and (II) second order spin–orbit coupling (out-of-state spin–orbit coupling) [56]. The first describes the direct mixing of spin and orbital angular momentum components in the ground electronic state of a system, whereas the latter describes the mixing of excited states, which possess a first-order orbital angular momentum, with the ground state, that possesses none. As an example we describe here the second order spin orbital coupling phenomena based on Mn(III) in octahedral and tetragonal (axial elongating) ligand field. The high-spin free Mn(III) ion with S = 2 has a ^5D ground term, which splits in octahedral ligand fields to form $^5T_{2g}$ and ^5E_g terms. Under Jahn–Teller distortion forming a tetragonal geometry (D_{4h} symmetry), these terms split from $^5T_{2g}$ to $^5B_{2g}$ and ^5E_g and from ^5E_g to $^5A_{1g}$ and $^5B_{1g}$ (Figure **I.9**)**.** If the complex has an axial-elongated geometry, the ground term is $^5B_{1g}$, while if the complex has a compressed form, $^5A_{1g}$ is the ground term. The spin degeneracy of the ground state is further removed by the second-order spin–orbit coupling, the so-called *zero-field splitting* (ZFS) (Figure **I.9**). The ZFS from the ground term, $^5B_{1g}$ or $^5A_{1g}$, produces the lowest magnetization levels of $M_S = \pm 2$ or 0, respectively, with a gap of 4D ($=|D|S^2$) between the spin ground state and the highest excited state (when $^5B_{1g}$ is the ground term, D is negative, and conversely, when $^5A_{1g}$ is the ground term, D is positive with a Hamiltonian of $H = D[S^2 - 1/3S(S+1)]$) [57].

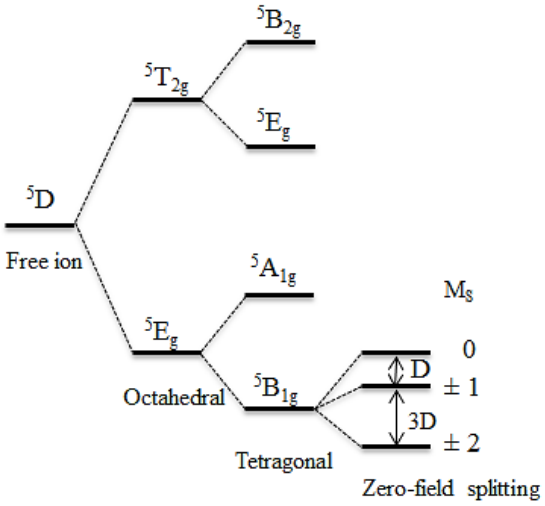

Figure I.9. Splitting of the ^5D term (d^4) by octahedral and tetragonal (axially elongating) fields and by second-order spin–orbit coupling (zero-field splitting).

Gerritsen and Sabinsky [58] have experimentally demonstrated that the anisotropy of the Mn(III) ion depends greatly on its Jahn–Teller distortion, leading in most cases to a negative ZFS parameter (D).

I.7.3. SMM Properties in the Absence of an External Field

In a complex with spin state *S*, there are *2S+1* possible spin states, i.e. sublevels with a spin quantum number M_S, where $-S \leq M_S \leq S$. When the magnetic coupling is larger than the thermal energy, SMM behavior is defined by the following Hamiltonian:

$$H = DS_{Tz}^2 + E(S_{Tx}^2 - S_{Ty}^2) \qquad \textbf{Eq. I.3}$$

where S_T is the total spin ground state, S_{Tx}^2, S_{Ty}^2, S_{Tz}^2 are spin operators along the three principal directions of magnetization (x- hard, y – intermediate, and z – easy axis), *D* and *E* are easy axis and transverse anisotropy parameters (that arise due to geometrical deviation from the ideal uniaxial symmetry for which $E = 0$). This effect is referred to as zero-field splitting (ZFS). Hence in the absence of the magnetic field and presence of a strong uniaxial anisotropy ($D < 0$ and $|D| \gg E$) the Hamiltonian can be simplified to:

$$H = DS_{Tz}^2 \qquad \textbf{Eq. I.4}$$

and the spin sublevels change their energy according to:

$$E_{ms} = Dm_S^2 \qquad \textbf{Eq. I.5}$$

In general, SMMs are characterized by the presence of a negative value of *D*, but recently, a few examples of mononuclear systems exhibiting a positive *D* value were reported to exhibit SMM properties; however, the underlying physics is still in debate [49]. When *D* is negative, the energy difference between $M_S = 0$ and $M_S = \pm S$, denoted *U*, represents an energy barrier to the thermal inversion of the magnetic moment (Figure **I.10**). There is no energy cost to reverse the direction of the total spin in the $M_S = 0$ state. Each M_S state corresponds to a different orientation of the spin projection, and $M_S = S$ can be considered 'spin up' and $M_S = -S$ 'spin down'. This means that if the thermal energy of a system (K_BT) is less than *U*, the system will be unable to randomly

reorientate its magnetic moment and will thus remain trapped in a potential energy minimum. Under such circumstances, if the system is magnetized under an applied field, upon removal of this field it can retain its magnetization (provided K_BT never becomes greater than U). This gives rise to a magnetic hysteresis effect at low temperatures of purely molecular origin, which is the defining feature of a SMM/SIM.

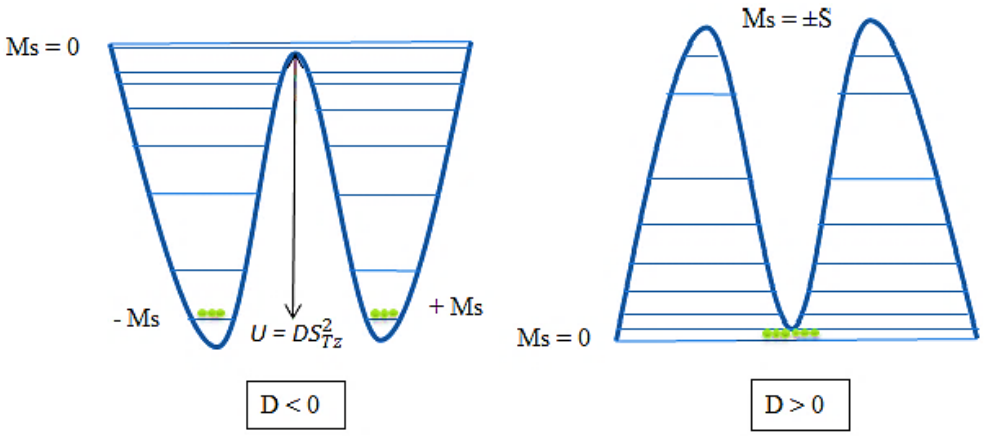

Figure I.10. Energy diagram for negative (left) and positive (right) D.

Due to the many crystal field parameters implied the environment of the 4f ion, the magnetism of the 4f metal complexes is much harder to model theoretically than 3d metal complexes [50]. Spin–orbit coupling splits the $^{2S+1}$L state into multiplets with different values of J. In most cases the multiplets are well separated in energy and so only the lowest lying is populated at room temperature. The ligand field, however, splits the $^{2S+1}L_J$ ground state multiplet into 2J + 1 sublevels (or 'Stark' levels), each with a quantum number M_J, rather than M_S (used in case of 3d metal complexes) [51]. The splitting of the M_J is typically of the order of ~10^2 cm^{-1}. The sublevels may be singlets or grouped as doublets, generally depending on whether the ion is of Kramers (odd number of unpaired electrons, e.g. Dy^{III}) or non-Kramers (even number of unpaired electrons, e.g. Tb^{III}) type [52]. In order to correlate the splitting of these sublevels to the observed slow relaxation, recently Ruiz and co-workers suggested that the difference between the first and second excitation energies of the ground $^6H_{15/2}$ multiplet of Dy^{III} is critically important in determining if the SMM is field-induced or not [53]. It is not possible de determine which sublevels lie at lowest energy, and the maximum value of $\pm M_J$ does not necessarily lie lowest in energy if the symmetry of the complex is low [54]. These particularities give rise to appearance of challenging problems in order to model theoretically the magnetic behavior of lanthanide complexes.

I.7.4. SMM Behavior in a Longitudinal Magnetic Field

The presence of a magnetic field changes the previously reduced Hamiltonian (Eq. I.3) to describe an SMM as follows:

$$H = DS_{Tz}^2 - g\mu_B\vec{S}_T\cdot\vec{H} \qquad \textbf{Eq.6}$$

where the last term is the Zeeman effect contribution which originates from the interaction of spin $\vec{S}_T$ with the external magnetic field $\vec{H}$. When an external longitudinal (parallel to the easy axis) magnetic field H_z is applied, the spin sublevels change their energy according to the Zeeman coupling:

$$E_{ms} = Dm_s^2 - g\mu_B m_s H_Z \qquad \textbf{Eq.7}$$

According to the **Eq. I.7**, the spin sublevels with $m_S < 0$ become energetically stabilized while those with $m_S > 0$ values become energetically destabilized (Zeeman effect) (Figure **I.11, b**). This leads to a preferred population of the m_S = -S sublevel. Thus a favored orientation of the microscopic magnetic moments in the direction of the external magnetic field is creating a magnetization $M \neq 0$ of the macroscopic sample.

I.7.5. Relaxation of Magnetization

If the system is magnetized under an applied field, upon removal of this field it can retain this magnetization. Since all processes tend to a stable state, the magnetized system requires a thermal equilibrium. Thus, the excited spins recover their thermodynamical energy, leading to the relaxation of magnetization. The magnetization and relaxation processes in SMMs are traditionally described by a 'double-well' diagram (Figure **I.11**). At zero-field all $M_S \neq 0$ levels form degenerate pairs (Figure **I.11, (a)**). However, when an external field is applied parallel to the magnetization axis, the $-M_S$ levels are stabilized and the $+M_S$ levels are destabilized (Figure **I.11, (b)**). When the system reaches its saturation state, then only the $M_S = -S$ level remains populated. Upon removal of the field the system returns to thermal equilibrium through a series of steps depicted in Figure **I.11, (c)**.

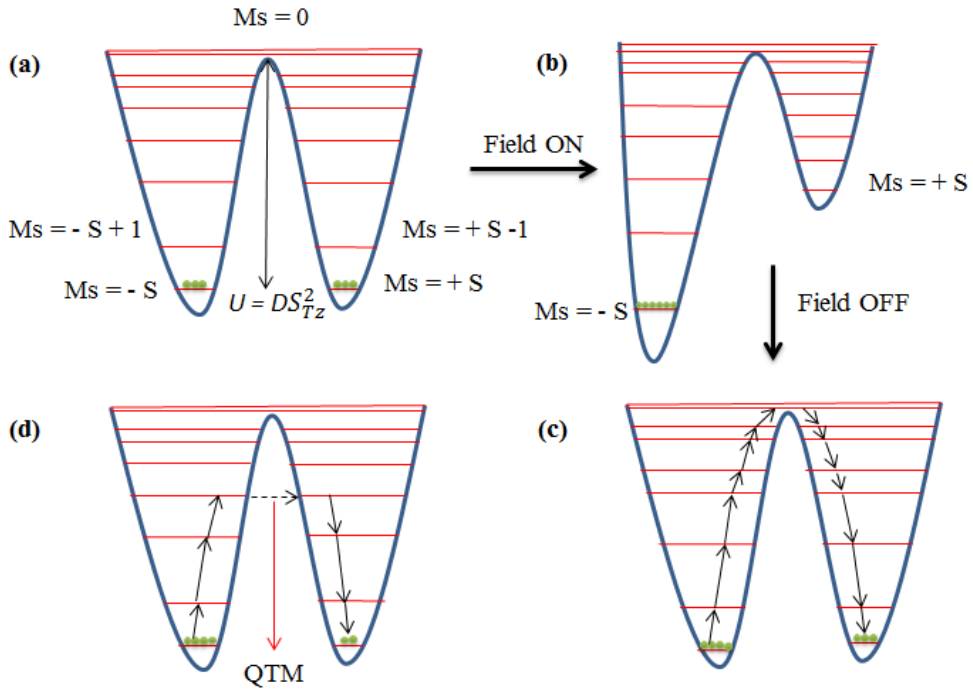

Figure I.11. Schematic diagram representing the magnetization and magnetic relaxation processes in SMMs: (**a**) effect of zero-field splitting (ZFS) on a spin state S; the two wells are equally populated; (**b**) application of an external magnetic field (Zeeman effect) on the magnetization of a sample. The left well is selectively populated in a magnetic field; (**c**) representation of slow relaxation of the magnetization over the anisotropy barrier after removing the external magnetic field, tunnel mechanism (ideal pathway); (**d**) quantum tunneling of the magnetization between thermally activated regime.

In general, to detect such a process and determinate its barrier to relaxation of magnetization in SMMs, temperature dependent alternating current (*ac*) susceptibility measurements are needed (weak field, typically 1 - 5 Oe, oscillating at a given frequency, ν_{exp}). This susceptibility manifests itself as a frequency dependent signal: in the phase (χ') and out-of phase (χ'') components of the ac susceptibility:

$$\chi_{ac} = \chi' + i\,\chi'' \qquad \textbf{Eq. I.8}$$

The presence of out-of-phase χ'' components suggests that the magnetization of the complex is not alternating as quickly as the phase of the field because of the energy barrier to spin reversal (this is an indication that the compound is an SMM). When the relaxation time τ of the compound is shorter than the characteristic experimental time τ_{exp} ($\tau_{exp} = (2\pi\nu_{exp})^{-1}$), the magnetization vector is oscillating with the *ac* field, and only a static behavior is observed (only the real component χ'). However, when τ is longer, a dynamic behavior is perceived and the magnetization vector is dephased (non-zero imaginary component χ''). Experimentally, we can measure χ'' versus temperature at fixed frequency (Figure **I.12, left**), or/and χ'' versus frequency at fixed temperature. The temperature or frequency where χ'' reaches its maximum value corresponds to the so-called blocking temperature (T_B), or blocking frequency (ν_B), respectively. The relaxation time (τ) can be deduced from the maxima of the $\chi''(T)$ and/or $\chi''(\nu)$ curves at T_B, and/or ν_B Figure **I.12**. Because of the maximum peak of $\chi''(T)$ or $\chi''(\nu)$ at which the angular frequency (ω) of the oscilating magnetic field is equal to the rate of spin revearsal ($1/\tau$), the extracted kinetic data permit to construct an Arrhenius plot. For the thermally activated regime over a single energy barrier, a plot of τ *vs* 1/T should be linear according:

$$\tau = \tau_0 \cdot \exp\left(\frac{U_{eff}}{k_B T}\right) \qquad \textbf{Eq. I.9}$$

where the τ_0 is a preexponential factor, k_B is the Boltzmann constant, and U_{eff} is the energy barrier. From Eq. I.9 we can deduce that higher temperature means smaller relaxation time.

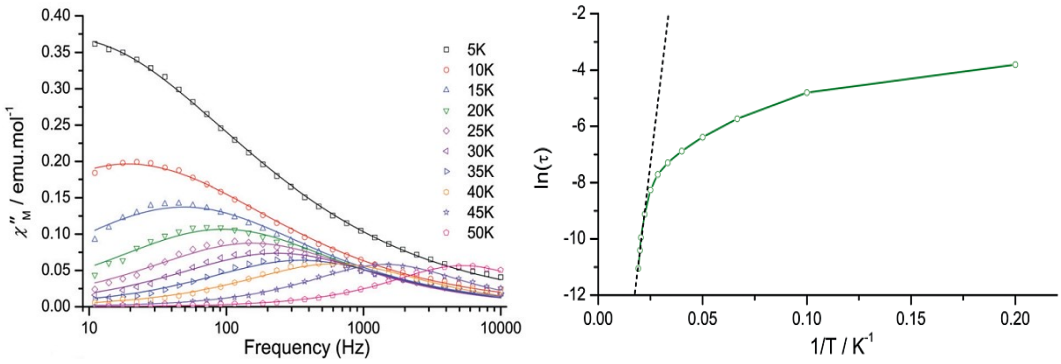

Figure I.12. (Left) Frequency dependent plot of the out-of-phase ac-magnetic susceptibility $\chi''_M(\nu)$ for [TBA][TbPc$_2$], between 5 and 50 K. [44f] (right) Arrhenius plot for [TBA][TbPc$_2$] extracted from the susceptibility plots of $\chi_{ac}(T)$. The dotted lines correspond to the linear fits of the thermally activated regimes of all three compounds.

Because SMM systems are composed of two parts, the spin system and the lattice system, the interaction between spin and lattice vibrations (phonons) offers an additional relaxation pathway. One of the

reasons of the deviation from liniearity of the Arrhenius plots is the presence of quantum tunneling of magnetization (QTM). This phenomenon mainly occurs at very low temperature (below 10 K) in cases where intermediate sublevels on either side of energy are degenerate and mixed to some extent, and $+m_S$ and $-m_S$ levels are equal in energy, facilitating a transition from one site to the other side almost instantly with no energy required. In many cases, QTM occurs competing with the thermal relaxation process below a certain temperature. Such kind of relaxation process implying both regimes is known as the quantum-assisted thermal regime Figure **I.11, (d)**. QTM can be effectively suppressed by performing the *ac* magnetic measurements in the presence of an external *dc* field, resulting in significant improvement of the ac response of the complex. The application of the *dc* field reduces the extent of sublevel mixing, which results in a lower rate of tunneling and allows the magnetization to relax predominately through the thermal regime down to lower temperatures. The presence of these SMM characteristics are also discussed based on experimental data in Chapter IV.

I.8. Objectives of This Research Work

Liquid crystalline materials combine order and mobility [59]. The premise of the formation of a liquid crystalline phase, which combines long-range order with the mobility of fluids, is the shape anisotropy of mesogens. While a rigid core, which often consists of aromatic rings, induces structural order, a flexible part, for example flexible alkyl chains, provides for necessary mobility within the liquid crystalline phase. Discotic liquid crystals based on large π-conjugated molecules are attractive to improve the charge carrier mobility. The stacking of discotic molecules into columns facilitates the π-π overlap, and charge transport by a repeated electron hopping process [60].

Phthalocyanine and its metal complexes are one of the most promising classes of molecules because of physicochemical properties such as: high chemical and thermal stability, an extended conjugated 18-π electron system, strong absorption in the visible region, presence of a metal in the central cavity, and the possibility to incorporate a variety of substituents. The design of novel functionalized phthalocyanines by attaching alkyl side chains, in order to induce liquid crystal properties and then use them as an organic semiconductor materials in electronic devices, is still a challenge. In this work, we aim to design and study the physico-chemical properties of new regioregular α-tetra alkylsubtituted M(II/III) phthalocyanines. In order to avoid addition of exceedingly large substituents, while at the same time favoring low clearing temperatures and maintaining the columnar order at ambient temperature, we consider that four-fold α-substitution offers yet unexplored opportunities. Because the four-fold substitution of the Pc core leads to a mixture of four regioisomers and the regioselectivety is a priority in order to obtain electronically homogeneous materials, this strategy poses indeed a synthetic challenge.

We present the electronic behavior in solution-processed organic diodes of metal-free (H_2-) and metalated (Cu- and Ni-) tetraoctylbutyl-PCs in order to correlate the optoelectronic properties with molecular organization and film structure (in chapter III). The phthalocyanine dianion (Pc^{2-}) gives an opportunity to introduce different metal ions, which constitutes an efficient means to vary the physico-chemical properties.

When bearing a paramagnetic central metal ion, phthalocyanine may give rise to original magnetic properties such as single molecule magnet (SMM) behavior. Based on this, the mononuclear Mn (III) tetra-α-2-butylhexyloxy-phthalocyanine, Dy(III) tetra-α-2-butylhexyloxy-monophthalocyanine and the corresponding monoleptic double decker Pc were synthesized and their magnetic properties studied (in chapter IV). Using the functionalized metal-free phthalocyanine in the synthesis of the SMM compounds is found to an enhance the solubility of the system in most solvents, but without providing liquid crystal properties.

I.9. References

[1] a) C. Tschierske;*Curr. Opin. Colloid Interface Sci.*, **2002**, 7, 355–370; b) Collings, P. *Introduction to Liquid Crystals, Chemistry and Physics,* Taylor & Francis: London, **1997.**

[2] T. Niori; T. Sekine; J. Watanabe; T. Furukawa; H. Takezeo; *J. Mater. Chem.,* **1966**, 6, 1231.

[3] S. Chandrasekhar; B. K. Sadashiva; K. A. Suresh; *Pramana,* **1977**, 9, 471.

[4] D. Demus; J. W. Goodby; G. W. Gray; H. W Spiess; V. Vill; (Eds) *Handbook of Liquid Crystals*, Wiley-VCH:Weinheim, **1998**.

[5] P. A. Heiney; *Handbook of Liquid Crystals*; J. W. Goodby; P. J. Collings; T. Kato; C. Tschierske; H. F. Gleeson; P. Raynes; Eds.; Wiley-VCH: Weinheim, **2014**; Vol. 4, 521–568.

[6] a) A. M Levelut; *J. Chim. Phys.*, **1983**, 80, 149–161; b) C. Destrade; P. Foucher; H. Gasparoux; N. H. Tinh; A. M Levelut; J. Malthete; *Mol. Cryst. Liq. Cryst.*, **1984**, 106, 121–146.

[7] a) K. Praefcke; D. Singer; B. Kohne; M. Ebert; A. Liebmann; J. H. Wendorff; *Liq. Cryst.*, **1991**, 10, 147–159; b) K. Praefcke; D. Singerl; M. Langner; B. Kohne; M. Ebert; A. Liebmann; J. H. Wendorff; *Mol. Cryst. Liq. Cryst. Sci. Technol., Sect. A,* **1992**, 215, 121–126; c) H. K. Bisoyi; S. Kumar; *Chem. Soc. Rev.*, **2010**, 39, 264–285; d) C. Tschierske; D. J. Photinos; *J. Mater. Chem.*, **2010**, 20, 4263–4294.

[8] U. J. Al-Hamdani; *Int. J. Mol. Sci.,* **2011**, *12*, 3182-3190.

[9] F. G. Starkulla; E. Kapatsina; A. Baro; F. Giesselmann; S. Tussetschlager; M. Kaller; S. Laschat; Beilstain *J. Org. Chem.*, **2009**, 5, 63.

[10] P. Apostol; A. Bentaleb; M. Rajaoarivelo; R. Clérac; H. Bock; *Dalton Trans.*, **2015**, 44, 5569-5576.

[11] Y.-H. Lin; Y. Ezhumalai; Y.-L. Yang; C. Liao; H. Hsu; C. Wu; *Crystals*, **2013**, 3, 339-349.

[12] a) S. K. Prasad; D.S. Shankar Rao; S. Chandrasekhar; S. Kumar; *Mol. Cryst. Liq. Cryst.*, **2003**, 396, 121-139; b) J. Szydłowska; P. Krzyczkowska; M. Salamończy; E. Górecka; D. Pociechaa; B. Maranowski; A. Krówczyński; *J. Mater. Chem. C*, **2013**, 1, 6883-6889.

[13] a) T. Geelhaar; K. Griesar; B. Reckmann; *Angew. Chem., Int. Ed.*, **2013**, 52, 8798–8809; b) M. Bremer, P. Kirsch, M. Klasen-Memmer; K. Tarumi; *Angew. Chem., Int. Ed.*, **2013**, 52, 8880–8896.

[14] R. J. Bushby; N. Boden; *Handbook of Liquid Crystals*; J. W. Goodby; P. J. T. CollingsKato; C.Tschierske; H. F. Gleeson, P.Raynes; Eds.; Wiley-VCH: Weinheim, **2014**; Vol. 5, 569–602.

[15] W. Pisula; X. Feng, K. Müllen; *Adv. Mater.*, **2010**, 22, 3634– 3649.

[16] a) E. O. Arikainen; B. Neville; R. J. Bushby; J. Clements; B. Movaghar; A. Wood; *J. Mater. Chem.*, **1995**, 5, 2161-2165; b) N. Boden; R. J. Bushby; J. Clements; *J. Chem. Phys.*, **1993**, 98, 5920-5931.

[17] S. Sergeyev; W. Pisula; Y. H. Geerts**;** *Chem. Soc. Rev.*, **2007**, 36, 1902-1929.

[18] R. A. Marcus; *Rev. Mod. Phys.*, **1993**, 65, 599-610.

[19] A. Demenev; S. H. Eichhorn; T. Taerum; D. F. Perepichka; S. Patwardhan; F. C. Grozema; L. D. A. Siebbeles; R. Klenkler; *Chemistry of Materials*, **2010**, 22, 1420-1428.

[20] W. Pisula; K. Müllen; *Handbook of Liquid Crystals*; J. W. Goodby; P. J. Collings; T. Kato; C. Tschierske; H. F. Gleeson; P. Raynes, Eds.; Wiley-VCH: Weinheim, **2014**; Vol. 8, 627– 674.

[21] M. J. Cook; I. Chambrier; in: K. M. Kadish; K. M. Smith; R. Guilard (Eds.); *The Porphyrin Handbook*, vol. 17, Academic Press, San Diego, CA, **2000**, 37–128.

[22] A. Brown; J. Tcherniac; *Ber. Dtsch. Chem. Ges.,* **1907**, 40, 2709.

[23] C. E. Dent; R. P. Linstead; A. R. Lowe, *J. Chem. Soc.*, 1934, 1033.

[24] a) J. M. Robertson; *J. Chem. Soc.*, **1935**, 615; b) J. M. Robertson; *J. Chem. Soc.*, **1936**, 1195; c) R. P. Linstead; J. M. Robertson; *J. Chem. Soc.*, **1936**, 1736; d) J. M. Robertson; I. Woodward; *J. Chem. Soc.*, **1937**, 219; d) J. M. Robertson, I. Woodward, *J. Chem. Soc.*, 1940, 36.

[25] S. M. Tadayyon; et, al., *Org. Electronics*, **2004**, 5, 157-166.

[26] C. Piechocki; J. Simon; A. Skoulios; D. Guillon; P. Weber; *J. Am. Chem. Soc.*, **1982**, 104, 5245–5247.

[27] K. Ohta; H. D. Nguyen-Tran; L. Tauchi; Y. Kanai; T. Megumi; Y. Takagi; in: K.M. Kadish; K.M. Smith; R. Guilard; (Eds.), *Handbook of Porphyrin Science*, vol. 12, World Scientific, **2011**, 1–120.

[28] M. K. Engel; P. Bassoul; L. Bosio; H. Lehmann; M. Hanack; J. Simon; *Liq. Cryst.*, **1993**, 15, 709–722.

[29] a) M. Hanack; A. Beck, H. Lehmann; *Synthesis*, **1987**, 8, 703–705; b) I. Cho; Y. Lim; *Mol. Cryst. Liq. Cryst.,* **1998,** 154, 9–26.

[30]] a) J. F. van der Pol; E. Neeleman; J. W. Zwikker; R. J. M. Nolte; W. Drenth; J. Aerts; R. Visser; S. J. Picken; *Liq. Cryst.,* **1989**, 6, 577–592; b) W. T. Ford; L. Sumner; W. Zhu; Y. H. Chang; P.-J. Um; K. H. Choi; P. A. Heiney; N.C. Maliszewskyj; *New J. Chem.*, **1994**, 18, 495–505.

[31] a) C. Rager; G. Schmid; M. Hanack; *Chem. Eur. J,* **1999**, 5, 280–288; b) B. Görlach; M. Dachtler; T. Glaser; K. Albert; M. Hanack; *Chem. Eur. J.*, **2001**, 7, 2459–2465.

[32] J. Tant; Y. H. Geerts; M. Lehmann; V. De Cupere; G. Zucchi; B. W. Laursen; T. Bjørnholm; V. Lemaur; V. Marcq; A. Burquel; E. Hennebic; F. Gardebien; P. Viville; D. Beljonne; R. Lazzaroni; J. Cornil; *J. Phys. Chem., B*, **2005**, 109, 20315–20323.

[33] a) J. Sleven; T. Cardinaels; C. Görller-Walrand; K. Binnemans; *Arkivoc*, **2003**, 4, 68–82. b) J. Hoogboom; P. M. L. Garcia; M. B. J. Otten; J. A. A. W. Elemans; J. Sly; S. V. Lazarenko; T. Rasing; A. E. Rowan; R. J. M. Nolte; *J. Am. Chem. Soc.*, **2005**, 127, 11047–11052.

[34] M. Durmus; C. Lebrun; V. Ahsen; *J. Porphyr. Phthalocyanines,* **2004**, 8, 1175–1186.

[35] a) A. S. Cherodian; A. N. Davies; R. M. Richardson; M. J. Cook; N. B. McKeown; A. J. Thomson; J. Feijoo; G. Ungar; K. J. Harrison; *Mol. Cryst. Liq. Cryst.,* **1991**, 196, 103–114; b) H. Iino; Y. Takayashiki; J.-I. Hanna; R. J. Bushby; *Jpn. J. Appl. Phys.*, **2005**, 44, L1310–L1312; c) H. Iino; J. Hanna; R. J. Bushby; B. Movaghar; B. J. Whitaker; M. J. Cook; *Appl. Phys. Lett.*, **2005**, 87, 132102.

[36] D. J. Tate; R. Anémian; R. J. Bushby; S. Nanan; S. L. Warriner; B. J. Whitaker; *Beilstein J. Org. Chem.*, **2012**, 8, 120–128.

[37]] S. Tuncel; T. V. Basova; V. G. Kiselev; S. A. Gromilov; I. V. Jushina; M. Durmus; A. G. Gürek; V. Ahsen; *J. Mater. Res.*, **2011**, 26, 2962–2973.

[38] K. Ban; K. Nishizawa; K. Ohta; A. M. van de Craats; J. M. Warman; I. Yamamoto; H. Shirari; *J. Mater. Chem.*, **2001**, 11, 321–331.

[39] a) A. G. Gürek; V. Ahsen; D. Luneau; J. Pecaut; *Inorg. Chem.*, **2001**, 40, 4793–4797; b) A. G. Gürek; T. Basova; D. Luneau; C. Lebrun; E. Kol'tsov; A. K. Hassan; V. Ahsen; *Inorg. Chem.*, **2006**, 45, 1667–1676.

[40] W. T. Ford; L. Sumner; W. Zhu; Y. H. Chang; P. J. Um; K. H. Choi; P. A. Heiney; N. C. Maliszewskyj; *New J. Chem.*, **1994**, 18, 495–505.

[41] a) J. F. van der Pol; E. Neeleman; J. W. Zwikker; R. J. M. Nolte; W. Drenth; J. Aerts; R. Visser; S. J. Picken; *Liq. Cryst.*, **1989**, 6, 577–592; b) K. Ban; K. Nishizawa; K. Ohta; H. Shirai; *J. Mater. Chem.*, **2000**, 10, 1083–1090.

[42] a) T. Komatsu; K. Ohta; T. Watanabe; H. Ikemoto; T. Fujimoto; I. Yamamoto; *J. Mater. Chem.*, **1994**, 4, 537–540; b) T. Basova; E. Kol'tsov; A. K. Hassan; A. Nabok; A. Ray; A. G. Gürek; V. Ahsen; *J. Mater. Sci. Mater. Electron,* **2004**,. 15, 623–628.

[43] a) F. Maeda; K. Hatsusaka; K. Ohta; M. Kimura; *J. Mater. Chem.*, **2003**, 13, 243–251; b) A. M. van de Craats; J. M. Warman; H. Hasebe; R. Naito; K. Ohta; *J. Phys. Chem. B*, **1997**, 101, 9224–9232; c) J. Sleven; C. Görller-Walrand; K. Binnemans; *Mater. Sci. Eng. C,* **2001**, 18, 229–238.

[44] a)M. Gonidec; F. Luis; A. Vilchez; J. Esquena; D. B. Amabilino; J. Veciana; *Angew. Chem. Int. Ed*. 2010, **49**, 1623-1626; b) S. Sakaue; A. Fuyuhiro; T. Fukuda; N. Ishikawa; *Chem. Commun.*, **2012**, 48, 5337-5339; c) F. Branzoli; P. Carretta; M. Filibian; G. Zoppellaro; M. J. Graf; J. R. Galan-Mascaros; O. Fuhr; S. Brink; M. Ruben; *J. Am. Chem. Soc.*, **2009**,131, 4387-4396; d) N. Ishikawa; M. Sugita; T. Ishikawa; S.-Y. Koshihara; Y. Kaizu; *J. Am. Chem. Soc.*, **2003**,125, 8694; e) N. Ishikawa; M. Sugita; W. Wernsdorfer; *J. Am. Chem. Soc.*, **2005**, 127, 3650-3651; f) M. Gonidec; D. B. Amabilinoa; J. Veciana; *Dalton Trans.*, **2012**, 41, 13632-13639.

[45] K. H. J. Buschowand; F. R. de Boer; *Physics of Magnetic Materials*, World Scientific, **1985**.

[46] a) R. Sessoli; L. Hui; A. R. Schake; S. Wang; J. B. Vincent; K. Folting; D. Gatteschi; G. Christou; *J. Am. Chem. Soc.,* **1993**, 115, 1804; b) R. Sessoli; D. Gatteschi; A. Caneschi; M. A. Novak; *Nature,* **1993**, 365, 141; c) R. Bagai; G. Christou; *Chem. Soc. Rev.*, **2009**, 38, 1011–1026.

[47] R. L. Carlin; *Magnetochemistry,* Springer-Verlag, Berlin, Heidelberg, **1986**.

[48] F. Branzoli; P. Carretta, M. Filibian, G. Zoppellaro; M. Graf; J. Galan-Mascaros; O. Fuhr; S. Brink; M. Ruben; *J. Am. Chem. Soc.,* **2009**, 131, 4387-4396.

[49] a) J. M. Zadrozny; J. Liu; N. A. Piro; C. J. Chang; S. Hill; J. R. Long; *Chem. Commun.,* **2012**, 48, 3927–3929; b) J. Vallejo; I. Castro; R. Ruiz-García; J. Cano, M. Julve; F. Lloret; G. De Munno; W. Wernsdorfer; E. Pardo; *J. Am. Chem. Soc.*, **2012**, 134, 15704–15707; c) E. Colacio, J. Ruiz, E. Ruiz, E. Cremades, J. Krzystek, S. Carretta, J. Cano, T. Guidi, W. Wernsdorfer and E. K. Brechin, *Angew. Chem., Int. Ed.*, **2013**, 52, 9130–9134; d) K. S.

Pedersen; M. Sigrist; M. A. Sørensen; A. L. Barra; T. Weyhermueller; S. Piligkos; C. A. Thuesen; M. G. Vinum; H. Mutka; H. Weihe; R. Clérac; J. Bendix; *Angew. Chem., Int. Ed.*, **2014**, 53, 1351–1354.

[50] L. Sorace; C. Benelli; D. Gatteschi; *Chem. Soc. Rev.*, **2011**, 40, 3092.

[51] a) M. L. Kahn; J.-P. Sutter; S. Golhen; P. Guionneau; L. Ouahab; O. Kahn; D. Chasseau; *J. Am. Chem. Soc.*, **2000**, 122, 3413; b) M.L. Kahn; R. Ballou; P. Porcher; O. Kahn; J.-P. Sutter; *Chem. Eur. J.*, **2002**, 8, 525; c) C. Benelli; D. Gatteschi; *Chem. Rev.*, 2002, 102 2369.

[52] J. D. Rinehart; J. R. Long; *Chem. Sci.*, **2011**, 2, 2078.

[53] D. Gatteschi; R. Sessoli; F. Villain; *Molecular Nanomagnets*, Oxford University Press, Oxford, **2006**.

[54] D. Aravena; E. Ruiz; *Inorg. Chem.*, **2013**, 52, 13770.

[55] J. D. Rinehart; J. R. Long; *Chem. Sci.*, **2011**, 2 2078.

[56] O. Kahn; *Molecular Magnetism*, Wiley-Blackwell, New York, **1993**,. 396.

[57] a) S. Mitra; *Prog. Inorg. Chem.*, **1977**, 22, 309; b) B. N. Figgis; *Trans. Faraday Soc.*, **1960**, 56, 1553.

[58] H. J. Gerritsen; E. S. Sabinsky; *Phys. Rev.*, **1963,** 132. 1507.

[59] a) P.-G. de Gennes, *Angew. Chem.*, **1992**, 104, 856; b) *Angew. Chem. Int. Ed. Engl.*, **1992,** 31, 842.

[60] a) H. Bässler, *Phys. Status Solidi B,* **1993**, 175, 15; b) N. Boden; R. Bushby; J. Clements; B. Movaghar; K. Donovan; T. Kreouzis; *Phys. Rev. B,* **1995**, 52, 13274; c) H. Cordes; S. Baranovskii; K. Kohary; P. Thomas; S. Yamasaki; F. Hensel; J.-H. Wendorff; *Phys. Rev. B,* **2001**, 63, 094201; d) K. Kohary; H. Cordes; S. Baranovskii; P. Thomas; S. Yamasaki; F. Hensel; J.-H. Wendorff; *Phys. Rev. B,* **2001**, 63, 094202.

Chapter II

Tetra-*α*-substituted Phthalocyanines and their Liquid Crystal Order

Table of Contents for Chapter II:

II.1. Introduction

II.1.1. Substitution Pattern and Liquid Crystal Behavior

When Piechocki et al. demonstrated for the first time mesogenicity in a substituted phthalocyanine ($CuPc\text{-}op\text{-}C_1OC_{12}$) with a remarkably large thermal range from 50 to > 300°C where the phthalocyanine molecules self-assemble into columns which form a 2-dimensional lattice [1], this opened up the perspective of using mesogenic phthalocyanines as anisotropic electronic conductors. The phthalocyanines exhibit a small intermolecular distance in the columns, and the π-π orbital overlapping of the aromatic cores facilitates the charge transport along the columns [2]. Therefore, these molecular objects appear to be promising units for the development of devices, such as molecular transistors, organic diodes etc. [3]. Such devices are operated mostly at room temperature. Therefore it is a priority to synthesize new mesogenic phthalocyanines which exhibit liquid crystal behavior close to ambient conditions. If linear side chains are attached directly and exclusively to the β-substitution positions, the resulting mesogenic phthalocyanines frequently exhibit a very high clearing temperature of more than 300°C [4]. At these high temperatures, the partial or total decomposition of these systems precludes homogeneous alignment of the columns by annealing in the vicinity of the clearing point. To lower this transition temperature to the isotropic liquid to a more workable value, eight or four very voluminous side chains have been introduced in some cases [5]. If the Pc core is surrounded by a vast amount of insulating alkyls chains, this reduces considerably the part of the electronically relevant aromatic core in the material [6[a, b]]. In order to avoid random variations in the π electronic system between molecules, the substitution should be into well-defined positions of the phthalocyanine core, avoiding electronically non-identical regioisomers.

This chapter deals with the synthesis and characterization of liquid crystal $M^{II}Pc$ derivatives. The chapter starts with the reasons for our choice of a non-peripheral substitution pattern, followed by a description of previously reported studies and of our studies of three series of Pcs that are α-substituted with four β-branched alkyl chains.

II.1.1.1. Why Regiosymmetrically Tetra-α-substituted Pcs?

The literature abounds with tetra- and octa-substituted metal–free and metalated phthalocyanine compounds, however only a very limited number of tetra-α-substituted phthalocyanines are known. Regio-randomly tetra-substituted phthalocyanines are usually more soluble than the corresponding octa-substituted phthalocyanines due to the formation of constitutional isomers and due to the dipole moment that results from the unsymmetrical arrangement of the substituents at the periphery [7[a, b]]. Substitution at the more sterically crowded α position reduces the aggregation tendencies compared to substitution at the β position [8[a, b]]. The cyclotetramerisation of substituted phthalonitrile leads to a mixture of four regioisomers, of which the most symmetrical (1,8,15,22-substituted) isomer of C_{4h} symmetry forms statistically in 12.5% yield, whilst the least symmetric (1,8,15,25-substituted) C_s isomer forms in 50% yield, if electronic and steric effects are negligible [9]. To avoid the mixture of regioisomers, and thus of variations in the π electron system between individual molecules, we set out to develop a regiospecific synthetic approach to tetra-subtituted phthalocyanines.

Rager et al. showed that in the presence of templating transition metal ions such as Ni^{II} or Cu^{II}, the yields of C_{4h} and C_s isomers from 3-alkoxyphthalonitriles are close to these statistically expected values. On the other hand, they found that if 3-(2-ethylhexyloxy)phthalonitrile is tetramerized with lithium alcoholate in the absence of templating transition metal ions, the sterically favored C_{4h} isomer is formed in 87% relative yield, together with 11% of the statistically favored C_s isomer, and 2% of the (1,8,18,25-substituted) C_{2V} isomer, whilst the sterically most hindered (1,11,15,25-substituted) D_{2h} isomer is not observed [9]. Although Rager et al. did not report liquid crystalline properties for their 1,8,15,22-tetrakis-(2-ethylhexyloxy)-phthalocyanine, we presumed that four such β-branched racemic or symmetrical alkyl substituents should efficiently favor mesophase formation, because they do so in a wide variety of tetra-substituted polycyclic arenes explored at the CRPP in the past [10[a, b, c, d]]. Racemically branched alkyl chains are an efficient means of stabilizing columnar mesophases by inducing a more evenly circular alkyl periphery. As a consequence, a better nanosegregation between aromatic column cores and aliphatic surrounding can be obtained, whilst hindering crystallization due to the presence of a mixture of several stereoisomers (six in the C_{4h} case: RRRR, RRRS, RRSS, RSRS, RSSS, SSSS, a priori with statistical abundances of 1 : 4 : 4 : 2 : 4 : 1).

Besides the expected regioselectivity, the tetra-substituted phthalocyanine derivatives are versatile from the chemical point of view. Their synthesis is cheap, easy and, in addition, it is possible to modify easily the substituents that surround aromatic core.

II.1.1.2. Synthetic Approaches to $M^{II}Pc$ Complexes

A number of ortho-disubstituted benzene derivatives can act as phthalocyanine precursors, of which 1, 2-dicyanobenzene gives particularly high yields. There are basically two synthetic procedures available for making $M^{II}Pc$ complexes. The first approach involves cyclotetramerisation of a phthalonitrile or other phthalic acid derivative in the presence of templating metal ions in a high boiling solvent. The second method is reaction between a metal-free phthalocyanine and an appropriate metal salt (Scheme **II.1**).

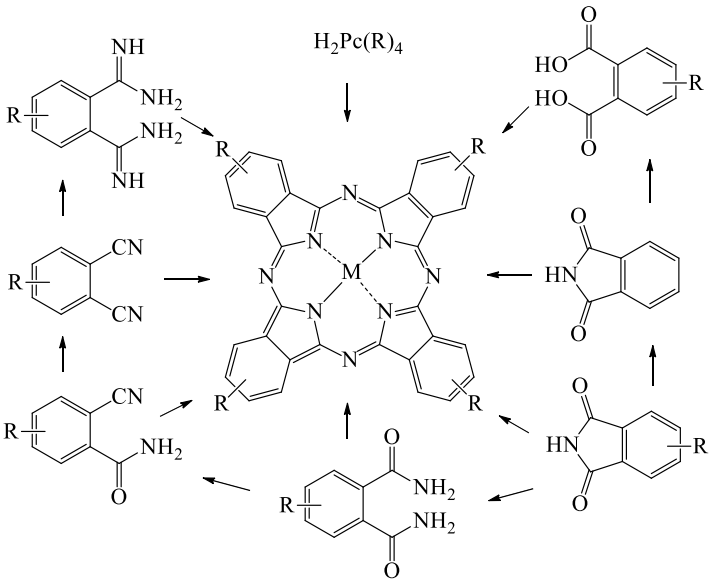

Scheme II.1. Synthetic routes for MPc-t-R.

Peripheral substituents can be introduced into the phthalocyanine core using one of two basic methods. The first approach involves modification of an already existing phthalocyanine core using aromatic electrophilic substitution reactions and cycloaddition reactions [11]. But the fact that unsubstituted phthalocyanines have very low solubility disfavors this synthetic route.

The second basic approach involves the tetramerization of already substituted phthalocyanine precursors, which leads to a controlled number of substituents on the target phthalocyanine (Scheme **II. 2**). For this method useful precursors include substituted derivatives of phthalic acid, anhydride, imide, amide, or nitrile. Phthalonitrile precursors are the most popular choice [12[a, b, c]].

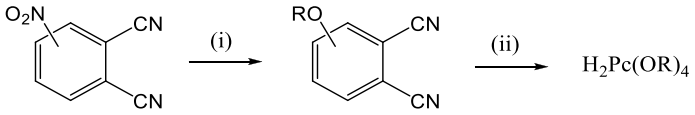

Scheme II.2. Synthesis of tetraalkoxy-substituted phthalocyanines: (i) ROH, DMF, K_2CO_3; (ii) LiOR'/R'OH.

The macrocycle usually exists as Pc^{2-} anion, and it is possible to place about seventy different elemental ions into its central cavity. Metal central ions strongly influence its physical properties. Depending on oxidation state and coordination number of the central atom, the metalated phthalocyanine compounds have various coordination geometries. For example in the case of $M^{II}Pc$ (CuPc, NiPc, ZnPc etc) the coordination symmetry is generally square planar, but can also be square pyramidal [13[a, b, c]] for $M^{III}Pc$, or even octahedral [14]. Lanthanide metal ions form complexes in which two phthalocyanine rings complex with the same ion. These so-called sandwich or double decker complexes have the coordination symmetry of a square antiprism. The complexes $M(Pc)_2$ (M = lanthanide) can be prepared by the template tetramerisation of phthalonitrile with the appropriate lanthanide salt or by direct reaction of the salt with free phthalocyanine ligands [15].

II.2. Functionalization Strategies Towards Liquid Crystalline Pcs

The peripheral substitution on the phthalocyanine aromatic core with aliphatic chains not only enhances the solubility but also induces liquid crystallinity [16]. Since the mesogenicity of Pcs was discovered, many examples of mesogenic phthalocyanines have been prepared by varying the number, length and position of the flexible side chains. Both the structure and pattern of the side chains and the nature of the central metal ion have substantial influence on the structure and thermal stability of the resultant mesophase. Changing number or position (peripheral or non-peripheral) of alkyl chains leads to large variations of transition temperatures and order of the mesophase.

There are many studies of liquid crystal properties of peripherally and non-peripherally substituted phthalocyanines. There often appears a remarkably linear relationship between the clearing point and the side chain length in a given homologous series of phthalocyanine mesogens (Figure **II.1**). Engel et al. [17] reported the influence of chain length on liquid crystallinity of R_8PcM with R: C_5H_{11}, C_6H_{13}, C_8H_{17}, $C_{10}H_{21}$, 2-Et-C_6H_{13} and M= H_2, Ni and Cu. The octa-alkyl substituted Pc complexes are stable up to 410-420°C. At such temperatures, the compounds are unstable in the isotropic phase. The domain of stability of the mesophase

increases with chain length up to the octyl derivative while the clearing temperatures decrease. For the metal-phthalocyanine complexes the transition temperatures are slightly higher than for the metal free phthalocyanine. For all compounds was determined by SAXS a hexagonal packing of the columns and an intercolumnar distance which linearly decreases with increasing alkoxy chain length.

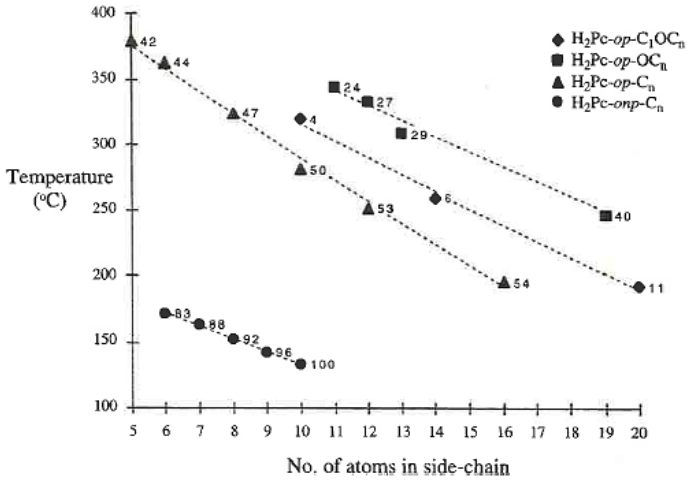

Figure II.1. A plot of side-chain length versus clearing temperatures for four different homologous series of mesogenic H_2Pcs [7, 17].

Octaalkoxy-substituted phthalocyanines are the most extensively studied phthalocyanine LCs. Introducing an oxygen atom in the side chain increases the solubility due to better dipolar interactions with the solvent molecules [17]. Introducing the oxygen atom in the side chains attached directly and exclusively to the peripheral position of the Pc core does not change much the transition temperatures and the mesomorphic structure [18].

Schouten et al. [19] synthesized and described two phthalocyanines peripherally substituted with branched alkoxy chains (H_2Pc12,3 and H_2Pc8,2). Such branched chains lead to more phase transitions detected by calorimetry than were observed for the corresponding homologs of Pcs with straight alkyl side chains. According to X-ray diffraction and optical microscopy both compounds have columnar hexagonal packing. As branched chains reduce the crystal → mesophase transition temperature, the columnar hexagonal mesophase was observed even at room temperature in case of H_2Pc12,3. Indeed, with sterically demanding branched substituents the columnar mesophase could be stabilized in several cases at room temperature [20[a, b, c]].

In non-peripherally substituted phthalocyanines much more sterical crowding may occur than in peripherally substituted ones. The strongest steric interaction for non-peripheral side chains are between chains facing each other from neighboring benzo-moieties. These interactions probably induce the displacement of some of the side chains out of the plane of the Pc core. This effect can greatly hinder the columnar stacking of the molecule at low temperature [21]. Metal-free octa-non-peripherally substituted phthalocyanines with side chains shorter than C_6 did not show any mesophase behavior [22].

Cammidge et al. [23] investigated a series of discotic liquid crystals based on non-peripheral octa(alkoxymethyl) phthalocyanines (Figure **II.2**). In all cases, decomposition of the phthalocyanines occurred

between 250 and 290 °C without formation of an isotropic liquid phase; separate samples heated below the decomposition temperatures showed reversible transition from the mesophase into the crystalline state but this was accompanied by supercooling.

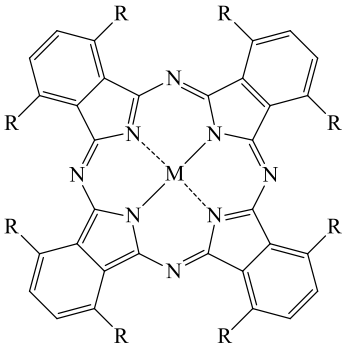

Figure II.2. Chemical structures of octa(alkoxymethyl) phthalocyanine derivatives used by Cammidge et al. [23].

The linear chain derivatives have a crystal–to–mesophase transition temperature between 64 and 185 °C, corresponding to longest straight chain and shortest chain respectively. DSC and POM analyses show that the columnar mesophases at high temperature of the branched chain derivatives have a very different thermotropic behavior than their linear homolog. Both branched derivatives are viscous liquid crystals even at room temperature. The DSC spectra registered a single peak which according to polarized optical microscopy corresponds to reversible clearing to the isotropic liquid.

To avoid excessive sterical crowding, our work has focused on the regioregular tetra- functionalization of the phthalocyanine in non-peripheral positions of the aromatic core with branched alkyl chains (Section II. 3). Several $M^{II}Pc$ complexes were synthesized from the metal free homolog (Scheme **II.3**). At first we used chains derived from racemic 2–butyloctanol, expecting a more efficient suppressing of crystallization by the electronically irrelevant, but sterically relevant presence of enantio- and diastereoisomers. We also chose 2-butyloctanol in the hope that the stronger crowding compared to Rager's 2-ethylhexyl would induce complete regioselectivety during the tetramerization. A next part of our work was the synthesis and study of phthalocyanines with branched but sterically well-defined substituents in α-position. We have chosen two symmetrically branched alkyl chains as substituents (Scheme **II.4**). Our goal was to follow how the symmetric alkyl chain, with either identical or slightly smaller mass than branched 2-butyloctyl chain, would influence the temperatures of the crystal-mesophase transition. We also were interested in probing the regioselectivity of the tetramerization of moderately sized symmetrically branched chains compared to 2-ethylhexyl and 2-butyloctyl. The phthalocyanine complexes of the metal ions M^{II} = Co^{II}, Ni^{II},Cu^{II}, Zn^{II}, were prepared, analyzed and compared.

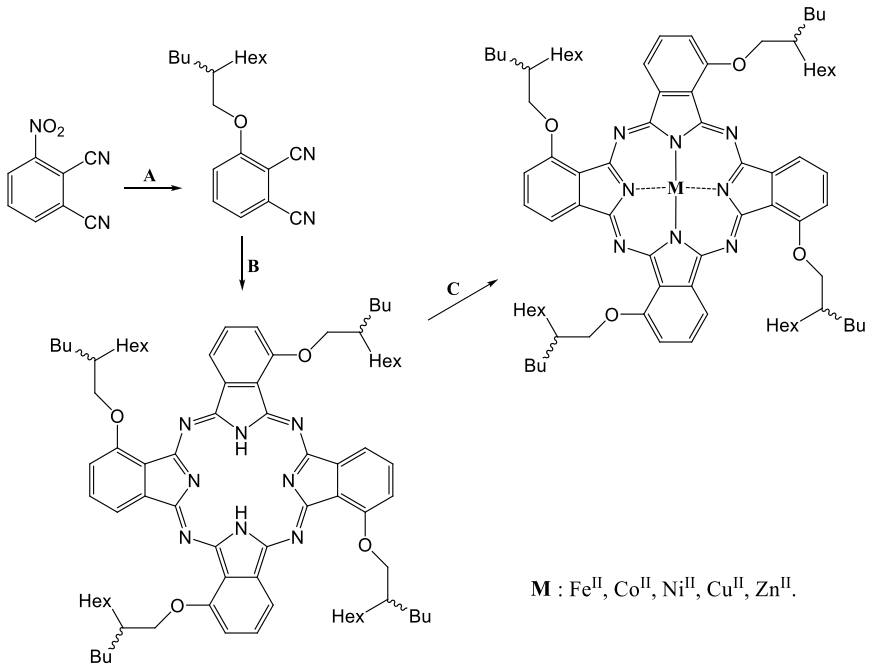

Scheme II.3. Synthesis of 1,8,15,22,-tetra(2-butyloctyloxy)-phthalocyanine and its metal (II) complexes. **A**: rac-2-butyloctanol, K_2CO_3, DMF, 25°C, 7 days; **B**: lithium octanolate/octanol, 100-130 °C, 3 hours, then water; **C**: $M(OAc)_2$, DMF, reflux under Ar. 12 hours. Hex=n-hexyl.

II.3. Functionalization of $M^{II}Pc$ with Racemic Branched Alkoxy Chains

II.3.1. Synthetic Procedures

1, 8, 15, 22-Tetra(2-butyloctyloxy)phthalocyanine was prepared following conditions similar to those used by Rager et al. [9]. We replaced 2-ethylhexanol by 2-butyloctanol in the reaction with 3-nitrophthalonitrile (**1a**) and cyclized the so-obtained 3-(2-butyloctyloxy)phthalonitrile (**2a**) to the corresponding phthalocyanine. The 3-(2-butyloctyloxy)phthalonitrile was obtained by nucleophilic substitution of the nitro group in 3-nitrophthalonitrile with 2-butyl-1-octanol in DMF in the presence of K_2CO_3 for one week at room temperature (see Supporting Material, Section II.7.1.1). Since the (electron withdrawing) nitrile group is an activator toward nucleophilic substitution, it allows the benzene carbon to which it is bonded to have a positive charge. The carbocation become bonded to the aromatic π-system which allows the ipso carbon to temporarily bond with the nitro group ($-NO_2$) and alkoxy group. In order to return to a lower energy state, either the alkoxy group leaves, or the nitro group leaves. In solution both processes happen. As consequence a small amount of intermediate loses the nitro group to become the 3-(2-butyloctyloxy)phthalonitrile, while the rest return to form the reactant. As the 3-(2-butyloctyloxy)phthalonitrile is of the lowest energy, it will not return to form the reactant. To reach the chemical equilibrium that favors the 3-(2-butyloctyloxy)phthalonitrile, the reaction takes a rather long time. Due to the long branched alkyl chain, the 3-(2-butyl octyloxy)phthalonitrile has a high solubility in most of the solvents, but we succeeded in isolating it by crystallization from a 1:2 ethanol : water mixture. The corresponding 1, 8, 15, 22-tetra(butyloctyloxy)phthalocyanine (**3a**) was synthesized by cyclotetramerisation of 3-(2-butyloctyloxy)phthalonitrile in the presence of lithium octanolate in octanol under argon under temperature increase over 2 hours from 100 to 130 °C. The lithium tetraalkoxy phthalocyanine was

treated with aqueous hydrochloric acid. The metal-free ligand was purified by column chromatography in chloroform on silica gel (see Supporting Material, Section II.7.).

The phthalocyanine complexes of the divalent transition metal ions M^{II} = Fe^{II} (**4a**), Co^{II} (**5a**), Ni^{II} (**6a**), Cu^{II} (**7a**), and Zn^{II} (**8a**) were synthesized by treating the metal free phthalocyanine with excess of $M(CH_3COO)_2$ in refluxing DMF for 12 hours under argon. All compounds were purified by column chromatography in chloroform on silica gel. The iron (II) 1, 8, 15, 22-tetra(butyloctyloxy)phthalocyaninate was synthesized by treating the metal free phthalocyanine with a small excess of $Fe(CH_3COO)_2$ in DMF at 100°C for 12 hours in the inert atmosphere of the glove box (see Supporting Material, Section II.3.). The cooled green emulsion of Fe^{II}Pc was filtered. The filtrate was kept for one week in the glove box. The high concentration of the solution leads to the slow appearance of a crystalline precipitate. Moreover, single crystals suitable for X-ray diffraction were obtained by this procedure. Purification of the Fe^{II}Pc using the column chromatography was excluded, because of the instability of Fe^{II} which easily oxidizes in ambient condition. As evident sign of oxidation a changing of color was observed from green to the characteristic brown color of Fe^{III}. The structural and physical properties of the synthesized complexes were characterized by ^{1}H NMR, X-ray for FePc, DSC, POM, SAXS, and elemental analysis.

II.3.1.2. Analytical Characterizations of M^{II}Pc Complexes

II.3.1.2.1 ^{1}H NMR Spectroscopic Analyses

The nucleophilic substitution of the nitro group in 3-nitrophthalonitrile with 2-butyl-1-octanol was confirmed by ^{1}H NMR spectra where a doublet peak is observed at δ = 4 ppm corresponding to the methylene group (H_d) of the substituted alkoxy chain (Figure **S.II.1**.). The phthalocyanine molecule contains four isoindoline units. The cyclotetramerisation of a 3-substituted phthalonitrile could lead to appearance of a mixture of four isomers of respectively C_{4h}, D_{2h}, C_{2v} and C_s symmetry (Figure **II.3**).

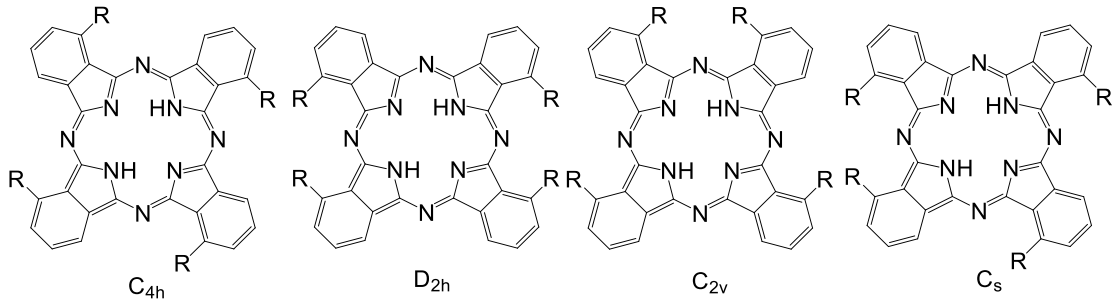

Figure II.3. Four possible positional isomers of tetrasubstituted phthalocyanine obtained from tetramerisation of a 3-substituted phthalonitrile.

According to the previous study of separation of four possible structural isomers of α-tetra substituted phthalocyanine by Hanack et al. [24], if the isomers C_{4h}, C_s, C_{2h} and C_{2v} are considered as pairs of isoindoline units, the alkoxy groups may or may not be neighbors. When alkoxy groups are neighbors, the electron density around of the H_a protons increases, explaining why signals are shifted downfield. According to this, the isomer with C_{4h} symmetry has only -CH_2O- signals between δ = 4.5 and 4.4 ppm. In comparison, the isomer with D_{2h}

symmetry shows the corresponding signal between δ = 5 - 4.85 ppm. In the cases of the C_s and C_{2h} isomers the spectra exhibit two -CH_2O- signals in 1:1 ratio in the regions around δ ~ 5 and 4.5 ppm respectively. The ^{1}H-NMR spectrum of the metal-free tetra-2-butyloctyloxy phthalocyanine which we synthesized shows only one -CH_2O- signal at about 4.4 ppm, without minor impurity peaks in the -CH_2O- region. We thus were successful in making the tetramerization regiospecific by the controlled increase of bulkiness of the 3-alkoxy substituent in the phthalonitrile, and the isomer obtained must be the C_{4h} isomer: C_s and C_{2h} can be excluded if there is only one -CH_2O- signal, and D_{2h} can be excluded by the rather up-field position, in addition to it, being sterically very disfavored. In the region of the aromatic signals the high symmetry and regiospecifity is confirmed by the the presence of only three distinct signals. The aromatic region of the ^{1}H-NMR spectrum recorded at room temperature of the metal-free phthalocyanine shows three peaks at δ = 9.05, 8.1 and 7.67 ppm, (doublet, triplet, doublet respectively), indicating the sterically controlled exclusive formation of the C_{4h} isomer (Figure **II.4**).

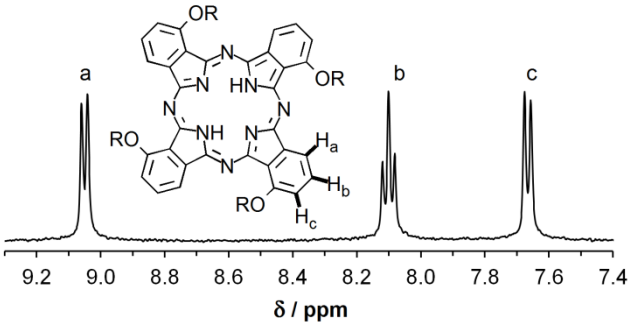

Figure II.4. ^{1}H NMR spectrum of 1, 8, 15, 22-tetra(2-butyloctyloxy)phthalocyanine in CD_2Cl_2 at 298 K. Resonance range of the aromatic region.

II.3.1.2.2. Single crystal X-ray analysis of $[Fe^{II}Pc(OCH_2CHBuHex)_4(DMF)_2]$

Generally, it is difficult to obtain single crystals suitable for X-ray crystallographic studies from substituted phthalocyanines with long alkyl chains. Moreover, if the substituted phthalocyanine compounds are designed to show liquid crystal properties, they usually form fibrous solid crystals if at all that are unsuitable for single crystal studies. The packing arrangements of the molecule are strongly influenced by the size and nature of the axial ligand [25]. Nevertheless, crystals of $[Fe^{II}Pc(OCH_2CHBuHex)_4(DMF)_2]$ (**4a**) suitable for X-ray diffraction were obtained by keeping a concentrated solution of **4** in DMF at room temperature for one week. The single crystal structure of **4** validated the C_{4h} symmetry (Figure **II.5**). In these single crystals obtained, the achiral RRSS isomer of the compound **4** crystallized in a triclinic *P-1* space group, with 2 molecules in the unit cell and half of each in the asymmetric unit. The coordination geometry of the iron (II) atom is octahedral with two dimethylformamide molecules coordinated in axial position, one of them being disordered. The central moiety is planar because the size of the iron(II) ion is appropriate to be accommodated in the central cavity of the Pc ring (Figure **II.6**). Two of the branched alkyl chains are approximately in the plane of the phthalocyanine ring with two having their butyl chains staggered in the plane and another two staggered out of the plane. The shortest distance between planes of phthalocyanine molecules is 8.08 Å with the nearest distance between the central iron ions being 8.8373(4) Å (value of the *a* axis of the unit cell). Structural parameters can be found in

Table **S.II.1**. Crystallographic data showed that the average Fe-N bond lengths for Fe^{II} ions at 120 K are 1.9355 Å. This is typical and representative of a low spin (LS) Fe^{II} bond distances. The X-ray structure and selected bond distances for **4** at 120 K are shown in Figure **II.5**.

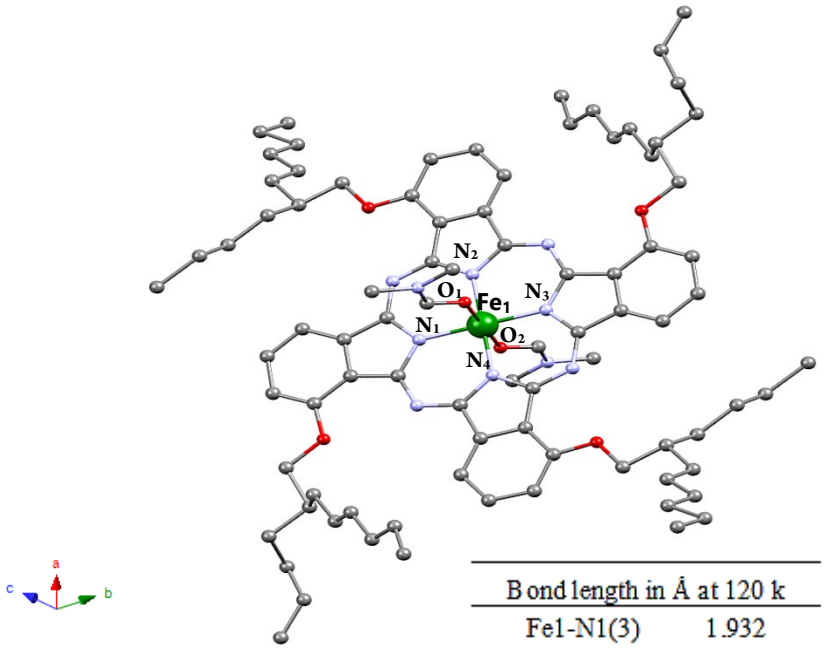

Bond length in Å at 120 k	
Fe1-N1(3)	1.932
Fe1-N2 (4)	1.939
Fe1-O1(2)	2.005

Figure II.5. Perspective view of the crystal structure of $[FePc(OCH_2BuHex)_4(DMF)_2]$ at 120 K. Hydrogen atoms are omitted for clarity. Color scheme: Fe^{II} green, N blue, O red, C gray.

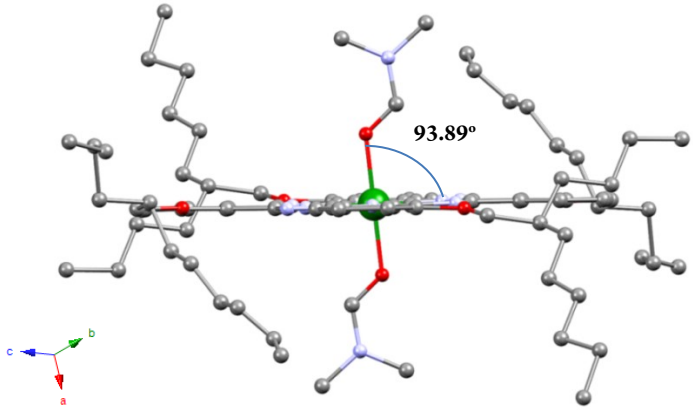

Figure II.6. Perspective view of the crystal structure of $[FePc(OCH_2BuHex)_4(DMF)_2]$ at 120 K, illustrating the planarity of the Pc core.

In octahedral configuration, the metal center produces a crystal field splitting where the d_{z2} and d_{x2-y2} orbitals rise in energy, while the other three orbitals d_{xz}, d_{xy} and d_{yz} are lower in energy. The ligand field runs almost straight into the d_{z2} and d_{x2-y2} orbitals, thus having direct contact with these two orbitals. Due to this direct contact, a lot of electron-electron repulsion occurs between the ligand fields and the d_{z2} and d_{x2-y2} orbitals, which results in the d_{z2} and d_{x2-y2} orbitals having high energy and d_{xz}, d_{xy}, and d_{yz}, are lower in energy. The coordinated DMF induces a strong ligand field which disfavors filling the d_{z2} and d_{x2-y2} orbitals, so that the Fe^{II}

ion apparently is stabilized in low spin configuration. Since the high spin state distributes electrons in a wider space than the low spin state, it makes ionic radii bigger than low spin state. In the octahedral molecular geometry, the ionic radius of Fe^{II} (LS) is 75 pm, while that of Fe^{II} (HS) is 92 pm. Therefore, depending of the system, the bond length for coordinated Fe^{II} (LS) is known to be between 1.85-1.98 Å and 2.0-2.20 Å for coordinated Fe^{II} (HS) [26]. The packing of $FePc(OCH_2HBuHex)_4(DMF)_2]$ shows a tilted columnar structure. The columns form tilted stacks within herringbone arrangements (Figure **II.7**). The molecular planes are arranged face to face along the *a* axis in the *bc* plane, separated by 8.8373(4) Å equal to the *a* parameter of the unit cell.

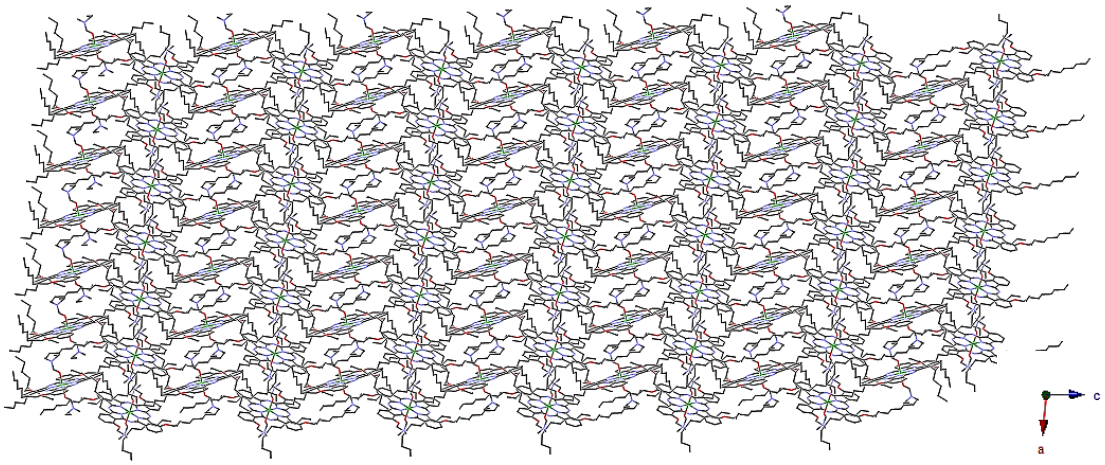

Figure II.7. Packing diagram of $[FePc(OCH_2BuHex)_4(DMF)_2]$ in the *ac* plane, illustrating tilted stacks within herringbone arrangements of the molecules. Color scheme: Fe II green, N blue, O red, C gray.

II.3.1.2.3. UV-Vis Spectroscopic Characterizations

UV-Vis measurements were carried out in $CHCl_3$ solutions. In the electronic absorption spectra of the phthalocyaninate complexes (Figure **II.8**), the typical intense Q-band absorptions are assigned to a π–π^* transition from the HOMO of a_{1u} symmetry to the eg symmetry LUMO.

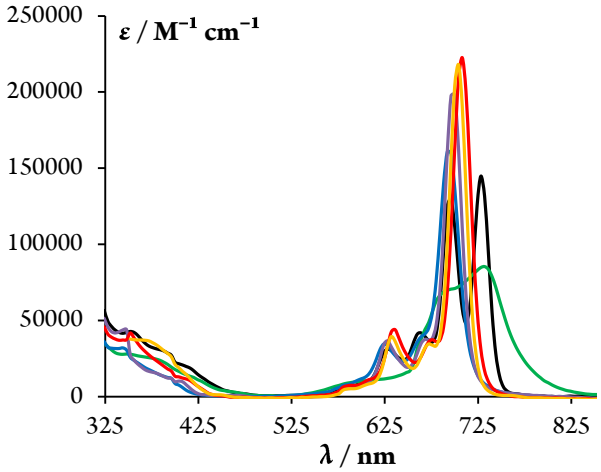

Figure II.8. Absorbtion spectra (5μM in $CHCl_3$) of metal-free 1, 8, 15, 22-tetra(2-butyloctyloxy)phthalocyanine **3a** (black) and corresponding metal(II) phthalocyaninates **4a** (Fe, green), **5a** (Co, blue), **6a** (Ni, purple), **7a** (Cu, red), **8a** (Zn, yellow).

This results in a doubly degenerate first excited state of ^1Eu symmetry [27]. The endoalkoxy substituents have no notable effect on the Q-band's position compared to unsubstituted Pcs. As shown in Figure **II.8**, the split Q-band absorption of the metal-free phthalocyanine **3** appears at around 727 and 698 nm while the metallophthalocyanines give intense single Q-bands at about 700 nm, together with relatively more intense bands (hyperchromic effect) at 667 and 628 nm compared to the corresponding bands of the metal-free phthalocyanine.

II.3.1.2.4. Thermotropic Properties

II.3.1.2.4.1. DSC and Temperature Dependent POM Investigations

The mesomorphic properties of the synthesized complexes were first investigated by temperature dependent polarized optical microscopy (POM), and differential scanning calorimetry (DSC). The observed phase transitions were thereafter determined with small angle X-ray scattering (SAXS) investigations. Thermal data of phase transitions and thermodynamic parameters for metal-free and metal(II) phthalocyanine complexes are summarized in Table **II.1**. Birefringent textures could be observed for metal-free and M^{II} phthalocyanines at room temperature after cooling through the isotropic liquid to liquid crystal phase transition as shown on the polarizing microscope images (Figure **S.II.5**). $H_2Pc(OCH_2CHBuHex)_4$ shows a preferred planar alignment between glass plates with a typical birefringent "fan texture" (Figure.**II.9, a, b**).

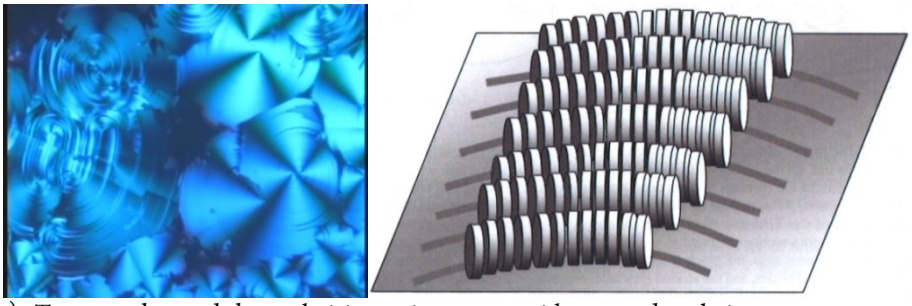

Figure II.9. a) Texture observed by polarizing microscopy with crossed polarizers at room temperature for $H_2Pc(OCH_2CHBuHex)_4$ b) stylized representation of the arrangement of columns in the radiating fan texture of the columnar phase.

The $M^{II}Pc(OCH_2CHBuHex)_4$ have similar alignment tendencies (Figure **S.II.5**). Usually the alignment of the thin films is strongly influenced by film thickness and cooling speed. As a consequence, for $ZnPc(OCH_2CHBuHex)_4$, $CoPc(OCH_2CHBuHex)_4$, $FePc(OCH_2\ CHBuHex)_4$ and $CuPc(OCH_2CHBuHex)_4$, less birefringent domains and near-hexagonal overall growth patterns can be observed, typical of a homeotropic or near-homeotropic alignment (Figure **S.II.5, 4-8**). Whilst disk-shaped mesogens with non-branched alkyl chains usually show their columnar mesophase only upon heating and revert to the crystalline state on cooling to room temperature, many mesogens bearing racemically branched alkyl chains do not transit to the crystalline state when cooling from the temperatures of the liquid and liquid crystalline phases to room temperature. With some racemic-chain materials, a crystalline state can be obtained by crystallization from a solvent, whereas crystallization from the columnar liquid crystalline state of the undiluted material cannot be observed because

crystal nucleation is inhibited by the high viscosity of the liquid crystalline state. With many other racemic chain materials, even precipitation from solution upon cooling does not yield a crystalline powder, but the material separates from solution directly in the waxy columnar liquid crystalline state [28]. As expected, metal-free $H_2Pc(OCH_2BuHex)_4$ and its metal derivatives show textures typical of columnar mesophases at moderate temperatures. The thermotropic properties are strongly dependent of the type of metal ion. Whilst the clearing point of $H_2Pc(OCH_2CHBuHex)_4$ is 192 °C, the clearing temperature of $ZnPc(OCH_2CHBuHex)_4$ (297 °C) and $CoPc(OCH_2CHBuHex)_4$ (292 °C) is about one hundred degrees higher. The clearing points of Cu and Fe homologs are similar, about 30 °C below the Zn and Co homologs, at 268 °C and 262 °C respectively. The compound with the lowest mesophase-isotropic phase transition temperature among the M^{II} homologs is $NiPc(OCH_2CHBuHex)_4$ which clears at 237°C (Figure **S.II.3, 6**). These temperatures are in good agreement with the geometric coordination preferences of the M^{II} ions. The Ni^{II} ion has a tendency to adopt a square planar coordination geometry. Therefore only weak interdisk Ni-N interactions exert a moderate mesophase stabilization manifested by an only moderate rise of the clearing point with respect to the metal-free homolog.

Table II.1. Thermotropic properties of the complexes: cr = crystalline, col_h= hexagonal columnar liquid crystalline; col_r= rectangular columnar liquid crystal-line; $col_{r,p}$ = rectangular columnar plastic crystalline; iso = isotropic liquid

Compound	**Phase sequence (top: first heating of pristine sample, bottom: second heating) [°C]**	**Clearing enthalpy $H_{col-iso}$ [kJ mol^{-1}]**
$H_2Pc(OCH_2CHBuHex)_4$ **(3a)**	cr-84-col_h-192-iso $col_{r,p}$-28-col_h-192-iso	7.7
$FePc(OCH_2CHBuHex)_4$ **(4a)**	cr-col-280-iso col-280-iso	12.0
$CoPc(OCH_2CHBuHex)_4$ **(5a)**	cr-54-col_r-294-iso $col_{r,p}$-42-col_r-294-iso	12.2
$NiPc(OCH_2CHBuHex)_4$ **(6a)**	cr-63-col_r-237-iso $col_{r,p}$-45-col_r-237-iso	9.2
$CuPc(OCH_2CHBuHex)_4$ **(7a)**	$col_{r,p}$-70-col_r-268-iso $col_{r,p}$-70-col_r-268-iso	12.7
$ZnPc(OCH_2CHBuHex)_4$ **(8a)**	cr-96-col_r-297-iso $col_{r,p}$ -80-col_r-297-iso	14.8

In the $ZnPc(OCH_2CHBuHex)_4$, $CoPc(OCH_2CHBuHex)_4$, $FePc(OCH_2CHBuHex)_4$ and $CuPc(OCH_2CHBuHex)_4$ homologs, the metal ions prefer an octahedral/square pyramidal coordination sphere that induces stronger interdisk M-N interactions and, due to the Jahn–Teller effect, leads to relatively high clearing points of the compounds [29].

In the DSC thermogram of $H_2Pc(OCH_2CHBuHex)_4$ between 0 and 250 °C (Figure **S.II.3, 3**), the first heating cycle shows an irreversible peak with a maximum at 92°C (38.6 kJ/mol) which corresponds to melting of a crystalline state and to the formation of a mesophase. The second peak observed at 192°C is corresponding to the clearing point. On cooling, no thermal hysteresis is observed for the clearing point (192 °C). On the

second heating cycle, a reversible small-enthalpy transition at around 40°C is observed. The DSC thermograms of $CoPc(OCH_2CHBuHex)_4$, $NiPc(OCH_2CHBuHex)_4$, and $ZnPc(OCH_2CHBuHex)_4$ show a similar thermal behavior. The first heating cycles show a melting peak for Co (54°C, 33.0 kJ/mol), Ni (63°C, 39.1 kJ/mol) and Zn (96 °C, 44.2 kJ/mol). In the case of $CuPc(OCH_2CHBuHex)_4$, no strong melting peak is observed in the first heating cycle, and the first and second heating cycles show no notable difference. This points to separation from solution of the compound directly in a waxy columnar liquid crystalline state. No noteworthy thermal hystereses between the heating and cooling DSC traces could be observed for clearing points of all homologs. On second heating, poorly expressed small-enthalpy transitions were detected between room temperature and 100°C for all M^{II} derivatives. These could be the signature of either (i) a transition between two mesophases of different column lattices, (ii) a mesophase-to-mesophase transition involving only an increase of inter-molecular order without change of column lattice, or (iii) a glass transition involving no increase of structural order.

II.3.1.2.4.2. Small Angle X-ray Scattering (SAXS) Investigations

Besides the POM and DSC studies, the arrangement of the molecules in the mesophase was investigated in much more detail by temperature dependent small angle X-ray scattering measurements for all compounds. Temperature dependent SAXS measurements were performed on cooling the sample from 160 °C to room temperature. In the pattern collected at 160 °C, for the metal free homolog **3a** three strikingly atypical diffraction peaks for the hexagonal columnar mesophase were detected (Figure **II.10**). Reflections observed in the low-angle region are in the ratio of $1:\frac{\sqrt{7}}{2}:\sqrt{3}$ and were indexed as (200), (210), (220). Whilst density considerations confirm that the main peak corresponds as usual to the distance between neighboring columns, the unusual closeness of the secondary (210) peak indicates that the main peak is the (200) peak instead of the usual (100) peak. As the result we were able to index all of the observed reflections (Figure **II.10**) on a hexagonal lattice. The average unit cell parameter was calculated as a = 41.5 Å. Therefore the edges of the hexagonal 2D unit cell span over two instead of one column-to-column distance, and the unit cell contains 12 instead of 3 columns, implying that there are several distinct sets of columns in the lattice.

Usually, hexagonal columnar mesophases consist of columns in which the molecular planes are on average perpendicular to the column axis, whereas the lower symmetry of rectangular columnar mesophases is a result of the tilt of the molecular planes out of the plane perpendicular to the column axis, breaking the circular symmetry of the columns. In addition, usually not all columns are tilted in the same direction, and most rectangular mesophases are made up of two sets of columns distinguished by their different tilt directions. Likewise, having several types of columns in a hexagonal mesophase can be explained by the tilting in some of the columns. Indeed Levelut and co-workers have identified in a chiral hexaalkoxy-triphenylene such a rare hexagonal mesophase with 12 columns per hexagonal unit cell (i.e. 4 columns in the lozenge-shaped minimal unit cell) [30]. In their case, at least 9 columns are tilted, three each in three symmetrically compensating tilt

directions. A similar tilt arrangement can thus be presumed for the high temperature hexagonal mesophase of our metal-free phthalocyanine.

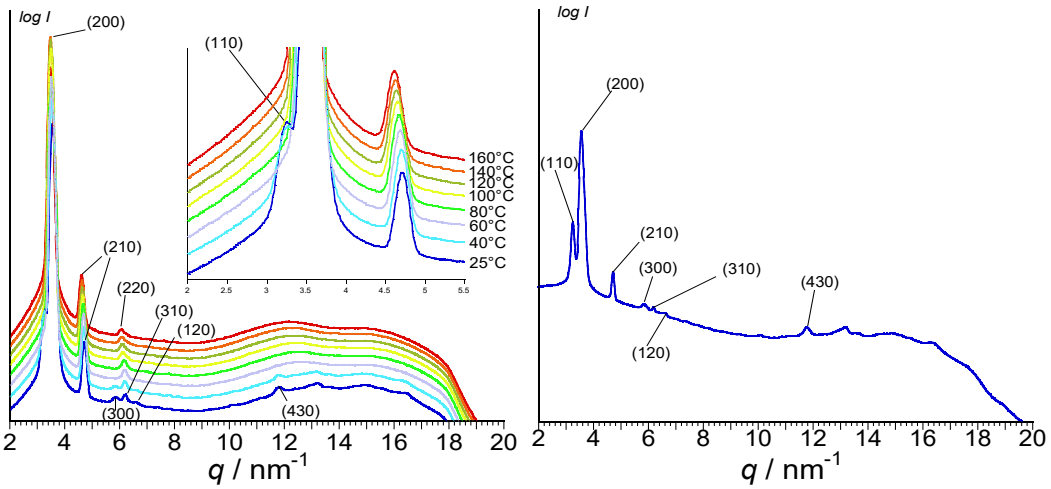

Figure II.10. (left) Indexed SAXS profiles for $H_2Pc(OCH_2CHBuHex)_4$ at different temperature upon stepwise cooling 160 to 25°C; (right) indexed SAXS profiles for metal-free phthalocyanine at 25 °C.

A small enthalpy transition in the DSC thermogram of $H_2Pc(OCH_2CHBuHex)_4$ (**3a**) at low temperature corresponds to the transition from a hexagonal mesophase at high temperature to a rectangular phase at low temperature. This transition is accompanied with the expected increased numbers of diffraction peaks in the rectangular phase due to the lowering of symmetry. This transition is testified by the splitting of a single main diffraction peak at higher temperature into two close (200) and (110) peaks at lower temperature (Figure **II.10**, **right**). Only part of the several high angle reflection appearing in the rectangular phase can be indexed in the frame of the rectangular column lattice as (hkl) = (300), (220), (310) and (120) peaks. This, together with the very small transition enthalpy to the hexagonal mesophase, indicates that the rectangular phase is best addressed as a plastic crystalline phase. The metal-free phthalocyanine is the only compound of the series which shows a hexagonal mesophase at high temperature. All metal complexes directly form a rectangular mesophase upon cooling from the isotropic liquid phase. In all metal homologs, the rectangular lattice is present at high temperatures (about 160 - 60°C). Close to ambient temperature, additional weak peaks in the wide angle region were detected that are not indexable (Figure **II.11, inset** and Figure **S.II.6**) and indicate that this phase exhibits not only order in the two dimensions of the column lattice, but additionally also partial order in the third dimension. This indicates, as in the metal-free homologue, a transition from liquid crystalline to plastic crystalline order. In contrast to the concomitant symmetry change in **3a**, this small-enthalpy transition to plastic crystalline order proceeds in **4a**–**8a** without significant change to the column lattice.

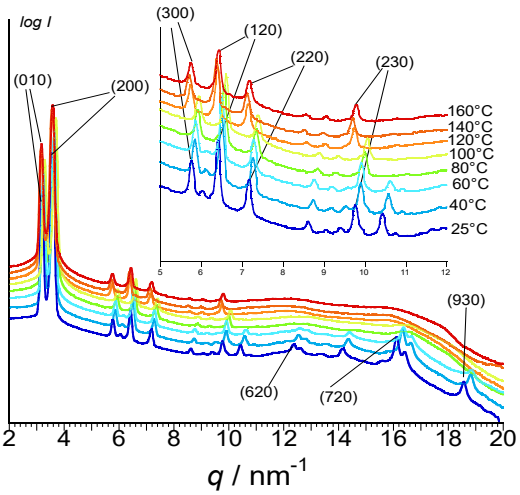

Figure II.11. Indexed SAXS profiles for $CuPc(OCH_2CHBuHex)_4$ at different temperatures upon stepwise cooling from 160 to 25°C.

II.3.1.2.5. Magnetic Measurements

Magnetic susceptibility measurements with *dc* magnetic fields were carried out in order to confirm the spin state value of the $M^{II}Pc(OCH_2CHBuHex)_4$, M = Co^{II}, Ni^{II}, Cu^{II}, Zn^{II}. The magnetic properties of the $H_2Pc(OCH_2CHBuHex)_4$ have also been investigated. Variable-temperature *dc* magnetic susceptibility χT data were collected in the range 1.8-300 K, in a 0.1 T magnetic field. In case of the metal-free phthalocyanine (χ_{dia}= -9.4(5)×10^{-4} cm^3 K mol^{-1}) and its Ni^{II}(χ_{dia}= -8.8(5)×10^{-4} cm^3 K mol^{-1}) and Zn^{II} (χ_{dia}= -9.4(5)×10^{-4} cm^3 K mol^{-1}) derivatives, the expected diamagnetic nature has been confirmed (Figure **S.II.7**). As was expected, the temperature dependence of magnetic susceptibility χ for the Co^{II} and Cu^{II} homolog reveals paramagnetic behavior (Figure **II.12** and **II.13**). At room temperature, the χT product estimated at 0.69 and 0.43 cm^3 K mol^{-1} for $Co^{II}Pc(OCH_2CHBuHex)_4$ and $Cu^{II}Pc(OCH_2CHBuHex)_4$ respectively corresponds well to the expected values for Co^{II} high spin, S = ½, and S= ½ for the Cu^{II} homologue, with a *g* factor of 2.7(1) and 1.96 respectively [31]. Upon cooling, below ca. 60 K, the χT product decreases significantly for the Co^{II} derivative typical for weak antiferromagnetic interaction between S=1/2 Co^{II} (the magnetic anisotropy of the Co^{II} metal ion can also be partially responsible for the observed decrease). Moreover the magnetization curves show an absence of magnetization saturation which is consistent with magnetic anisotropy of the Co^{II} ions (Figure **II.12, inset**). In the case of the Cu^{II} homologue the temperature dependence of the χT product (Figure **II.13**) displays a Curie-like paramagnetic behavior indicating the quasi-absence of magnetic interactions between S = 1/2 Cu^{II} magnetic centers. Moreover the field dependence of the reduced magnetization (*M vs H/T,* Figure **II.13, (left), inset**) characterizes the Cu^{II} derivative as magnetically isotropic. The fit of the experimental data to the Curie–Weiss law confirms this with Weiss constants of -1.335 K and – 0.90 K for Cu^{II} and Co^{II} respectively (while Curie constants are estimated at 0.40 and 0.69 cm^3 K mol^{-1} respectively). This result is well in line with the discussion of the clearing points (vide supra) that support stronger inter-disk Metal–N interactions in the Co^{II} complex

(thus mediating strong magnetic interactions) than in the Cu^{II} homologue due to the expected Jahn–Teller distortion of the Cu^{II} square bipyramidal coordination sphere.

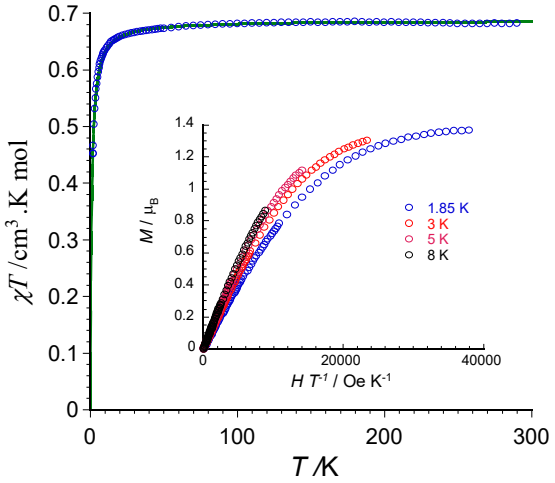

Figure II.12. Temperature dependence of χT at 1000 Oe for $Co^{II}Pc(OCH_2CHBuHex)_4$ between 1.8-300 K (χ is defined as magnetic susceptibility equal to *M/H* per mole of $Co^{II}Pc(OCH_2CHBuHex)_4$). Inset: *M* vs *H/T* data for $Co^{II}Pc(OCH_2CHBuHex)_4$) (50-300 Oe min^{-1}).

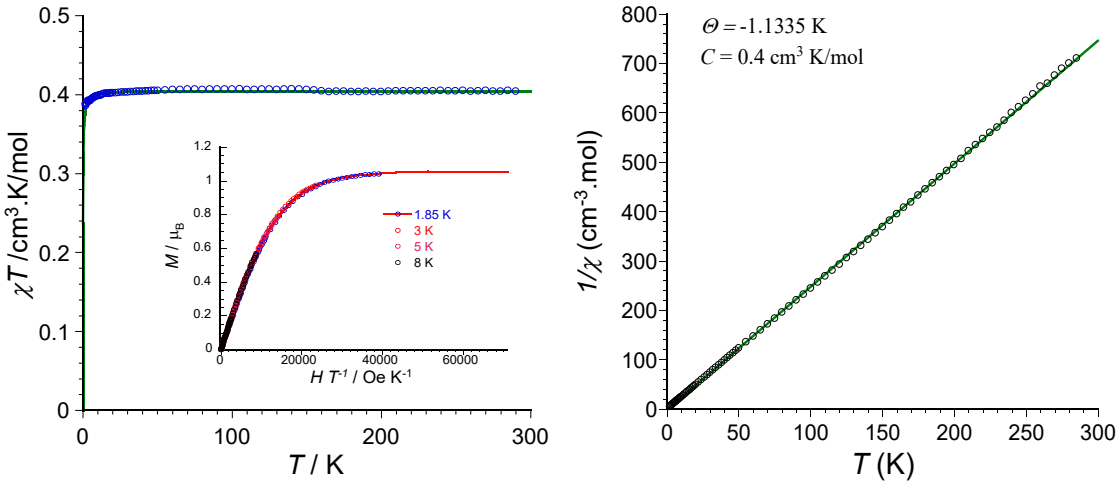

Figure II.13. Temperature dependence of χT (left) and 1/χ (right) for $Cu^{II}Pc(OCH_2BuHex)_4$ at 1000 Oe between 1.8-300 K (χ is defined as magnetic susceptibility equal to *M/H* per mole of $Cu^{II}Pc(OCH_2BuHex)_4$); Red line represents the Curie-Weiss fit, $\chi = C/(T-\theta)$, with θ = -1.335 K, and *C* = 0.4 cm^3·K/mol. Inset: M vs H/T data for $Cu^{II}Pc(OCH_2CHBuHex)_4$ at the temperature indicated (50–300 Oe min^{-1}).

II.4. Conclusion of Section II.3

The introduction of a moderately voluminous racemic β-branched 3-(2-butyloctyl)oxy substituent in the phthalonitrile precursor allows not only the regiospecific formation of an all-endo-tetraalkoxy-phthalocyanine but also leads to liquid crystalline self-assembly with attainable clearing temperatures and persisting columnar organization at room temperature. The synthesis and characterizations of six functionalized metal-free and metal(II) phthalocyanine compounds were described. A rare hexagonal mesophase with twelve columns per hexagonal unit cell is found in the metal-free homologue, whereas the metal complexes show rectangular mesophases. The clearing temperature increases with increasing axial component of the metal ion coordination sphere. At low temperature, significant antiferromagnetic exchange between magnetic centers is observed for the Co^{II} homologue, whereas the magnetic centers are magnetically independent in the Cu^{II}

derivative, in line with the observed higher clearing temperature in the Co^{II} case that testifies of stronger interdisk interactions.

II.5. Functionalization of M^{II}Pcs with Symmetrically Branched Alkoxy Chains

II.5.1. Synthetic Procedures

In order to avoid the mixture of several stereoisomers (six in the C_{4h} case: RRRR, RRRS, RRSS, RSRS, RSSS, SSSS) as present in the case of a tetrasubstituted Pc with racemic branched alkyl chains, the symmetric 3-(2-pentylheptyloxy-) (**2b**) and 3-(2-butylhexyloxy-)phthalonitrile (**2c**) precursors were synthesized (Scheme **II.4**). As a consequence, the probability and ability of crystallization is potentially increased. The two symmetrical branched alkyl chains with the same or slightly smaller mass compared to 2-butyloctyloxy were chosen for the following reasons: (i) interest in testing the regioselectivity of the tetramerization of 3-(2-pentylheptyloxy)- and 3-(2-butylhexyloxy)-phthalonitrile precursors; (ii) to analyze and to understand the influence of the symmetrical branched alkyl chains on the temperature of the crystal-mesophase transition.

The phthalonitrile precursors are obtained in three steps (see Scheme **II.4** and Supporting Material for detailed protocols). First, 2-pentyl-heptanol and 2-butyl-hexanol were obtained following procedures reported for similar compounds [32]. Sodium heptanoate and sodium hexanoate (starting materials for 2-pentyl-heptanol and 2-butyl-hexanol respectively) have a poor solubility in THF solution, and as a consequence, reduced yields of branched acids where observed. An improvement of the alkylation reaction was possible when the emulsion of sodium hexanoate or sodium heptanoate in THF was stirred around 1-2 h at room temperature, prior to deprotonation and alkylation. The obtained dialkylacetic acids were purified by *vacuum* distillation. The branched alcohols (**1b** and **1c**) were obtained by reduction of the corresponding dialkylacetic acids and purified by *vacuum* distillation. Finally, the 3-alkoxyphthalonitrile (**2b** and **2c**) precursors were prepared by nucleophilic substitution of the nitro group in 3-nitrophthalonitrile with the branched alcohols.

The corresponding metal-free phthalocyanine compounds were obtained in conditions described in Section II.3. The cyclo-tetramerisation of the 3-(2-butylhexyloxy)-phthalonitrile (**2c**) with lithium alcoholate leads to a mixture of four regioisomers, of which the most symmetrical (1,8,15,22-substituted) isomer of C_{4h} symmetry forms as main product. Formation of the isomers of D_{2h}, C_s, and C_{2V} symmetry is not fully suppressed by this sterically less demanding alkyl group. The C_{4h} isomer could be separated as a first fraction by column chromatography in dichloromethane on silica gel (see Supporting Material for detailed protocols). The cyclo-tetramerization of 3-(2-pentylheptyloxy)phthalonitrile (**2b**) in contrast to the shorter homolog, was fully stereospecific. Thus with these two chain lengths, we luckily hit exactly the limit of stereospecificity of the tetramerization. The $MPc(OCH_2CHPent_2)_4$ (M = Co^{II} (**4b**), Ni^{II} (**5b**), Cu^{II} (**6b**), Zn^{II} (**7b**)) and $MPc(OCH_2CHBu_2)_4$ (M = Co^{II} (**4c**), Ni^{II} (**5c**), Cu^{II} (**6c**), Zn^{II} (**7c**)) complexes were synthesized according the procedure described in Section II.3. The structural and physical properties of the synthesized complexes were characterized by ^1H NMR, X-ray, DSC, POM, SAXS and elemental analysis.

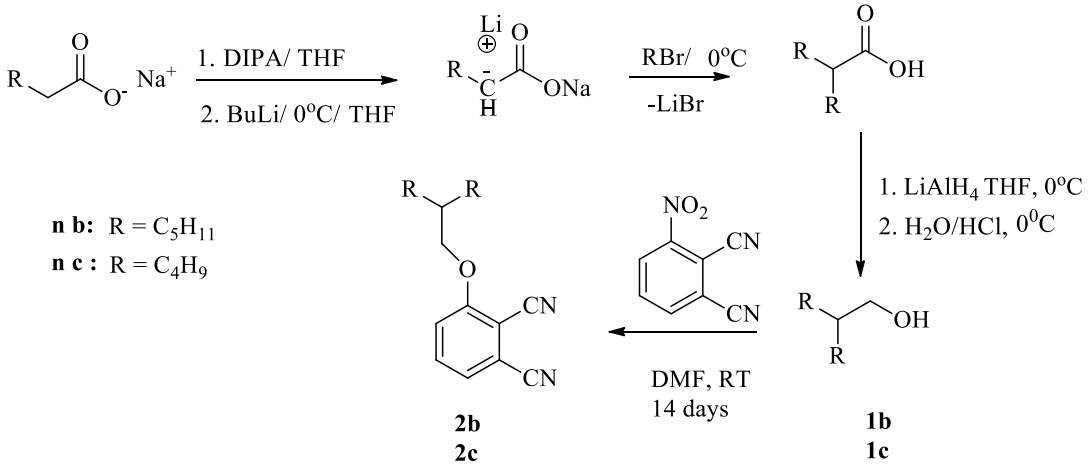

Scheme II.4. Synthesis of branched alcohols and 3-alkoxy-phthalonitrile precursors.

II.5.2. Analytical Characterizations of $M^{II}Pc$ Complexes

II.5.2.1. ^1H NMR Spectroscopic Analyses

The presence of the septet pattern at δ = 2.3 ppm in the ^1H NMR spectra of the prepared symmetric branched acids confirms the successful deprotonation of the sodium alkanoate followed by alkylation (Figure **S.II.8, top** and **S.II.9, top**). The broad signal of the acid proton at δ = 11.4 ppm could be also detected (Figure **S.II.9, top**). The reduction of the branched acids to the corresponding alcohols was confirmed by the appearance of a doublet peak at δ = 3.5 ppm which corresponds to the methylene protons adjacent the hydroxyl group (Figure **S.II.8** and **S.II.9, bottom**). The nucleophilic substitution of the nitro group in 3-nitrophthalonitrile with the symmetric branched alcohols was confirmed by the shift of this doublet peak observed towards δ = 4 ppm (Figure **S.II.10, top** and **bottom**).

The cyclotetramerization of the 3-(2-butylhexyloxy)-phthalonitrile (**4b**) leads to a mixture of four regioisomers. The ^1H-NMR spectra of the majority product (separated as a first fraction by column chromatography) obtained in 30 % yield shows the minimal set of peaks as in the case of 1, 8, 15, 22-(4-tetra-(2-butyloctyloxy)-phthalocyanine corresponding to the C_{4h} isomer. The ^1H-NMR spectrum of the metal-free 1, 8, 15, 22-(4-tetra-(2-pentylheptyloxy)-phthalocyanine testifies of the exclusive formation of the C_{4h} isomer, with only three peaks in the aromatic region (Figure **S.II.11**, and Figure **S.II.12**).

II.5.2.2. Single Crystal X-ray Analyses of 7b and 7c

Suitable crystals for X-ray diffraction measurements were obtained by slow evaporation of solutions of $ZnPc(OCH_2CHPent_2)_4$ (**7b**) and $ZnPc(OCH_2CHBu_2)_4$ (**7c**) in dimethylformamide at room temperature over three days. While $ZnPc(OCH_2CHPent_2)_4$ crystallized in the monoclinic $P2_1/c$ space group with twelve molecules in the unit cell, $ZnPc(OCH_2CHBu_2)_4$ crystallized in the triclinic *P-1* space group with two molecules per unit cell. In both types of the supramolecular ZnPc-derivatives, zinc(II) is penta-coordinated with a disordered square pyramidal geometry, with one dimethylformamide molecule as axial ligand (Figure **II.14**). In the case of $ZnPc(OCH_2CHBu_2)_4$ one of the DMF molecules on the axial position was found to be disordered

on 3 positions with 0.5 : 0.25 : 0.25 ratios. The phthalocyanine macrocycle in both ZnPc-complexes is not strictly planar due to the interactions of the Zn center with the axial DMF molecule. The interaction between the oxygen atom of the DMF molecule, with its lone pair of electrons, and the Zn^{II} center leads to a deviation of Zn^{II} from the central Pc ligand ($ZnPc(OCH_2CHPent_2)_4$: 0.36 Å; $ZnPc(OCH_2CHBu_2)_4$: 0.35 Å from the plane defined by the four isoindole nitrogen atoms). As a result of the interaction of Zn^{II} with the axially ligated DMF molecule, the Pc ligand adopts a saucer shape. A similar non-planarity of a ZnPc has been reported previously [33[a, b, c, d]]. The equatorial Zn-O bonds in **7b** ranging from 2.04(1) to 2.071(8) are slightly shorter than in **7c** where they range from 2.098(4) to 2.121(5). The packing of **7b** shows a tilted columnar structure. The columns form tilted stacks within herringbone arrangements (Figure **S.II.13**) where plane-to-plane distances range from 8.149 to 8.589 Å. In the unit cell four pairs of $ZnPc(OCH_2CHPent_2)_4$ molecules are oriented face-to-face (coordinated DMF molecules are in-between Pc planes) with a distance between the N4-planes of 8.589 Å. Two of these are oriented with the next molecule back-to-back with a distance between the N4-planes of 8.202 Å. The two other pairs are oriented back-to-face with the next molecule, the distance between the planes being 8.149 Å (Figure **S.II.13**). The mutual arrangement of $ZnPc(OCH_2CHBu_2)_4$DMF and the crystal packing is illustrated in Figure **II.15.** The packing is very similar with the $ZnPc(OCH_2CHPent_2)_4$DMF homolog. Two by two molecules are arranged face-to-face with the coordinated DMF molecules between the Pc planes. The distance between two Pcs with disordered coordinated DMF units is around 9.022 Å. The gap between adjacent pairs of molecules is about 8.374 Å. These values are slightly higher than in the case of $ZnPc(OCH_2CHPent_2)_4$DMF. While the distances between pairs with disordered DMF is around 8.374 Å, in case of the adjacent pairs from the next column the distances between them is slightly higher: 8.852 Å. Due to the steric effect of the coordinated DMF and the bulky alkyl chains, in both homologs there are no π-π interactions between Pc cores.

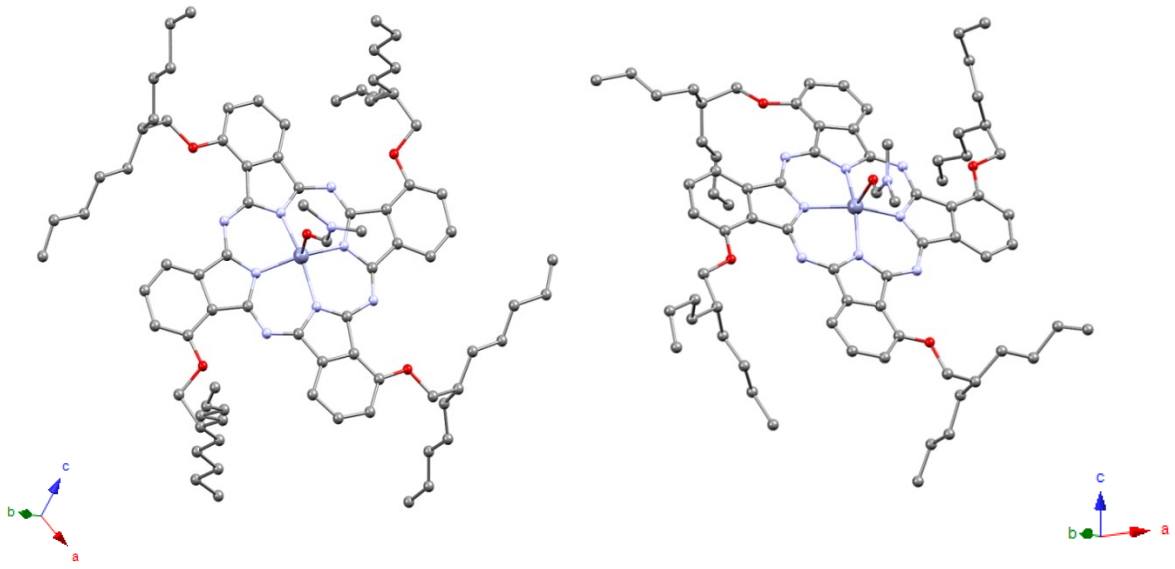

Figure II.14. Perspective view of the crystal structure of **7b** (left) and **7c**·DMF at 120 K. Hydrogen atoms are omitted for clarity. Color scheme: Zn^{II} purple, N blue, O red, C gray.

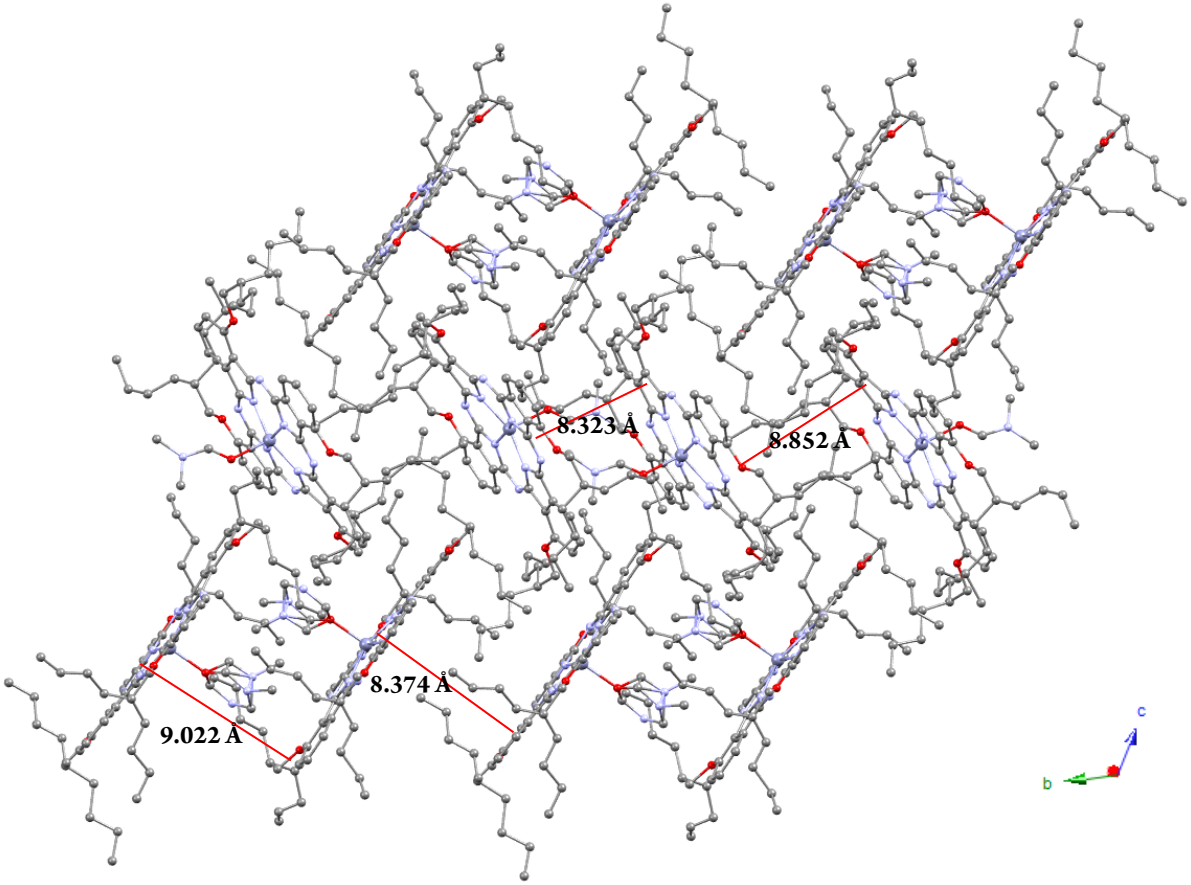

Figure II.15. Perspective view of the crystal packing of **7c** at the 120 K illustrating the distances between molecular planes of the phthalocyanines. Hydrogen atoms are omitted for clarity.

II.5.2.3. UV-Vis Spectroscopic Characterizations

The electronic absorption spectra of the $MPc(OR^{1\text{-}2})_4$ (M^{II} = Co^{II}, Ni^{II} Cu^{II}, Zn^{II}; R^1 = 2-pentylheptyl; R^2 = 2-butylhexyl) complexes were recorded in CH_2Cl_2 solutions. The peripheral endo-alkoxy substituents have no significant effect on the absorption spectra [10^d]; the spectra obtained for compounds $MPc(OR^{1\text{-}2})_4$ are typical for such compounds (Figure **II.16**). The Q bands of the non-peripherally alkoxy substituted Pcs were red-shifted (*bathochromic effect*) when compared to the corresponding peripherally substituted and unsubstituted Pcs [$34^{a, b, c}$]. As shown in Figure **II.16,** the splitting of the Q band of the $H_2Pc(OR^{1\text{-}2})_4$ appears at around 695 and 728 nm while the phthalocyanine complexes give intense single absorption Q bands at around 705 nm, assigned to a π–π* transition from the HOMO of a_{1u} symmetry to the e_g symmetry LUMO [35].

The $ZnPc(OCH_2CHPent_2)_4$ and $ZnPc(OCH_2CHBu_2)_4$ complexes show an extra peak at 760 nm in DCM solution. The observed new red-shifted absorption band occurred due to the protonation of the meso-nitrogens in the phthalocyanine. It was most likely caused by acidic impurities in dichloromethane [$36^{a, b, c, d}$].

Upon adding a small amount of base (triethylamine) to the ZnPc solution, the new red-shifted absorption band totally disappears (Figure **II.17**).

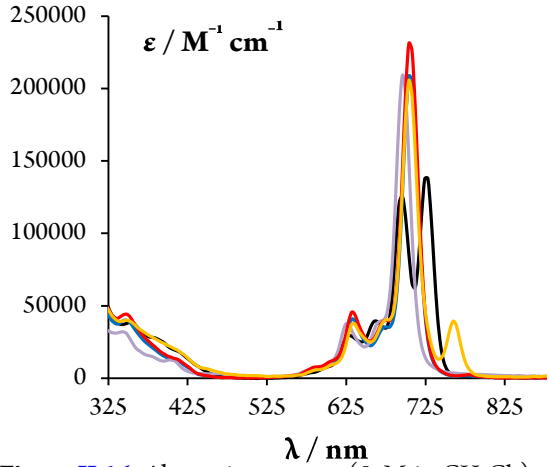

Figure II.16. Absorption spectra (5μM in CH_2Cl_2) of the $H_2Pc(OCH_2CHPent_2)_4$ **3b** (black) and corresponding metal(II) phthalocyaninates, **4b** (Co, blue), **5b** (Ni, purple), **6b** (Cu, red), **7b** (Zn, yellow).

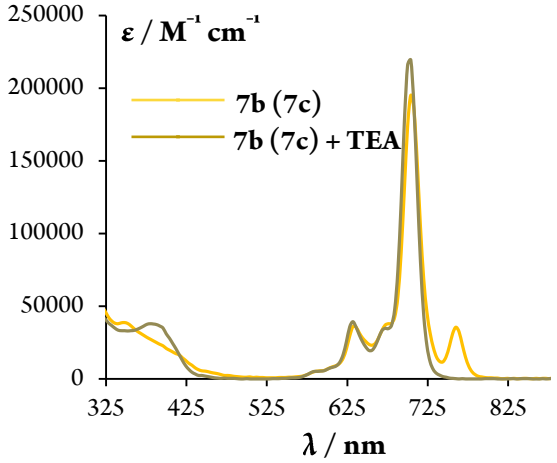

Figure II.17. Absorption spectra (5μM in CH_2Cl_2) of $ZnPc(OR^1)_4$ (**7**) (yellow) and $ZnPc(OR^2)_4$ (**14**) with added triethylamine (brown). R^1 = 2-pentylheptyl; R^2 = 2-butylhexyl.

II.5.2.4. Thermotropic Properties

$H_2Pc(OCH_2CHPent_2)_4$ (**3b**) and $H_2Pc(OCH_2CHBu_2)_4$ (**3c**) were separated as a crystalline needles. Upon heating, the (**3b**) melts at 137°C into semi-viscous and birefringent mass. On further heating, the sample becomes fluid above 200 °C. Upon slow cooling, the characteristic fan-shaped birefringent texture appears. This characteristic columnar texture is maintained at room temperature, with small dynamics of the planar birefringent domains (Figure **II.18, a, b, c**). These reversible optical changes do not give rise to an energy peak in the DSC thermograms (Figure **II.19**). Earlier Guillon et al. observed such an optical transition for an octa(dodecyloxymethyl)phthalocyanine where no definite link with any changes in the internal structure was found [37]. Surprisingly, the birefringent columnar texture could be observed in case of the $MPc(OCH_2CHPent_2)_4$ unchanged even at room temperature, in contrast to their metal free homologues**.** While the metal-free phthalocyanine with asymmetric branched chains (see Section II.3) and $H_2Pc(OCH_2CHPent_2)_4$ showed columnar mesophase behavior at room temperature, the $H_2Pc(OCH_2CHBu_2)_4$ homologue shows its mesophase with a characteristic columnar texture only at high temperature, between 135 and 209°C; below 135°C the columnar texture became somewhat striated (Figure **II.18, d, e**) and then slowly gives way to crystals upon standing at room temperature (Figure **II.18, f**). In this case, the optical changes are accompanied by an enthalpy transition on DSC thermograms (Figure **II.20, left**).

For $MPc(OCH_2CHBu_2)_4$ (M = Ni^{II} (**5c**), Cu^{II} (**6c**)), upon slow cooling the birefringent mesophase formed at high temperature suffers optical changes through the appearance of some striations, similar to the optical behavior of their metal free homolog. In the work of Mamlok et al., striations appear in mesomorphic 2,3,7,8,12,13-hexaalkanooyloxybenzo[1,2-b:2,4-b':5,6-b'']trisbenzofurans as a consequence of a transition from a hexagonal ordered to a rectangular disordered or from a rectangular disordered to an oblique disordered

mesophase structure [38]. As in previous series of phthalocyanine complexes (See Section II.3) the thermotropic properties of the $MPc(OCH_2CHPent_2)_4$ and $MPc(OCH_2CHBu_2)_4$ homologs are strongly dependent on the nature of the metal ion. Whilst the clearing points of $H_2Pc(OCH_2CHPent_2)_4$ and $H_2Pc(OCH_2CHBu_2)_4$ are around 200 and 209 °C respectively, in the case of the phthalocyanine complexes the clearing temperatures are about one hundred degrees higher. $NiPc(OCH_2CHPent_2)_4$ (T_c = 255°C) and $NiPc(OCH_2CHBu_2)_4$ (T_c = 270°C) have the lowest mesophase-isotropic phase transition temperatures (Table **II.2.**). The clearing temperature of the metal complexes $MPc(OR^{1\text{-}2})_4$ (M = Co^{II}, Cu^{II}, Zn^{II}; R^1 = 2-pentylheptyl; R^2 = 2-butylhexyl) are, as previously, in line with the coordination geometry tendencies of the M^{II} ions.

The Ni^{II} metal ion has a tendency to adopt square planar coordination geometry with weak interdisk Ni-N interactions, whose mesophase stabilizing effect is manifested by an only moderate rise of the clearing point. In the cases of the $CoPc(OR^{1\text{-}2})_4$, $CuPc(OR^{1\text{-}2})_4$ and $ZnPc(OR^{1\text{-}2})_4$ analogues, the metal ions prefer an octahedral/square pyramidal coordination sphere that induces stronger interdisk M-N interactions and leads to relatively high clearing points. The phase transition temperatures and clearing enthalpies for the $MPc(OR^{1\text{-}2})_4$ (M^{II} = Co^{II}, Ni^{II} Cu^{II}, Zn^{II}; R^1 = 2-pentylheptyl; R^2 = 2-butylhexyl) are indicated in Table **II.2.** The identification and clear assignment of mesophases and phase transitions was achieved by the combination of DSC and SAXS measurements.

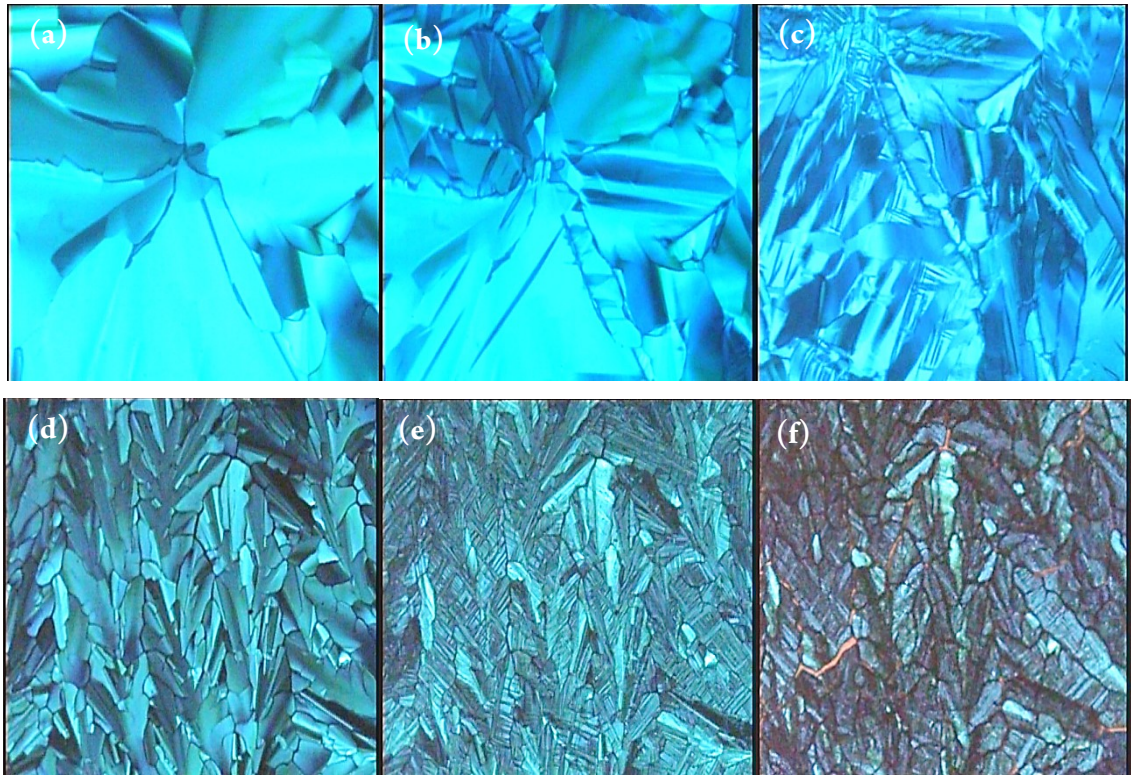

Figure II.18. Mesophase domains growing from the isotropic liquid between glass plates on cooling range seen through crossed polarizers for $H_2Pc(OCH_2CHPent_2)_4$: (a) 150 °C; (b) 100 °C; (c) 25 °C; for $H_2Pc(OCH_2CHBu_2)_4$; (d) 150 °C, (e) 130 °C; (f) 25 °C.

Table II.2. Thermotropic properties of the complexes. cr = crystalline, col_h= hexagonal columnar liquid crystalline; col_r= rectangular columnar liquid crystal-line; $col_{r,p}$ = rectangular columnar plastic crystalline; iso = isotropic liquid. (M^{II} = Co^{II}, Ni^{II} Cu^{II}, Zn^{II}; R^1 = 2-pentylheptyl; R^2 = 2-butylhexyl).

	Compound	Phase sequence (top: first heating of pristine sample, bottom: second heating) [°C]	Clearing enthalpy $H_{col-iso}$ [kJ mol^{-1}]
$MPc(OCH_2CHPent_2)_4$	**(3b)** $H_2Pc(OR^1)_4$	Cr – 137 - col_h – 200 - iso $col_{h,p}$ - 140 - col_h - 200 - iso	6.7
	(4b) $CoPc(OR^1)_4$	cr – 173 - col_r – 310 - iso $col_{r,p}$ - 310 - iso	12.0
	(5b) $NiPc(OR^1)_4$	Cr - 160 - col_r – 255 - iso $col_{r,p}$ – 255 - iso	8.0
	(6b) $CuPc(OR^1)_4$	Cr - 162 - col_r – 292 - iso $col_{r,p}$ - 292 - iso	11.3
	(7b) $ZnPc(OR^1)_4$	Cr - 75 - col_r – 312 - iso $col_{r,p}$ - 312-iso	14.1
$MPc(OCH_2CHBu_2)_4$	**(3c)** $H_2Pc(OR^2)_4$	Cr – 135 - col_h - 209 - iso cr – 150 - col_h – 209 - iso	7.0
	(4c) $CoPc(OR^2)_4$	Cr – 146 - col_r – 328 - iso $col_{r,p}$ – 160 - col_r – 328 - iso	14.2
	(5c) $NiPc(OR^2)_4$	Cr – 168 - col_r – 270 - iso $col_{r,p}$ – 153 - col_r - 270 - iso	11.2
	(6c) $CuPc(OR^2)_4$	Cr – 150 - col_r – 305 - iso $col_{r,p}$ – 190 - col_r - 305 - iso	14.0
	(7c) $ZnPc(OR^2)_4$	Cr – 158 - col_r – 326 - iso $col_{r,p}$ – 187 - col_r – 326 - iso	13.4

II.5.2.4.1. $H_2Pc(OCH_2CHR^{1-2})_4$

The symmetric alkyl chain in $H_2Pc(OCH_2CHPent_2)_4$ **(3b)** and $H_2Pc(OCH_2CHBu_2)_4$ **(3c)** leads to a slight increase of the clearing point compared with the asymmetric homolog (see Section II.3). **3b** melts at around 200 °C whereas **3c** melts at 209 °C, with no hysteresis for the clearing point in both cases. The characteristic columnar texture observed by POM at high temperature was correlated to a columnar hexagonal symmetry by small angle X-ray scattering. Diffraction patterns recorded for H_2Pc homologues **3b** and **3c** at high temperature were quite similar. At 200°C, three reflections were detected in the low angle range for which the reciprocal *q* spacing where in the ratio $1:\frac{\sqrt{7}}{2}:\sqrt{3}$ suggesting the same hexagonal lattice as in the racemic homolog. Observed reflections were indexed with 200, 210, 220 and 300/310 Miller indices and, by applying Bragg's law, 2D cell parameter of 41.43 Å for **3b** and 39.77 Å for **3c** were calculated (see Table **S.II.12** and Table **S.II.13**). Considering the density 1-1.2 g/cm^3, the calculated *a* hexagonal 2D unit cell parameter reveals to be spanned over two instead one column-to-column distance. Therefore the unit cell contains 12 instead of 3 columns as is known for usually hexagonal columnar mesophase (Figure **II.35, b**). This atypical columnar mesophase is very similar to the one of the asymmetric metal free phthalocyanine at high temperature. **3b** shows a monotropic columnar mesophase between the melting point of 140 °C and the clearing point of 200 °C. Differential scanning calorimetry (DSC) showed no crystallization enthalpy upon slow cooling (-2° C min^{-1}) from above 200 °C to room temperature, and upon immediate reheating (at +2 °C min^{-1}) crystallization sets in

upon heating above about 90 °C (Figure **19, left**) with a very poorly expressed small-enthalpy transition (1.5 kJ/mol). We were expected that the mesophase is viscous enough at room temperature to suppress a kind of crystallization, but the SAXS pattern at room temperature shows the appearance of intense and numerous secondary peaks, which may hint to some form of plastic crystal with residual molecular mobility. Even though polarized optical microscopy didn't show significant changes in the mesophase texture at room temperature, and DSC did not reveal any enthalpy transition below the clearing temperature (within the cooling range of the DSC thermogram), the diffraction pattern showed a main peak split into three and additional reflections at low temperature indicating the transition to a plastic crystalline phase.

The short symmetric alkyl chains in **3c** lead to the appearance of a transition from a Col_h to a Col_r mesophase, accompanied by an enthalpy transition at 135°C (37.2 kJ/mol) as revealed by differential scanning calorimetry Figure **II.20**. According to the SAXS measurements, the Col_h-Col_r transition is accompanied by splitting of the single main diffraction peak at 120 and 140°C into two close (010) and (110/200) peaks, and an increase of the number of indexable peaks in the high angle range, which testifies to a rectangular columnar mesophase (Figure **II.21**).

At 120 and 140 °C, up to 11 reflections were detected in the low and high angle range, which were indexed as (010), (110/200), (310/020), (130), (430), (320), (420/510), (230), (600), (610) and (540). The reciprocal spacing (q) of rectangular phases is related to the lattice parameters (a and b): $a = d_{(calc)}\sqrt{h^2 + 3k^2}$; b: $\frac{d_{110}2d_{200}}{\sqrt{4d_{200}^2 - d_{110}^2}}$, where h and k are Miller indices.

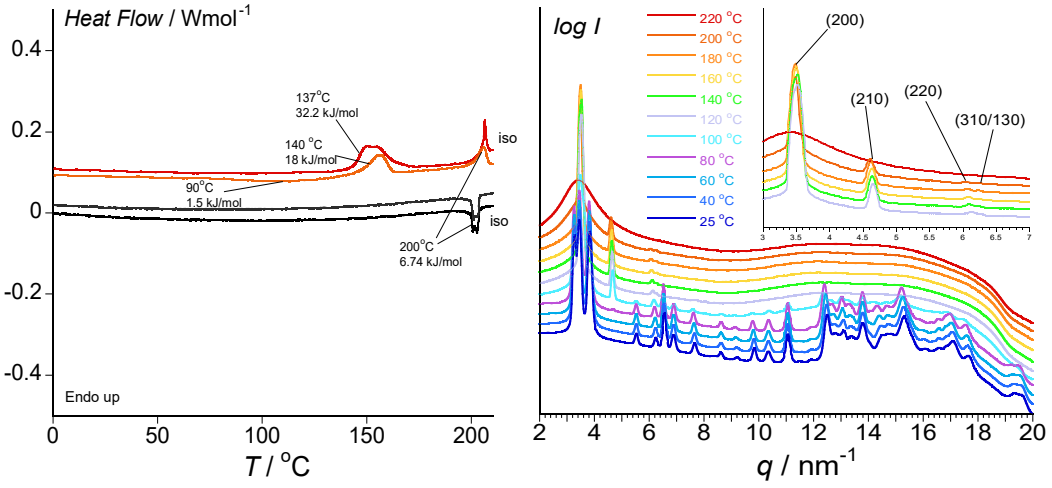

Figure II.19. (left) DSC traces of **3b** showing the transition sequence. Onset temperatures of the melting and clearing transitions are given with transition enthalpies. Scan rates: 2 °C min^{-1} on first heating/cooling (red/black), and second heating/cooling (orange/gray); (right) Indexed SAXS diffraction profile of **3b** at temperatures indicated.

On the heating/cooling of the second cycle the melting occurs with a hysteresis of 15 ° C. The melting enthalpies for the second heating cycle are 5 kJ mol^{-1} and 10.8 kJ mol^{-1} and 7 kJ mol^{-1} for the cooling cycle (Figure **II.20, left**). While heating, the transition from crystal to the mesophase requires more thermal energy

than the transition from the liquid crystalline to the liquid phase. These numbers, and also the different viscosity of the phases, might indicate larger structural changes during the first phase transition. This is in agreement with the thermal hysteresis values found for the reversible melting of the crystalline state.

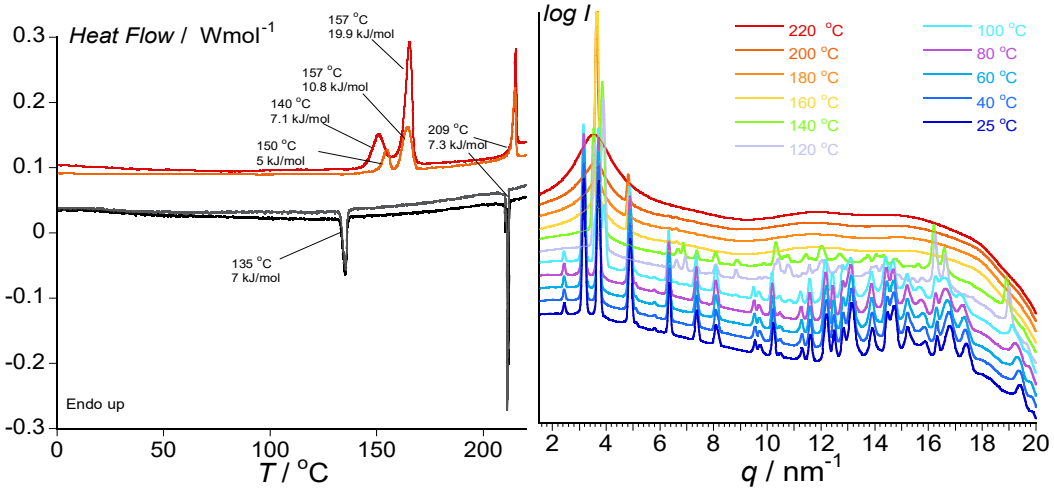

Figure II.20. (left) DSC traces of **3c** showing the transition sequence. Onset temperatures of the melting and clearing transitions are given with transition enthalpies. Scan rates: 2 K min^{-1} on first heating/cooling (red/black), and on second heating/cooling (orange/gray); (right) Indexed SAXS diffraction profile of **3c** at temperatures indicated.

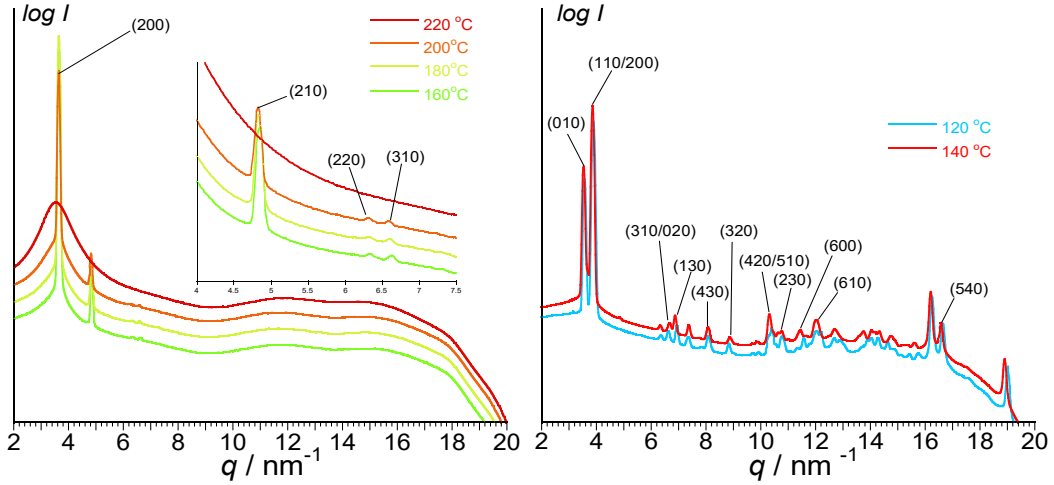

Figure II.21. Powder X-ray diffraction spectra at different temperatures for **3c**: (left) at 220 and 160 °C temperature range with Miller indices indicated in brackets corresponding to a column lattice of hexagonal symmetry; (right) at 140 and 120° C with Miller indices indicated in brackets corresponding to a column lattice of rectangular symmetry.

All summarized indexation parameters at 140 and 200 °C are shown in Table **S.II.12**. On cooling to room temperature, $H_2Pc(OCH_2CHBu_2)_4$ forms a crystalline state with many well-expressed SAXS peaks indicating that this phase exhibits partial order in the third dimension. The characteristic crystalline texture also was observed with POM at room temperature (Figure **II.18, f**). For **3b** and **3c** no reflection peak at *ca* 18 nm^{-1} characteristic of the π–π stacking is observed, thus indicating a poor order along the columnar axis [39].

With two columns per rectangular unit cell or three columns per hexagonal unit cell and assuming one molecule per disk, the unit cell obtained by SAXS yields densities between 1-1.2 g/cm^3 in both cases, which indicates that neighboring disks within a column should have a tendency to orient themselves with their alkyl moieties trough intercalation on alternating sides of the column (Figure **II.35**). It is postulated that the steric

effect of the alkoxy groups at the α-position might disfavor intra-columnar packing, and that the Pc core, with an anti-parallel orientation (or at least tilted) of adjacent discs, forms intercalated inter-columnar packing (Figure **II.36.**) The reversible small enthalpy transitions and the striations observed by POM at low temperature together with the appearance with additional diffraction peaks as revealed SAXS measurements, could justify a transition from columnar rectangular disordered to an oblique disordered mesophase.

II.5.2.4.2. CoPc(OCH_2CHR^{1-2})$_4$

$CoPc(OCH_2CHPent_2)_4$ **(4b),** which melts at 173 °C (30.1 kJ/mol) and clears at 310 °C (12 kJ/mol), shows a enantiotropic columnar liquid crystalline phase after cooling down from the isotropic liquid as revealed by polarizing optical microscopy (Figure **S.II.14**.). Small-angle X-ray scattering (SAXS) at 200°C in the mesophase, compared to the metal-free ligand where a single main column lattice peak is present, shows two close (200) and (110) peaks accompanied by weak secondary peaks that are indexable as (120), (220/400), (410), (420) and (520) in the frame of the 2D rectangular column lattice. The average unit cell parameter was calculated as a = 39.13 Å and b = 19.49 Å (see also Table **S.II.4**). DSC thermograms do not show any enthalpy transition on cooling down to room temperature (Figure **II.22, left**). The powder X-ray diffraction reveals that the Bragg peaks of the rectangular column lattice of the high temperature phase are maintained. At lower temperatures additional poorly expressed peaks could be observed at high angle range (Figure **II.22, right**). These peaks could be not indexable in the frame of the bidimensional rectangular column lattice, and indicate, similarly to $MPc(OCH_2CHBuHex)_4$, the appearance of a transition from liquid crystalline to plastic crystalline order. On the other hand, the DSC traces for $CoPc(OCH_2CHBu_2)_4$ (**4c**) which clears at 328 °C, showed a large endothermic peak at 146 °C (20 kJ mol^{-1}) on first heating cycle, which significantly is decreased at 160 °C (2.16 kJ mol^{-1}) on subsequent cooling. On second heating, the peak is even more reduced (160 °C; 1.72 kJ mol^{-1}), and disappears totally on the second cooling (Figure **II.23, left**). Besides the irreversible melting transition, the SAXS pattern recorded from 220 to 25 °C (see Figure **II.23, right**), as in **4b** homolog, shows in the low angle region two close main reflections, and supplementary peaks in the high angle profile. At 220 °C, the SAXS reflections were indexated as (200), (110), (120), (220/400) and (520) in the frame of the rectangular column lattice.

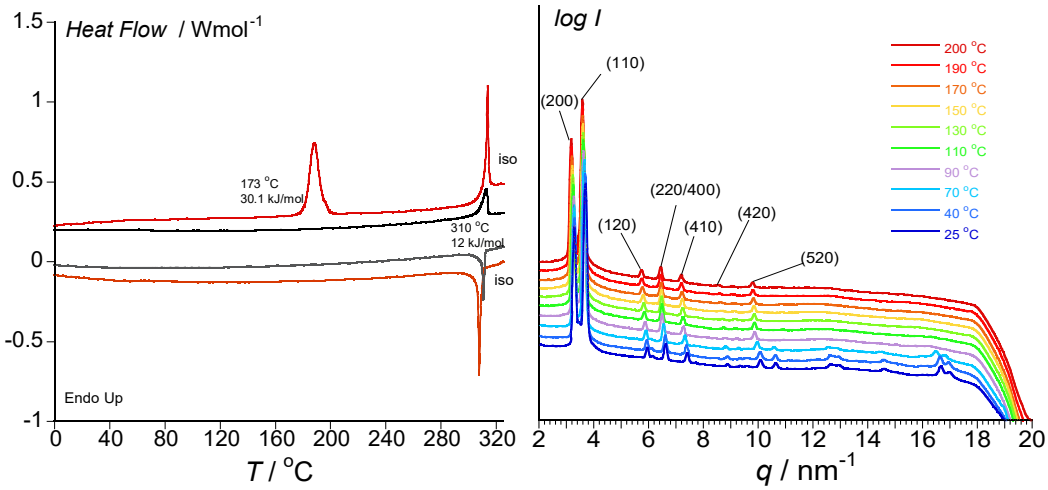

Figure II.22. (left) DSC traces of **4b** showing the transition sequence. Onset temperatures of the melting and clearing transitions are given with transition enthalpies. Scan rates: 10 K min^{-1} on first heating/cooling (red/black), 3 K min^{-1} on second heating/cooling (orange/gray); (right) Indexed SAXS diffraction profile of **4b** at temperatures indicated.

The average unit cell parameter was calculated as a = 37.27 Å and b = 18.56 Å (see also Table **S.II.5**). Further cooling induces a slow dynamics noticeable by the appearance of additional high angle range peaks that are more expressed compared to its homologue, but still with unchanged peak intensities in the low angle range.

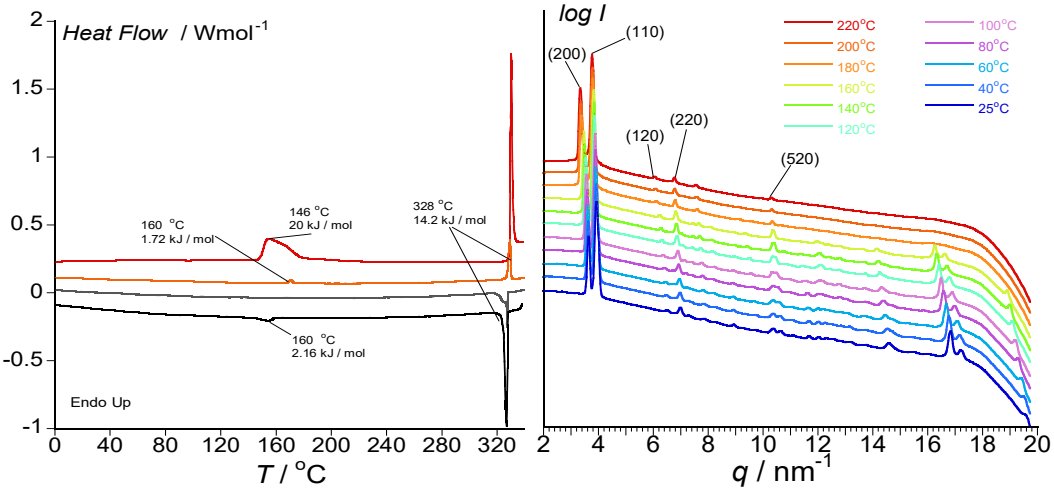

Figure II.23. (left) DSC traces of **4c** showing the transition sequence. Onset temperatures of the melting and clearing transitions are given with transition enthalpies. Scan rates: 10 K min^{-1} on first heating/cooling (red/black), 3 K min^{-1} on second heating/cooling (orange/gray); (right) Indexed SAXS diffraction profile of **4c** at temperatures indicated.

II.5.2.4.3. NiPc(OCH$_2$CHR$^{1\text{-}2}$)$_4$

NiPc(OCH$_2$CHPent$_2$)$_4$ (**5b**) and its homolog have the lowest mesophase - isotropic transition temperatures. The DSC traces for **5b**, which clears at 255 °C, shows an irreversible large-enthalpy melting transition at 160 °C (32.6 kJ/mol), which reappears diminished upon subsequent second heating (Figure **II.24**, **left**). Similar to the Co homologue (**4b**), the powder x-ray scattering for **5b**, with typical planar birefrigent domains (see Figure **II.25**), shows at 200 °C two close (200) and (110) reflections in the low angle range with supplementary well expressed sharp peaks in the wide angle range. The two main (200) and (110) and the

secondary (120), (220/400), (410), (420) and (520) reflections were indexed in the framework of a rectangular latice (see Table **S.II.6**).

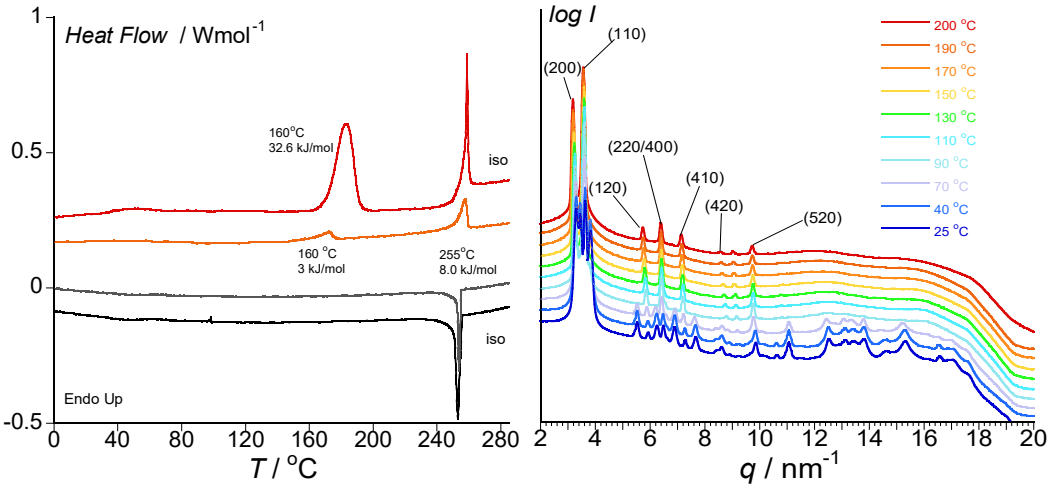

Figure II.24. (left) DSC traces of **5b** showing the transition sequence. Onset temperatures of the melting and clearing transitions are given with transition enthalpies. Scan rates: 10 K min^{-1} on first heating/cooling (red/black), 3 K min^{-1} on second heating/cooling (orange/gray); (right) Indexed SAXS diffraction profile of **5b** at temperatures indicated.

On cooling from 200 °C to 90 °C the diffraction pattern remained unchanged. Further cooling to room temperature, besides the high temperature peaks, the two close (200) and (110) are split into four, accompanied by secondary peaks in the wide angle region which are not indexable in the frame of the rectangular lattice (Figure **II.24**, **right**). This indicates that at lower temperatures is induced a very slow organization, and whereas on cooling in the DSC traces no enthalpy transition is detected, we conclude that, here as well, the rectangular phase is best addressed as a plastic crystalline phase.

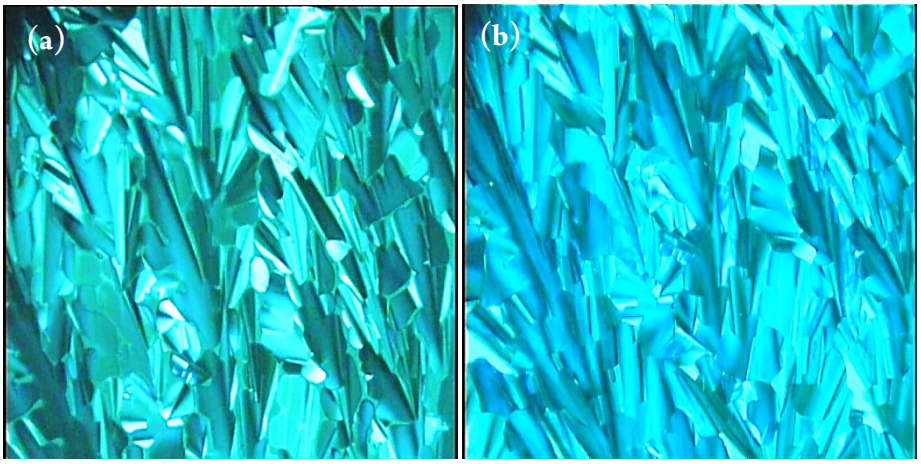

Figure II.25. Mesophase domains of **5b** growing from the isotropic liquid between glass plates on cooling range seen through crossed polarizers (a) at 245 °C; (b) at 25 °C.

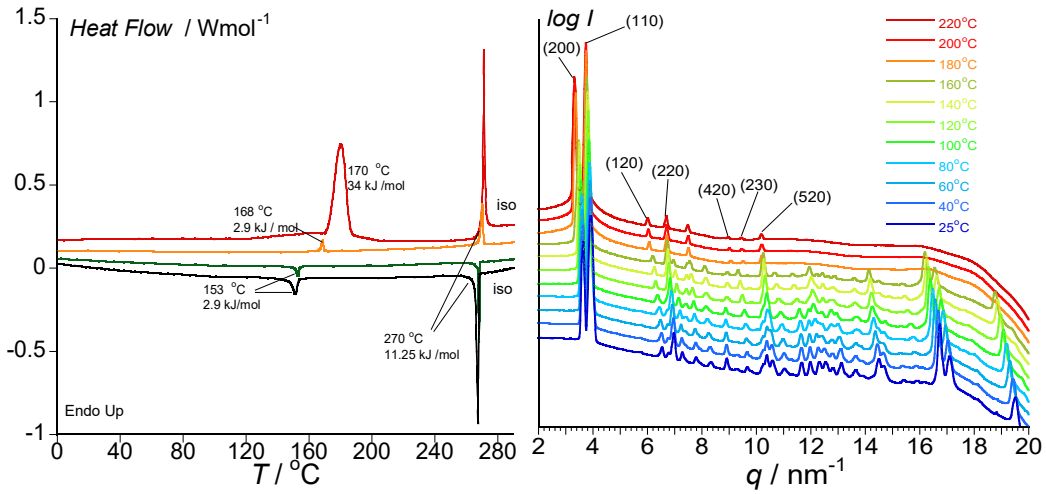

Figure II.26. (left) DSC traces of **5c** showing the transition sequence. Onset temperatures of the melting and clearing transitions are given with transition enthalpies. Scan rates: 10 K min^{-1} on first heating/cooling (red/black), 3 K min^{-1} on second heating/cooling (orange/gray); (right) Indexed SAXS diffraction profile of **5c** at temperatures indicated.

Compared to **5b**, for $NiPc(OCH_2CHBu_2)_4$ (**5c**) a significant transition enthalpy from the columnar rectangular to the crystalline phase was detected, as reveal the DSC thermograms and SAXS patterns (Figure **II.26**). On first heating a large-enthalpy melting transition is detected at 170 °C (34 $kJmol^{-1}$), which on cooling appears significantly reduced to 2.9 kJ mol^{-1} at 153 °C. On the second heating-cooling cycles, the enthalpy of the melting transition is equivalent with that from the first cooling cycle on cooling. From 220 °C to 180 °C the diffraction pattern remained unchanged, similarly with its homologue, with two close (200) and (110) main reflections and (120) ,(220), (420), (230) and (520) secondary peaks in the wide angle range which are consistent with a columnar rectangular lattice (see also Table **S.II.7**).

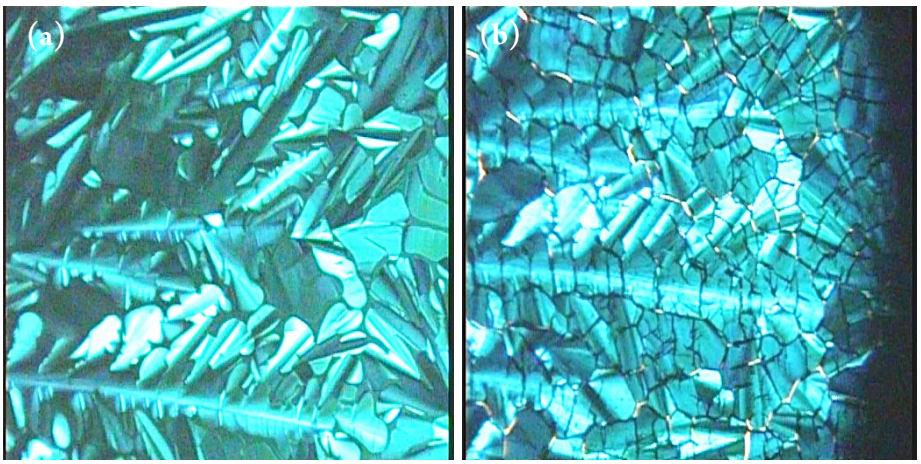

Figure II.27. Mesophase domains of **5c** growing from the isotropic liquid between glass plates on cooling range seen through crossed polarizers (a) at 260 °C; (b) at 25 °C.

The unit cell parameters at 200 °C was calculated as a = 37.55 Å, and b = 18.75 Å. Below 180°C, additional numerous well-expressed reflections at high angles are recorded with persistence of the more intense high temperature peaks (Figure **II.26, right**). Therefore, taking into account the equal enthalpies of the transitions on heating and cooling, and the appearance at low temperature of not indexable peaks, a reversible transition from a rectangular to a crystalline phase is evidenced. Contrasting with its homologue, the

birefringent texture observed by POM shows at low temperature notable changes in the planar domains (see Figure **II.27**) which are in agreement with DSC and SAXS.

II.5.2.4.4. $CuPc(OCH_2CHR^{1\text{-}2})_4$

An extremely similar thermal behavior to the racemic substituted MPcs (see Section II.3) and to $CoPc(OCH_2CHPent_2)_4$ was found for $CuPc(OCH_2CHPent_2)_4$ (**6b**). With an irreversible large-enthalpy melting transition at 162°C (26.10 $kJmol^{-1}$) and a reversible mesophase-isotropic transition at about 292 °C (11.30 $kJmol^{-1}$), as revealed by differential scanning calorimetry (Figure **II.28, left**), **6b** shows an enantiotropic columnar mesophase below the clearing temperature, identified by its growth in birefringent planar domains and non-birefringent quasi-homeotropic domains (Figure **II.29**). On cooling from 220 °C to 90 °C, the SAXS measurements (Figure **II.28, right**) showed diffraction patterns similar with its homologues, with the same number of reflections, i.e. with two sharp main reflection indexed as (200), (110) in the small angle region and (120), (220/400), (410), (520) peaks in the high angle area. All indexed reflections were consistent with a rectangular lattice (Table **S.II.8**). Diffraction patterns collected below 90 °C on further cooling additionally show peaks appearing in the wide angle region, assigning the transition as being from rectangular liquid crystalline to rectangular plastic crystalline. This transition was not detectabile by DSC measurements.

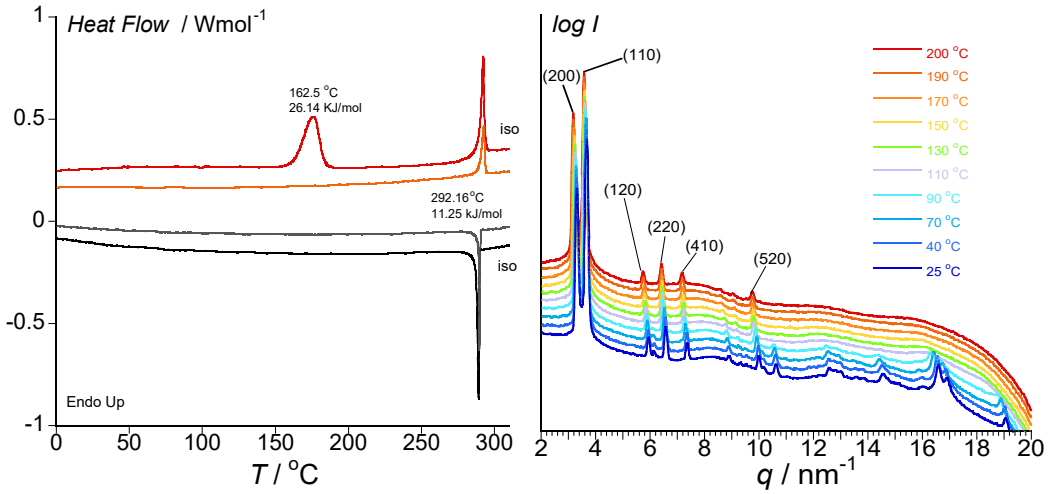

Figure II.28. (left) DSC traces of **6b** showing the transition sequence. Onset temperatures of the melting and clearing transitions are given with transition enthalpies. Scan rates: 10 K min^{-1} on first heating/cooling (red/black), 3 K min^{-1} on second heating/cooling (orange/gray); (right) Indexed SAXS diffraction profile of **6b** at temperatures indicated.

In $CuPc(OCH_2CHBu_2)_4$ (**6c**) the shorter symmetric alkoxy groups lead not only to an increase of the liquid crystalline - isotropic phase transition temperature (305 °C; 14 $kJmol^{-1}$) but also induce a reversible melting transition (with thermal hysteresis of 10 °C) at 190 °C (3.2 $kJmol^{-1}$) on heating and 180 °C on cooling (Figure **II.30, left**). Above 180 °C, SAXS measurements showed diffraction patterns whose sharp reflections (identical with its homologue) were indexated in a rectangular lattice (see Table **S.II.9**).

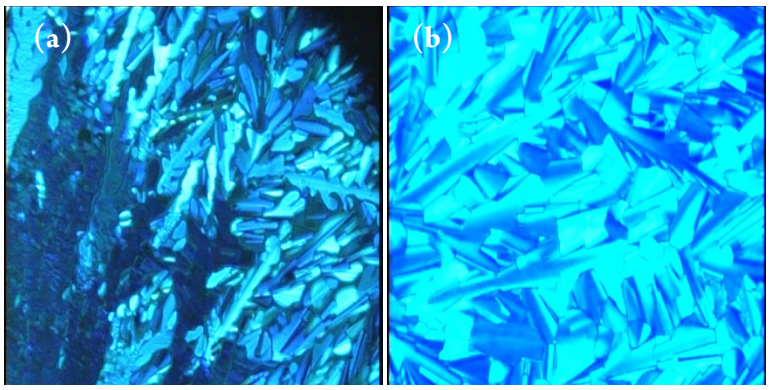

Figure II.29. Mesophase domains growing from the isotropic liquid between glass plates on cooling range seen through crossed polarizers for **6b**: (a) at 285 °C; (b) at 25°C.

The presence of the reversible, only weakly hysteretic, melting enthalpy transition, plus SAXS measurements after comparison of diffraction patterns with its additional intensified peaks collected below 180 °C (Figure **II.30, right**), again indicate a transiton from rectangular liquid crystalline to rectangular plastic crystalline. In addition to this, by POM (Figure **II.31**) we could observe minor but significant changes in the typical planar birefringent domains, corrobating the DSC and SAXS measurements.

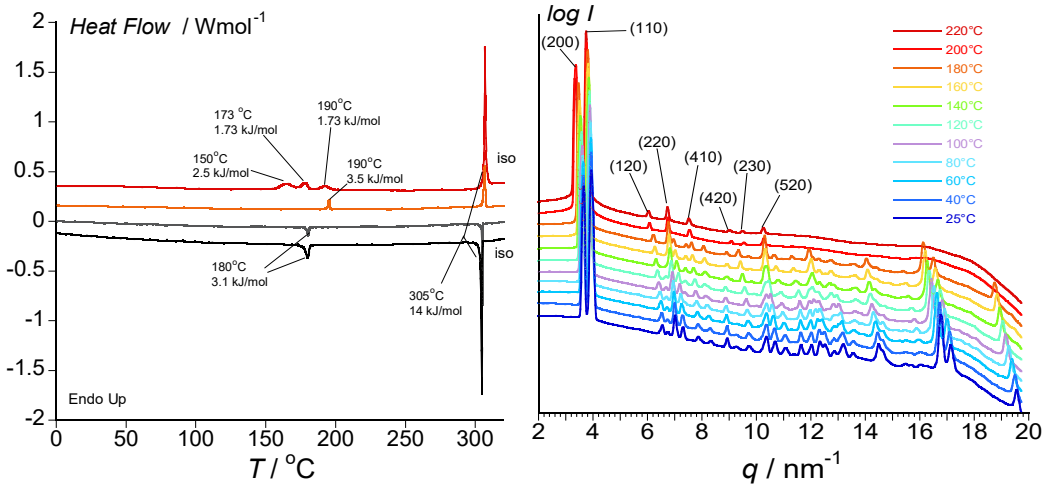

Figure II.30. (left) DSC traces of **6c** showing the transition sequence. Onset temperatures of the melting and clearing transitions are given with transition enthalpies. Scan rates: 10 K min^{-1} on first heating/cooling (red/black), 3 K min^{-1} on second heating/cooling (orange/gray); (right) Indexed SAXS diffraction profile of **6c** at temperatures indicated.

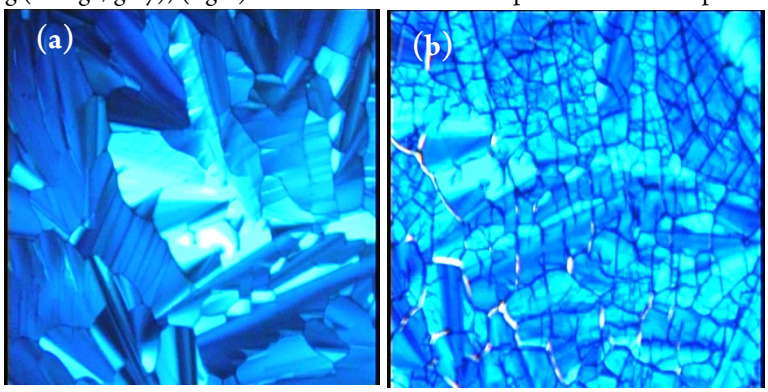

Figure II.31. Mesophase domains of **6c** growing from the isotropic liquid between glass plates on cooling seen through crossed polarizers: a) at 280 °C; b) at 25°C.

II.5.2.4.5. ZnPc(OCH$_2$CHR$^{1\text{-}2}$)$_4$

ZnPc(OCH$_2$CHPent$_2$)$_4$ (**7b**) and ZnPc(OCH$_2$CHBu$_2$)$_4$ (**7c**), as analyzed by X-ray crystallography, were obtained as cystalline solids with one molecule of dimethylformaminde coordinated in axial positon of Zn^{II}. Because the coordinated DMF could induce some hindrance of columnar packing and in order to avoid any vagueness in the the DSC, SAXS and POM analysis (even simple DMF elimination by heating could lead to a confusing peak in the DSC thermogram), the compexes were solubilized in diclormethane and recrystalised by adding methanol. The elimination of the coordinated DMF was confirmed by IR-spectroscopy through disappearance of the strong band at 1659 cm^{-1} (Figure **S.II.14**). **7b** and **7c** have the highest mesophase – isotropic liquid transition temperatures amongst the compounds described in this chapter. The high clearing temperature of the Zn^{II} complexes, and to a lesser extent of the Co^{II} and Cu^{II} analogs, is due to their strong octahedral or square pyramidal tendency, compared to the Ni^{II} homolog. **7c,** which clears at 312°C, has an irreversible large-enthalpy melting transition at 75 °C (73.7 kJmol^{-1}) as reveals the first heating cycle of the DSC thermogram (Figure **II.32, left**). In the SAXS diffraction pattern (Figure **II.32**, **right**), as in case of MPc(OCH$_2$CHBuHex)$_4$, CoPc(OCH$_2$CHPent$_2$)$_4$ and CuPc(OCH$_2$CHPent$_2$)$_4$, the same number of high temperature reflections could be indexated in the frame of the rectangular lattice (see Table **S.II.10**).

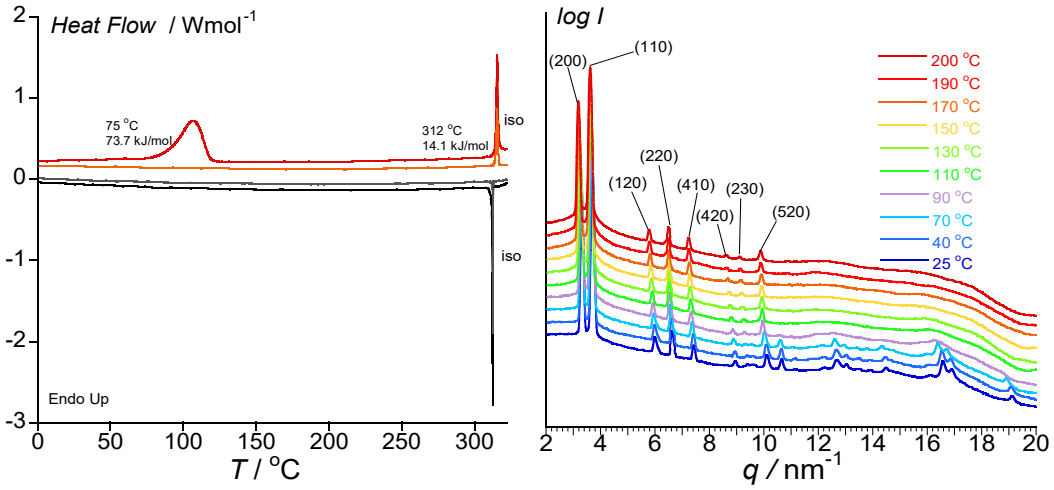

Figure II.32. (left) DSC traces of **7b** showing the transition sequence. Onset temperatures of the melting and clearing transitions are given with transition enthalpies. Scan rates: 10 K min^{-1} on first heating/cooling (red/black), 3 K min^{-1} on second heating/cooling (orange/gray); (right) Indexed SAXS diffraction profile of **7b** at temperatures indicated.

As was expected, differential scanning calorimetry for **7c** showed a reversible small-enthalpy melting transition at 201°C on heating and 187 °C on cooling (Figure **II.33, left**) which we were able to assign to a Col$_r$-Col$_{r,p}$ transition with the help of SAXS measurements after comparison of diffraction patterns collected at 220 °C and after cooling to room temperature (see Figure **II.33, right**). As in the previous cases, a number of well-expressed peaks in the wide angle region was recorded confirming the Col$_r$-Col$_{r,p}$ transition. The two main (200) and (110) peaks together with supplementary (120), (220/400), (410), (420) and (520) reflections were indexated in the framework of the rectangular lattice (see Table **S.II.11**). When cooling through the transition from the isotropic liquid to the mesophase, **7c** shows a typical planar birefringent texture that is stable until room

temperature, suggesting that, compared with the metal-free ligand, that the presence of the Zn^{II} ion in the Pc core stabilizes the columnar order (Figure **II.34**).

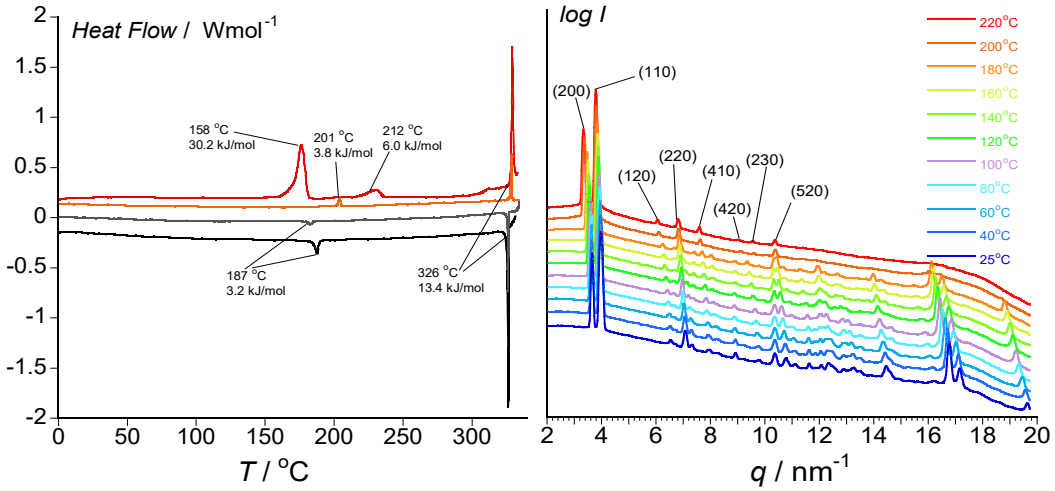

Figure II.33. (left) DSC traces of **7c** showing the transition sequence. Onset temperatures of the melting and clearing transitions are given with transition enthalpies. Scan rates: 10 K min^{-1} on first heating/cooling (red/black), 3 K min^{-1} on second heating/cooling (orange/gray); (right) Indexed SAXS diffraction profile of **7c**at temperatures indicated.

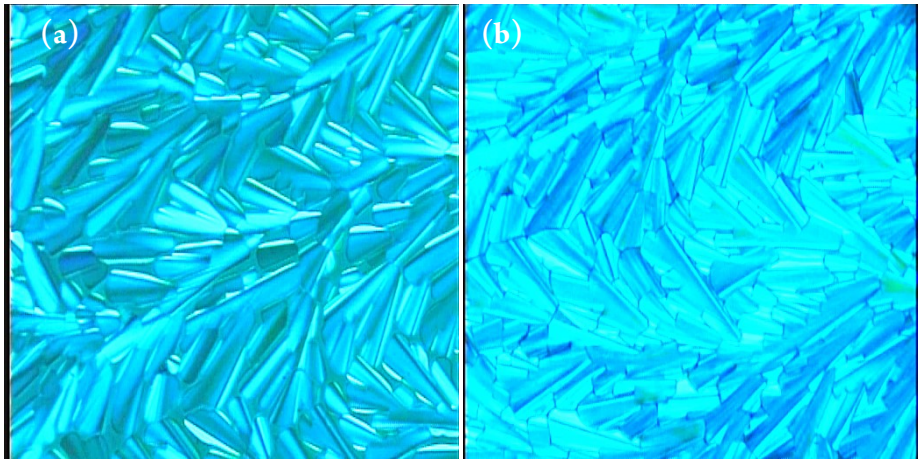

Figure II.34. Mesophase domains growing from the isotropic liquid between glass plates on cooling range seen through crossed polarizers for **7c**: (a) at 308 °C; (b) at 25 °C.

II.6. Conclusion of Section II.5

In order to analyze the impact on the liquid crystal behavior, two different symmetric branched chains were synthesized and used as α-substituents of the phthalocyanine core. Shortening of the aliphatic chains in the 3-alkoxy-phthalonitrile precursor from 2-butyloctyl to 2-butylhexyl leads to loss of regioselectivity and thus to the formation of an isomeric mixture during the cyclotetramerization. By column chromatography, it was possible to separate and determine by ^{1}H-NMR spectroscopy the C_{4h} symmetry of the major isomer. If the symmetrically branched 3-alkoxy phthalonitrile bears 2-pentylheptyl alkyl groups, of same mass as racemic 2-butyloctyl, the tetramerization is fully regiospecific, as in the racemic case. From both metal-free PCs with symmetrically branched chains, single crystals suitable for crystal structure determination of **7b** and **7c** could be obtained. Thus C_{4h} symmetry of the metal free phthalocyanine could be confirmed. A series of ten functionalized phthalocyanine complexes $MPc(OCH_2CH(R^{1\text{-}2})_2)_4$, (M = Co^{II}, Ni^{II}, Cu^{II}, Zn^{II} ; R^1 = Bu; R^2 =

Pent) was synthetized and characterized. The metal-free $H_2Pc(OCH_2CHPent_2)_4$ (**3b**) which clears at about 200°C, shows a liquid crystalline mesophase whose columnar order is maintained upon cooling to room temperature, whereas the shorter chain homolog $H_2Pc(OCH_2CHBu_2)_4$ (**3c**) shows its hexagonal mesogenicity only at high temperature. The same atypical hexagonal mesophase as in the racemic 2-butyloctyl homolog, with twelve columns per hexagonal unit cell, is found in both symmetric metal-free phthalocyanines. Rectangular columnar mesophases are obtained with all metal derivatives. The metal ion in the cavity of the phthalocyanine core ($MPc(OR^{1\text{-}2})_4$, M^{II} = Co^{II}, Ni^{II}, Cu^{II}, Zn^{II}) exerts a strong influence on the thermal range of the columnar mesophase. The clearing temperature increases with the deviation from square-planarity coordination geometry of the metal ion, with passing from planar to octahedral or tetrahedral. Their clearing temperature follow the order Ni < Cu < Co ≤ Zn. In case of the $MPc(OCH_2CHPent_2)_4$, the rectangular mesophase persists at room temperature, on the other hand, for $MPc(OCH_2CHBu_2)_4$ the rectangular mesophase is maintained only at high temperature. The common difference between $MPc(OCH_2CHPent_2)_4$ and $MPc(OCH_2CHBu_2)_4$ derivatives is that for $MPc(OCH_2CHBu_2)_4$ as revealed by DSC and SAXS analysis, a pronounced transition enthalpy from the liquid crystal to the plastic crystal state could be detected. For the $MPc(OCH_2CHPent_2)_4$ homologues, this transition could be inferred mainly from the appearance of additional peaks in the wide angle range of the powder X-ray pattern.

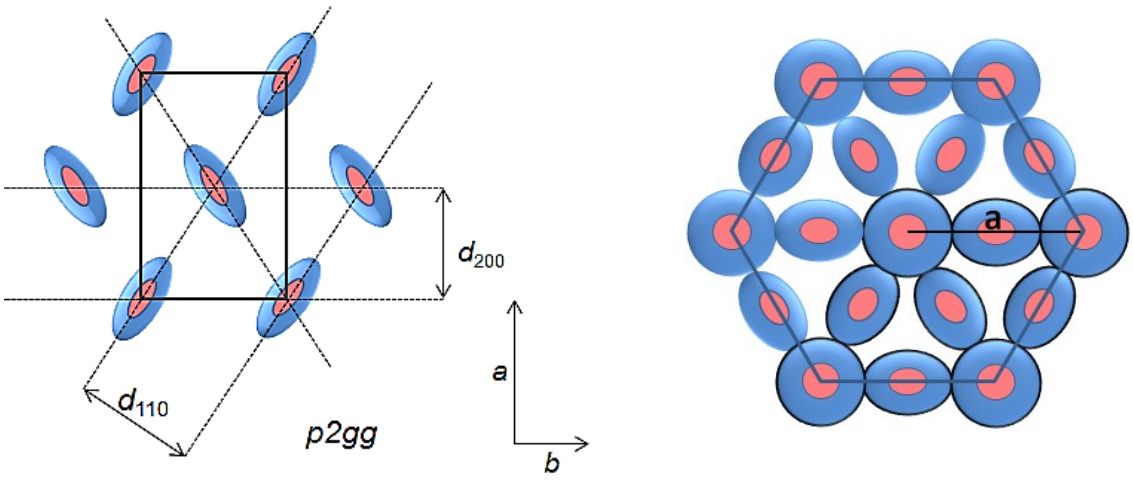

(a) (b)

Figure II.35. Schematic representation: (a) the column cross-sections of a rectangular columnar lattice with a *p2gg* plane group; (b) structure of a hexagonal columnar lattice with several tilted columns.

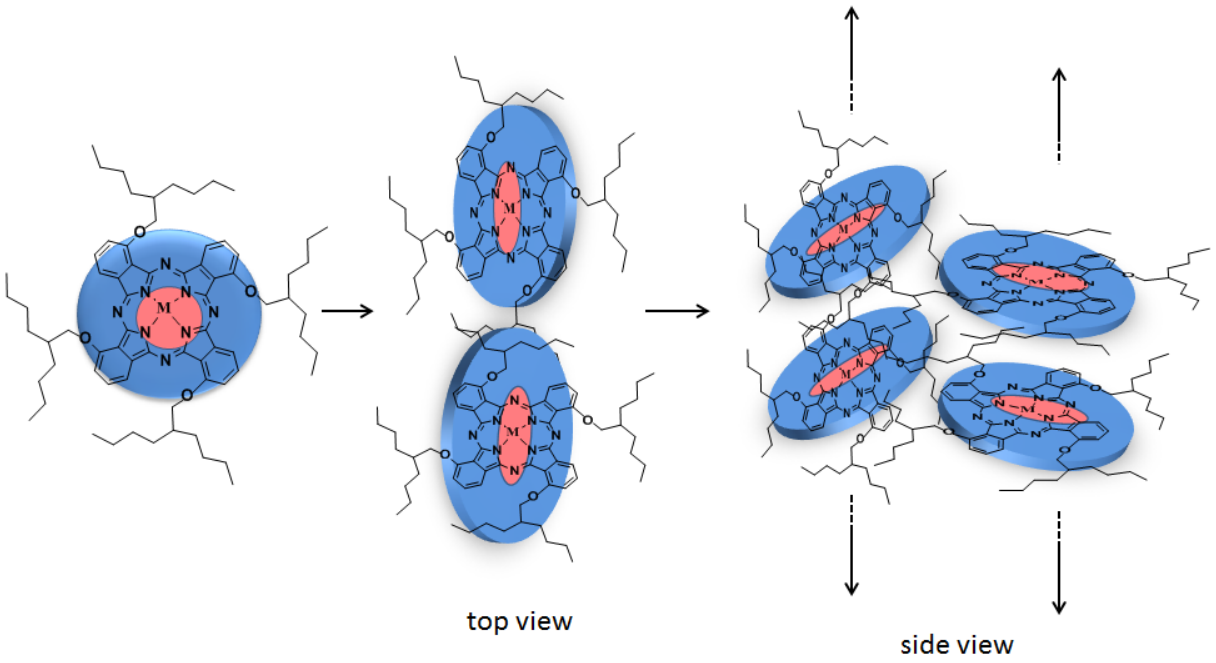

Figure II.36. Schematic representation of complete intercalation of the aliphatic chains.

II.7. Supporting Material

II.7.1. Supporting Material for Tetrasubstituted $M^{II}Pc$ with 2-Butyloctyloxy Substituent

II.7.1.1. Synthesis Protocols

3-(2-butyloctyloxy)phthalonitrile (2a). 3-nitrophthalonitrile **1** (24.0 g, 0.144 mol), K_2CO_3 (60 g, 0.56 mol) and racemic 2-butyl-1-octanol (40.3 ml, 0.833 g/ml, 0.180 mol) were thoroughly stirred in anhydrous DMF (250 ml) for 7 days at room temperature. After adding water and extracting three times with ethyl acetate, the solvent was evaporated in *vacuum*. The residue was chromatographed in DCM on silica gel and crystallized from ca 1500 ml of a 2:1 water : ethanol mixture. Yield: 13.35 g (31%) of white solid. ^{1}H NMR (400 MHz, CD_2Cl_2, TMS): δ = 7.61 (t, J = 8 Hz, 1H), 7.31 (d, J = 8 Hz, 1H), 7.22 (d, J = 8.5 Hz, 1H), 4.0 (d, J = 5.5 Hz, 2H), 1.84 (hept, J = 6 Hz, 1H), 1.48–1.38 (m, 4H), 1.34–1.23 (m, 12H), 0.88 ppm (t, J = 7.0, 3H), 0.86 ppm (t, J = 7.0, 3H); ^{13}C NMR (100 MHz, CD_2Cl_2, TMS): δ = 162.7, 135.1, 125.4, 117.5, 117.4, 116.2, 113.8, 105.3, 73.3, 38.2, 32.4, 31.6, 31.3, 30.2, 29.5, 27.3, 23.5, 23.2, 14.42, 14.37 ppm; IR (ATR): ῡ = 3081 (w), 2955 (vs), 2925 (s), 1855 (s), 2230 (m, CN) cm^{-1}; elemental analysis calcd (%) for $C_{20}H_{28}N_2O$: C 76.88, N 8.96, H 9.03; found C 76.70, N 9.05, H 9.10.

1, 8, 15, 22-(4-tetra-(2-butyloctyloxy)-phthalocyanine (3a). Lithium wire (0.40 g, 0.057 mol) was heated in 1-octanol in (70 ml) at 170°C until the all the metal was dissolved. After cooling to 100°C, 3-(2-butyloctyloxy)phthalonitrile (2.0 g, 6.40 mmol) was added the temperature was raised in small steps over 2h to 130°C whereupon the mixture became green. After stirring for a further hour at 130°C, the dark green solution was cooled at room temperature, poured into water and extracted with chloroform. The solvent was evaporated and the residue was purified by column chromatography in chloroform on silica gel followed by recrystallization from butanol. Yield: 0.83 g (43%) of blue-green powder. ^{1}H NMR (400 MHz, CD_2Cl_2, TMS): δ = 9.05 (d, J = 7.5 Hz, 4H), 8.10 (t, J = 7.5 Hz, 4H), 7.67 (d, J = 7.5 Hz, 4H), 4.59 (d, J = 5.5 Hz, 8H), 2.46 (hept, J = 6 Hz, 4H), 2.15 (m, 8H), 1.96 (m, 8H), 1.71–1.61 (m, 16H), 1.50–1.24 (m, 32H), 0.96 (t, J = 7.5 Hz, 12H), 0.79 (t, J = 7.5 Hz, 12H), −0.39 ppm (s, 2H); ^{13}C NMR (100 MHz, CD_2Cl_2, TMS): δ = 157.4, 150.4, 140.0, 131.3, 123.8, 115.8, 113.1, 72.7, 39.3, 32.6, 32.0, 31.7, 30.6, 29.9, 27.6, 23.9, 23.3, 14.6, 14.4 ppm; IR (ATR): ῡ= 3292 (w) 2952 (w), 2922 (vs), 2853 (s), 1586 (s), 1494 (m), 1458 (m), 1333 (s), 1264 (s), 1225 (s), 1142 (s), 1058 (s), 1010 (s), 931 (w), 864 (w), 797 (w), 743 (w), 726 (s), 705 (s) cm^{-1}; UV-Vis ($CHCl_3$): λ_{max} = 727(146 000), 696(131 000), 662(42 800), 627(32 200) nm(M^{-1} cm^{-1}); magnetic susceptibility measurements: diamagnetic constant of about -9.3×10^{-4} cm^3 K mol^{-1} that compares well with the expected theoretical value ($M_W \times 10^{-6}$ cm^3 K mol^{-1}); elemental analysis calcd (%) for $C_{80}H_{114}N_8O_4$: C 76.75, N 8.95, H 9.18; found 76.45, N 9.05, H 9.48.

Iron (II) 1, 8, 15, 22-(4-tetra-(2-butyloctyloxy)-phthalocyaninate (4a). Compound **3** (0.514 g (0.041 mmol) was heated at 100°C with $Fe(CH_3COO)_2$ (0.014 g (0.08 mmol) in DMF (50ml) for 12 h carried out

under a argon atmosphere in glove-box. The complex was separated by filtration after crystallization from cold solution. Yield: 78.8% of green crystals. IR (ATR): ῡ = 2952 (w), 2921 (vs), 2853 (s), 1590 (s), 1491 (m), 1463 (m), 1334 (s), 1270 (s), 1243 (s), 1134 (s), 1080 (s), 1036 (s), 944 (w), 878 (w), 798 (w), 750 (w), 735 (s) cm^{-1}; UV-Vis ($CHCl_3$): λ_{max}= 698, 671, 627, 574, 355 nm.

Cobalt (II) 1, 8, 15, 22-(4-tetra-(2-butyloctyloxy)-phthalocyaninate (5a). Compound **3** (0.50 g, 0.40 mmol) was refluxed with $Co(CH_3COO)_2 \cdot 4H_2O$ (0.70 g, 2.81 mmol) in DMF (50 ml). for 12 h under argon. After cooling to room temperature, the dark green solution was poured into water and extracted with chloroform, and purified by column chromatography in chloroform on silica gel followed by recrystallization from butanol/ethanol. Yield: 0.35g (67%) of blue solid. IR (ATR): ῡ = 2952 (w), 2921 (vs), 2854 (s), 1593 (s), 1491 (m), 1459 (m), 1331 (s), 1270 (s), 1250 (s), 1172 (s), 1060 (s), 1045 (s), 956 (w), 897 (w), 795 (w), 750 (w), 735 (s) cm^{-1}; UV-Vis ($CHCl_3$): λ_{max} = 694(163 000), 625(36 600) nm(M^{-1} cm^{-1}); MS: m/z $[M + H]^+$ calcd 1308.8, found 1309.1; magnetic susceptibility measurements: paramagnetic behaviour with an effective moment at 300 K of 2.3 μ_B (χT = 0.69 cm^3 K mol^{-1} and thus g = 2.7(1)) indicating a low spin S = 1/2 species; elemental analysis calcd (%) for $C_{80}H_{112}CoN_8O_4$: C 73.41, N 8.56, H 8.62; found C 72.91, N 8.72, H 8.95.

Nickel 1, 8, 15, 22-(4-tetra-(2-butyloctyloxy)-phthalocyaninate (6a). Compound **3** (0.50 g, 0.40 mmol) was refluxed with $Ni(CH_3COO)_2 \cdot 4H_2O$ (0.6 g, 2.4 mmol) in DMF (50 ml) for 12 h under argon. The complex was purified by column chromatography as described above for the cobalt complex and recrystallization from butanol. Yield: 0.48g (92%), of green solid IR (ATR, cm^{-1}): ῡ = 2953 (w), 2922 (vs), 2854 (s), 1597 (s), 1493 (m), 1459 (m), 1332 (s), 1270 (s), 1250 (s), 1143 (s), 1080 (s), 1060 (s), 956 (w), 899 (w), 794 (w), 750 (w), 735 (s); UV-Vis ($CHCl_3$): λ_{max} = 700(200 000), 668(39 600), 627(38 600) nm(M^{-1} cm^{-1}); MS: m/z $[M + H]^+$ calcd 1307.8, found 1308.1; magnetic susceptibility measurements: diamagnetic constant of about -8.8×10^{-4} cm^3 K mol^{-1} that compares well with the expected theoretical value ($M_W \times 10^{-6}$ cm^3 K mol^{-1}); elemental analysis calcd (%) for $C_{80}H_{112}NiN_8O_4$: C 73.43, N 8.56, H 8.62; found C 73.11, N 8.72, H 9.00.

Copper (II) 1, 8, 15, 22-(4-tetra-(2-butyloctyloxy)-phthalocyaninate (7a). Compound **3** (0.22 g, 176 μmol) was refluxed with $Cu(CH_3COO)_2 \cdot H_2O$ (0.60 g, 3 mmol) in DMF (50 ml) for 12 h under argon. The complex was purified by column chromatography as described above for the cobalt complex and recrystallization from butanol. Yield: 0.18g (73%) of dark green waxy solid. IR (ATR, cm^{-1}): ῡ = 2952 (w), 2921 (vs), 2854 (s), 1590 (s), 1490 (m), 1461 (m), 1330 (s), 1270 (s), 1250 (s), 1138 (s), 1080 (s), 1060 (s), 941 (w), 886 (w), 797 (w), 750 (w), 739 (s); UV-Vis ($CHCl_3$): λ_{max} = 707(225 000), 675(39 400), 635(46 000) nm(M^{-1} cm^{-1}); MS: m/z $[M + H]^+$ calcd 1312.8, found 1313.1; magnetic susceptibility measurements: paramagnetic behaviour with an effective moment at 300 K of 1.8 μ_B (χT = 0.42 cm^3 K mol^{-1} and thus g = 2.1(1)) indicating an S = 1/2 species; elemental analysis calcd (%) for $C_{80}H_{112}CuN_8O_4$: C 73.16, N 8.53, H 8.59; found C 73.05, N 8.20, H 8.83.

Zinc 1, 8, 15, 22-(4-tetra-(2-butyloctyloxy)-phthalocyaninate (8a). Compound **3** (0.50 g, 0.40 mmol) was refluxed with $Zn(CH_3COO)_2 \cdot 2H_2O$ (0.60 g, 2.73 mmol) in DMF (50 ml) for 12 h under argon. The complex was purified by column chromatography as described above for the cobalt complex and recrystallization from butanol. Yield: 0.38g (72%), of blue-green solid. IR (ATR, cm^{-1}): $\bar{\upsilon}$ = 2952 (w), 2921 (vs), 2853 (s), 1585 (s), 1490 (m), 1459 (m), 1338 (s), 1270 (s), 1250 (s), 1133 (s), 1080 (s), 1042 (s), 947 (w), 876 (w), 798 (w), 750 (w), 735 (s); UV-Vis ($CHCl_3$): λ_{max} = 704(220 000), 673(36 600), 632(41 400) nm(M^{-1} cm^{-1}); MS: m/z $[M + H]^+$ calcd 1313.8, found 1314.1; magnetic susceptibility measurements: diamagnetic constant of about -9.4×10^{-4} cm^3 K mol^{-1} that compares well with the expected theoretical value ($M_W \times 10^{-6}$ cm^3 K mol^{-1}); elemental analysis calcd (%) for $C_{80}H_{112}ZnN_8O_4$: C 73.06, N 8.52, H 8.58; found C 72.95, N 8.54, H 8.75.

II.7.1.2. Analytical Characterizations

II.7.1.2.1. ^{1}H-NMR Analyses

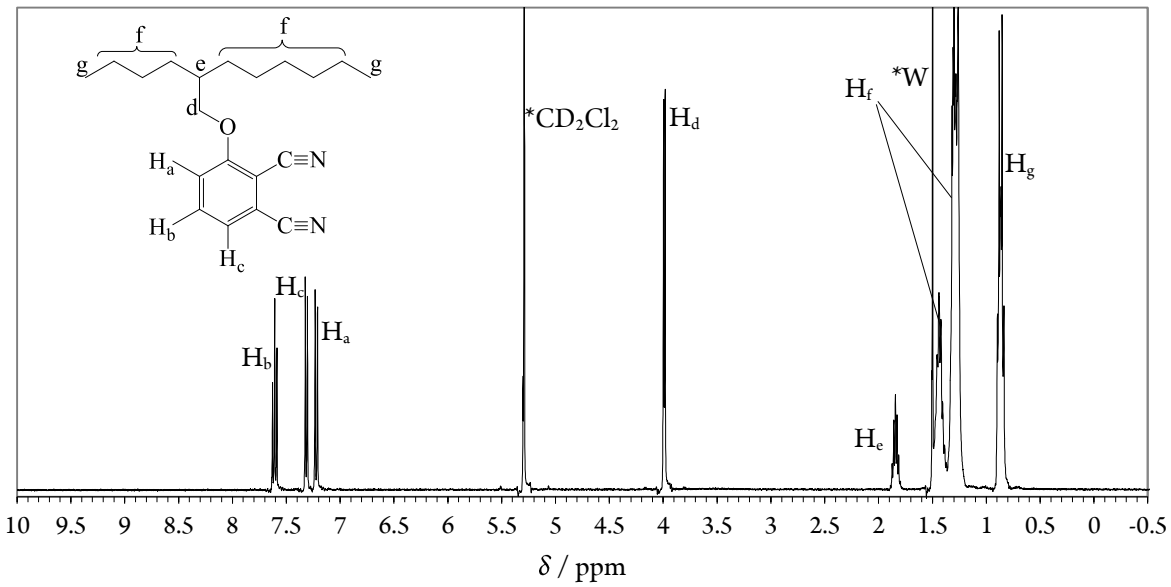

Figure S.II.1. ^{1}H-NMR spectrum of 3-(2-butyloctyloxy)phthalonitrile (**2a**) in CD_2Cl_2. The signal assignment is given in the left.

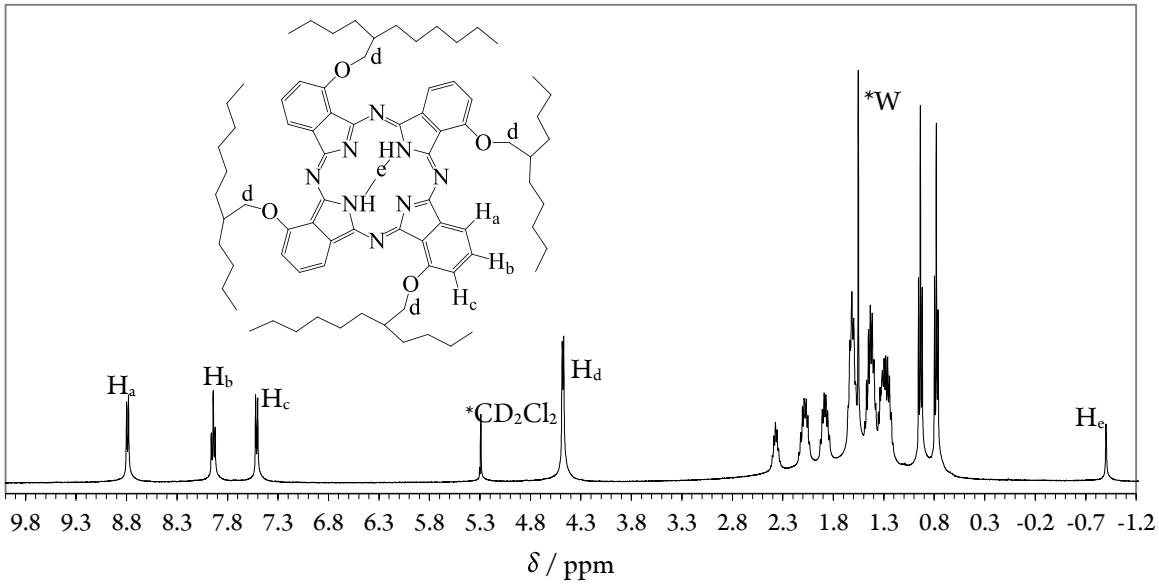

Figure S.II.2. ^{1}H-NMR spectrum of **3a** in CD_2Cl_2. The signal assignment is given in the left.

II.7.1.2.2. Crystallographic Data for $[Fe^{II}Pc(OCH_2CHBuHex)_4(DMF)_2]$ (4a)

Table S.II.1. Crystal data and structure refinement for $[Fe^{II}Pc(OCH_2CHBuHex)_4(DMF)_2]$ at 120 K.

Moiety formula	$C_{86}H_{126}Fe_1N_{10}O_6$
Empirical formula	$C_{86}H_{126}Fe_1N_{10}O_6$
Formula weight	1451.81
Crystal system	Triclinic
Space group	P-1
Wavelength, Å	0.71073
a, Å	8.8373(4)
b, Å	21.3513(13)
c, Å	22.9910(14)
α, °	109.301(2)
β, °	94.587(2)
γ, °	94.166(2)
V, Å^3	4058.5(4)
Z	2
ρ_{calcd}, g/cm^3	1.188
μ, 1/mm	0.244
Reflections collected	202093
Independent reflections	8542
R_1[a]	0.0826
wR_2[a]	0.2641
GoF[a]	1.045

[a] $I > 2\sigma(I)$, $R_1 = \Sigma|(|F_o| - |F_c|)|/\Sigma|F_o|$; $wR_2 = \{\Sigma[w(F_o^2 - F_c^2)^2]/\Sigma[w(F_o^2)^2]\}^{1/2}$; GoF (goodness of fit on F^2) = $\{\Sigma[w(F_o^2 - F_c^2)^2]/(n\text{-}p)\}^{1/2}$, where n is the number of reflections and p is the total number of refined parameters.

II.7.1.2.3. Thermotropic Properties

II.7.1.2.3.1. DSC Traces

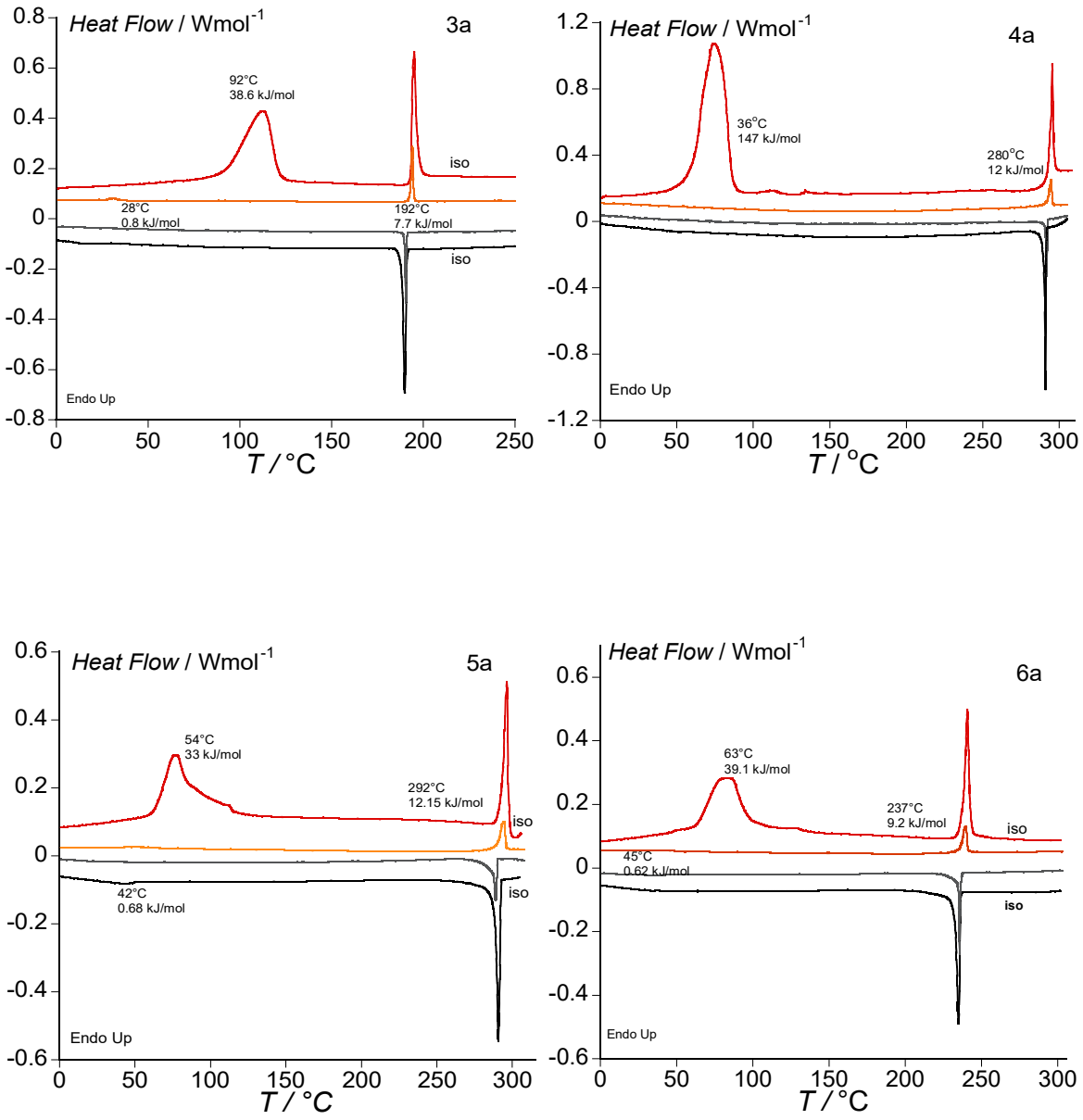

Figure S.II.3. Differential scanning calorimetry (DSC) thermograms of $H_2Pc(OCH_2CHBuHex)_4$ (**3a**), $Fe^{II}Pc(OCH_2CHBuHex)_4$ (**4a**), $CoPc(OCH_2CHBuHex)_4$ (**5a**), $NiPc(OCH_2CHBuHex)_4$ (**6a**). Onset temperatures of the melting and clearing transitions are given, with transition enthalpies. Scan rates: 10 K min^{-1} on first heating/cooling (red/black), 3 K min^{-1} on second heating/cooling (orange/grey).

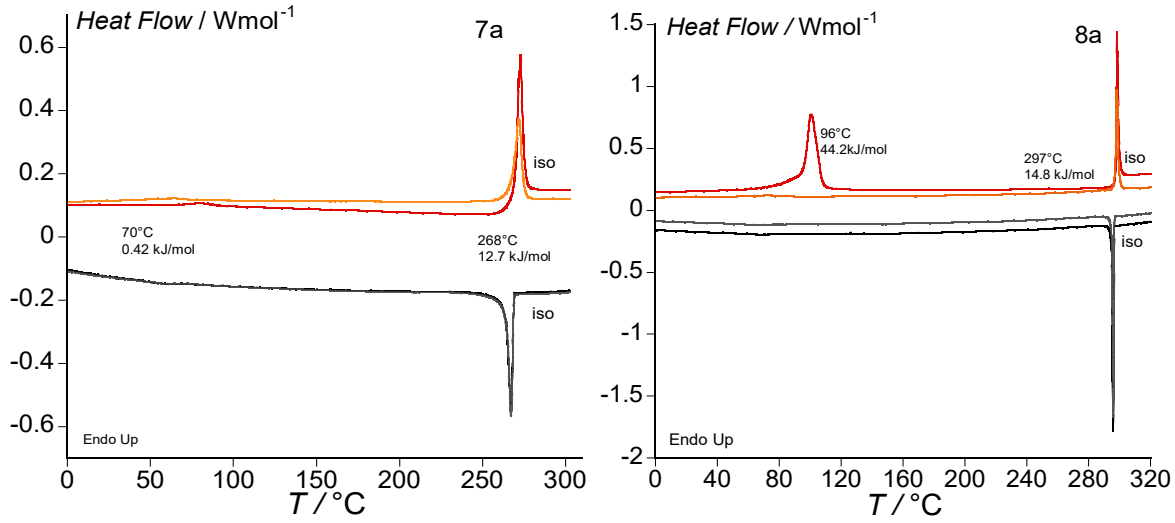

Figure S.II.4. Differential scanning calorimetry (DSC) thermograms of $Cu^{II}Pc(OCH_2CHBuHex)_4$ (**7**) and $Zn^{II}Pc(OCH_2CHBuHex)_4$ (**8**). Onset temperatures of the melting and clearing transitions are given, with transition enthalpies. Scan rates: 10 K min^{-1} on first heating/cooling (red/black), 3 K min^{-1} on second heating/cooling (orange/gray).

II.7.1.2.3.2. Polarized Optical Microscopy Images

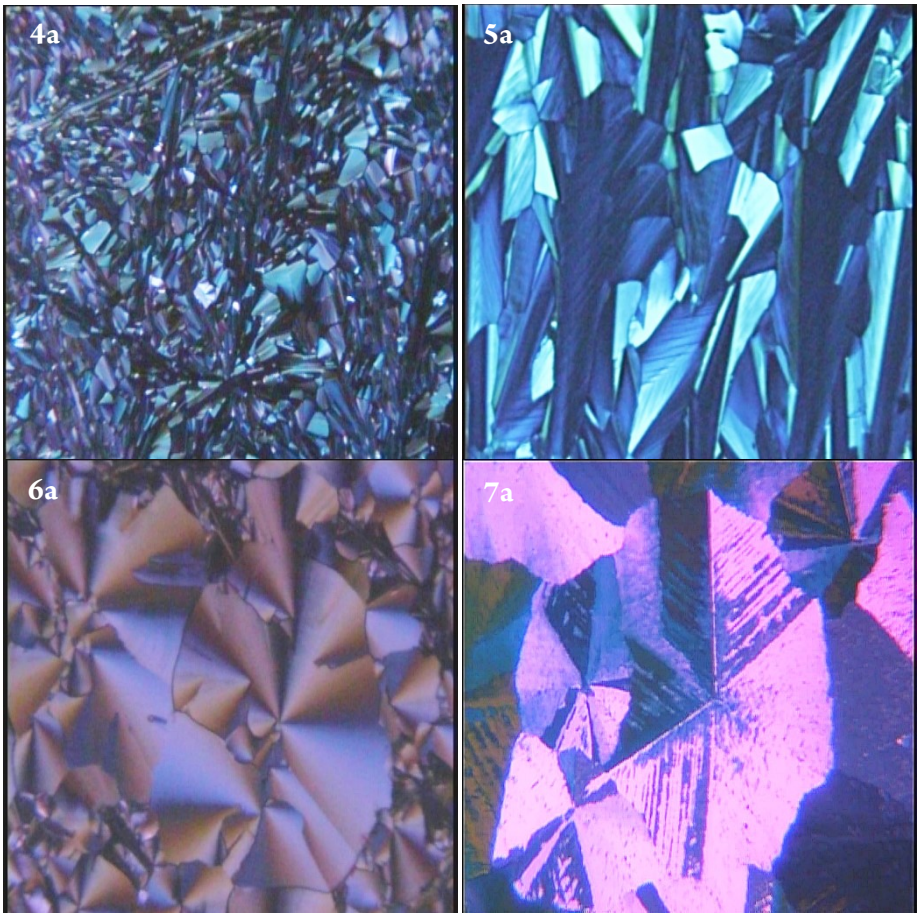

Figure S.II.5. Texture observed by polarized microscopy at room temperature after cooling though the isotropic liquid to liquid crystal phase transition for **4a** (Fe^{II}), **5a** (Co^{II}), **6a** (Ni^{II}), and **7a** (Cu^{II}),

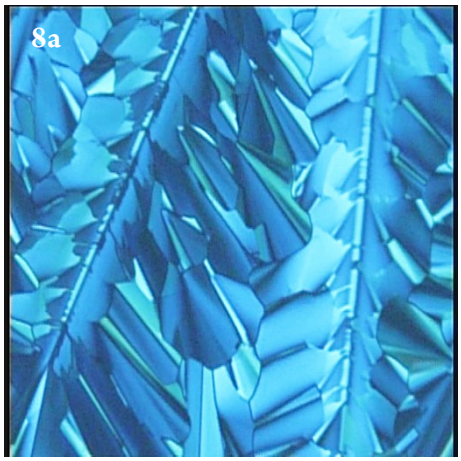

Figure S.II.5. cont. Texture observed by polarized microscopy at room temperature after cooling though the isotropic liquid to liquid crystal phase transition for **8a** (Zn^{II}) complexes.

II.7.1.2.4. Small Angle X-ray Scattering (SAXS) Investigations

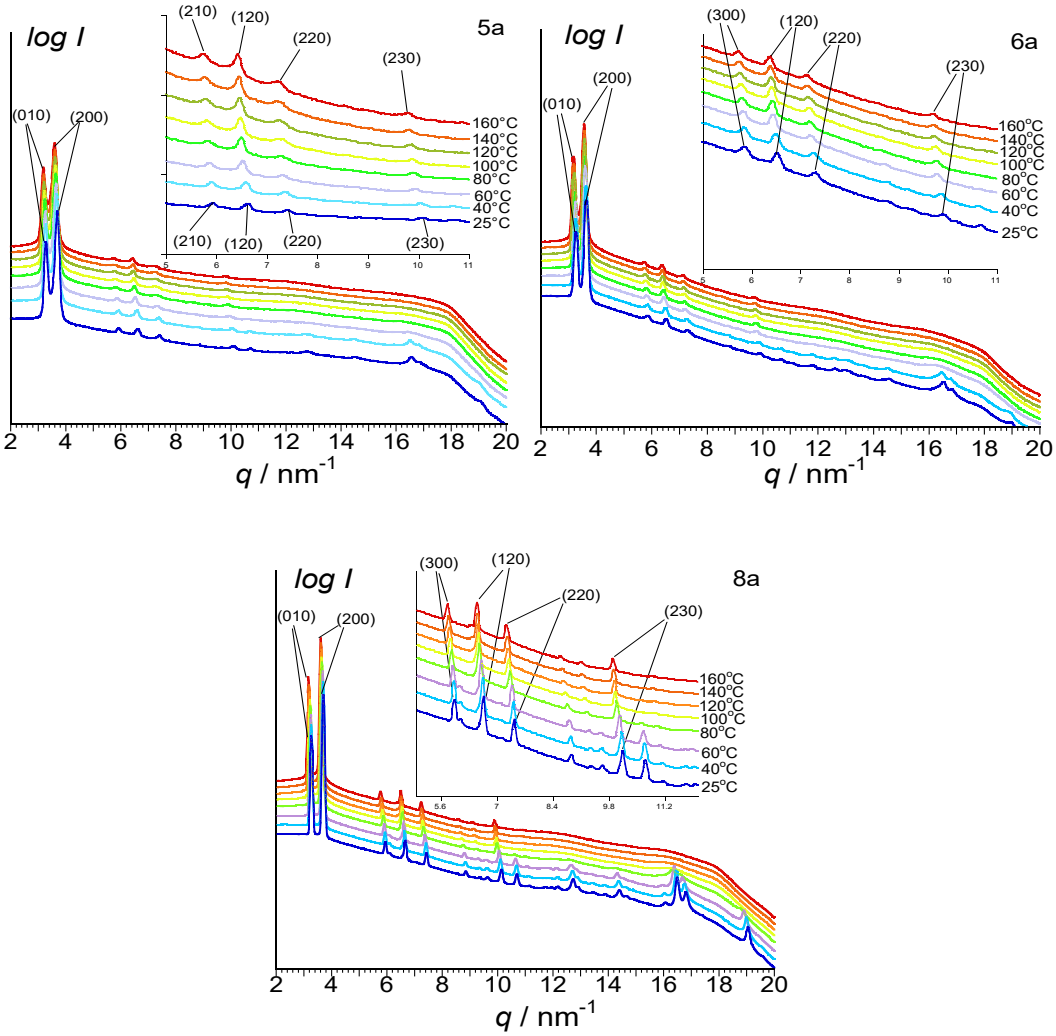

Figure S.II.6. Powder X-ray diffraction spectra at different temperatures upon stepwise cooling from 160 to 25 °C for **5a** (Co^{II}), **6a** (Ni^{II}), and **8a** (Zn^{II}). The Miller indices indicated in brackets correspond to a column lattice of hexagonal/rectangular symmetry.

Table S.II.2. Indexation of the reflections on 2nd cooling at 25 and 160°C for $H_2Pc(OCH_2CHBuHex)_4$ (**3a**).

T / °C	Peak number	$q_{(obs)}$ / nm^{-1}	$d_{(obs)}$ / Å	hkl	h^2+3k^2	$d_{(calc)}$ / Å	Calculated cell parameters (Å)
25	1	3.26	19.25	110	4	19.23	a = 35.43
	2	3.52	17.77	200	4	17.73	b = 21.41
	3	4.72	13.31	210	7	13.28	
	4	5.86	10.72	300	11	10.69	
	5	6.19	10.15	310	12	10.13	
	6	6.58	9.55	120	14	9.47	
	7	7.1	8.85	220/4	16	8.83	
					h^2+hk+k^2		
160	1	3.48	18.04	200	4	17.96	a = 41.50
	2	4.63	13.57	210	7	13.58	V = 71473 Å^3
	3	6.09	13.31	220	12	10.37	Z = 4

$q_{(obs)}$ is the observed/measured reciprocal spacing, $q = 4\pi \cdot sin\theta/\lambda$, where λ is the wavelength, 2θ is the diffraction angle, $d_{(obs)}$ and $d_{(calc)}$ are observed and calculated diffraction spacings: $d_{(obs)} = 2\pi/q_{(obs)}$, $d_{(calc\ rec)} = \frac{a}{\sqrt{h^2+3k^2}}$, and $d_{(calc\ hex)} = \frac{\sqrt{3}}{2}\frac{a}{\sqrt{h^2+hk+k^2}}$; a is the lattice parameter of the rectangular and hexagonal phase respectively, V is the volume of the cubic cell unit ($V = a^3$), $Z = (\rho \cdot V \cdot N_A)/Mw$, where ρ is the density ≈ 1.2 g/cm^3, N_A is the Avogadro constant $6.0225 \cdot 10^{23}$ (note: 1 Å^3 = $1.0 \cdot 10^{-24}$ cm^3).

Table S.II.3. Indexation of the reflections on 2nd cooling at 25 and 160°C for $CoPc(OCH_2CHBuHex)_4$ (**5a**).

T / °C	Peak number	$q_{(obs)}$ / nm^{-1}	$d_{(obs)}$ / Å	hkl	h^2+3k^2	$d_{(calc)}$ / Å	Calculated cell parameters (Å)
25	1	3.28	19.18	010	3	19.53	a = 33.82
	2	3.70	16.98	200	4	16.91	b = 23.24
	3	5.93	10.59	300	10	10.70	
	4	6.62	9.49	120	13	9.38	
	5	7.40	8.49	220/400	16	8.46	
	6	10.1	6.23	420	30	6.18	
160	1	3.18	19.72	010	3	20.06	a = 34.74
	2	3.60	17.46	110/200	4	17.37	b = 23.89
	3	5.73	10.96	300	10	10.98	
	4	6.42	9.77	120	13	9.63	
	5	7.20	8.72	220/400	16	8.68	
	6	9.78	6.42	420	30	6.45	

$q_{(obs)}$ is the observed/measured reciprocal spacing, $q = 4\pi \cdot sin\theta/\lambda$, where λ is the wavelength, 2θ is the diffraction angle, $d_{(obs)}$ and $d_{(calc)}$ are observed and calculated diffraction spacings: $d_{(obs)} = 2\pi/q_{(obs)}$, $d_{(calc\ rec)} = \frac{a}{\sqrt{h^2+3k^2}}$; a is the lattice parameter of the rectangular phase.

Table S.II.4. Indexation of the reflections on 2nd cooling at 25 and 160°C for NiPc(OCH$_2$CHBuHex)$_4$ (**6a**).

T / °C	Peak number	$q_{(obs)}$ / nm^{-1}	$d_{(obs)}$ / Å	hkl	h^2+3k^2	$d_{(calc)}$ / Å	Calculated cell parameters (Å)
25	1	3.25	19.31	010	3	19.82	a = 34.32
	2	3.63	17.27	110/200	4	17.16	b = 23.31
	3	5.85	10.74	300	10	10.85	
	4	6.51	9.64	120	13	9.52	
	5	7.28	8.63	220/400	16	8.58	
	6	9.91	6.34	230	30	6.27	
160	1	3.17	19.79	010	3	20.20	a = 35.00
	2	3.56	17.65	110/200	4	17.5	b = 23.91
	3	5.73	10.96	300	10	11.07	
	4	6.37	9.87	120	13	9.70	
	5	7.12	8.82	220/400	16	8.75	
	6	9.68	6.49	230	30	6.50	

$q_{(obs)}$ is the observed/measured reciprocal spacing, $q = 4\pi \cdot sin\theta/\lambda$, where λ is the wavelength, 2θ is the diffraction angle, $d_{(obs)}$ and $d_{(calc)}$ are observed and calculated diffraction spacings: $d_{(obs)} = 2\pi/q_{(obs)}$, $d_{(calc\ rec)} = \frac{a}{\sqrt{h^2+3k^2}}$; a is the lattice parameter of the rectangular phase.

Table S.II.5. Indexation of the reflections on 2nd cooling at 25 and 160°C for CuPc(OCH$_2$CHBuHex)$_4$ (**7a**).

T / °C	Peak number	$q_{(obs)}$ / nm^{-1}	$d_{(obs)}$ / Å	hkl	h^2+3k^2	$d_{(calc)}$ / Å	Calculated cell parameters (Å)
25	1	3.19	19.70	010	3	19.82	a = 33.80
	2	3.58	17.57	110/200	4	17.44	b = 23.40
	3	5.78	10.87	300	10	11.02	
	4	6.42	9.79	120	13	9.67	
	5	7.18	8.75	220/400	16	8.72	
	6	8.62	7.28	-	23	7.27	
	7	9.77	6.43	230	30	6.47	
	8	10.44	6.02	-	34	5.98	
	9	12.38	5.08	620	48	5.03	
	10	14.16	4.32	-	62	4.28	
	11	16.11	3.90	720	81	3.87	
	12	18.57	3.38	930	108	3.36	
160	1	3.17	19.80	010	3	20.07	
	2	3.59	17.49	200	4	17.38	
	3	5.74	10.94	300	10	11.00	
	4	6.43	9.77	120	13	9.64	a = 34.80
	5	7.19	8.74	220/400	16	8.69	b = 23.89
	6	9.80	6.41	230	30	6.45	

$q_{(obs)}$ is the observed/measured reciprocal spacing, $q = 4\pi \cdot sin\theta/\lambda$, where λ is the wavelength, 2θ is the diffraction angle, $d_{(obs)}$ and $d_{(calc)}$ are observed and calculated diffraction spacings: $d_{(obs)} = 2\pi/q_{(obs)}$, $d_{(calc\ rec)} = \frac{a}{\sqrt{h^2+3k^2}}$; a is the lattice parameter of the rectangular phase.

Table S.II.6. Indexation of the reflections on 2nd cooling at 25 and 160°C for $ZnPc(OCH_2CHBuHex)_4$ (**8a**).

T / °C	Peak number	$q_{(obs)}$ / nm^{-1}	$d_{(obs)}$ / Å	hkl	h^2+3k^2	$d_{(calc)}$ / Å	Calculated cell parameters (Å)
25	1	3.29	19.12	010/120	3	19.43	a = 33.65
	2	3.72	16.90	110/200	4	16.83	b = 23.17
	3	5.93	10.59	300	10	10.64	
	4	6.55	9.45	120	13	9.33	
	5	7.42	8.47	220/400	16	8.41	
	6	10.11	6.21	230	30	6.25	
160	1	3.17	19.79	010/120	3	19.98	a = 34.60
	2	3.62	17.34	110/200	4	17.30	b = 24.08
	3	5.77	10.88	300	10	10.94	
	4	6.51	9.65	120	13	9.60	
	5	7.24	8.67	220/400	16	8.65	
	6	9.89	6.35	230	30	6.31	

$q_{(obs)}$ is the observed/measured reciprocal spacing, $q = 4\pi \cdot sin\theta/\lambda$, where λ is the wavelength, 2θ is the diffraction angle, $d_{(obs)}$ and $d_{(calc)}$ are observed and calculated diffraction spacings: $d_{(obs)} = 2\pi/q_{(obs)}$, $d_{(calc\ rec)} = \frac{a}{\sqrt{h^2+3k^2}}$; a is the lattice parameter of the rectangular phase.

II.7.1.2.5. Magnetic Measurements

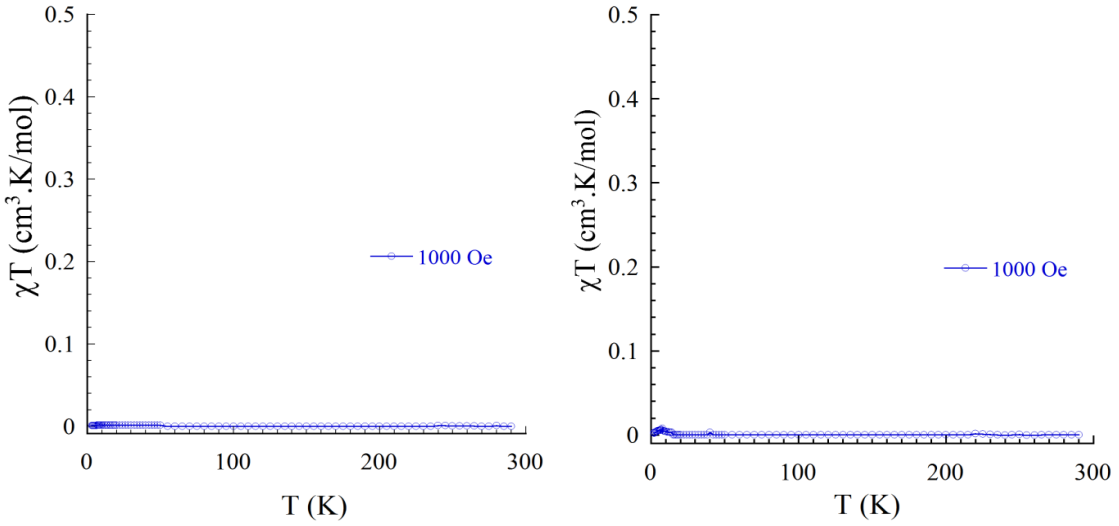

Figure S.II.7. χT versus T plots at 0.1 T (with χ being the molar magnetic susceptibility defined as M/H per complex) for **6a** (Ni^{II}) (left) and for **8a** (Zn^{II}) complexes (right). The solid lines are guides for the eyes.

II.7.2. Supporting Material for Tetrasubstituted MIIPcs with 2-Pentylheptyloxy and 2-Butylhexyloxy Substituents

II.7.2.1. Synthesis Protocols

Solvents and starting materials were purchased from Acros, Matrix Scientific, Alfa Aesar or Aldrich, and used without further purification unless otherwise stated.

Preparation of 2-pentylheptan-1-ol (1). A 2.5M solution of butyl-lithium in THF (100 ml, 87.5 mmol) was added dropwise to a stirred suspension of sodium heptanoate (25.23g, 0.166mol) and diisopropylamine (35 ml,

0.722 g cm^{-1}, 0.25mol) in dry THF (250 ml) under argon, at 0°C (ice-bath), and the mixture was stirred for 2h at 0°C. The mixture was warmed and stirring was continued for 2h at room temperature. The mixture was cooled again to 0°C, and bromopentane (37 ml, 1.218 g/cm^{-1}, 45 g, 0.3 mol) was added dropwise, and the mixture was stirred for 16h. The mixture was poured into 2M aqueous hydrochloric acid (200 ml), extracted with CH_2Cl_2 (3 ~200 ml), and the combined organic phases were dried over sodium sulfate and concentrated. The obtained acid was purified by vacuum distillation (180°C, 15mmHg). Yield: 28.9 g, 87% reddish liquid. ^{1}H NMR (400 MHz, CD_2Cl_2, TMS): δ = 11.3 (br, 1H), 2.32 (hept. 1H), 1.58(m, 2H), 1.45 (m, 2H), 1.26(m, 12H), 0.85(t, 6H) ppm. To a part of corresponded acid (16.4g, 8.2mmol) an excess of 1M solution of $LiAlH_4$ in THF was added drop wise in dry THF under argon, at 0°C (ice-bath). The stirring was continued at room temperature for 1 h, and then refluxed for 16h. The mixture was cooled again to 0°C and carefully was added drop wise distilled water. The mixture was poured into 2M aqueous hydrochloric acid (100 ml), extracted with CH_2Cl_2 (3 ~150 ml), and the combined organic phases were dried over sodium sulfate and concentrated. The product was purified by vacuum distillation (180°C, 15mmHg). Yield: 14.1g, (92%) colorless liquid. ^{1}H NMR (400 MHz, CD_2Cl_2, TMS): δ = 3.51 (d, 2H), 1.51-1.10(m, 18 H), 0.85(t, 6H) ppm.

Preparation of 3-(2-pentylheptyloxy-)phthalonitrile (2). 3-nitrophthalonitrile (10.0 g, 57.7 mmol), K_2CO_3 (80 g, 0.58 mol) and **1** (12 g, 64.4 mmol) were thoroughly stirred in anhydrous DMF (150 ml) for 14 days at room temperature. After adding water and extracting three times with ethyl acetate, the solvent was evaporated in *vacuo*. The residue was chromatographed in DCM on silica gel and crystallized from ca 1000 ml of a 2:1 water: ethanol mixture. Yield: 8 g (46%) of white solid. ^{1}H NMR (400 MHz, CD_2Cl_2, TMS): δ = 7.61 (t, J = 8 Hz, 1H), 7.31 (d, J = 8 Hz, 1H), 7.22 (d, J = 8.5 Hz, 1H), 4.0 (d, J = 5.5 Hz, 2H), 1.84 (hept, J = 6 Hz, 1H), 1.48–1.38 (m, 4H), 1.34–1.10 (m, 12H), 0.85 ppm (m, 6H); IR (ATR): ῡ = 3081 (w), 2950 (vs), 2924 (s), 2856 (s), 2229 (m, CN) cm^{-1}; elemental analysis calcd (%) for $C_{20}H_{28}N_2O$: C 76.88, N 8.97, H 9.03; found C 76.75, N 9.08, H 9.10.

Preparation of $H_2Pc(OCH_2CHPent_2)_4$ (3b). Lithium wire (0.50 g, 0.072 mol) was heated in 1-pentanol in (50 ml) at 130°C until the all the metal was dissolved. After cooling to 90°C, 3-(2-pentylheptyloxy-) phthalonitrile (4.0 g, 12.80 mmol) was added and the temperature was raised in small steps over 2h to 130°C whereupon the mixture became green. After stirring for 16 hours at 130°C, the dark green solution was cooled at room temperature, poured into water and extracted with dichloromethane. The solvent was evaporated and the residue was purified by column chromatography in dichloromethane on silica gel followed by recrystallization from methanol. Yield: 0.62 g (16%) of blue-green crystalline solid. ^{1}H NMR (400 MHz, CD_2Cl_2, TMS): δ = 8.95 (d, J = 7.5 Hz, 4H), 8.03 (t, J = 7.5 Hz, 4H), 7.60 (d, J = 7.5 Hz, 4H), 4.54 (d, J = 5.5 Hz, 8H), 2.41 (hept, J = 6 Hz, 4H), 2.11 (m, 8H), 1.90 (m, 8H), 1.71–1.58 (m, 16H), 1.48–1.28 (m, 32H), 0.83 (t, 24H), −0.52 ppm (s, 2H); ^{13}C NMR (100 MHz, CD_2Cl_2, TMS): δ = 157.1, 150.0, 139.7, 131.1, 123.6, 115.5, 112.8, 72.2, 38.8, 32.5, 31.5, 29.7, 26.8, 22.8, 13.9 ppm; IR (ATR): ῡ = 3292 (w) 2950 (w), 2921 (vs), 2853 (s), 1906 (s), 1587

(s), 1494 (m), 1458 (m), 1333 (s), 1264 (s), 1242 (s), 1224 (s), 1143 (s), 1058 (s), 1009 (s), 927 (w), 865 (w), 796 (w), 743 (w), 725 (s), 705 (s), 611 (s) cm^{-1}; UV-Vis (CH_2Cl_2): λ_{max} = 728(161400), 696(146800), 664(46200), 628(34400) nm(M^{-1} cm^{-1}); elemental analysis calcd (%) for $C_{80}H_{114}N_8O_4$: C 76.75, N 8.95, H 9.18; found 76.43, N 9.08, H 9.29.

Preparation of $CoPc(OCH_2CHPent_2)_4$ (4b). Compound **3** (0.11 g, 0.090 mmol) was refluxed with $Co(CH_3COO)_2 \cdot 4H_2O$ (0.31 g, 1.24 mmol) in DMF (18 ml) for 12 h under argon. After cooling to room temperature, the dark green precipitate was filtrated. The product was purified by recrystallization from dichloromethane/methanol mixture. Yield: 0.10g (87%) of blue solid. IR (ATR): $\bar{\upsilon}$ = 2948 (w), 2922 (vs), 2853 (s), 1901 (s), 1593 (s), 1520 (s), 1491 (m), 1459 (m), 1375 (s), 1332 (s), 1270 (s), 1250 (s), 1172 (s), 1092 (s), 1061 (s), 1045 (s), 956 (w), 897 (w), 795 (w), 750 (w), 738 (s), 640 (s) cm^{-1}; UV-Vis (CH_2Cl_2): λ_{max} = 704(231 200), 672(39 600), 632(45 600) nm(M^{-1} cm^{-1}); elemental analysis calcd (%) for $C_{80}H_{112}CoN_8O_4$: C 73.41, N 8.56, H 8.62; found C 73,16 N 8.33, H 8.80.

Preparation of $NiPc(OCH_2CHPent_2)_4$ (5b). Compound **3** (0.12 g, 0.096 mmol) was refluxed with $Ni(CH_3COO)_2 \cdot 4H_2O$ (0.36 g, 1.45 mmol) in DMF (15 ml) for 12 h under argon. The complex was purified as described above for the cobalt complex and recrystallization from dichloromethane/methanol mixture. Yield: 0.115g (92%), of green solid IR (ATR, cm^{-1}): $\bar{\upsilon}$ = 2948 (w), 2922 (vs), 2854 (s), 1902 (s), 1726 (s), 1599 (s), 1530 (s), 1493 (m), 1493 (s), 1459 (m), 1375 (s), 1333 (s), 1271 (s), 1252 (s), 1172 (s), 1145 (s), 1090 (s), 1060 (s), 956 (w), 933 (s), 899 (w), 794 (w), 750 (w), 737 (s), 640 (w) UV-Vis (CH_2Cl_2): λ_{max} = 797(213 400), 668(40 500), 624(38 000) nm(M^{-1} cm^{-1}); elemental analysis calcd (%) for $C_{80}H_{112}NiN_8O_4$: C 73.43, N 8.56, H 8.62; found C 73.20, N 8.27, H 8.80.

Preparation of $CuPc(OCH_2CHPent_2)_4$ (6b). Compound **3** (0.10 g, 0.08 mmol) was refluxed with $Cu(CH_3COO)_2 \cdot H_2O$ (0.31 g, 1.55 mmol) in DMF (15 ml) for 12 h under argon. The complex was purified as described above for the cobalt complex and dichloromethane/methanol mixture. Yield: 0.10g (100%) of blue solid. IR (ATR): $\bar{\upsilon}$ = 2949 (w), 2923 (vs), 2854 (s), 1906(w), 1591 (s), 1504 (m), 1490 (m), 1459 (m), 1332 (s), 1270 (s), 1245 (s), 1141 (s), 1090 (s), 1060 (s), 1015 (s), 954 (w), 886 (w), 795 (s), 750 (5), 736 (s), 633 (w) cm^{-1}; UV-Vis (CH_2Cl_2): λ_{max} = 707(208 600), 675(39 400), 632(40 800) nm(M^{-1} cm^{-1}); elemental analysis calcd (%) for $C_{80}H_{112}CuN_8O_4$: C 73.16, N 8.53, H 8.59; found C 73.05, N 8.32, H 8.9.

Preparation of $ZnPc(OCH_2CHPent_2)_4$ (7b). Compound **3** (0.1 g, 0.08 mmol) was refluxed with $Zn(CH_3COO)_2 \cdot 2H_2O$ (0.34 g, 1.55 mmol) in DMF (12 ml) for 12 h under argon. After cooling to room temperature, the dark green solution was filtrated (in order to retain any post-reaction impurities) and has been left for slow evaporation. After four days, the crystalline product was filtrated, washed several times with methanol and dried at room temperature. According to the X-ray measurements (see section II.5.2.2), the

compound contains one molecule of dimethylformamide as a coordinated axial ligand. Yield: 91 mg (87%), of blue-green crystalline compound. IR (ATR, cm^{-1}): $\bar{\upsilon}$ = 2921 (vs), 2853 (s), 1912 (w), 1656 (s), 1586 (s), 1489 (m), 1464 (m), 1377 (w), 1336 (s), 1264 (s), 1235 (s), 1129 (s), 1087 (s), 1060 (s), 1019 (m), 931 (w), 874 (w), 801 (w), 750 (w), 740 (s), 679 (w), 629 (w);UV-Vis (CH_2Cl_2): λ_{max} = 760(39 200), 704(187 600), 676(37 400), 636(34 400) nm(M^{-1} cm^{-1}); elemental analysis calcd (%) for $C_{83}H_{119}ZnN_9O_5$: C 71.81, N 9.08, H 8.64; found C 71.63, N 9.24, H 8.69.

Preparation of 2-butylhexan-1-ol (?). The alcohol **8** was obtained from sodium hexanoate (27.62g, 0.2mol) and 1-bromobutane (32 ml, 1.2676 g cm^{-1}, 40.5mol) following the described preceding procedure for synthesizing compound **2**. Yield (two steps): 15.2g, (76%) colorless liquid. ^{1}H NMR (400 MHz, CD_2Cl_2, TMS): δ = = 3.52 (d, 2H), 1.51-1.15(m, 14 H), 0.85(t, 6H) ppm.

Preparation of 3-(2-butylhexyloxy-)phthalonitrile (9). 3-nitrophthalonitrile (9.0 g, 52.3 mmol), K_2CO_3 (40 g, 0.29 mol) and symmetric 2-butyl-1-hexanol (9 g, 56.8 mmol) were thoroughly stirred in anhydrous DMF (150 ml) for 7 days at room temperature. The compound was purified by column chromatography as described above for **3** and crystallized from ca 1000 ml of a 2:1 water: ethanol mixture. Yield: 10 g (68%) of white crystalline solid. ^{1}H NMR (400 MHz, CD_2Cl_2, TMS): δ = 7.61 (t, J = 8 Hz, 1H), 7.31 (d, J = 8 Hz, 1H), 7.22 (d, J = 8.5 Hz, 1H), 4.0 (d, J = 5.5 Hz, 2H), 1.84 (hept, J = 6 Hz, 1H), 1.5–1.35 (m, 4H), 1.34–1.20 (m, 12H), 0.88 ppm (m, 6H); IR (ATR): $\bar{\upsilon}$ = 3087 (w), 2955 (vs), 2928 (s), 2858 (s), 2229 (m, CN) cm^{-1}; elemental analysis calcd (%) for $C_{18}H_{24}N_2O$: C 76.02, N 9.85, H 8.51; found C 76.10, N 9.75, H 8.42.

Preparation of $H_2Pc(OCH_2CHBu_2)_4$ (3c). Lithium wire (0.50 g, 0.072 mol) was heated in 1-hexanol in (50 ml) at 130°C until the all the metal was dissolved. After cooling to 90°C, 3-(2-butylhexyloxy-)phthalonitrile (3.0 g, 10.50 mmol) was added and the temperature was raised in small steps over 2h to 130°C whereupon the mixture became green. After stirring for 16 hours at 130°C, the dark green solution was cooled at room temperature, the solvent was evaporated, added water and extracted with dichloromethane. The solvent was evaporated and the residue was purified by column chromatography in dichloromethane on silica gel followed by recrystallization from methanol. Yield: 0.80 g (30%) of blue-green crystalline solid. ^{1}H NMR (400 MHz, CD_2Cl_2, TMS): δ = 9.15 (d, J = 7.5 Hz, 4H), 8.05 (t, J = 7.5 Hz, 4H), 7.65 (d, J = 7.5 Hz, 4H), 4.45 (d, J = 5.5 Hz, 8H), 2.45 (hept, J = 6 Hz, 4H), 2.15 (m, 8H), 1.95 (m, 8H), 1.71–1.58 (m, 16H), 1.48–1.28 (m, 32H), 0.90 (t, 24H), – 0.36 ppm (s, 2H); ^{13}C NMR (100 MHz, CD_2Cl_2, TMS): δ = 157.1, 150.0, 139.7, 131.1, 123.6, 115.5, 112.8, 72.2, 38.8, 32.5, 31.5, 29.7, 26.8, 22.8, 13.9 ppm; IR (ATR): $\bar{\upsilon}$ = 3295 (w) 2951 (w), 2923 (vs), 2855 (s), 1906 (s), 1587 (s), 1495 (m), 1460 (m), 1374 (s), 1334(s), 1263 (s), 1226 (s), 1143 (s), 1115 (s), 1057 (s), 1009 (s), 932 (w), 864 (w), 796 (w), 743 (w), 725 (s), 705 (s), 678 (w), 639 (w), 611 (s) cm^{-1}; UV-Vis (CH_2Cl_2): λ_{max} = 724(137600), 696(13400), 664(37800), 628(30600) nm(M^{-1} cm^{-1}); elemental analysis calcd (%) for $C_{72}H_{98}N_8O_4$: C 75.88, N 9.83, H 8.67; found 75.92, N 9.85, H 8.80.

Preparation of $MPc(OCH_2CHBu_2)_4$ M = Co^{II} (4c), Ni^{II} (5c), Cu^{II} (6c), Zn^{II} (7c). Compound **3c** (0.11 g, 0.087 mmol) was refluxed with $M(CH_3COO)_2 \cdot nH_2O$ (for **4c** with 60 mg (0.24 mmol) of $Co(CH_3COO)_2 \cdot 4H_2O$; for **5c** with 31.3 mg (0.125 mmol) of $Ni(CH_3COO)_2 \cdot 4H_2O$; for **6c** with 60 mg (0.3 mmol) of $Cu(CH_3COO)_2 \cdot H_2O$; for **7c** with 85 mg (0.38 mmol)of $Zn(CH_3COO)_2 \cdot 2H_2O$) in DMF (18 ml) for 12 h under argon. After cooling to room temperature, the compounds **4c**, **5c** and **6c** was filtrated. The precipitate was purified by column chromatography in dichloromethane on silica gel followed by recrystallization from methanol. The **7c** compound the dark green solution was filtrated (in order to retain any post-reaction impurities) and has been left for slow evaporation. After four days, the crystalline product was filtrated, washed several times with methanol and dried at room temperature. The yields were: 118 mg (83%) for **4c**, 94 mg (85.6%) for **5c**, 84 mg (79%) for **6c**, 98 mg (92.7%) for **7c**. According the x-Ray measurements compound **7c** contains one molecule of dimethylformamide as a coordinated axial ligand. Elemental analysis (%) – Calc. (Found) for **(4c)** $CoC_{72}H_{96}N_8O_4$: C, 72.27 (72.15); H, 8.09 (8.11); N, 9.36 (9.25); IR (ATR): $\bar{\upsilon}$ = 2947 (w), 2920 (vs), 2855 (s), 1905 (s), 1591 (s), 1521 (s), 1489 (m), 1460 (m), 1376 (s), 1331 (s), 1270 (s), 1251 (s), 1172 (s), 1091 (s), 1061 (s), 1047 (s), 956 (w), 896 (w), 796 (w), 750 (w), 738 (s), 639 (s) cm^{-1}; UV-Vis (CH_2Cl_2): λ_{max} = 704(231 200), 672(39 600), 632(45 600) nm(M^{-1} cm^{-1}). Elemental analysis (%) – Calc. (Found) for **(5c)** $NiC_{72}H_{96}N_8O_4$: C, 72.29 (72.32); H, 8.09 (8.01); N, 9.37 (9.23); IR (ATR): $\bar{\upsilon}$ = 2951 (w), 2923 (vs), 2856 (s), 1600 (s), 1529 (s), 1494 (m), 1461 (m), 1374 (s), 1333 (s), 1271 (s), 1254 (s), 1173 (s), 1144 (w) 1090 (s), 1061 (s), 1045 (s), 959 (w), 897 (w), 795 (w), 750 (w), 738 (s), 637 (s) cm^{-1}; UV-Vis (CH_2Cl_2): λ_{max} = 704(231 200), 672(39 600), 632(45 600) nm(M^{-1} cm^{-1}). Elemental analysis (%) – Calc. (Found) for **(6c)** $CuC_{72}H_{96}N_8O_4$: C, 72.00 (71.80); H, 8.06 (7.95); N, 9.33 (9.26); IR (ATR): $\bar{\upsilon}$ = 2951 (w), 2923 (vs), 2856 (s), 1905 (s), 1591 (s), 1502 (s), 1490 (m), 1460 (m), 1376 (s), 1330 (s), 1268 (s), 1247 (s), 1172 (s), 1138 (s), 1089 (s), 1061 (s), 1034 (s), 949 (w), 885 (w), 797 (w), 737 (s), 632 (s) cm^{-1}; UV-Vis (CH_2Cl_2): λ_{max} = 704(231 200), 672(39 600), 632(45 600) nm(M^{-1} cm^{-1}). Elemental analysis (%) – Calc. (Found) for **(7c)** $ZnC_{72}H_{96}N_8O_4$: C, 70.59 (70.80); H, 8.14 (8.25); N, 9.88 (9.70); IR (ATR): $\bar{\upsilon}$ = 2952 (w), 2923 (vs), 2856 (s), 1656 (s), 1586 (s), 1489 (m), 1376 (s), 1336 (s), 1266 (s), 1235 (s), 1130 (s), 1087 (s), 1061 (s), 1039 (s), 1019 (w), 942 (w), 874 (w), 800 (w), 750 (w), 737 (s), 678 (s), 631 (w) cm^{-1}; UV-Vis (CH_2Cl_2): λ_{max} = 704(231 200), 672(39 600), 632(45 600) nm(M^{-1} cm^{-1}).

II.7.2.2. Analytical Characterizations

II.7.2.2.1. ^{1}H-NMR Analyses

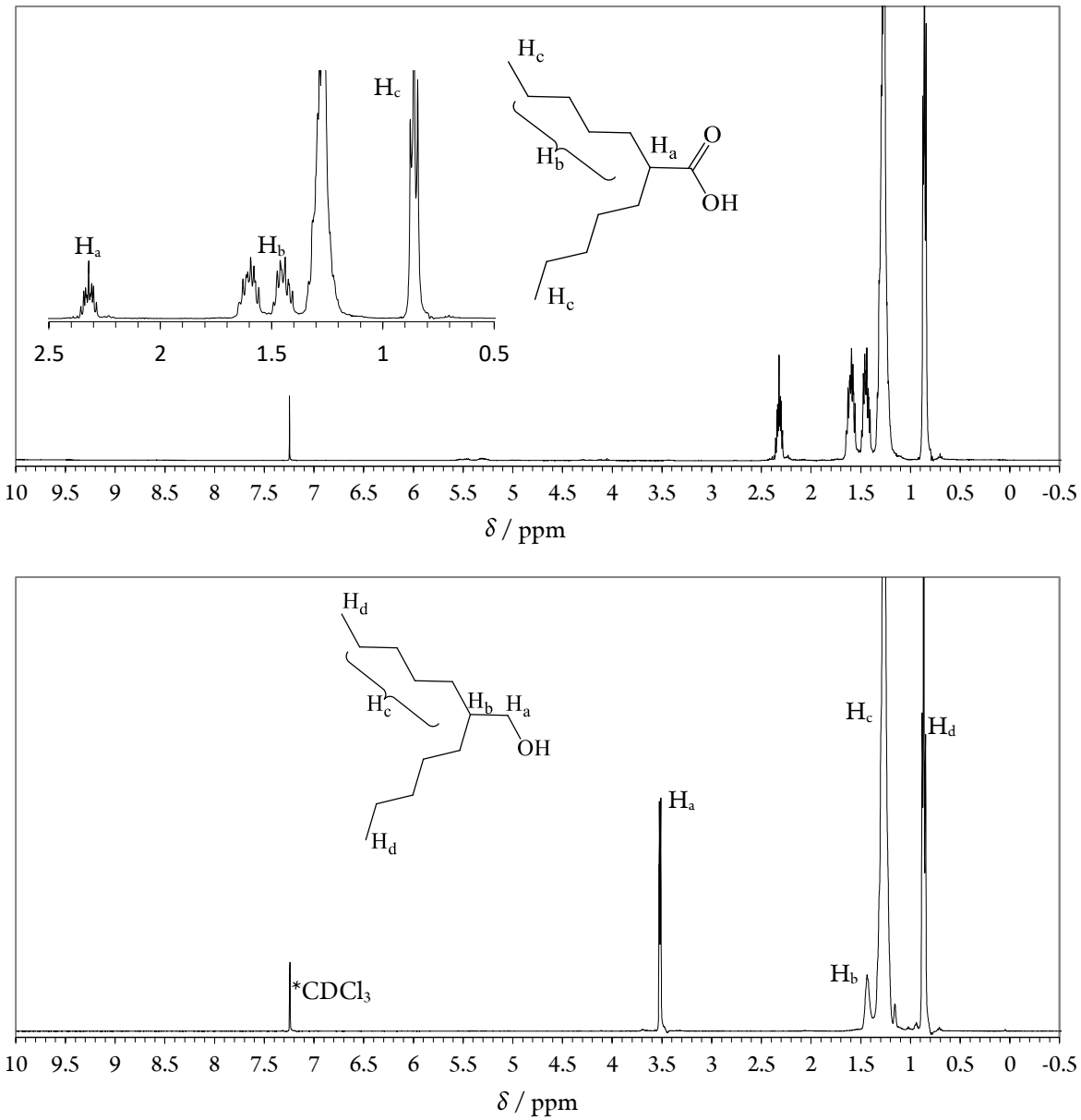

Figure S.II.8. ^{1}H-RMN spectra in $CHCl_3$ at 25 °C: (top) 2-pentylheptanoic acid; (bottom) 2-pentylheptan-1-ol.

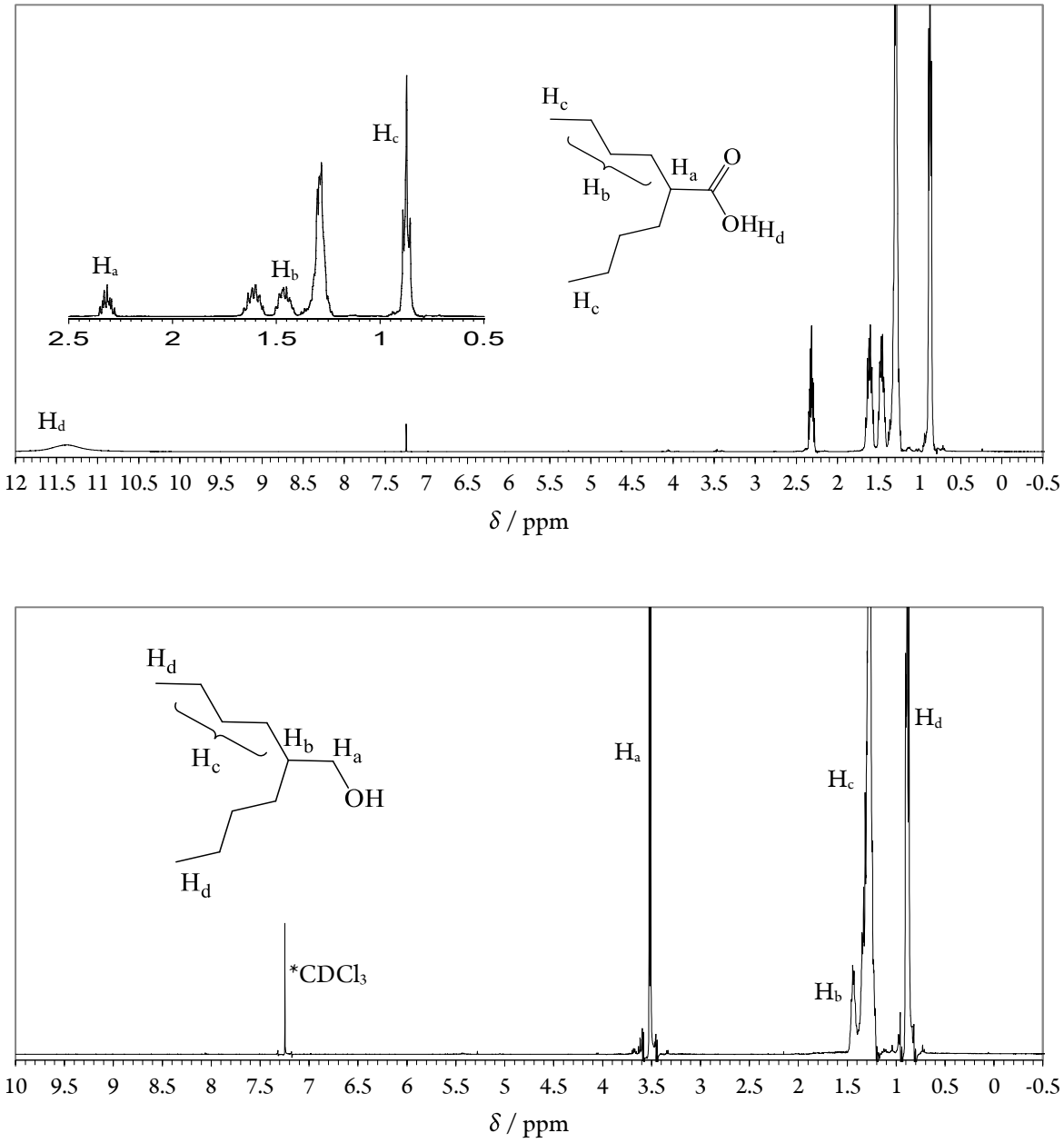

Figure S.II.9. ^{1}H-RMN spectra in $CHCl_3$ at 25 °C: (top) 2-butylhexanoic acid; (bottom) 2-butylhexan-1-ol.

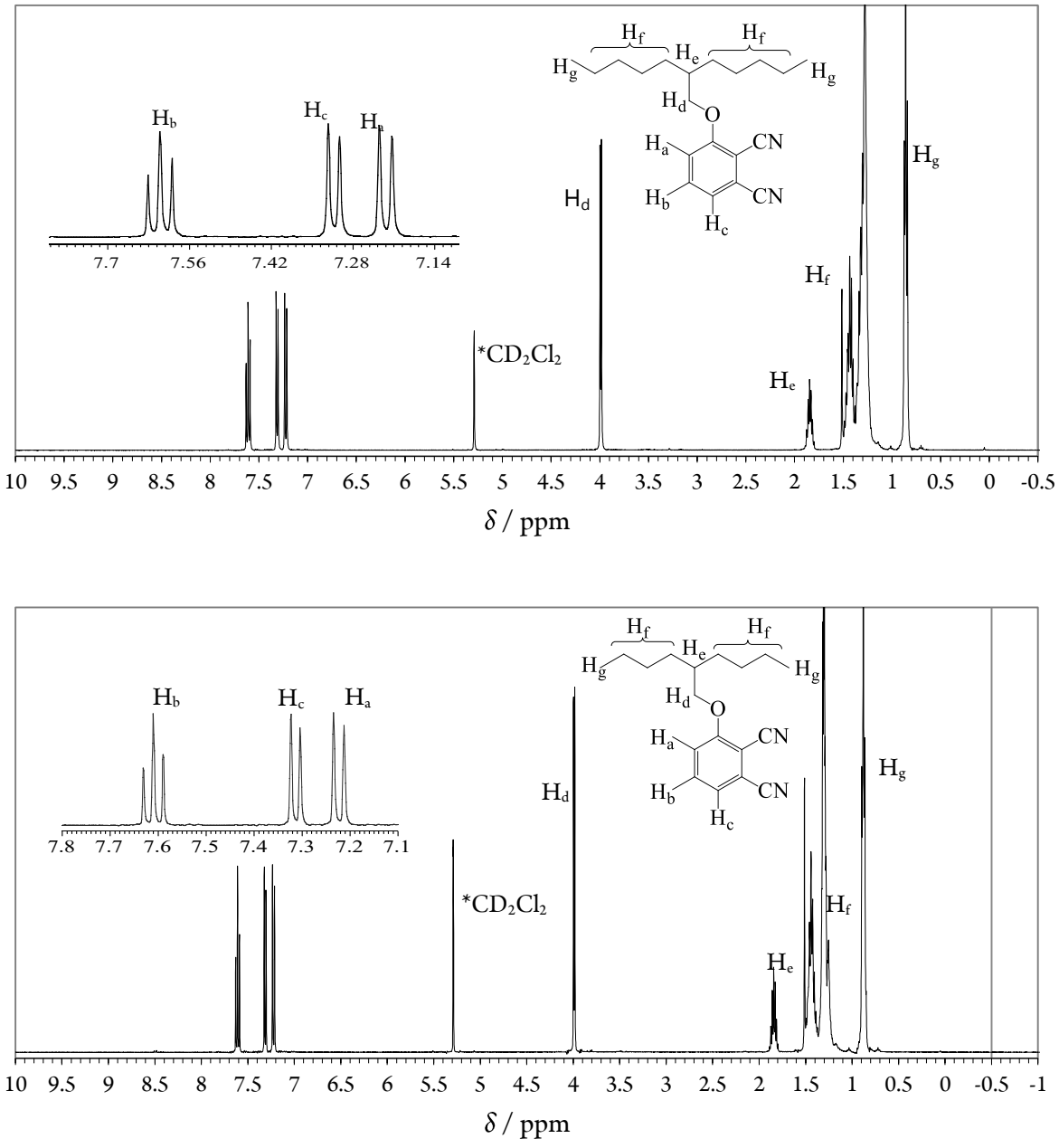

Figure S.II.10. 1H-RMN spectra in CH_2Cl_2 at 25 °C : (top) 3-(2-pentylheptyloxy-) phthalonitrile; (bottom) 3-(2-butylhexyloxy-) phthalonitrile.

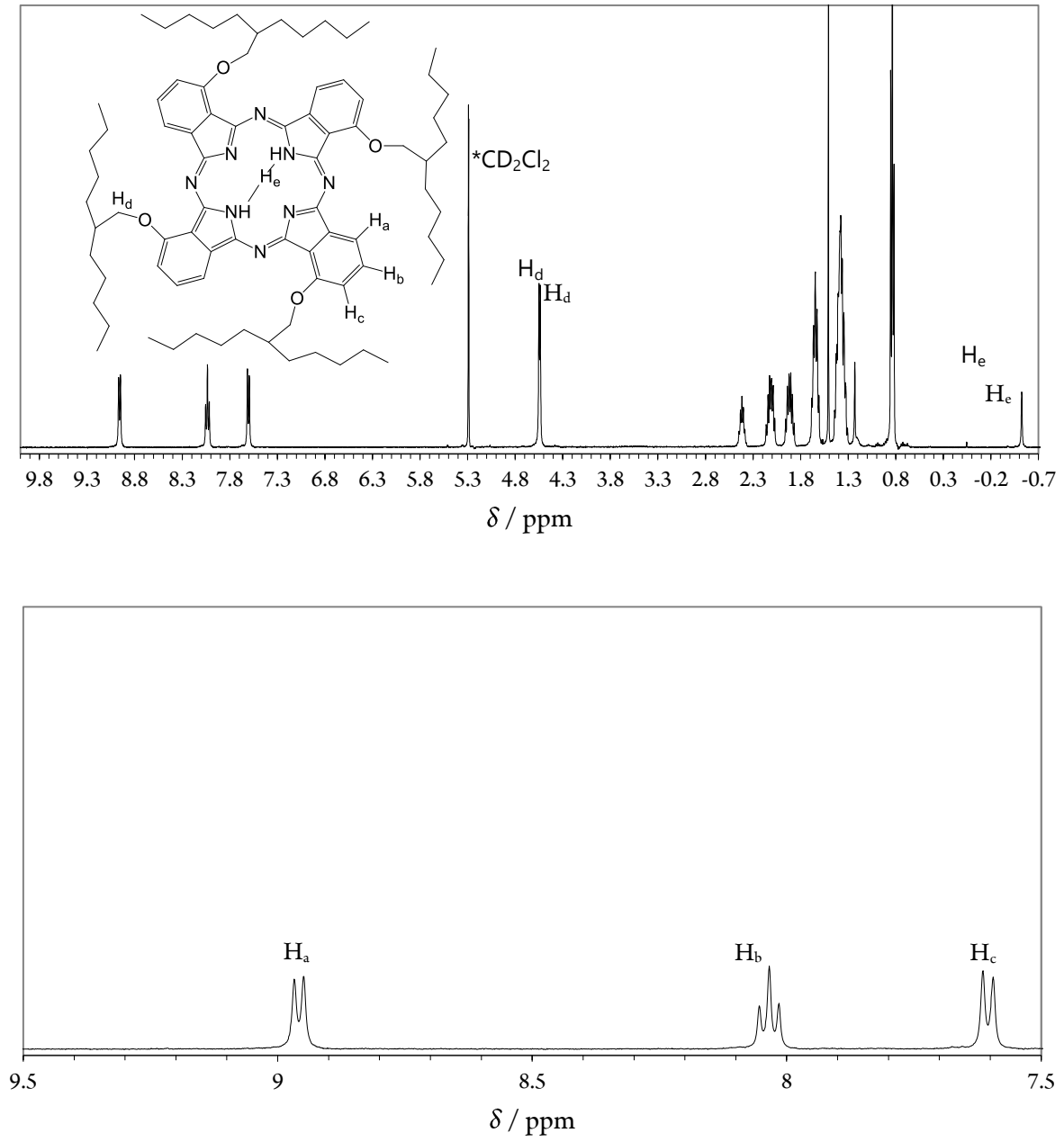

Figure S.II.11. ^{1}H-RMN spectra of $H_2Pc(OCH_2CHPent_2)_4$ (top), and resonance range of the its aromatic protons (bottom) in CH_2Cl_2 at 25 °C.

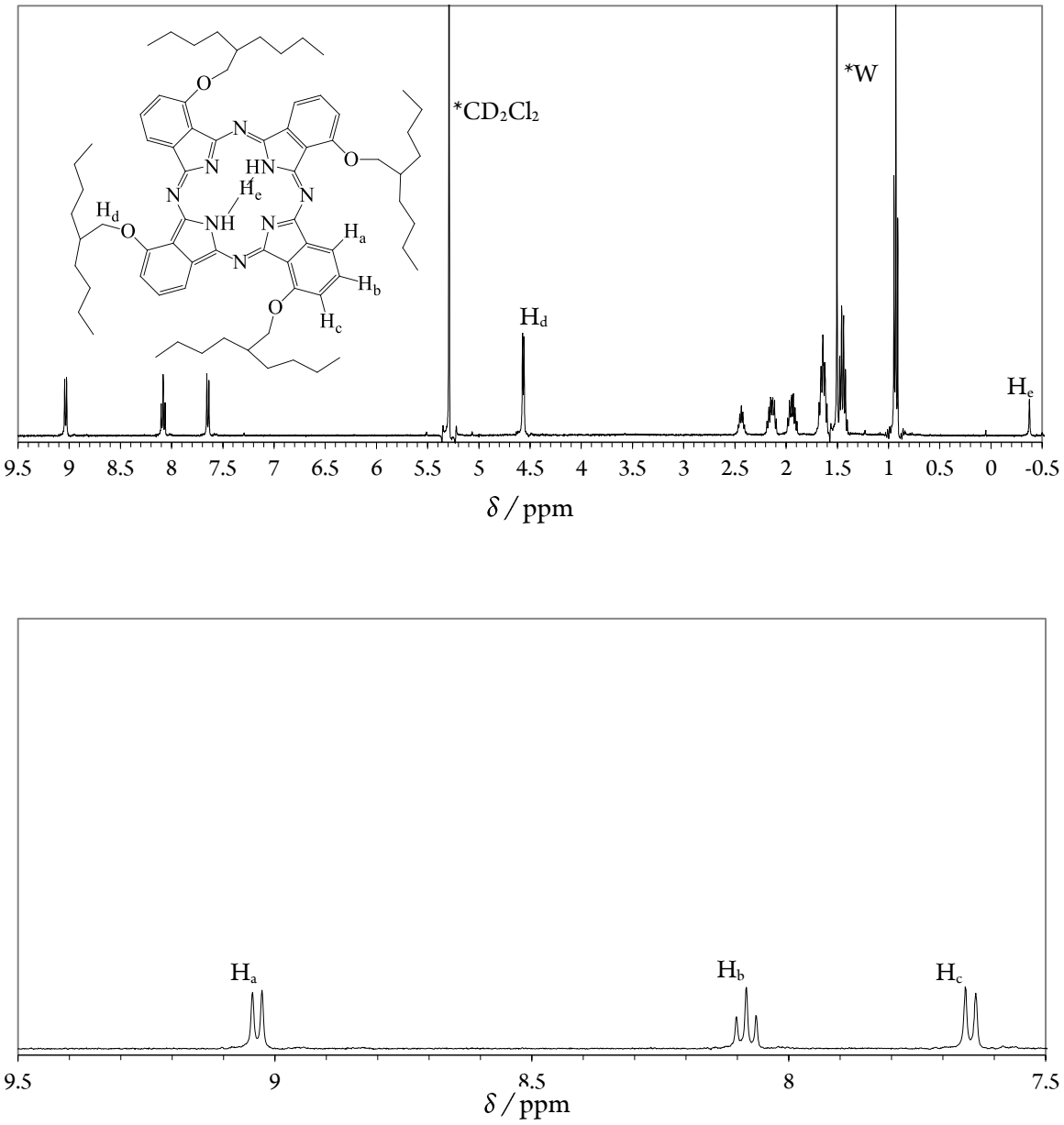

Figure S.II.12. ^{1}H-RMN spectra of $H_2Pc(OCH_2CHBu_2)_4$ (top), and its resonance range of the aromatic protons (bottom) in CH_2Cl_2 at 25 °C.

II.7.2.2.2. Crystallographic Data for 7b and 7c

Table S.II.2. Crystal data and structure refinement for $[ZnPc(OCH_2CHPent_2)_4DMF]$ **(7b)** at 120K

Moiety formula	$3(C_{83}H_{119}ZnN_9O_5)$, C_3H_7NO
Empirical formula	$C_{252}H_{364}Zn_3N_{28}O_{16}$
Formula weight	4237.90
Crystal system	Monoclinic
Space group	$P2_1/c$
Wavelength, Å	0.71073
a, Å	21.4770(7)
b, Å	29.6198(9)
c, Å	38.6473(11)
α, °	90
β, °	104.714(2)
γ, °	90
V, Å^3	23767.9(13)
Z	4
ρ_{calcd}, g/cm^3	1.071
μ, 1/mm	0.362
Reflections collected	168897
Independent reflections	14488
R_1[a]	0.1067
wR_2[a]	0.1233
GoF[a]	1.6960

[a] $I > 2\sigma(I)$, $R_1 = \Sigma|(|F_o| - |F_c|)|/\Sigma|F_o|$; $wR_2 = \{\Sigma[w(F_o^2 - F_c^2)^2]/\Sigma[w(F_o^2)^2]\}^{1/2}$. GoF (goodness of fit on F^2) $= \{\Sigma[w(F_o^2 - F_c^2)^2]/(n\text{-}p)\}^{1/2}$, where n is the number of reflections and p is the total number of refined parameters.

Table S.II.3. Crystal data and structure refinement for $[ZnPc(OCH_2CHBu_2)_4DMF]$ **(7c)** at 120 K

Moiety formula	$2(C_{75}\,H_{103}\,N_9\,O_5\,Zn)$
Empirical formula	$C_{150}\,H_{206}\,N_{18}\,O_{10}\,Zn_2$
Formula weight	2552.06
Crystal system	Triclinic
Space group	P-1
Wavelength, Å	0.71073
a, Å	16.7335(5)
b, Å	20.3834(6)
c, Å	23.2598(6)
α, °	115.5660(10)
β, °	95.3920(10)
γ, °	94.4430(10)
V, Å^3	7063.3(4)
Z	2
ρ_{calcd}, g/cm^3	1.200
μ, 1/mm	0.244
Reflections collected	25626
Independent reflections	15484
R_1[a]	0.0976
wR_2[a]	0.1551
GoF[a]	1.032

a$I > 2\sigma(I)$, $R1 = \Sigma||Fo| - |Fc||/\Sigma|Fo|$;$wR2 = \{\Sigma[w(Fo2 - Fc2)2]/\Sigma[w(Fo2)2]\}1/2$; GoF (goodness of fit on $F2$) = $\{\Sigma[w(Fo2 - Fc2)2]/(n\text{-}p)\}1/2$; where n is the number of reflections and p is the total number of refined parameters.

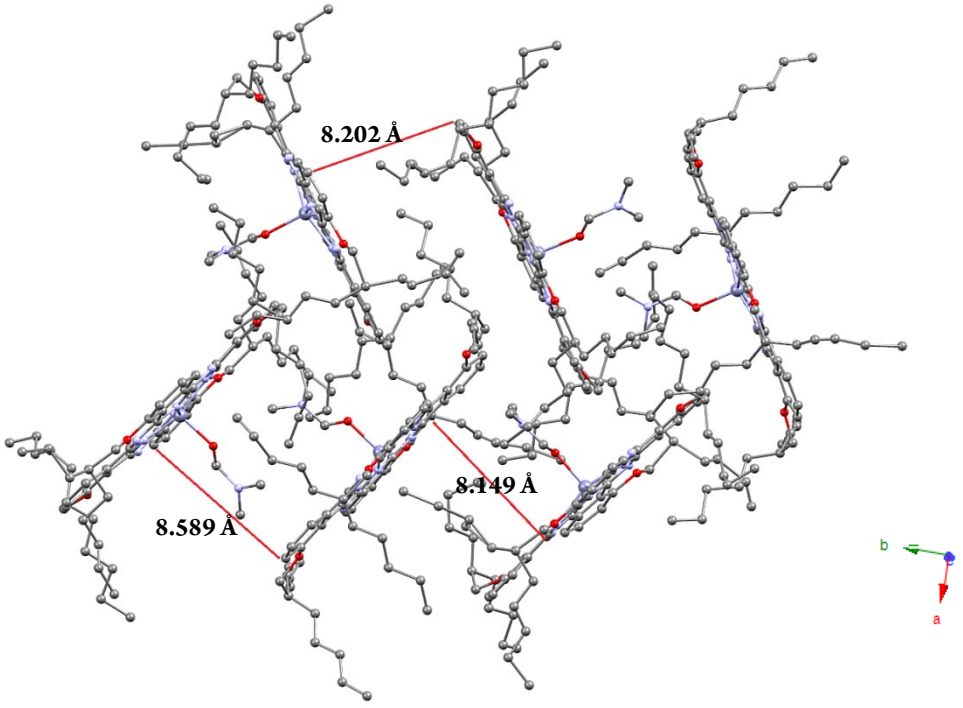

Figure S.II.13. Perspective view of the crystal packing of $ZnPc(OCH_2CHPent_2)_4DMF$ **(7b)** at 120 K illustrating the distances between molecular planes of the phthalocyanines. Hydrogen atoms are omitted for clarity.

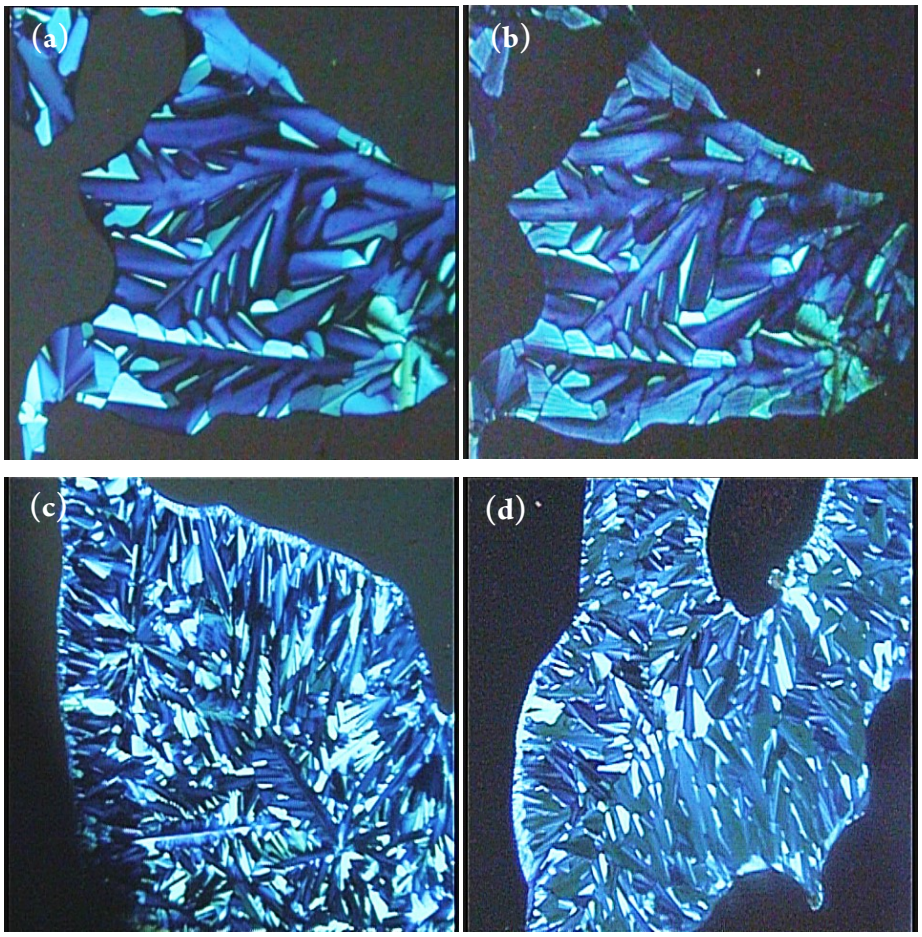

Figure S.II.14. Mesophase domains of **4b** growing from the isotropic liquid between glass plates on cooling seen through crossed polarizers**:** (a) at 240 °C; (b) at 25 °C and **4c:** (c) at 300 °C; (d) at 25 °C.

II.7.2.2.3. Small angle X-ray scattering (SAXS) investigations

Table S.II.4. Indexation of the reflections on 2nd cooling at 200°C for $CoPc(OCH_2CHPent_2)_4$ **(4b).**

T / °C	Peak number	$q_{(obs)}$ / nm^{-1}	$d_{(obs)}$ / Å	hkl	h^2+3k^2	$d_{(calc)}$ / Å	Calculated cell parameters (Å)
200	1	3.18	19.75	200	4	19.56	a = 39.13
	2	3.59	17.48	110	4	17.50	b = 19.49
	3	5.76	10.91	120	13	10.85	
	4	6.45	9.74	400	16	9.78	
	5	7.19	8.73	410	20	8.75	
	6	8.55	7.35	420	28	7.39	
	7	9.06	6.93	-	32	6.92	
	8	9.80	6.40	52	37	6.43	

$q_{(obs)}$ is the observed/measured reciprocal spacing, $q = 4\pi \cdot sin\theta/\lambda$, where λ is the wavelength, 2θ is the diffraction angle, $d_{(obs)}$ and $d_{(calc)}$ are observed and calculated diffraction spacings: $d_{(obs)} = 2\pi/q_{(obs)}$, $d_{(calc\ rec)} = \frac{a}{\sqrt{h^2+3k^2}}$; a and b are the lattice parameters of the rectangular phase.

Table S.II.5. Indexation of the reflections on 2nd cooling at 220°C for $CoPc(OCH_2CHBu_2)_4$ **(4c).**

T / °C	Peak number	$q_{(obs)}$ / nm^{-1}	$d_{(obs)}$ / Å	hkl	h^2+3k^2	$d_{(calc)}$ / Å	Calculated cell parameters (Å)
220	1	3.34	18.79	200	4	18.63	a = 37.27
	2	3.78	16.64	110	4	16.66	b = 18.56
	3	6.05	10.39	120	13	10.33	
	4	6.77	9.28	220	16	9.31	
	5	7.56	8.30	-	20	8.33	
	6	10.30	6.10	520	37	6.12	

$q_{(obs)}$ is the observed/measured reciprocal spacing, $q = 4\pi \cdot sin\theta/\lambda$, where λ is the wavelength, 2θ is the diffraction angle, $d_{(obs)}$ and $d_{(calc)}$ are observed and calculated diffraction spacings: $d_{(obs)} = 2\pi/q_{(obs)}$, $d_{(calc\ rec)} = \frac{a}{\sqrt{h^2+3k^2}}$; a and b are the lattice parameter of the rectangular phase.

Table S.II.6. Indexation of the reflections on 2nd cooling at 200°C for $NiPc(OCH_2CHPent_2)_4$ **(5b).**

T / °C	Peak number	$q_{(obs)}$ / nm^{-1}	$d_{(obs)}$ / Å	hkl	h^2+3k^2	$d_{(calc)}$ / Å	Calculated cell parameters (Å)
200	1	3.17	19.81	200	4	19.66	a = 39.33
	2	3.57	17.58	110	4	17.58	b = 19.61
	3	5.74	10.94	120	13	10.90	
	4	6.38	9.84	220	16	9.83	
	5	7.14	8.80	410	20	8.79	
	6	8.57	7.33	420	28	7.43	
	7	9.03	6.95		32	6.95	
	8	9.72	6.46	520	37	6.46	

$q_{(obs)}$ is the observed/measured reciprocal spacing, $q = 4\pi \cdot sin\theta/\lambda$, where λ is the wavelength, 2θ is the diffraction angle, $d_{(obs)}$ and $d_{(calc)}$ are observed and calculated diffraction spacings: $d_{(obs)} = 2\pi/q_{(obs)}$, , $d_{(calc\ rec)} = \frac{a}{\sqrt{h^2+3k^2}}$; a and b are the lattice parameters of the rectangular phase.

Table S.II.7. Indexation of the reflections on 2nd cooling at 220°C for $NiPc(OCH_2CHBu_2)_4$ **(5c).**

T / °C	Peak number	$q_{(obs)}$ / nm^{-1}	$d_{(obs)}$ / Å	hkl	h^2+3k^2	$d_{(calc)}$ / Å	Calculated cell parameters (Å)
220	1	3.32	18.89	200	4	18.77	a = 37.55
	2	3.74	16.80	110	4	16.79	b = 18.75
	3	6.00	10.47	120	13	10.41	
	4	6.69	9.39	220	16	9.39	
	5	7.48	8.39	-	20	8.39	
	6	8.97	7.00	420	28	7.09	
	7	9.45	6.65	230	32	6.64	
	8	10.19	6.16	520	37	6.17	

$q_{(obs)}$ is the observed/measured reciprocal spacing, $q = 4\pi \cdot sin\theta/\lambda$, where λ is the wavelength, 2θ is the diffraction angle, $d_{(obs)}$ and $d_{(calc)}$ are observed and calculated diffraction spacings: $d_{(obs)} = 2\pi/q_{(obs)}$, ;$d_{(calc\ rec)} = \frac{a}{\sqrt{h^2+3k^2}}$; a and b are the lattices parameter of the rectangular phase.

Table S.II.8. Indexation of the reflections on 2nd cooling at 200°C for $CuPc(OCH_2CHPent_2)_4$ **(6b).**

T / °C	Peak number	$q_{(obs)}$ / nm^{-1}	$d_{(obs)}$ / Å	hkl	h^2+3k^2	$d_{(calc)}$ / Å	Calculated cell parameters (Å)
200	1	3.18	19.75	200	4	19.65	a = 39.29
	2	3.58	17.56	110	4	17.57	b = 19.60
	3	5.74	10.94	120	13	10.90	
	4	6.42	9.79	220	16	9.82	
	5	7.18	8.75	-	20	8.78	
	6	9.03	6.96	-	32	6.95	
	7	9.75	6.44	520	37	6.46	

$q_{(obs)}$ is the observed/measured reciprocal spacing, $q = 4\pi \cdot sin\theta/\lambda$, where λ is the wavelength, 2θ is the diffraction angle, $d_{(obs)}$ and $d_{(calc)}$ are observed and calculated diffraction spacings: $d_{(obs)} = 2\pi/q_{(obs)}$, ; $d_{(calc\ rec)} = \frac{a}{\sqrt{h^2+3k^2}}$; a and b are the lattice parameters of the rectangular phase.

Table S.II.9. Indexation of the reflections on 2nd cooling at 220°C for $CuPc(OCH_2CHBu_2)_4$ **(6c).**

T / °C	Peak number	$q_{(obs)}$ / nm^{-1}	$d_{(obs)}$ / Å	hkl	h^2+3k^2	$d_{(calc)}$ / Å	Calculated cell parameters (Å)
220	1	3.33	18.88	200	4	18.69	a = 37.38
	2	3.76	16.71	110	4	16.72	b = 18.63
	3	6.03	10.42	120	13	10.37	
	4	6.73	9.33	220	16	9.34	
	5	7.53	8.35	410	20	8.36	
	6	9.00	6.98	420	28	7.06	
	7	9.49	6.62	230	32	6.61	
	8	10.25	6.13	520	37	6.15	

$q_{(obs)}$ is the observed/measured reciprocal spacing, $q = 4\pi \cdot sin\theta/\lambda$, where λ is the wavelength, 2θ is the diffraction angle, $d_{(obs)}$ and $d_{(calc)}$ are observed and calculated diffraction spacings: $d_{(obs)} = 2\pi/q_{(obs)}$, ; $d_{(calc\ rec)} = \frac{a}{\sqrt{h^2+3k^2}}$; a and b are the lattice parameters of the rectangular phase.

Table S.II.10. Indexation of the reflections on 2nd cooling at 200°C for $ZnPc(OCH_2CHPent_2)_4$ **(7b).**

T / °C	Peak number	$q_{(obs)}$ / nm^{-1}	$d_{(obs)}$ / Å	hkl	h^2+3k^2	$d_{(calc)}$ / Å	Calculated cell parameters (Å)
220	1	3.18	19.73	200	4	19.75	a = 38.92
	2	3.62	17.38	110	4	17.40	b = 19.35
	3	5.79	10.86	120	13	10.79	
	4	6.49	9.68	220	16	9.73	
	5	7.24	8.68	410	20	8.70	
	6	8.61	7.30	420	28	7.35	
	7	9.11	6.60	230	32	6.88	
	8	9.89	6.35	520	37	6.40	

$q_{(obs)}$ is the observed/measured reciprocal spacing, $q = 4\pi \cdot sin\theta/\lambda$, where λ is the wavelength, 2θ is the diffraction angle, $d_{(obs)}$ and $d_{(calc)}$ are observed and calculated diffraction spacings: $d_{(obs)} = 2\pi/q_{(obs)}$, $d_{(calc\ rec)} = \frac{a}{\sqrt{h^2+3k^2}}$; a and b are the lattice parameters of the rectangular phase.

Table S.II.11. Indexation of the reflections on 2nd cooling at 220°C for $ZnPc(OCH_2CHBu_2)_4$ **(7c).**

T / °C	Peak number	$q_{(obs)}$ / nm^{-1}	$d_{(obs)}$ / Å	hkl	h^2+3k^2	$d_{(calc)}$ / Å	Calculated cell parameters (Å)
220	1	3.34	18.79	200	4	18.54	a = 37.07
	2	3.79	16.55	110	4	16.58	b = 18.43
	3	6.06	10.36	120	13	10.28	
	4	6.82	9.21	220	16	9.27	
	5	7.60	8.27	-	20	8.29	
	6	9.02	6.96	420	28	7.00	
	7	9.56	6.57	230	32	6.55	
	8	10.37	6.06	520	37	6.09	

$q_{(obs)}$ is the observed/measured reciprocal spacing, $q = 4\pi \cdot sin\theta/\lambda$, where λ is the wavelength, 2θ is the diffraction angle, $d_{(obs)}$ and $d_{(calc)}$ are observed and calculated diffraction spacings: $d_{(obs)} = 2\pi/q_{(obs)}$, $d_{(calc\ rec)} = \frac{a}{\sqrt{h^2+3k^2}}$; a and b are the lattice parameters of the rectangular phase.

Table S.II.12. Indexation of the reflections on 2nd cooling at 200 and 140°C for $H_2Pc(OCH_2CHBu_2)_4$ **(3c).**

T / °C	Peak number	$q_{(obs)}$ / nm^{-1}	$d_{(obs)}$ / Å	hkl	h^2+hk+k^2	$d_{(calc)}$ / Å	Calculated cell parameters (Å)
200	1	3.65	17.19	200	4	17.22	
	2	4.83	13.02	210	7	13.02	
	3	6.31	9.96	220	12	9.94	a = 39.77
	4	6.57	9.56	310	13	9.55	
					h^2+3k^2		
140	1	3.54	17.75	010	3	17.63	a = 32.51
	2	3.87	16.24	110	4	16.25	b = 18.26
	3	6.33	9.93	120	11	9.80	
	4	6.66	9.72	310	12	9.38	
	5	6.86	9.15	130	13	9.01	
	6	7.38	8.52	-	14	8.69	
	7	8.06	7.79	-	17	7.88	
	8	8.87	7.09	320	21	7.09	
	9	9.85	6.38	-	26	6.37	
	10	10.32	6.09	420	28	6.14	
	11	10.77	5.83	230	31	5.83	
	12	11.45	5.49	600	35	5.49	
	13	12.01	5.23	610	39	5.20	

$q_{(obs)}$ is the observed/measured reciprocal spacing, $q = 4\pi \cdot sin\theta/\lambda$, where λ is the wavelength, 2θ is the diffraction angle, $d_{(obs)}$ and $d_{(calc)}$ are observed and calculated diffraction spacings: $d_{(obs)} = 2\pi/q_{(obs)}$, $d_{(calc\ rec)} = \frac{a}{\sqrt{h^2+3k^2}}$, and $d_{(calc\ hex)} = \frac{\sqrt{3}}{2}\frac{a}{\sqrt{h^2+hk+k^2}}$; a and b are the lattice parameters of the rectangular and hexagonal phase respectively.

Table S.II.13. Indexation of the reflections on 2nd cooling at 200°C for $H_2Pc(OCH_2CHPent_2)_4$ **(3b).**

T / °C	Peak number	$q_{(obs)}$ / nm^{-1}	$d_{(obs)}$ / Å	hkl	h^2+hk+k^2	$d_{(calc)}$ / Å	Calculated cell parameters (Å)
200	1	3.48	18.05	200	4	18.05	a = 41.43
	2	4.65	13.50	210	7	13.64	
	3	6.12	10.27	220	12	10.42	
	4	6.22	10.09	310	13	10.09	

$q_{(obs)}$ is the observed/measured reciprocal spacing, $q = 4\pi \cdot sin\theta/\lambda$, where λ is the wavelength, 2θ is the diffraction angle, $d_{(obs)}$ and $d_{(calc)}$ are observed and calculated diffraction spacings: $d_{(obs)} = 2\pi/q_{(obs)}$, $d_{(calc\ hex)} = \frac{\sqrt{3}}{2}\frac{a}{\sqrt{h^2+hk+k^2}}$; a is the lattice parameter of the rectangular and hexagonal phase respectively.

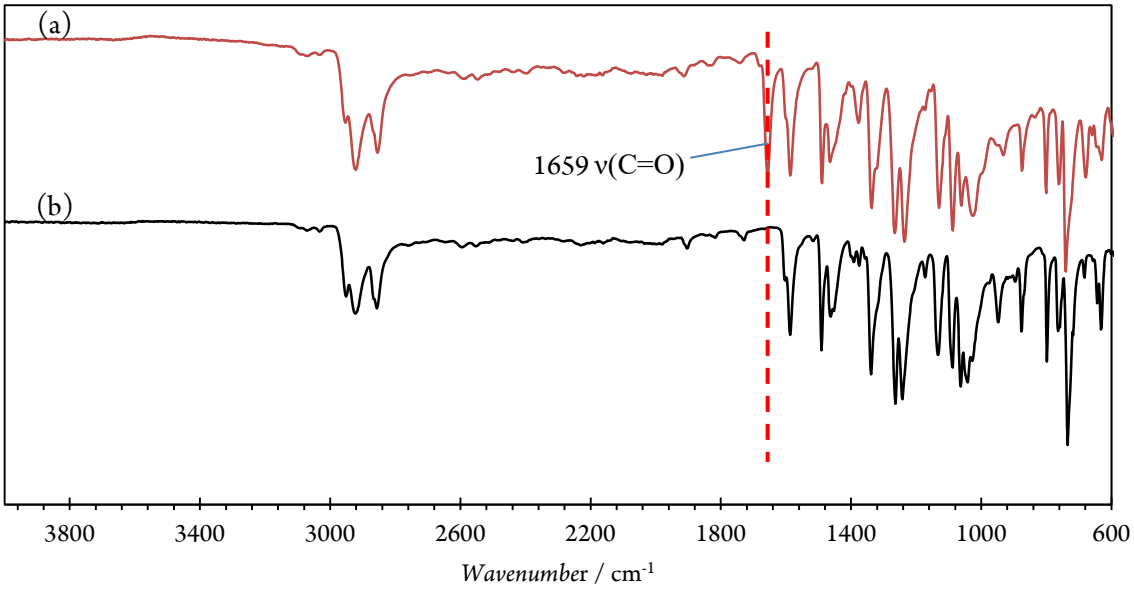

Figure S.II.14. FT-IR spectra of compound **7b** showing **(a)** the presence of the coordinated DMF and **(b)** its disappearance after recrystallization from CH_2Cl_2/CH_3OH mixture.

II.8. References

[1] C. Piechocki; J. Simon; A. Skoulios; D. Guillon; P. Weber; *J. Am. Chem. Soc.,* **1982**, 104, 5245-5247.

[2] J. Zaumseil; H. Sirringhaus; *Chem Rev.*, **2007**, 107, 1296–1323.

[3] a) S. R. Forrest; *Nature,* **2004** 428-911; b) C. D. Dimitrakopoulos; P. R. L. Malenfant; *Adv Mater.*, **2002**, 14-99.

[4] T. Basova; A. Hassan; M. Durmuş; A. G. Gürek; Vefa Ahsen; Coord. Chem. Rev., 2016, 310, 131–153.

[5] D. Demus; J. Goodby; G. W. Gray; H. -W. Spiess; V. Vill; *Handbook of Liquid Crystals*, Low Molecular Weight Liquid Crystals, Vol. 2B, **1998**.

[6] a) S. Sergeyev; E. Pouzet; O. Debever; J. Levin; J. Gierschner; J. Cornil; R. G. Aspe; Y. H. Geerts; *J. Mater. Chem.*, **2007**, 17, 1777-1784; b) M. J. Cook; M. F. Daniel; K. J. Harrison; N. B. McKeown; A. J. Thomson; *J. Chem. Soc., Chem Commun.*, **1987**, 1086-1088.

[7] a) W. Eberhardt; M. Hanack; *Synthesis*, **1997**, 95–100; b) C. C. Leznoff; S. M. Marcuccio; S. Greenberg; A. B. P. Lever; K. B. Tomer; *Can. J. Chem.*, **1985**, 63, 623–631; c) J. F. Van der Pol; E. Neeleman; J. W. Zwikker; R. J. M. Nolte; W. Drenth; J. Aerts; R. Visser; S. J. Picken; *Liquid crystals*, **1989**, 6, 577-592.

[8] a) D. George; A. W. Snow; J. S. Shirk; W. R. Barger; *J. Porphyrins Phthalocyanines*, **1998**, 2, 1–7; b) M. J. Cook; J. McMurdo; D. A. Miles; R. H. Poynter; *J. Mater. Chem.*, **1994**, 4, 1205–1243.

[9] C. Rager; G. Schmid; M. Hanack; *Chem. – Eur. J.*, **1999**, 5, 280-288.

[10] a) T. Hassheider; S. A. Benning; H.-S. Kitzerow; M.-F. Achard; H. Bock; *Angew. Chem., Int. Ed.*, **2001**, 40, 2060-2063; b) S. Saïdi-Besbes; E. Grelet; H. Bock; *Angew. Chem., Int. Ed.*, **2006**, 45, 1783-1786; c) H. Bock; M. Rajaoarivelo; S. Clavaguera; E. Grelet; *Eur. J. Org. Chem.*, **2006**, 2889-2893; d) P. Apostol; A. Bentaleb; M. Rajaoarivelo, R. Clérac; H. Bock; *Dalton Trans.*, **2015**, 44, 5569-5576.

[11] a) W.M. Sharman; J. E. van Lier; *The Porphyrin Handbook;* Academic Press: New York, **2003**; Vol. 15, 1 – 60; b) N. B. McKeown; *The Porphyrin Handbook*; Academic Press: New York, **2003**; Vol. 15, 61 –124; c) M., S. Rodriguez-Morgade; G. de la Torre; T. Torres; *The Porphyrin Handbook*; Academic Press: New York, **2003**; Vol. 15, 125 – 160.

[12] a) J. Wang, A. K. Khanamiryan; G. C. Leznof; *J. Porphyrins Phthalocyanines* **2004**, 08, 1293-1299; b) R. D. George; A. W. Snow; *J. Heterocyclic Chem.*, **1995**, 32, 495-498; c) E. Gürel; M. Pişkin; S. Altun; Z. Odaba; M. Durmu; *Dalton Trans.*, **2015**, 44, 6202–6211.

[13] a) A. V. Zakharov; S. A. Shlykov; Y. A. Zhabanov; G. V. Girichev; *Phys. Chem. Chem. Phys.*, **2009**, 11, 3472–3477; b) G. Winter; H. Heckmann; P. Haisch; W. Eberhardt; M. Hanack; L. Lu1er; H.-J. Egelhaaf; D. Oelkrug; *J. Am. Chem. Soc.*, **1998,** 120, 663; c) W.-F. Law; K. M. Lui; D. K. P. Ng; *Mater. Chem.*, **1997**, 7, 10, 2063–2067.

[14] P. Ona-Burgos; M. Casimiro; I. Fernandez; A. V. Navarro; J. F. F. Sanchez; A. S. Carreteroand; A. F. Gutierrez; *DaltonTrans.*, **2010**, 39 , 6231–6238.

[15] a) V. E. Pushkarev; L. G. Tomilova; Y. V. Tomilov; *Russian Chemical Reviews*, **2008**, 77:10, 875–907; b) A. Y. Tolbin; V. E. Pushkarev; L. G. Tomilova; *Mendeleev Commun.*, **2008**, 18, 94–95; c) D. K. P Ng; J. Jiang; *Chem. Soc. Rev.*, **1997**, 26, 433-442; d) V. N. Nemykin; S. V. Volkov; *Koord. Khim.*, **2000**, 26 465; e) P. N. Moskalev; *Koord. Khim.,* **1990**, 16; 147; f). B. I. Kharisov; M. A. Mendes-Rokhas; E. A. Ganich; *Koord. Khim.*, **2000,** 26, 301-310; g) J. W. Buchler; D. K. P. Ng; *Porphyrin Handbook*, Vol. 3 (Eds M Kadish; K M Smith; R Guilard) (San Diego: Academic Press, **2000**. 245; h). R. Weiss; J. Fischer; *Porphyrin Handbook*. Vol. 16, San Diego: Academic Press, **2003**, 171; i) N. Kobayashi; *Coord. Chem. Rev.*, **2002** 227, 129-152; j) J. Jiang; W. Liu; D. P. Arnold; *J. Porphyrins Phthalocyanines,* **2003**, 7, 459-473.

[16] M. K. Engel; P. Bassoul; L. Bosio; H. Lehmann; M; Hanack; J. Simon; *Liq. Cryst.*, **1993**, 15, 709–722.

[17] P. Haisch; S. Knecht; U. Schlick; L. R. Subramanian, M. Hanack; *Mol. Cryst. Liq. Cryst*. **1995**, 270, 7–16.

[18] J. F. van der Pol; E. Neeleman; J. W. Zwikker; R. J. M. Nolte; W. Drenth; , J. Aerts; R. Visser; S. Picken; *J. Liq. Cryst.*, **2006**, 33, 1378–1387.

[19] P. G. Schouten; J. F. Van Der Pol; J. W. Zwikker; W. Drenth; S. J. Picken; *Mol. Cryst. Liq. Cryst.,* **1991**, 195, 291-305.

[20] a) M. Ferreira; E. Girotto; A. Bentaleb; E. A. Hillard; H. Gallardo; F. Durola; H. Bock; *Chem. Eur. J.,* **2015**, 21, 4391-4397; b) E. Girotto; M. Ferreira; P. Sarkar; A. Bentaleb; E. A. Hillard; H. Gallardo; F. Durola; H. Bock; *Chem. Eur. J.,* **2015**, 21, 7603-7610; c) S. Sergeyev; E. Pouzet; O. Debever; J. Levin; J. Gierschner; J. Cornil; R. G. Aspec; Y. H. Geerts; *J. Mater. Chem.*, **2007**, 17, 1777–1784.

[21] I. Chambrier; M. J. Cook; M. Helliwell; A. K. Powell; *J. Chem. Soc. Chem. Commun.*, **1992**, 444–445.

[22] M. J. Cook; M. F. Daniel; K. J. Harrison; N. B. McKeown; A. J. Thomson; *J Chem Soc, Chem Commun*; **1987**, 1086–1088.
[23] A. N. Cammidge; M. J. Cook; K. J. Harrison; N. B. McKeown; *J. Chem. Soc. Perkin Trans.*, **1991** 3053–3058.
[24] M. Hanack; G. Schmidt; M. Sommeruuer; *Angew. Chem. Int. Ed. Engl.*, **1993**, 32, 1422-1424..
[25] a) P. Turner; M. J. Gunter; B. W. Skelton; A. H. White; *Aust. J. Chem.*, **1998,** 51, 853 – 864; b) Neil B. McKeown; *Phthalocyanine Materials:Synthesis, Structure and Function,* **1998**.
[26] J. B. Mann; Atomic Structure Calculations II. Hartree-Fock wave functions and radial expectation values: hydrogen to lawrencium, LA-3691, **1968.**
[27] M. Gouterman; G. H. Wagniere; *J. Mol. Spectrosc.*, **1963**, 11, 108-127.
[28] S. Alibert-Fouet; I. Seguy; J. F. Bobo; P. Destruel; H. Bock; *Chem.–Eur. J.*, **2007**, 13, 1746-1753; e) J. Kelber; M. F. Achard. B. Garreau de Bonneval. H. Bock; *Chem.–Eur. J.*, **2011**, 17, 8145-8155; f) J. Kelber; H. Bock; O. Thiebaut; E. Grelet; H. Langhals[Eur. *J. Org. Chem.*, **2011**, 707-712.
[29] M. J. Hook; *Journal of Materials science: Materials in Electronic,* **1994**, 5, 117-128.
[30] A. M. Levelut; P. Oswald; A. Ghanem; J. Malthete; *J. Phys.*, 1**984**, 45, 745-754.
[31] R. L. Carlin; *Magnetochemistry;* Springer-Verlag; Berlin Heidelberg; **1986**
[32] P. L. Creger; *J. Am. Chem. Soc.*, **1970**, 92, 5, 1397–1398.
[33] a) M. Mossoyan-Deneux; D. Benlian; M. Pierrot; A. Fournel; J. P. Sorbier; *Inorg. Chem.,* **1985**, 24, 12, 1878–1882; b) J. Janczak; R. Kubiak; J. Lisowski; *Polyhedron*, **2011** 30, , 253–258; c) J.Janczak; R. Kubiak; *Polyhedron*, **2009**, 28, 2391–2396; d) W. R. Scheidt, W. Dow; *J. Am. Chem. Soc.*, **1977,** 99, 1101-1104.
[34] a) G. J. Clarkson; N. B. McKeown; K. E. Treacher; *J.Chem. Soc. Perkin Trans.*, **1995**, 1, 1817-1823; b) J. H. Sharp; M. Lardon; *J. Phys. Chem.* **1968**, 72, 3230-323; c) N. Kobayashi; H. Ogata; N. Nonaka; E. A. Luk'yanets; *Chem.–Eur. J.*, **2003**, 9, 5123-5134.
[35] M. Gouterman; G. H. Wagniere; *J. Mol. Spectrosc.*, **1963**, 11, 108-127.
[36] a) A. Atsay; A. Gül; M. B. Koçak; *Dyes Pigm.*, **2014**, 100, 177–183; b) E. Gürel; M. Pişkin; S. Altun; Z. Odabaş; M. Durmuş; *Dalton Trans.*, **2015**, 44 ,6202–6210; c) K. Kasuga; K. Yashiki; T. Sugimori; M. Handa; *J. Porphyrins Phthalocyanines,* **2005**, 9, 646–650; d) X.-F. Zhang; Q. Xi; J. Zhao; *J. Mater. Chem.,* **2010**, 20, 6726–6733; e) Ö. Kurt; İ. Özçeşmeci; B. Ş. Sesalan; M. B. Koçak; *New J. Chem.,* **2015**, 39, 5767-5775.
[37] D. Guillon; A. Skoulios; C. Piechocki; P. Weber; *Mol. Cryst. Liq. Cryst.*, **1983**, 100, 275-284.
[38] L. Mamlok; J. Malthete; N. H. Tinh; C. Destrade; A. M. Levelut; *J. Phys. Lett,*, **1982,** 43, 641-647.
[39] J. Tant; Y. H. Geerts; M. Lehmann; V. De Cupere; G. Zucchi; B. W. Laursen; T. Bjørnholm; V. Lemaur; V. Marcq; A. Burquel; E. Hennebicq; F Gardebien; P. Viville; D. Beljonne; R. L. J. Corni; *Phys. Chem. B*, 109, **2005**, 20315-20323.

Chapter III

Diodes based on Tetrasubstituted Liquid Crystalline Phthalocyanines

Table of Contents for Chapter III:

III.1. Introduction

Devices based on organic semiconductors, such as organic light-emitting diodes (OLEDs), organic field effect transistors (OFETs), organic solar cells (OSCs) or printed microelectronic circuits require stable p- and n-type organic semiconductors with excellent electrical and optoelectronic properties. Additionally, it is desired that these organic semiconductors are easily synthesized and stable during the whole life-time. The degree of the mobility of the carriers through the organic material, induced by the presence of intermolecular π-π orbital overlap which provides the route for carrier transport, has a significant role in the efficiency of the devices. The mobility ultimately controls the switching speed of the OFETs, the intensity of the LEDs and the separation of the charges in photovoltaic cells [1]. The structural order in the material is important for carrier mobility. The crystalline state of the materials is on first sight the ideal for a high mobility (μ) of the carriers due to the well-organized stacking (π-π orbital overlap). For an organic single crystal, μ is around 1 $cm^2 V^{-1}s^{-1}$ for the crystal axis direction with the maximum intermolecular π-π orbital overlap [2]. The major disadvantage in this approach are the cost, time and complexity associated with the growth of single crystal thin films. On the other hand, the charge-carrier mobilities in processable non-crystalline materials are usually several orders of magnitude lower, about 10^{-5} – 10^{-4} $cm^2 V^{-1}s^{-1}$. Obtaining organic semiconductors with high mobility, low fabrication cost and good air stability is still a big challenge. It is now widely accepted that the π-overlap between the electronically active transport units is probably the most important parameter for the charge-carrier transport process in organic systems. Since order phenomena are often dominated by the supramolecular assembly of the molecular transport sites, our approach towards high-mobility organic systems involves the use of columnar discotic liquid crystals.

Phthalocyanines (PCs) are based on an 18 π-electron disk-like aromatic macrocycle with 2D π-electron delocalization over the hole molecule. In crystals, Pc molecules usually adopt a packing motif preferring strong intermolecular π – π interactions, which makes them useful as charge transport materials in organic electronics research [3]. These materials are deposited as thin films typically by vapor deposition techniques which are not suitable for large area deposition. Whilst unsubstituted PCs are insoluble in common organic solvents, four-fold or eight-fold alkyl or alkoxy substitution leads to highly soluble PCs that can be solution-processed [4]. The addition of large solubilizing substituents might worsen the charge transport properties due to the dilution of the electronically active molecular cores by a large amount of electronically inert alkyl groups, and may alter the packing motif of the Pc molecules, leading to large intermolecular distances and a smaller π electron orbital overlap, but the introduction of suitably shaped flexible substituents might improve intermolecular π-electron contacts *via* the formation of columns of closely stacked aromatic disks surrounded by a nano-segregated alkyl periphery in a columnar liquid crystal (LC) or plastic crystal state [5]. One of the main advantages of liquid crystalline PCs in relation to other discotic macrocycles is their strong absorption in the visible and NIR regions [6]. Columnar LC PCs have been regarded as promising candidates for photovoltaic applications [7] and a columnar LC CuPc was efficiently applied as an organic active layer in thin film transistors, where the device

performance was shown to strongly depend on the annealing procedure [8]. Tian and et al. were able to separate the isomers of non-pheripheral tetrahexyl-substituted vanadyl phthalocyanine, by simple column chromatography, and used them as active layer in OTFT devices. The isomer mixture, compared to each pure isomer, gave a lower liquid crystal transition temperature. Using the isomer mixture as an active layer in OTFTs devices yielded μ values from 3.0 to $7.1 \cdot 10^{-4}$ cm^2 V^{-1} s^{-1}. In comparison, the purified isomers such as C_{4h} and C_s which in this case, have lower π–π stacking distances, as determined by XRD, have a tendency to form larger grains when annealed. Therefore, OTFTs based on C_{4h} and C_s gave the best device performance with a maximum μ value after annealing of $1.3\text{-}1.6 \cdot 10^{-3}$ and 0.13 $cm^2V^{-1}s^{-1}$ respectively [9].

We have mentioned that racemic 3-(2-butyloctyloxy)phthalonitrile can be tetramerized to a regiosymmetrically tetrasubstituted PC and its transition metal(II) complexes, where the four branched alkoxy substituents lead to the formation of columnar mesophases with moderate phase transition temperatures [10] (see Section II.3, chapter II). Such organized macroscopic structures merit special attention due to the self-organizing characteristics that allow the modification and control of the optoelectronic properties. These metal-free and metal(II) tetra-alkoxy substituted phthalocyanines, whose columnar stacking is maintained upon cooling to ambient conditions, have are relatively high content of conjugated core within the molecular mass, making them potentially useful as uniformly orientable charge transporters in organic electronic devices.

The study presented in this chapter focuses on the electronic behavior in solution processed organic diodes of metal-free (2H-) (**3a**) and metalated Ni^{II} (**6a**)- and (Cu^{II} (**7a**)-) 1, 8, 15, 22-tetra-(2-butyloctyloxy)-phthalocyanine, in order to correlate the optoelectronic properties with molecular organization and film structure. The chapter starts with a short description of role of the molecular organization on the substrate of the organic semiconductor layer and its contribution to the electronic device efficiency.

III.1.1. Alignment of Columnar Liquid Crystals

The molecular disk-shaped units self-organize on cooling from the isotropic phase into a columnar phase. The discotic liquid crystal columns have a tendency of orientation on substrates in the planar (edge-on) or homeotropic (face-on) alignment [11] (Figure **III.1**). Planar alignment of the columns, with the columnar axis parallel to the substrate, is preferred in field-effect transistors [12], whereas homeotropic alignment, that is, with the column axis perpendicular to the electrodes, is preferred in photovoltaic cells [13] and light emitting diodes [14]. Thus the performance of these devices depends on solving the difficult problem of how to control the alignment of columnar phases. The macroscopically uniform alignment of the columns is critical since effective transport requires that the columns are all oriented in the direction of the charge flow. The control of columnar alignment is determined by the confinement induced by solid substrates rather than by the nature if those substrates (e.g. glass, ITO, PCBM, gold, or PEDOT:PSS).

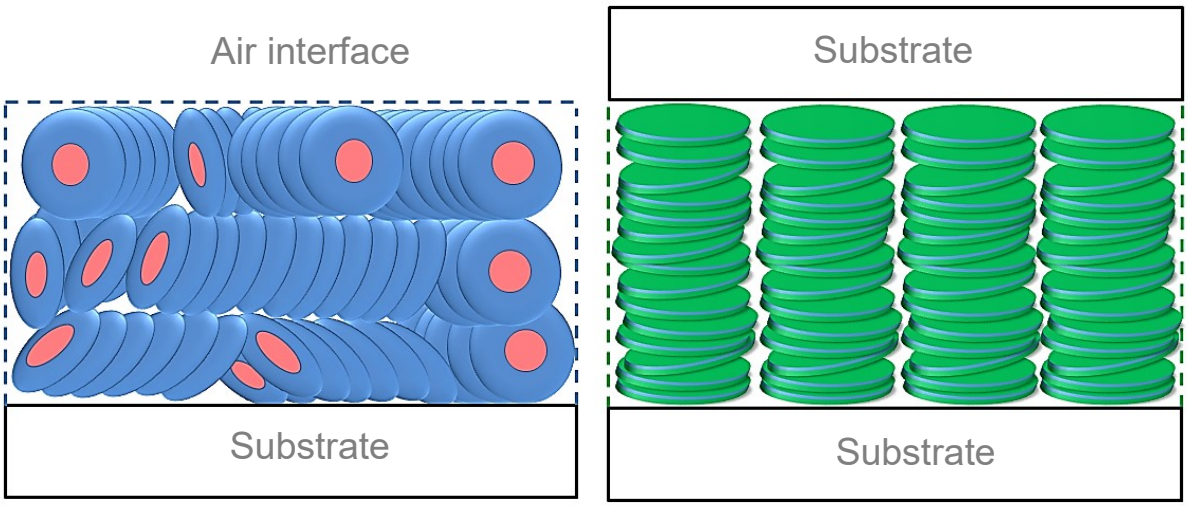

Figure III.1. Schematic representation of the planar (left) and homeotropic (right) alignments of a uniaxial columnar liquid crystal. The optical axis is along the column direction.

If a liquid crystalline Pc film is spin-coated on a substrate, whatever its surface energy or roughness, a planar alignment is always observed. This can be explained by the fact that forces acting at the liquid crystal-air interface favor planar alignment, because the alkyl chains of the discotic molecules preferentially orient toward the *air-to-liquid-crystal interface* [15[a, b]]. On the other hand, if the film is confined between two substrates, whatever their surface energy and roughness, homeotropic alignment is predominantly detected, especially in with hexagonal (non-tilted) columnar mesophases, because the aromatic centers orient toward the *solid-to-liquid-crystal interface* [16] [17[a,b]]. Spin-coating [18] or shearing samples [19] can sometimes achieve uniaxial planar alignment (where the columns are not only parallel to the surface, but also all oriented in the same direction), but more generally reliable methods are Langmuir–Blodget deposition [21[a]] the use of PTFE rubbed substrates, [20[a,b,c,d,e]] zone-casting, [21[a,b,c,d,e,]] zone-melting [22] and alignment within channels [23[a,b]]. By mechanical shearing, or use of external magnetic fields [24] large macroscopically aligned films can be generated. Choi et al. reported the effect of film thickness on the columnar packing [25]. For alignment of cobalt octa(n-decylthio)prophyrazine (CoS10) films with a range of film thicknesses (49– 845 nm) they have used the magnetic alignment technique. They conclude that the orientation of the columnar packing in the plane perpendicular to the applied magnetic field is strongly dependent on the film thickness. While it is damped by the elasticity of the side chains of CoS10, the strong interfacial interaction at the film-substrate interface propagates up to 50–100 nm from the substrate, maintaining the orientation of columnar packing in the plane perpendicular to the applied magnetic field. When the distance from the film-substrate interface is larger than about 100 nm, longitudinal edge dislocations may be formed, resulting in symmetric tilting of the orientation which saturates at 11.58°.

Spin coating is a straightforward and fast technique for organic film fabrication. It involves the rapid drying of a drop of solution containing the organic material as it is spread under centrifugal forces on the substrate. The thickness of the resultant films is controlled both by the concentration of the solution and by the rate of rotation of the substrate.

Thermal alignment is the most used procedure to control the liquid crystalline molecular order in the film, because it is cheap, simple, fast and thus efficient. The device performance of the liquid crystalline materials was enhanced by thermal alignment with an increase of mobility of the charge carriers by several orders of magnitude. For example, Bechtold et al. managed to improve the mobility by obtaining a homeotropic alignment of the molecular columns for a perylene based molecule, with an increase of 5 orders of magnitude [26]. The same author reported the conductivity of the diode based on a columnar hexagonal ZnPc derivative, where mobilities of 10^{-3} and 10^{-2} $cm^2 V^{-1} s^{-1}$ were obtained for the nonannealed and annealed films [27].

Geng et al. were able to produce OTFTs with μ values as high as 0.96 $cm^2 V^{-1} s^{-1}$, using TiOPcs (2,3,16,17-tetraalkyl titanyl Pcs), and 0.4 $cm^2V^{-1} s^{-1}$ for the corresponding VOPc (2,3,16,17-tetraalkyl vanadyl Pc) analogue. Thermal annealing is found to have produced a significant effect on the transistor performance of the OTFTs, as the μ of the TiOPc devices increased by 4% and of the VOPc devices by 25%.[28].

III.2.Thin Film Studies

III.2.1. Substrate Preparation

For preliminary analyses such as AFM, POM and XRD of the thin films, glass was used as substrate. Square pieces of glass substrates were cleaned with three successive ultrasonic baths of 10 min each in acetone and ethanol. The substrates were then dried in an oven before coating with Pc films by spin coating. For construction of diodes, ITO coated glass substrates, whose cleaning was similar to the one of simple glass substrates, were used. We noted that the ITO resistivity remains constant after two surface treatments, and no change of the ITO surface morphology has been observed by atomic force microscopy. Indium tin oxide (ITO) is commonly used as the anode material. It is transparent to visible light and has a high work function which promotes injection of holes into the HOMO level of the organic layer. Indium tin oxide covered by a film of poly(ethylene dioxythiophene):poly(styrene sulfonic acid) (ITO/PEDOT:PSS) has become a favorite combination for the transparent anode, as this provides efficient electron-injecting contacts [29]. A thin layer of poly(3,4-ethylenedioxythiophene):poly(styrenesulfonate) (PEDOT:PSS) was deposited by spin-coating on ITO substrates at 3000 rpm for 30 seconds, followed by annealing at 110 °C for 5 minutes. The active organic Pcs layers were spin-coated at 3000 rpm for 30 seconds. Top electrodes were obtained by vacuum deposition (10^{-7} mbar) of Al (80 nm) at a deposition rate of 1 Å s^{-1}. The active area of the diodes was 10 mm^2. The diode configuration is schematically presented in Figure **III.2.**

In order to correlate the thickness and morphology of the films with the efficiency of the target devices, the spin-coated films were produced using solutions of 20, 30 and 40 mg mL^{-1} in THF. The thickness of the films made using the solution of 20 mg mL^{-1} in THF was about 250 nm, for 30 mg mL^{-1} it was 300 nm, and for 40 mg mL^{-1} it was 500 nm (see Figure **S.III.3-5**). The device structure used for electrical characterization was ITO/PEDOT:PSS/ColLC/Al. The electrical measurements for diodes whose the active layer thickness was only 250 nm gave often short circuits between the electrodes, due to the dewetting of the thin film which could

be detected by AFM measurements (see Figure **S.III.3**, **a**). Due to this, our further experiments focused on the construction of diodes with 300 nm thick Pc active layers.

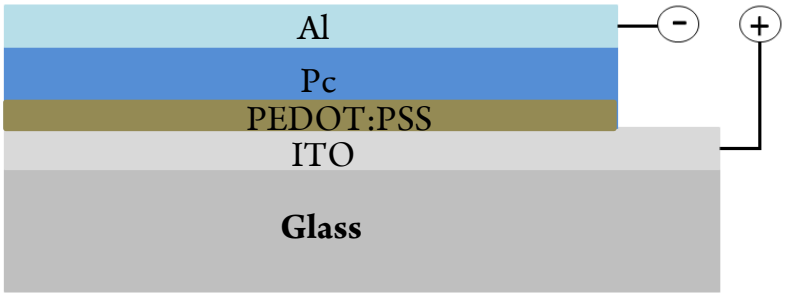

Figure III.2. Schematic representation of the diode

III.2.2. X-ray Diffraction Analysis

As reported previously, metal-free (2H-) (**3a**) and metalated (Ni^{II} (**6a**)-and (Cu^{II} (**7a**)-) 1, 8, 15, 22-(4-tetra-(2-butyloctyloxy)-phthalocyanine exhibit a plastic crystalline columnar mesophase of rectangular symmetry at room temperature that forms upon cooling (**3a**:below 40°C, **6a**: below 45°C, and **7a**: below 70 °C) from a higher-temperature LC mesophase of hexagonal (**3a**) and rectangular (**6a, 7a**) symmetry, the transition enthalpies between the liquid crystal-line and plastic crystalline states being barely noticeable by calorimetry (see Section II.4). **3a** and **6a** can be obtained in a conventional state (with a strong melting enthalpy to the LC state of ca. 40 kJ mol^{-1} in both cases) by slow crystallization from a polar solvent, whereas in the case of **7**, the plastic crystalline state is directly obtained by slow precipitation from solution. In order to correlate and to identify the molecular arrangement in the thin film, the XRD patterns of compounds **3a, 6a** and **7a** were measured at room temperature after cooling from the isotropic state (Figure **III.3**). The peaks could be identically indexed as in the powder XRD experiments presented in Section II.3, wherein a detailed discussion about the molecular organization is presented. Despite the fact that all the three compounds present a rectangular tilted columnar plastic crystalline phase at room temperature, compound **3a** is the only one to show a hexagonal mesophase upon cooling from the isotropic liquid, indicating that delocalized π-π intermolecular interactions are more pronounced in **3a**, whereas tilt-induced metal–nitrogen interactions play a dominant role in the intermolecular interactions in **6a** and **7a**. In all three cases, it is to be presumed that spin-coating leads to the same plastic crystalline state at room temperature that is observed after cooling down the pure material from elevated temperatures.

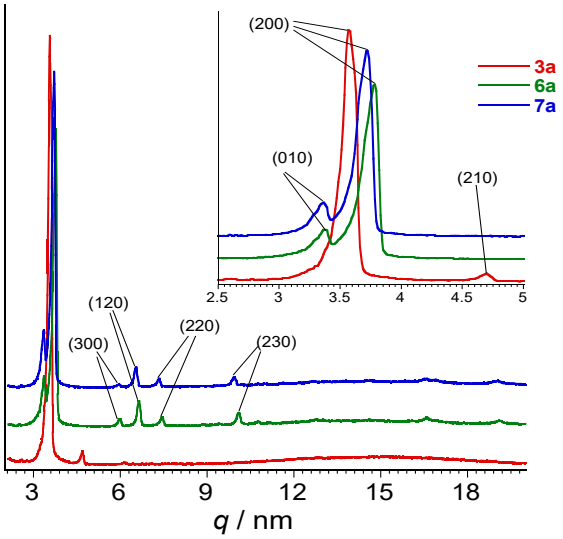

Figure III.3. Powder X-ray diffractogram at room temperature of the $H_2Pc(OCH2CHButylHexyl)_4$ (**3a**), $NiPc(OCH2CHButylHexyl)_4$ (**6a**) $CuPc(OCH2CHButylHexyl)_4$ (**7a**) derivatives showing the Bragg reflections as the typical signature of a hexagonal (**3a**) and rectangular (**6a**) and (**7a**) packing of columns. Inset: low angle regions with Miller indices.

III.2.3. Atomic Force Microscopy Measurements

We found that rather smooth homogeneous PC layers of uniform thickness are obtained with thickness of 300 nm for **3a, 6a,** and **7a**. AFM images obtained before and after annealing for **3a**, **6a** and **7a** are shown in Figure **III.4**. The R_{rms} (Root Mean Square Roughness) of the film as-spun was 9.0 nm. After annealing, the R_{rms} value increased to 25.0 nm and the morphology of the film surface is quite different, where domains corresponding to birefringent textures typical of planar surface alignment are clearly seen (also observed by POM in Figure **III.5**) and suggest partial dewetting, which leads to short-circuits after metallization. Films of metal-free **3a** are somewhat less smooth in comparison with samples **6a** and **7a** before annealing. Before annealing, the R_{rms} values for **3a** and **7a** are 18 nm and 7.5 nm, respectively. After annealing, the R_{rms} for PC **7** increased to 18.8 nm, whereas for metal-free **3a** the R_{rms} is unchanged. In all cases, the nonaligned thin film exhibits a mosaic texture formed by birefringent domains of about a few μm in size observed by POM (Figure **III.5, a, b, c**), and annealing after fast cooling from the isotropic phase (**3a**: 183°C, **6a**: 237°C, **7a**: 268°C) leads to birefringent textures typical of planar surface alignment (column axes parallel to substrate plane) (Figure **III.5, a', b', c'**). As such a planar surface orientation is unfavorable to good electrode-to-electrode charge transport in diodes (which in columnar LCs is found to be better within columns than from column to column) [30 [a, b]], and as indeed diodes made with annealed films tended to be short-circuited (probably due to partial dewetting during annealing, [31[a, b]] we explored diodes with as-spun PC layers, whose birefringence also suggests predominantly planar alignment (in line with previous studies of unannealed open columnar LC films [32]), but which did not tend to short-circuits.

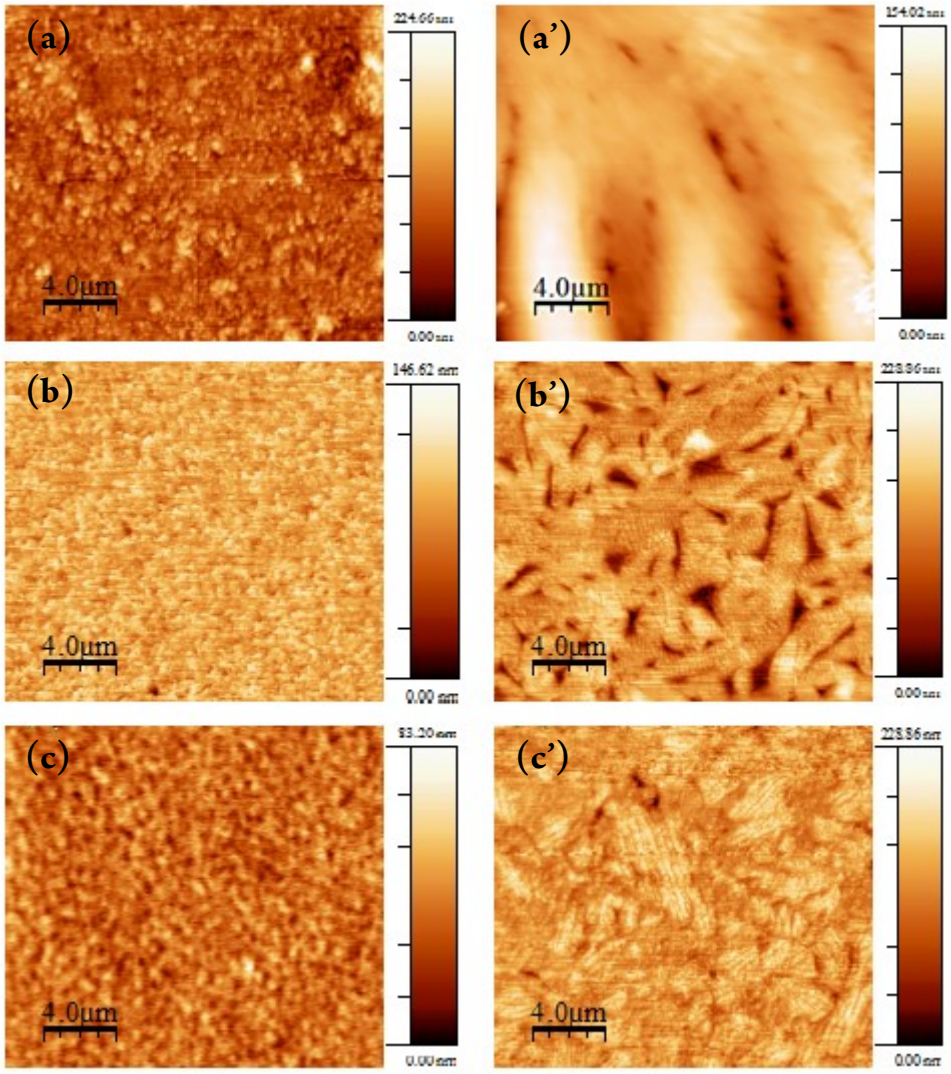

Figure III.4. AFM images of **3a** (a, a'), **6a** (b, b') and **7a** (c, c'). (a, b, c - before annealing and a' b' c' - after annealing).

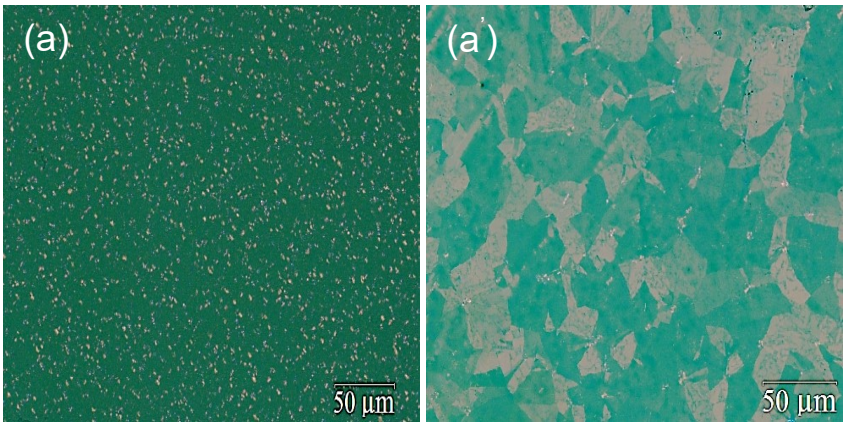

Figure III.5. POM textures of **3a** (a, a'), of the as-spun films (a) and after fast cooling from the isotropic phase (a').

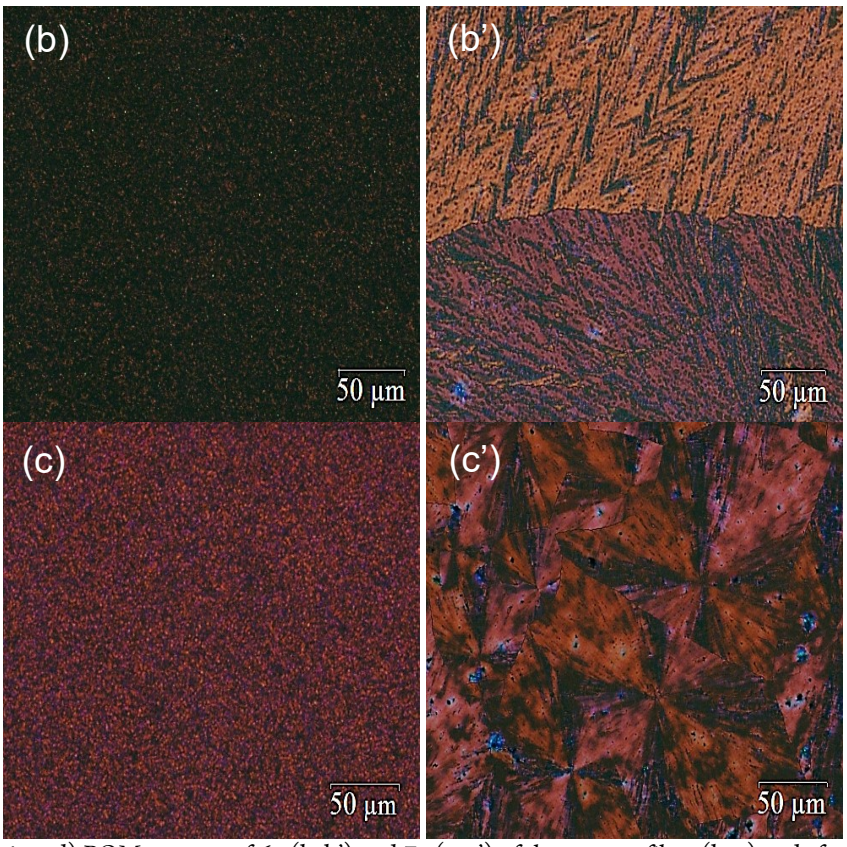

Figure III.5. (continued) POM textures of **6a** (b, b') and **7a** (c, c') of the as-spun films (b, c) and after fast cooling from the isotropic phase (b' c').

III.2.4. Electrochemical and Optical Bandgaps Estimation

The electrical and optical properties of the π-conjugated molecules are determined by the highest occupied molecular orbital (HOMO) and the lowest unoccupied molecular orbital (LUMO).[10] The HOMO and LUMO energy levels represent the ionization potential and electron affinity, respectively, characterizing the material's abilities to donate and accept electrons. It is well known that materials with high HOMO levels usually function as electron-donating and hole-transport media (*electron donor material*), while those with low LUMO levels function as electron-accepting and electron-transport media (*electron acceptor material*). Some materials that have both high HOMO levels and low LUMO levels exhibit bipolar transport characteristics; they are capable of transporting both holes and electrons. An Increased HOMO level of the hole-transport material facilitates hole injection from anodes to lower the operation voltage for electronic devices. However, materials with high-lying HOMO levels are prone to oxidation by ambient air and hence are less stable. Lowering the LUMO levels of electron-transport materials allows for the fabrication of electronic devices using stable high-work-function cathode metals [33]. Coupling the cyclic voltammetry and UV–vis spectroscopy, we can estimate if two materials can work together as a donor-acceptor system.

Cyclic voltammetry was performed in a three-electrode cell: a platinum wire counter-electrode, a 1.6 mm platinum disc working electrode, and a non-aqueous reference electrode that is comprised of a silver wire in a 0.01 M solution of $AgNO_3$ and 0.1 M tetrabutylammonium perchlorate in acetonitrile; the analytes (approximately 1 mM) were dissolved in DCM supplemented with 0.1 M tetrabutylammonium

hexafluorophosphate and degassed by bubbling argon prior to measurement. After each experiment, the potential of the Ag/Ag^+ electrode was calibrated against the ferrocene/ferrocenium (Fc/Fc^+) redox couple. The electrochemical HOMO–LUMO energy gap was determined as the difference between the onsets of the oxidation and the reduction potentials ($E_g^{elc} = E_{ox}^{onset} - E_{red}^{onset}$). The HOMO and LUMO energy values were estimated from the onset potentials of the first oxidation and reduction events, respectively. After calibration of the measurements against Fc/Fc^+, the HOMO and LUMO energy levels were calculated according to the following equations:

$$E_{LUMO}\,(eV) = -[(E_{red}^{onset} - E_{1/2(ferrocene)}) + 4.8]$$

$$E_{HOMO}\,(eV) = -[(E_{ox}^{onset} - E_{1/2(ferrocene)}) + 4.8]$$

The electrochemical behavior of **3a, 6a** and **7a** is characterized by three quasi-reversible oxidation waves and two reversible reduction waves in the cyclic voltammograms between −2.2 and 1.4 V vs. Fc/Fc^+ (Figure **III.6**). The potential of the first oxidation wave depends on the presence of a metal; it is found at significantly lower potential (ca. 0.021 V) for the metal-containing compounds than for the free ligand (0.098 V). The second oxidation wave is less sensitive with potentials of 0.292 (±0.006), 0.280 (±0.001) and 0.287 (±0.003) V for **3a**, **6a** and **7a**, respectively. A third, larger peak occurs at potentials between 0.854 (±0.003) and 0.765 (±0.005) V. Differences between the free ligand and metal-containing compounds are more marked in the reduction chemistry, with a significant shift to more negative potentials for the coordination compounds. Two reversible waves are observed at −1.339 (±0.001) and −1.734 (±0.006) V for the free ligand, while **6a** and **7a** are very similar, with potentials of −1.457 (±0.003) and −1.895 (±0.01) V, and −1.446 (±0.003) and −1.855 (±0.01) V, respectively.

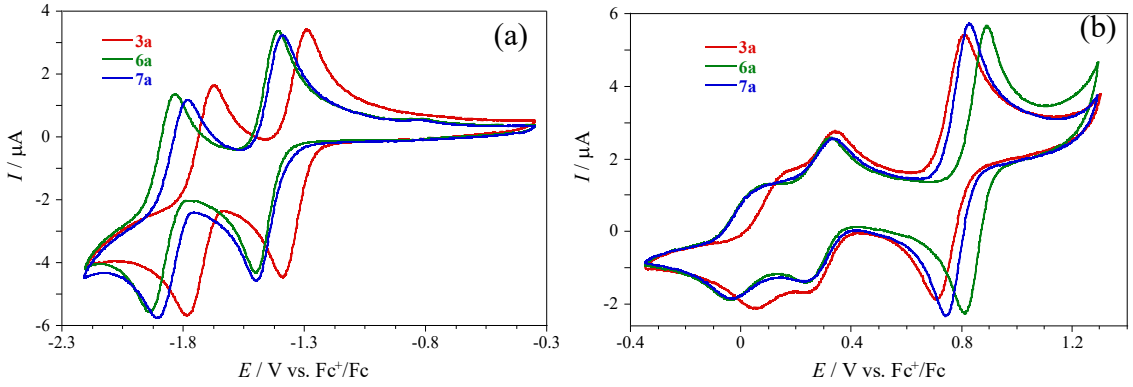

Figure III.6. Cyclic voltammograms of **3a, 6a** and **7a** in CH_2Cl_2 supplemented with 0.1 M Bu_4NPF_6. 1.6 mm Pt working electrode: (a) reduction and (b) oxidation processes. Current intensities were normalized for concentrations using the factor 1.15 for **3a** and 1.06 for **6a**.

The qualitative similarity of the CVs for **3a, 6a** and **7a** is consistent with the previous observation that the first reduction and oxidation in Ni, Cu and metal-free phthalocyanines occur on the ligand [34]. From the first oxidation and reduction potentials and with ferrocene/ferrocenium at −4.80 eV with respect to vacuum, HOMO and LUMO energies of E_{HOMO} (**3a**) = −4.90 eV, E_{LUMO} (**3a**) = −3.46 eV, E_{HOMO} (**6a**) = −4.82 eV and E_{LUMO} (**6a**) = −3.34 eV, (**7a**) = −4.82 eV, E_{LUMO} (**7a**) = −3.35 eV are obtained. These values are approximately

0.2 eV closer to vacuum than those of unsubstituted PCs [35] illustrating the moderately electron-donating effect of the four *endo*-alkoxy substituents.

The absorbance spectrum of **3a** in Figure **III.7** is characteristic of phthalocyanines with two kinds of energy bands [36], a so-called B (or Soret) band between 320 and 400 nm in the UV region and a Q band between 600 and 720 nm. The Q band is attributed to the π–π^* transitions from the HOMO to the LUMO. In the spin-coated thin film the Soret band is relatively more intense, whereas the Q band is broader and less defined than in solution, being associated to the aggregation of molecules via intermolecular interactions between the aromatic planes [37]. The vibronic structure clearly seen in the solution spectrum reflects the different coupling patterns in solution and solid state [38]. The band gap energies of the Q band were determined from the analysis of the absorption edges in solid films [39] from the cross point of absorption onset line and corrected base line, and were estimated to be 1.48, 1.57 and 1.55 eV for **3a**, **6a** and **7a**, respectively. These values agree within ±0.1 eV with the electrochemical band gaps determined by CV, 1.44 eV (**3a**), 1.48 eV (**6a**) and 1.47 eV (**7a**). The electrochemical and optical band gaps of the PCs are summarized in Table **III.1**. The absorption spectra of PCs **6a** and **7a** in THF and films were similar to PC **3a** and can be seen in Figure **S.III.1.**

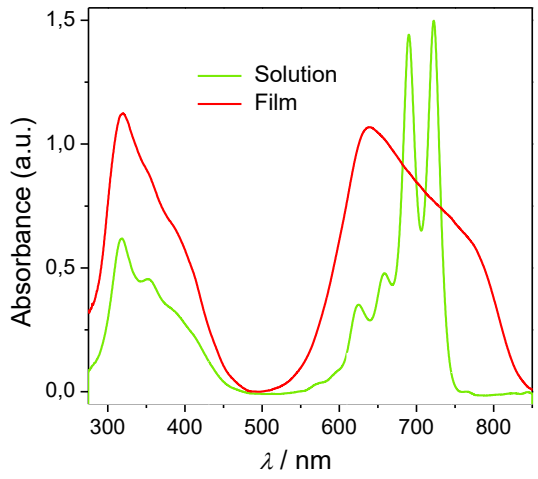

Figure III.7. UV-vis absorption spectra of **3a** in THF and film.

Table III.1. CV data for **3a**, **6a**, and **7a**

Compound	$^*E_{red}$ / V *vs.*Fc^+/Fc	$^*E_{ox}$ / V *vs.* Fc^+/ Fc	HOMO (eV)	LUMO (eV)	$E_{gap\ (eV)}$	$E_{gap\ (eV)}$ Optical
H_2Pc (**3a**)	-1.339 (±0.001)	0.098	-4.90	-3.46	1.44	1.48
NiPc (**6a**)	-1.457 (±0.003)	0.021	-4.82	-3.34	1.48	1.57
CuPc (**7a**)	-1.446 (±0.003)	0.021	-4.82	-3.35	1.47	1.55

(*) first E_{red} and E_{ox} process

III.2.5. Time-resolved Spectroscopy

The singlet excited-state lifetimes of **3a, 6a** and **7a** in THF solution and spin-coated thin films were investigated by time-resolved fluorescence spectroscopy. The lifetimes of the PCs in solution and spin-coated

films are shown in Table III.2. PCs **3a, 6a** and **7a** in solution exhibited mono-exponential decays with singlet excited-state lifetimes in the nanosecond range. The lifetimes found for all PCs in THF are similar to long-lived excited states observed for monomeric PCs in solution [40] Bi-exponential decay is usually observed for aggregated PC species in solution where their lifetimes are characterized by intermediate and fast fluorescence lifetimes, and where the fastest component becomes dominant upon increasing the concentration [41].

Table III.2. Emission wavelength maxima, lifetimes and relative amplitudes of **3a, 6a** and **7a** in THF solutions and spin-coated films after excitation at 636 nm.

	λ_{max} /nm	τ_1 / ns	A_1 (%)	τ_2 / ps	A_2 (%)	χ^2
Solution in THF						
3a	730.0	5.7 ± 0.1	100.0	-	-	1.00
6a	727.0	4.9 ± 0.1	100.0	-	-	0.978
7a	728.0	4.1 ± 0.2	100.0	-	-	0,997
Spin-coated film						
3a	695.0	1.4 ± 0.3	10.3	281 ± 20	89.7	0.995
6a	695.0	1.8 ± 0.2	27.6	359 ± 80	72.4	1.005
7a	695.0	1.6 ± 0.7	16.1	320 ± 55	83.9	0.990

[a] Excited state lifetimes were measured at maxima of the emission intensities. The fluorescence spectra of **3a, 6a** and **7a** excited at 636 nm in solution and thin films are presented in Figure III.8.

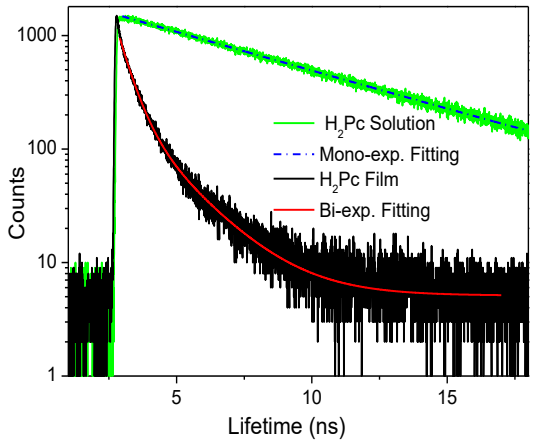

Figure III.8. Comparison between the mono-exponential fitting for **3a** in solution and bi-exponential in spin-coated film.

The shorter excited state lifetimes in the condensed film, and especially, the fact that the second time is dominant, agrees with the evidence from the absorption measurements where a broader Q band is observed in the film. These effects indicate a strong aggregation of the molecules in the spin-coated films driven by π–π interactions. On comparing the film absorption spectra of the free-metal and the metalated PCs it is evident that the Q band broadening of the metal-free PC **3a** is larger (see Figure S.III.1). In addition, the highest A_2 value is also observed for **3a**. Both results suggest that the π–π interactions are more pronounced for the metal-free PC. This can be explained by the fact that metal–nitrogen interactions between adjacent molecules may constrain the establishment of maximal π–π interactions in **6a** and **7a**.

III.2.6. Electrical Measurements

To conform with well-established procedures [43] we used poly(ethylenedioxythiophene):poly(styrenesulfonic acid) (PEDOT:PSS)-coated indium-tin-oxide (ITO) as a glass-supported anode, on which the PC layer was spun, and an aluminum cathode that was vacuum-deposited on top. The device structure used for electrical characterization of the PCs was ITO/PEDOT:PSS (80 nm)/PC **3a**, **6a** or **7a** (300 nm)/Al (80 nm). The electrical measurements were performed at room temperature and under ambient conditions. The current density–voltage (J–V) characteristics are presented in Figure **III.9**. The energy levels of the PCs determined by cyclic voltammetry match well with the work functions of the PEDOT:PSS (~5.2 eV) and Al electrodes (~4.3 eV), leading to good charge carrier injection. To our surprise, diodes made from any of the three homologs **3a, 6a** and **7a** shows a degree of rectification higher than three orders of magnitude, see Figure **III.9, a.**

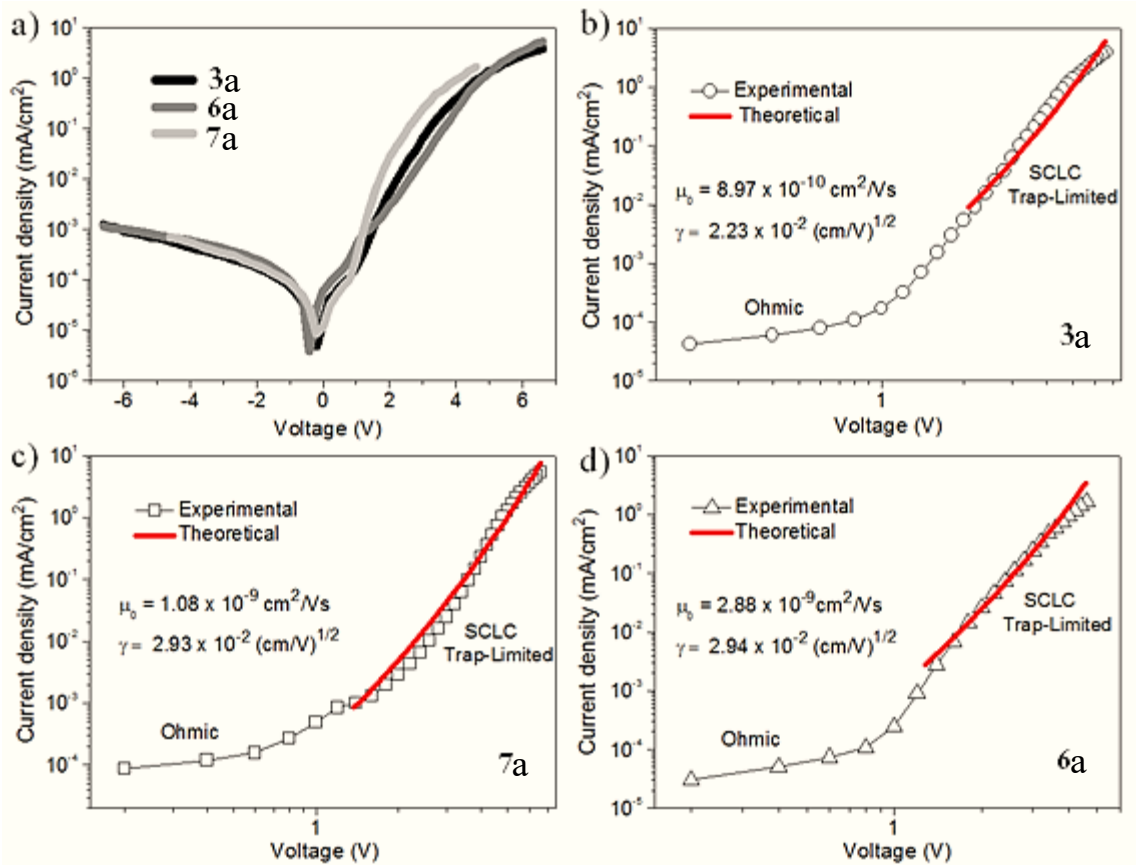

Figure III.9. Electrical characterization of the PC spin-coated films in the device configuration ITO – PEDOT:PSS (80nm) – PC (300nm) – Al (80nm). (**a**) Current density versus voltage. (**b**), (**c**) and (**d**) log-log plots of the J-V curves for compounds **3a**, **6a** and **7a**. The red solid lines indicate the fitting at the trap-limited SCLC regimes.

These rectification ratios are much higher than those reported for a less regularly substituted PC, a hexagonal columnar liquid crystalline zinc PC derivative with a considerably larger electronically inert alkyl periphery [27], giving rectification ratios of less than 10 : 1 in a very similar device configuration with ITO/PEDOT:PSS and Ca/Al electrodes. The strong rectification might result from the close and regular molecular packing in well-ordered plastic rectangular columnar mesophases present in materials **3a, 6a** and **7a** [10], which provides intimate intermolecular π-orbital and metal–nitrogen interactions and therewith an

efficient charge transport through the PC columns even in a planar alignment, and thus leads to efficient charge evacuation after injection, avoiding the build-up of a counter-field that would outplay the built-in rectifier geometry. A rectification of three orders of magnitude was also obtained for a perylene-based columnar LC in a diode structure in a similar edge-on configuration. Such an effect results from a compact molecular packing induced in the organic film by thermal evaporation of the molecules [44]. Substrate–PC interactions were investigated using structural analysis by Chang-Hyun Kim et al. [45]. They showed that in CuPC films deposited on ITO/PEDOT:PSS the molecules crystallized in an edge-on orientation whereas the deposition on graphene led to a face-on orientation, providing higher rectification ratios. For CuPC films deposited in the device structure ITO/PEDOT:PSS/CuPC/Al, they obtained a ratio of rectification lower than two orders of magnitude. Mativetsky et al. [46] also used graphene to induce face-on stacking of CuPC thus improving the out-of-plane hole mobility. The log–log plots of the current densities for **3, 6** and **7** are presented in Figure **III.9, b, c, d**. The current densities follow an *ohmic regime* at low voltages and a trap-limited space-charge-limited current regime (SCLC, where the current from the injection of charge carriers from the electrodes becomes dominant) at higher voltages. As the measurements do not obey the Mott–Gurney law ($J \propto V^2$), the charge mobilities were obtained directly from the *J–V* curves by fitting the trap-limited SCLC regimes with a theoretical model presented previously [26]. This model considers an electric field dependent mobility, given by $\mu(E) = \mu_0 e^{\gamma\sqrt{E}}$, where μ_0 is the carrier mobility at zero field and γ the field dependence of the mobility, with μ_0 and γ being the parameters extracted from the fitting. The values of μ_0 and γ were extracted for **3a, 6a** and **7a,** and the respective fits are displayed as red solid lines in Figure **III.9, b, c, d**. The fits agree well with the experimental data obtained in the trap-limited SCLC regime. The μ_0 and γ values found for **3a, 6a** and **7a** are listed in Table **III.3**, where the mobility values calculated from $\mu = \mu_0 e^{\gamma\sqrt{E}}$ are presented for an applied voltage of +4.6 V. The voltage dependence of the mobility is shown in Figure **S.III.6.**

Table III.3. Fitting values obtained for μ_0 and γ

Parameter	3a	6a	7a
μ_0 (cm^2/Vs)	8.97×10^{-10}	2.88×10^{-9}	1.08×10^{-9}
γ $(cm/V)^{1/2}$	2.23×10^{-2}	2.94×10^{-2}	2.93×10^{-2}
μ at applied +4.6 V (cm^2/Vs)	**1.28×10^{-5}**	**2.46×10^{-4}**	**5.53×10^{-5}**

At the same given voltage, the mobility of **3** is the lowest and that of **6** is the highest. These mobilities of the order of 10^{-5} to 10^{-4} $cm^2\ V^{-1}\ s^{-1}$ perpendicular to the column direction are low compared to the mobilities typically of 10^{-3} to 1.0 in the column direction reported for columnar liquid or plastic crystals, in agreement with the known anisotropy of mobility in columnar mesophases [47]. The higher Poole–Frenkel coefficients γ indicate that the hopping transport is easier for **6a** (NiPc) and **7a** (CuPc) than for **3a**(H_2Pc). From the XRD patterns collected at room temperature on cooling from the isotropic and from the singlet excited-state lifetime measurements, where the exponential component (A_2) is higher, it is to be inferred that the metal-free PC **3a**

presents a higher contribution coming from the π–π intermolecular interactions, as is also corroborated by its broader absorption spectrum in the film compared to the metal derivatives **6a** and **7a**. On the other hand, the mobility obtained for the metalated PCs **6a** and **7a** is higher, which is consistent with the fact that the metallic center plays an important role in the charge conduction inside these organic layers. In the metalated PCs, the electrons from nitrogens of neighboring molecules interact with the metallic center, which thus acts as a bridge between the nitrogen atoms of the stacking molecules, contributing to the enhancement of the π-electron delocalization in comparison to the corresponding metal-free PC. Thus, the higher mobility of Ni- and Cu-PCs is due to an increased interaction of the molecular orbitals between parallel aligned molecules. Non-mesogenic Ni- and Cu-PCs exhibit in general a higher mobility than H_2PCs [48].

III.3. Conclusion

The regioregularly all-endo tetrasubstituted PCs exhibiting a highly ordered plastic crystalline columnar phase at room temperature give rise to pronounced current rectification in simple ITO/PEDOT:PSS/PC/Al diode structures. These good diode characteristics are obtained despite the preponderant in-plane alignment of the columns and thus of the axis of preferred charge migration within the PC layer. The field dependent charge carrier mobilities across the devices were obtained in the trap-limited *SCLC* regimes from the current–voltage curves to be of the order of 10^{-5} cm^2 V^{-1} s^{-1} for the metal-free PC homologue, and of the order of 10^{-4} cm^2 V^{-1} s^{-1} for the metalated Cu and Ni derivatives at +4.6 V. This mobility could still be improved by obtaining a homeotropic alignment of the molecular columns, as previously demonstrated for a perylene based molecule, where an increase of 5 orders of magnitude was obtained [26]. The planar alignment is disadvantageous in diode-type devices since in this way the charges have to be transported perpendicular to the π-stacking direction. On the other hand such an orientation is beneficial for thin film transistors. The XRD patterns, excited-state lifetimes and optical absorption characterization suggest that the π–π intermolecular interactions are stronger for metal-free PC **3a**, whereas NiPC **6a** and CuPC **7a** presented better electrical response. This demonstrates that for phthalocyanines the intermolecular ligand–ligand π–π interactions do not dominate the electrical conduction, confirming that the metallic center plays an important role in the charge transport inside these materials.

III.4. Supporting Material

III.4.1. Uv-vis Spectroscopy of the Thin Films

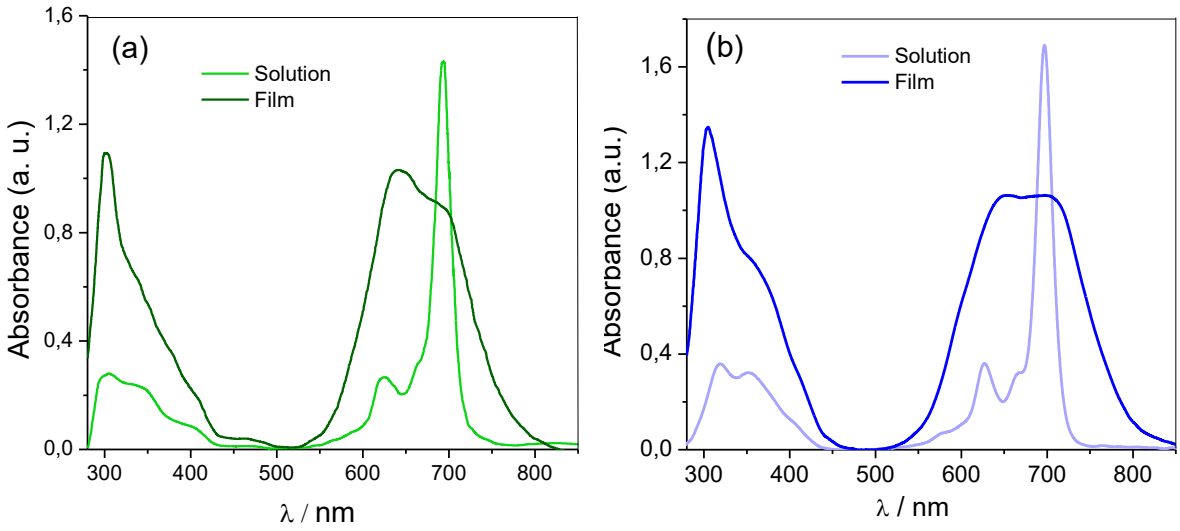

Figure S.III.1. Absorbance spectra of PCs in solution and film. (a) NiPc and (b) CuPc.

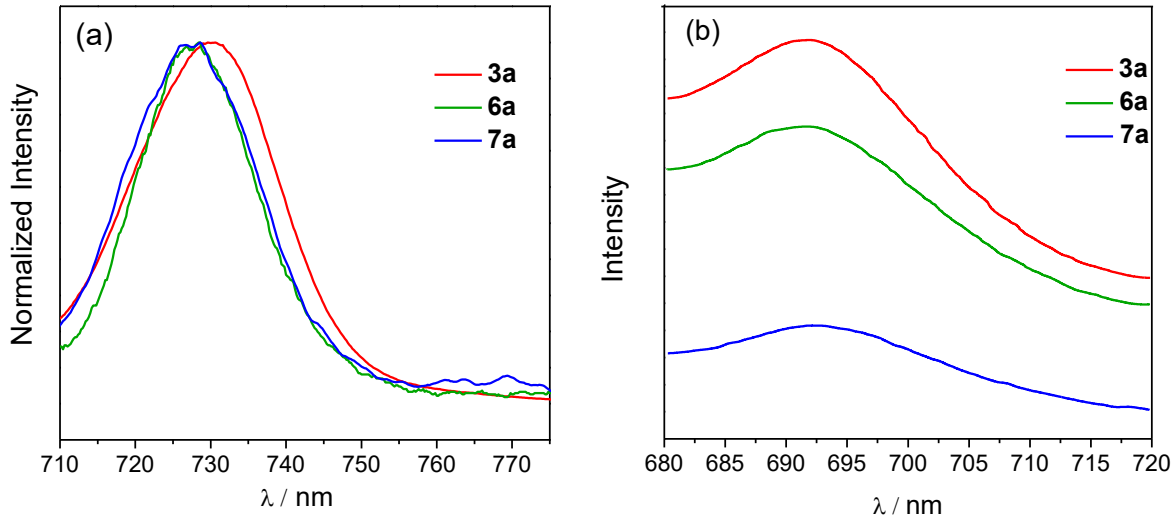

Figure S.III.2. Fluorescence spectra of **3a, 6a** and **7a** excited at 636 nm in solution (a) and thin film (b).

III.4.2. Atomic Force Microscopy

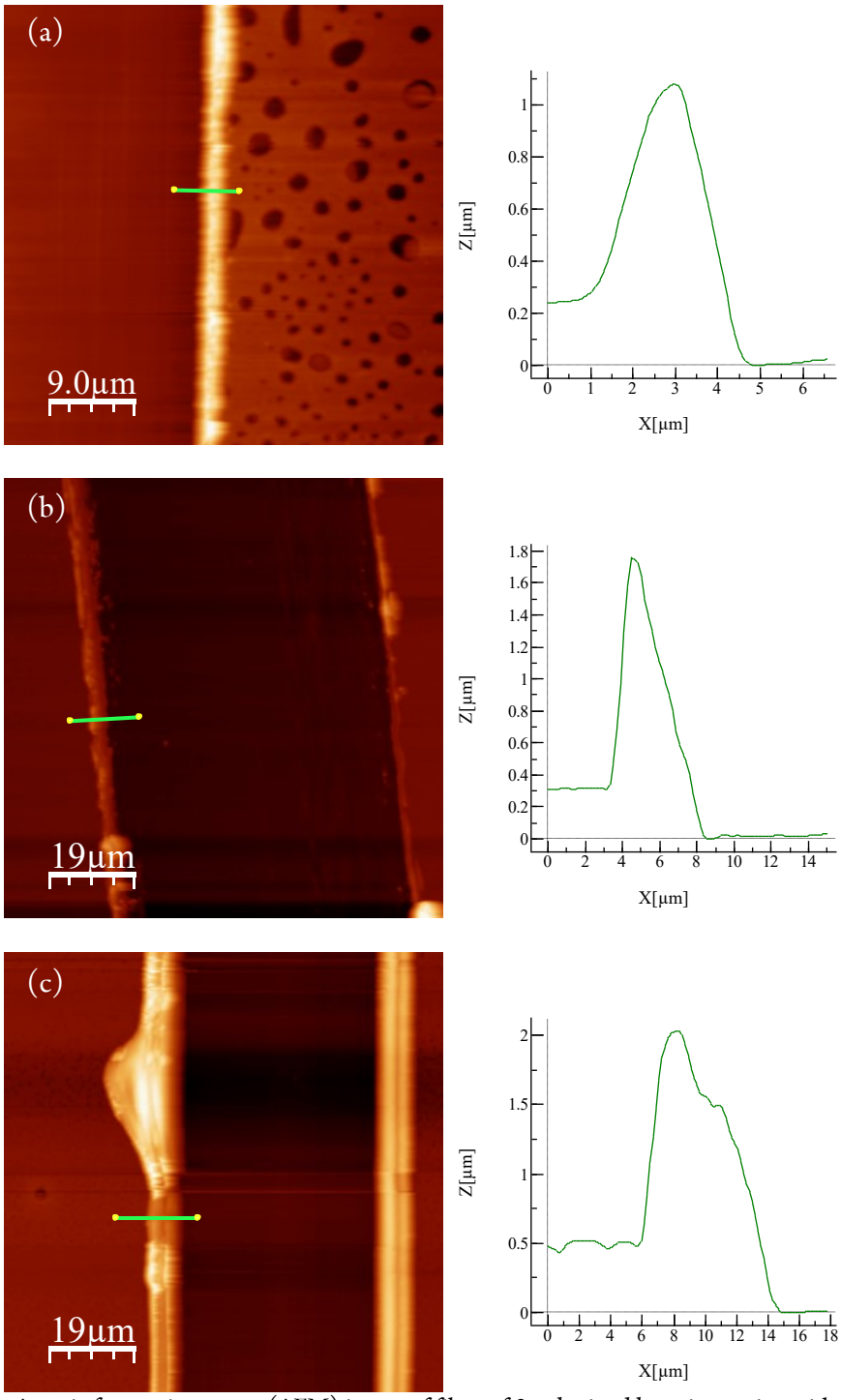

Figure S.III.3. Atomic force microscopy (AFM) image of films of **3a** obtained by spin-coating with concentrations: 20 (a), 30 (b), 40 (c) mg/ml. The scan direction is marked by the dashed line.

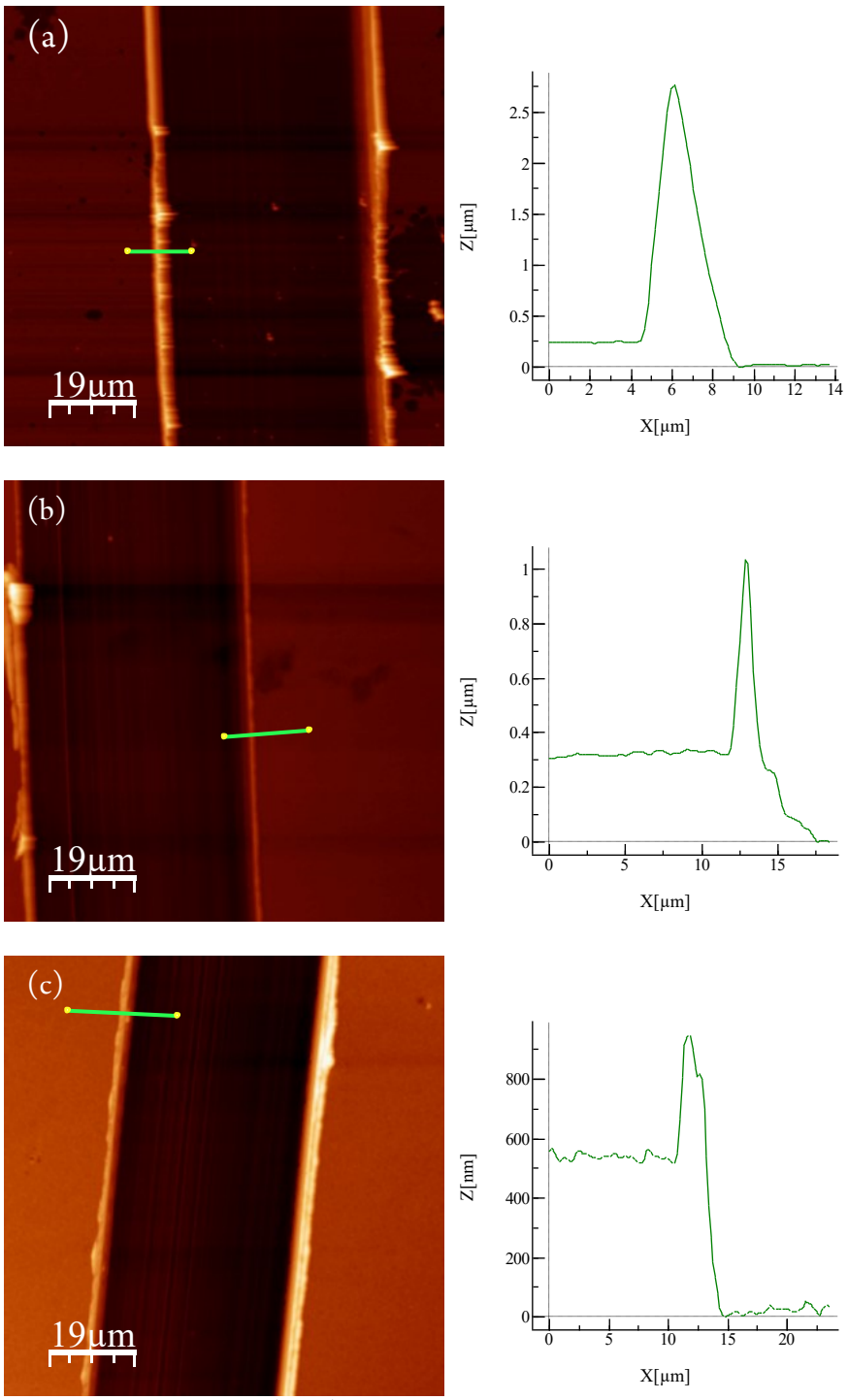

Figure S.III.4. Atomic force microscopy (AFM) image of films of **6a** obtained by spin-coating with concentrations: 20 (a), 30 (b), 40 (c) mg/ml. The scan direction is marked by the dashed line.

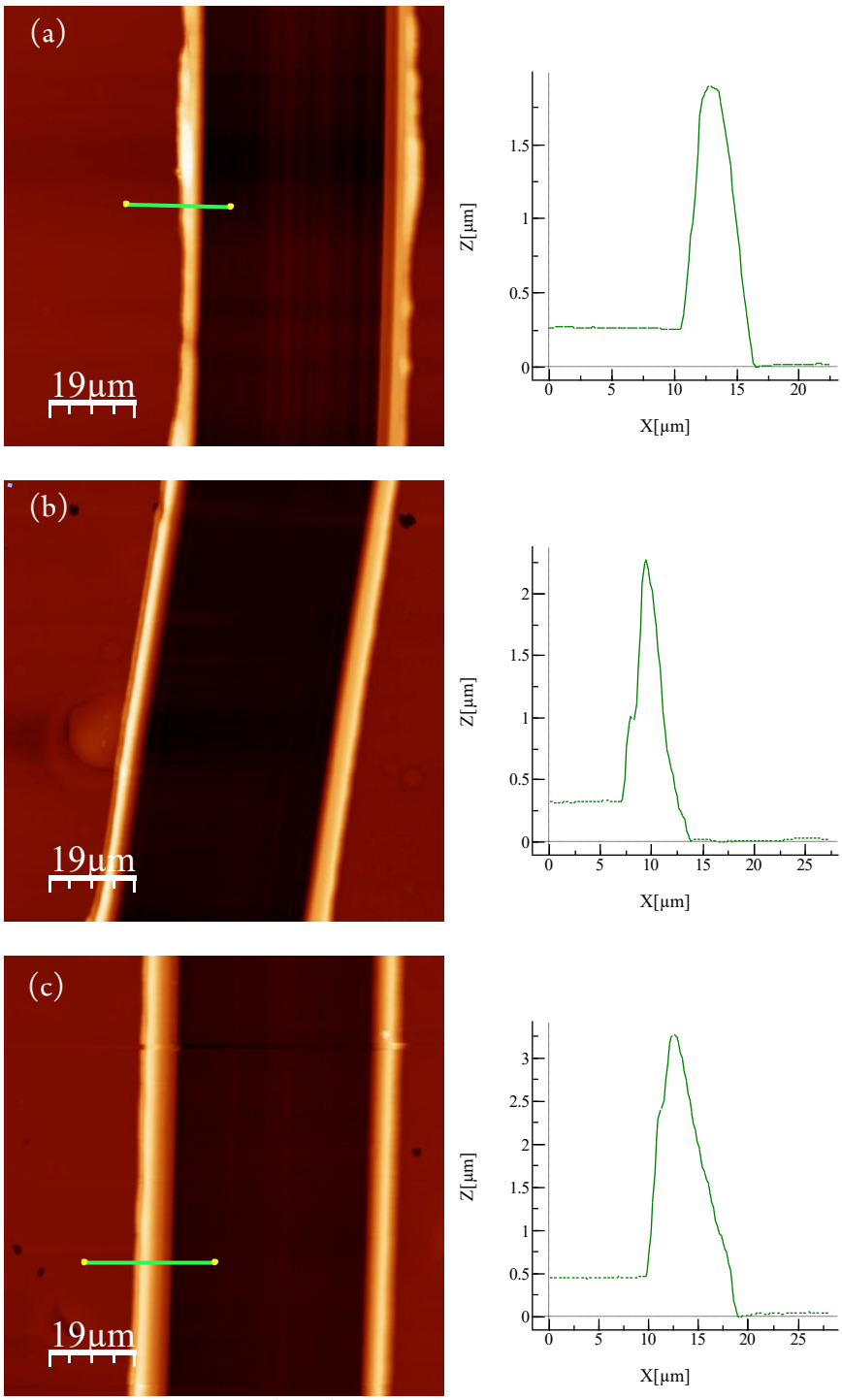

Figure S.III.5. Atomic force microscopy (AFM) image of films of **7a** obtained by spin-coating with concentrations: 20 (a), 30 (b), 40 (c) mg/ml. The scan direction is marked by the dashed line.

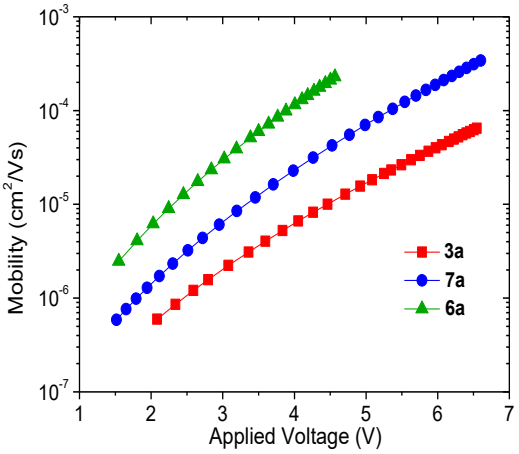

Figure S.III.6. Mobility of the $H_2Pc(OCH_2CHBuHex)_4$ (**3a**), $NiPc(OCH_2CHBuHex)_4$ (**6a**) and $CuPc(OCH_2CHBuHex)_4$ (**7a**) at the SCLC regime as a function of the applied voltage.

III.5. References

[1] J. M. Warman; M. P.de Haas; G. Dicker; F. C. Grozema; J. Piris; M. G Debije; Chem. Mater. **2004**, 16, 4600–4609.

[2] a) A. N. Sokolov; S. Atahan-Evrenk; R. Mondal; H. B. Akkerman; R. S. Sánches-Carrera; S. Granados-Focil; J. Schrier; S. C. B. Mannsfeld; A. P. Zoombelt; Z. Bao, A. Aspuru-Guzic; *Nat. Commun.*, **2011**, 2, 437, 1-8; b) Y. Yuan; G. Giri; A. L. Ayzner; A. P. Zoombelt; S. C. B. Mannsfeld; J. Chen; D. Nordlund; M. F. Toney; J. Huang; Z. Bao; *Nat. Commun.*, **2014**, 5, 3005, 1-9.

[3] a) D. Wohrle; G. Schnurpfeil; S. G. Makarov; A. Kazarin; O. N. Suvorova; *Macroheterocycles* , **2012**, 5, 191–202; b) F. Yakuphanoglu; M. Kandaz; M. N. Yarasir; F. B. Senkal; *Phys. B*, **2007**, 393, 235–238; c) C. W. Tang; *Appl. Phys. Lett.*, **1986**, 4, 183–185; d) L. M. Ozer; M. Ozer; A. Altindal; A. R. Ozkaya; B. Salih; O. Bekaroglu; *Dalton Trans.*, **2013**, 42, 6633–6644.

[4] N. B. McKeown; *Phthalocyanine Materials: Synthesis, Structure and Function*, Cambridge University Press, Cambridge, UK, **1998**.

[5] a) C. Piechocki; J. Simon; A. Skoulios; D. Guillon; P. Weber; *J. Am. Chem. Soc.*, **1982**, 104, 5245–5247;.b) D. Atilla; G. Aslibay; A. G. Gurek; H. Can; V. Ahsen; *Polyhedron*, **2007**, 26, 1061–1069.

[6] S. Laschat; A. Baro; N. Steinke; F. Giesselmann; C. Hagele; G. Scalia; R. Judele; E. Kapatsina; S. Sauer; A. Schreivogel; M. Tosoni; *Angew. Chem., Int. Ed.* , **2007,** 46, 4832–4887.

[7] a) J. Meiss; A. Merten; M. Hein; C. Schuenemann; S. Schafer; M. Tietze; C. Uhrich; M. Pfeiffer; K. Leo; M. Riede; *Adv. Funct. Mater.*, **2012**, 22, 405–414; b) H. Hayashi; W. Nihashi; T. Umeyama; Y. Matano; S. Seki; Y. Shimizu; H. Imahori; *J. Am. Chem. Soc.* , **2011**, 133, 10736–10739.

[8] N. B. Chaure; C. Pal, S. Barard; T. Kreouzis; A. K. Ray; A. N. Cammidge; I. Chambrier; M. J. Cook; C. E. Murphy; M. G. Cain; *J. Mater. Chem.*, **2012**, 22, 19179–19189.

[9] S. Dong; H. Tian; L. Huang; J. Zhang; D. Yan; Y. Geng; F. Wang; *Adv. Mater.* **2011**, 23, 2850–2854.

[10] P. Apostol; A. Bentaleb; M. Rajaoarivelo; R. Clerac; H. Bock; *Dalton Trans.,* **2015**, 44 , 5569–5576.

[11] H. Krishna Bisoyi; S. Kumar; *Chem. Soc. Rev.*, **2010**, **39**, 264-285.

[12] A. M. van de Craats; , N. Stutzmann; O.; Bunk; M. M. Nielsen; M. Watson; K. Müllen; H. D.Chanzy; H.Sirringhaus; R. Friend; *Ad V. Mater*. **2003**, 15, 495-499.

[13] L. Schmidt-Mende; A. Fechtenkötter; K. Müllen; E. Moons; R. H. Friend; J. D. MacKenzie; *Science* **2001**, 293, 1119-1122.

[14] a) G. Lüssem; J. H. Wendorff; *Polym. Ad V. Technol.* **1998**, 9, 443-460; b) I. Seguy; P. Destruel; H. Bock; *Synth. Met.* **2000**, 15, 111-112.

[15] a) V. De Cupere; J. Tant; P. Viville; R. Lazzaroni; W. Osikowicz; W. R. Salaneck; Y. H. Geerts; *Langmuir,* **2006**, 22, 7798 – 7806; b) Z. H. Al-Lawati; R. J. Bushby; S. D. Evans; *J. Phys. Chem. C*, **2013**, 117, 10702 – 1070.

[16] W. Pisula; Z. Tomovic; B. El Hamaoui; M. D. Watson; T. Pakula; K.Müllen; *Chem. Mater.,* **2005**, 17, 4296-4303.

[17] a) K. Hatsusaka; K. Otha; I. Yamamoto; H. Shirai; *J. Mater. Chem.*, **2001**, 11, 423-433; b) K. Hatsusaka; M. Kimura; K. Otha; *Bull. Chem. Soc. Jpn.*, **2003**, 76, 781-787.

[18] S. Xiao, M. Myers; Q. Miao; S. Sanaur; K. Pang; M. L. Steigerwald; C. Nuckolls; *Angew. Chem. Int. Ed.* **2005**, 44, 7390 – 7394.

[19] G. Scherowsky; X. H. Chen; *J. Mater. Chem.*, **1995**, 5, 417 – 421.

[20] a) J. Piris; M. G. Debije; N. Stutzmann; B. W. Laursen; W. Pisula; M. D. Watson; T. Bjornholm; K. Mullen; J. M. Warman; *Adv. Funct. Mater.*, **2004**, 14, 1053 – 1061; b) J. C. Wittmann; P. Smith; *Nature,* **1991**, 352, 414 – 417; c) S. Zimmermann; J. H. Wendorff; C. Weder; *Chem. Mater.* **2002**, 14, 2218 – 2223; d) A. M. van de Craats; N. Stutzmann; O. Bunk; M. M. Nielsen; M. Watson; K. Mullen; H. D. Chanzy; H. Sirringhaus; R. H. Friend; *Adv. Mater.*, **2003**, 15, 495 – 499; e) E. Charlet; E. Grelet; *Phys. Rev. E.*, **2008**, 78, 041707-*1-8*.

[21] a) W. Pisula; A. Menon; M. Stepputat; I. Lieberwirth; U. Kolb; A. Tracz; H. Sirringhaus; Y. Pakula; K. Mullen; *Adv. Mater.*, **2005**, 17, 684 – 689; b) A. Tracz; J. K. Jeszka; M. D. Watson; W. Pisula; K. Mullen; T. Pakula; *J. Am. Chem. Soc.*, **2003**, 125, 1682 – 1683; c) M. Kastler; W. Pisula; D. Wasserfallen; T. Pakula; K. Mullen; *J. Am. Chem. Soc.*, **2005**, 127, 4286 – 4296; d) D. W. Breiby; O. Bunk; W. Pisula; T. I. Solling; A. Tracz; T. Pakula; K. Mullen; M. M. Nielsen; *J. Am. Chem. Soc.*, **2005**, 127, 11288 – 11293; e) D. W. Breiby; F. Hansteen; W. Pisula; O. Bunk; T. I. Solling; U. Kolb; J. W. Andreasen; K. Müllen; M. M. Nielsen; *J. Phys. Chem. B,* **2005**, 109 , 22319 – 223250.

[22] C.-Y. Liu; A. J. Bard; *Chem. Mater.*, **2000**, 12, 2353 – 2362.
[23] a) P. O. Mouthuy; S. Melinte; Y. H. Geerts; A. M. Jonas; *Nano Lett.*, **2007**, 7, 2627 – 2632; b) P. O. Mouthuy; S. Melinte; Y. H. Geerts; B. Nysten; A. M. Jonas; *Small* **2008**, 4, 728 – 732.
[24] J.-H. Lee; S.-M. Choi; B. D. Pate; M. H. Chisholm; Y.-S. Han; *J. Mater. Chem.*, **2006**, 16, 2785–2791.
[25] H.-S. Kim; S.-M. Choi; B. D. Pate; P. Gyu Park; *Chem. Phys. Chem.*, **2009**, 10, 2642 – 2646.
[26] J. Eccher; G. C. Faria; H. Bock; H. von Seggern; I. H. Bechtold; *Acs Appl Mater Inter.*, **2013**, 5, 11935-11943.
[27] I. H. Bechtold; J. Eccher; G. C. Faria; H. Gallardo; F. Molin; N. R. S. Gobo; K. T. de Oliveira; H. von Seggern; *J Phys Chem B*, **2012**, 116, 13554-13560.
[28] S. Dong; C. Bao; H. Tian; D. Yan; Y. Geng; F. Wang; *Adv. Mater.*, **2013**, 25, 1165-1169.
[29] T. M. Brown; F. Cacialli; *J. Polym. Sci., Part B: Polym. Phys.*, **2003**, 41, 2649–2664.
[30] a) I. O. Shklyarevskiy; P. Jonkheijm; N. Stutzmann; D. Wasserberg; H. J. Wondergem; P. C. M. Christianen; A. P. H. J. Schenning; D. M. de Leeuw; Z. Tomovic; J. S. Wu, K. Mullen; J. C. Maan; *J. Am. Chem. Soc.*, **2005**, 127, 16233–16237; b) J. Piris; M. G. Debije; N. Stutzmann; A. M. van de Craats; M. D. Watson; K. Mullen; J. M. Warman; *Adv. Mater.*, **2003**, 15, 1736–1740.
[31] a) E. Charlet; E. Grelet; P. Brettes; H. Bock; H. Saadaoui; L. Cisse; P. Destruel; N. Gherardi; I. Seguy; *Appl. Phys. Lett.,* **2008**, 92, 024107-1–*024107*-3; b) S. Archambeau; I. Seguy; P. Jolinat; J. Farenc; P. Destruel; T. P. Nguyen; H. Bock; E. Grelet; *Appl. Surf. Sci.*, **2006**, 253, 2078–2086.
[32] E. Grelet; S. Dardel; H. Bock; M. Goldmann; E. Lacaze; F. Nallet; *Eur. Phys. J. E: Soft Matter Biol. Phys.*, **2010**, 31, 343–349.
[33] D. A. McQuarrie; *Quantum Chemistry University Science Books*, Sausalito: **1983**.
[34] L. D. Rollmann; R. T. Iwamoto; *J. Am. Chem. Soc.*, **1968**, 90, 1455–1463.
[35] M. Hiramoto; M. Kubo; Y. Shinmura, N. Ishiyama; T. Kaji; K. Sakai; T. Ohno; M. Izaki; *Electronics*, **2014**, 3, 351–380.
[36] M. Gouterman; G. H. Wagniere; *J. Mol. Spectrosc.*, **1963**, 11, 108-111.
[37] a) S. Verma; A. Ghosh; A. Das; H. N. Ghosh; *J. Phys. Chem. B.,* **2010** 114, 8327–8334; b) Y. Alfredsson; J. Ahlund; K. Nilson; Kjeldgaard, Lisbeth., JN. O'Shea; J. Theobald; Z. Bao; N. Martensson; A. Sandell; C. Puglia; *Thin Solid Films.*, **2005**, 493, 13–19; c) M. Muccini; M. Murgia; C. Taliani; A. Degli Esposti; R. Zamboni; *J. Opt. A Pure Appl. Opt.,* **2000**, 2, 577–583.
[38] a) A. S. Davydov; *Theory of Molecular Excitons,* Plenum, **1971**; b) W. F. Freyer; C. C. Neacsu; M. B. Raschke; *J. Lumin,.* **2008**, 128, 661–672; c) M. Kasha, H. R. Rawls;. M. A. El-Bayoumi,. *Pure Appl. Chem.* **1965**, 11, 371–392 d). R. Tempelaar; A. Stradomska; J. Knoester; , F. C. Spano; *J. Phys. Chem. B.* **2013**, 117, 457–466.
[39] S. Hellstrom; F. L. Zhang; O. Inganas; M. R. Andersson; *Dalton Trans.*, **2009**, 10032–10039.
[40] a) M. N. Sibata; A. C. Tedesco; J. M. Marchetti; *Eur. J. Pharm. Sci.,* **2004**, 23, 131–138; b) M. Ambroz; A. Beeby; A. J. Macrobert; M. S. C. Simpson; R. K. Svensen; D. Phillips; *J. Photochem. Photobiol.,* B, **1991**, 9, 87–95.
[41] G. Valduga; E. Reddi; G. Jori; R. Cubeddu; P. Taron; G. Valentini; *J. Photochem. Photobiol., B*, **1992**, 16, 331–340.
[42] P. Bertoncello; M. Peruffo; *Colloids Surf., A*, **2008**, 321, 106–112.
[43] T. M. Brown; F. Cacialli; *J. Polym. Sci., Part B: Polym. Phys.*, **2003**, 41, 2649–2664.
[44] J. Eccher; W. Zajaczkowski; G. C. Faria; H. Bock; H. von Seggern; W. Pisula; I. H. Bechtold; *ACS Appl. Mater. Interfaces*, **2015**, 7, 16374–16381.
[45] C. H. Kim; H. Hlaing; S. Yang; Y. Bonnassieux; G. Horowitz; I. Kymissis; *Org. Electron.*, **2014**, 15, 1724–1730.
[46] J. M. Mativetsky; H. Wang; S. S. Lee; L. Whittaker-Brooks; Y. L. Loo; *Chem. Commun.*, **2014**, 50, 5319–5321.
[47] a) J. M. Warman; P. G. Schouten; *J. Phys. Chem.,* **1995**, 99, 17181–17185; b) M. G. Debije; J. Piris; M. P. de Haas; J. M. Warman; Z. Tomovic; C. D. Simpson; M. D. Watson; K. Mullen; *J. Am. Chem. Soc.,* **2004**, 126, 4641–4645; c) J. Simmerer; B. Glusen; W. Paulus; A. Kettner; P. Schuhmacher; D. Adam; K. H. Etzbach; K. Siemensmeyer; J. H. Wendorff; H. Ringsdorf; D. Haarer; *Adv. Mater.,* **1996**, 8, 815–819.
[48] L. Q. Li; Q. X. Tang; H. X. Li; W. Hu; X. O. Yang; Z. Shuai; Y. Q. Liu; D. Zhu; *Pure Appl. Chem.*, **2008**, 80, 2231–2240.

Chapter IV

Single-Molecule Magnet Behavior in Mononuclear Mn^{III} and Dy^{III} Tetra-α-alkoxy-Pc Complexes

Table of Contents for Chapter IV:

IV.1. Introduction

After the first observation of a slow relaxation of the magnetization in the famous dodecametallic manganese-acetate complex $[Mn_{12}O_{12}(OAc)_{16}(H_2O)_4]$ ($Mn_{12}Ac$) [1], a number of mononuclear and polynuclear single-molecule magnets has been added to this subclass of molecular magnetic materials. However, for the first 15 years, the SMM field was dominated by the high-spin Mn^{III} ion with Jahn–Teller distortion. In 3d-SMMs, the general way to increase the spin-reversal barrier U_{eff} further is to create a very high spin ground state (S) and a large easy-axis anisotropy D. Thus, several manganese complexes were separated and studied. Apart of $Mn_{12}Ac$ which became a strategic benchmark for its derivate complexes, the hexametallic manganese(III) cage $[Mn_6O_2(sao)_6(O_2CPh)_2(EtOH)_4]$ ({Mn_6}) ($saoH_2$ = 2-hydroxybenzaldehye oxime) showed one of the largest anisotropy barriers in a 3d-SMM (measured in zero magnetic field) where a combination of S = 12 and D = −0.43 cm^{-1} results in U_{eff} = 62 cm^{-1} [2]. On the other hand, $[Mn_{19}O_8(N_3)_8(HL)_{12}(MeCN)_6]^{2+}$, or {$Mn_{19}$} ($H_3L$ = 2,6- bis(hydroxymethyl)-4-methylphenol), which has a large total spin of S = 83/2, should have a large energy barrier: instead, {Mn_{19}} has no SMM behavior [3]. This apparent contradiction was explained by the presence of high symmetry of the {Mn_{19}} molecule, which means that the anisotropies on the individual manganese(III) centers cancel each other out almost completely.

In parallel with manganese based SMMs, SMMs containing other 3d metal ions have been also reported, mainly based on iron and cobalt [4]. Of the 3d monometallic complexes, only a few examples of monometallic manganese (III) complexes that display slow relaxation of magnetization were reported [5]. Moreover, a slow relaxation of magnetization of manganese (III) phthalocyanine was not reported until now.

Since 2003, Ishikawa's group reported the first monometallic [6] SMMs and also the first lanthanide ion containing SMMs, and a special attention was given to a group of elements whose single-ion anisotropies are unrivalled: lanthanides. The lanthanide ions most commonly used in SMMs are terbium (III), dysprosium (III), erbium (III), and holmium (III). Because of the strong angular contribution and the crystal field effect of the 4f orbitals, the electronic origination of the terbium (III) and dysprosium (III) ions possess substantial anisotropy. The majority of Ln-SMMs contain either terbium or dysprosium, and in Ln-SMMs containing two or more lanthanide ions dysprosium is ubiquitous. Ishikawa reported a new method to determine sublevel structures of ground-state multiplets of the lanthanide complexes, and showed that a suitable ligand field can yield a situation where the lowest sublevel states have a large projection of the total angular momentum, $|J_z|$ value, and the energy gap between the lowest and second-lowest doublets is more than a few hundred wavenumbers [7b,c]. The implication for SMMs is that we can increase single-ion anisotropy simply by judiciously choosing the coordination environment of the lanthanide ion [7].

Recent developments in lanthanide chemistry show that even small ligand changes can drastically influence the overall physical properties of the molecule. Supramolecular organization beyond the molecule has also a significant influence on the energy barrier. For example Ishikawa and co-workers obtained an increase of the energy barrier for Tb double decker phthalocyanine by reduction of the intermolecular interactions via

dilution with a diamagnetic homolog (i.e. $Y^{III}(Pc)_2$). Other studies have confirmed the effectiveness of the dilution technique in order to suppress QTM as well as slow relaxation dynamics of bis(phthalocyanine)-based SMMs [8]. Most studies have focused on double deckers with either unsubstituted phthalocyaninato ligands or the tetra- or octa-β-substituted analogues [9]. Sandwich type complexes with α-substitution phthalocyaninato ligands are extremely rare [10].

The study presented in this chapter, divided in two parts, focuses in the first part on the structural investigations of $FMn^{III}Pc(OCH_2CH(Bu)_2)_4$ (**1**) and $(AcO)Mn^{III}Pc(OCH_2CH(Bu)_2)_4$ (**2**) and the influence of the apical ligand on the slow relaxation of the magnetization.

The second part deals with the structural investigations and influence of the supramolecular architecture on the magnetic properties of the half-sandwich Dy complex $Dy^{III}Pc(OCH_2CH(Bu)_2)_4(AcO)(DMF)_2$ (**3**) and of the homoleptic α-substituted bis(phthalocyaninato) Dy double-decker $[Bu_4N][Dy^{III}(Pc(OCH_2CH(Bu)_2)_4)_2]$ (**4**).

IV.2. Synthesis and Characterizations of $FMn^{III}Pc(OCH_2CH(Bu)_2)_4$ and $AcMn^{III}Pc(OCH_2CH(Bu)_2)_4$

The complex $FMn^{III}Pc(OCH_2CH(Bu)_2)_4$ (**1**) was prepared by reacting 1.5 equiv of MnF_3 with 1 equiv of $H_2Pc(OCH_2CH(Bu)_2)_4$ (the synthesis of the Pc ligand is described in chapter II, section II.5) in dimethylformamide for 12 hours at reflux. After filtration of the cold solution, crystallization by slow evaporation of the mother liquor afforded crystals suitable for X-ray crystallographic analysis. $AcMn^{III}Pc(OCH_2CH(Bu)_2)_4$ (**2**) was prepared from the reaction of 1.5 equiv of Mn(III) acetate dihydrate with 1 equiv of $H_2Pc(OCH_2CH(Bu)_2)_4$ in dimethylformamide for 6 hours at reflux. Recrystallization from dichloromethane/acetonitrile (1:1) produced dark-green crystals suitable for X-ray crystallographic analysis. Both complexes are soluble in most non-polar solvents.

IV.2.1. Structural Characterization

IV.2.1.1. $FMn^{III}Pc(OCH_2CH(Bu)_2)_4$·DMF

Compound **1** crystallizes as thin green-brown needles in the triclinic P-1 space group with two molecules per unit cell. The crystal structure contains one dimethylformamide solvent molecule per Mn(III) complex. The Mn^{III} atom in complex **1** is in a slightly distorted square pyramidal environment (Figure **IV.1**). The equatorial plane is formed by four nitrogen atoms of the phthalocyanine whereas the apical position is occupied by the fluoride ligand. The average equatorial $Mn–N_{(pyrrole)}$ distance is 1.9755 Å, while the Mn-F bond length is 1.912(2) Å. The manganese atom is displaced by 0.3317 Å from the $4N_{iso}$ plane. The F-Mn-N angles are not equal; two of them are smaller whereas the other two are larger than 100° by about ±1.5°, indicating a significant breaking of the Pc ligand's four-fold symmetry. The near-planar aromatic Pc ligand units are in slipped-stack arrangements, *i.e.* the overlapping neighboring molecules in a stack are tilted out of the plane

perpendicular to the stacking *a* axis. The inter-planar spacing within a stack is 3.309 Å, and a layer structure is formed along the crystallographic *a* axis with a stacking angle of 55.0° (Figure **IV.2**). The molecules from adjacent layers are parallel towards each other. Such arrangements are also found for most of the phthalocyanine complexes especially of the unsubstituted phthalocyanine (both α and β forms) [11]. This extended arrangement leads to nearest and next-nearest Mn···Mn distances of 5.438 Å and 8.365 Å respectively (Figure **IV.3**).

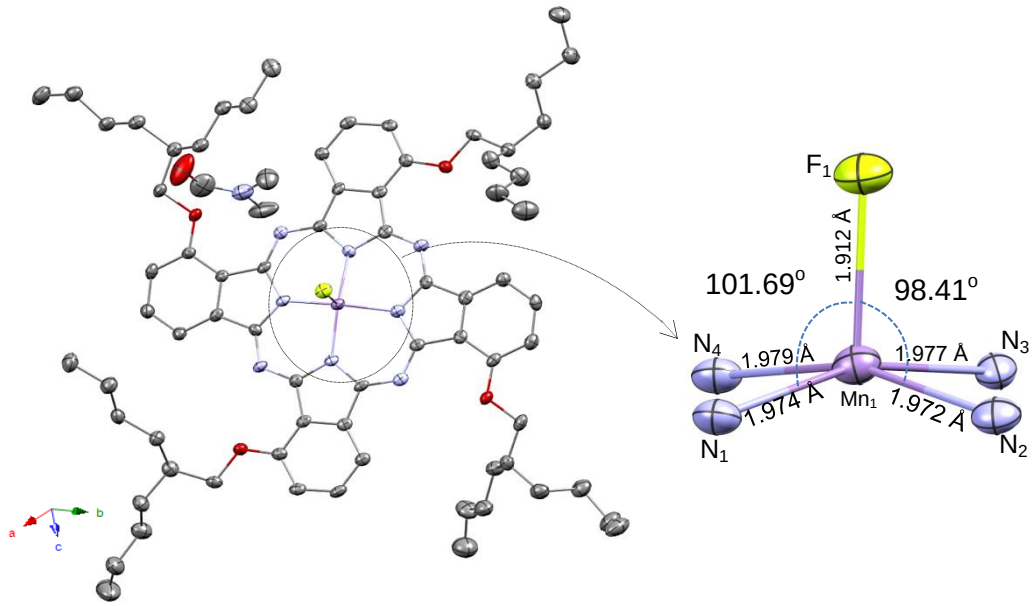

Figure IV.1. (left) Molecular structure of **1·DMF** at 120 K. Thermal ellipsoids are at 50% probability. (right) Geometric spheres of square pyramidal Mn^{III}. Hydrogen atoms are omitted for clarity. Color scheme: C gray, Mn purple, N blue, O red, F yellow.

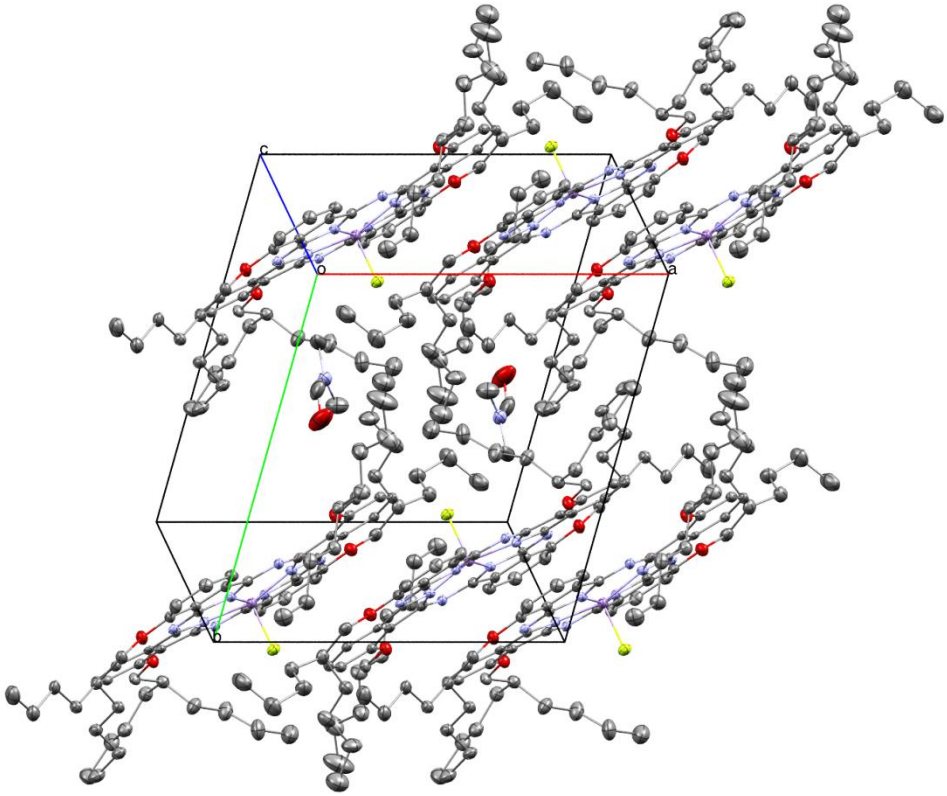

Figure IV.2. Perspective view along the *a* axis of the crystal packing of **1**. Hydrogen atoms are omitted for clarity. Thermal ellipsoids are at 50% probability.

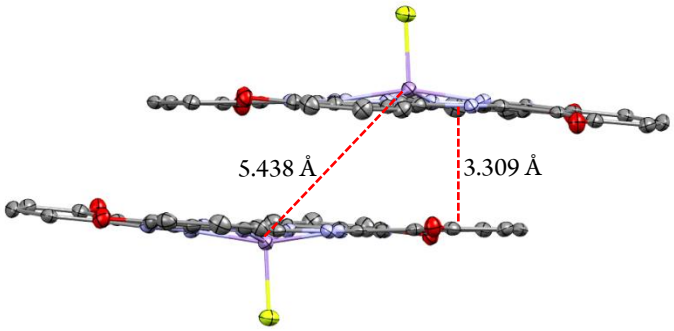

Figure IV.3. Edge-on view of **1**. Chains and hydrogen atoms are omitted for clarity.

IV.2.1.2. $AcMn^{III}Pc(OCH_2CH(Bu)_2)_4$

Suitable crystals for X-ray diffraction measurements of $AcMn^{III}Pc(OCH_2CH(Bu)_2)_4$ (**2**) were obtained by slow evaporation of a small amount of **2** in dichlormethane / acetonitrile (1:1). Compound **2** crystallizes in the monoclinic space group $P2_1/c$. The crystals contain in its asymmetric unit two complex of **2**, arranged in staggered back-to-back pairs. Similar to complex **1**, the Mn^{III} atom is in a slightly distorted square pyramidal environment (Figure **IV.4**). The equatorial plane is formed by four nitrogen atoms of the phthalocyanine whereas the apical position is occupied by the acetate ligand. The acetate ion is found to be disordered in two positions of about 50:50 abundance. The average equatorial Mn–$N_{(pyrrole)}$ distance is 1.9707 Å, while the Mn-OAc bond length is 2.028(2) Å. These and other structural parameters are presented in Table **S.IV.2.**

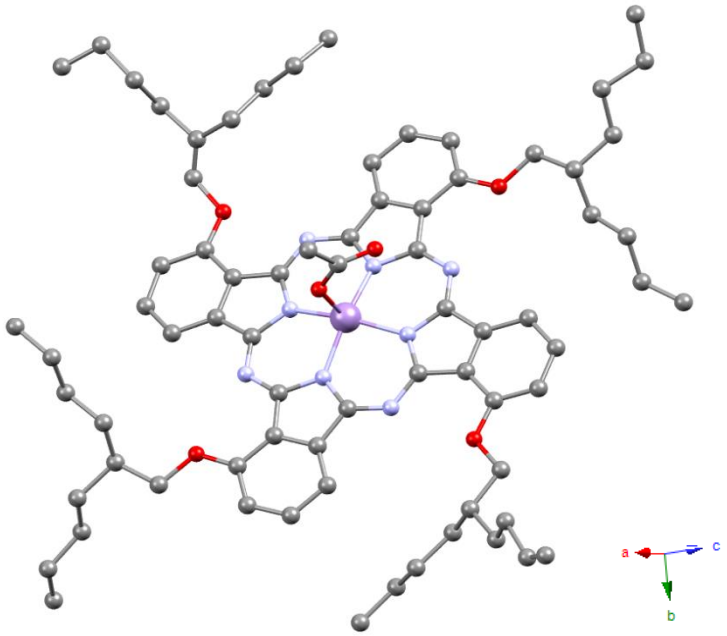

Figure IV.4. Molecular structure of **2** at 120 K. Hydrogen atoms are omitted for clarity. Color scheme: C gray, Mn purple, N blue, O red.

The Mn(III) is slightly shifted out of plane by 0.28 Å, 0.05 Å less than the Mn(III) in complex **1**. The molecules have a slipped-stack arrangement pattern, where overlapping occurs between an azamethine bridging nitrogen and the center of the molecule (Mn^{III}), of paired molecules. The distance between Pc planes is 3.533 Å, suggesting the presence of π-π interactions between ligands. The shortest distances between neighboring Mn(III) centers within a pair is 5.215 Å; hence, they would be expected to magnetically interact with each other

(Figure **IV.5**). The crystal packing of **2** consists in stacking of the tilted 'pairs' along the 2-fold axis, with a tilt angle of about 45° in-between 'pairs' (Figure **IV.6**).

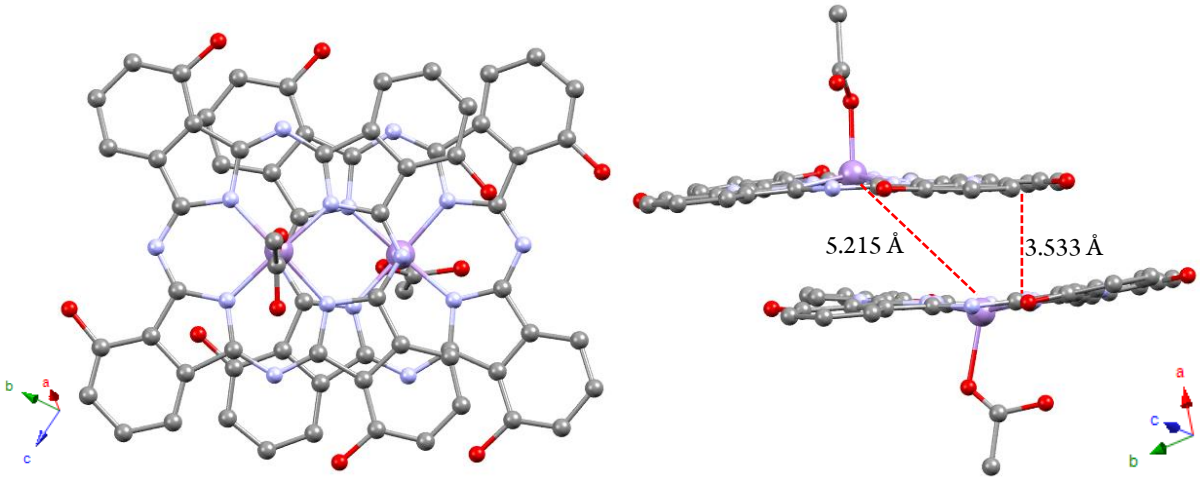

Figure IV.5. Perpendicular views (left) and edge-on view (right) of **2**. The directly overlapping molecules are shown; alkyl chains and hydrogens are omitted for clarity.

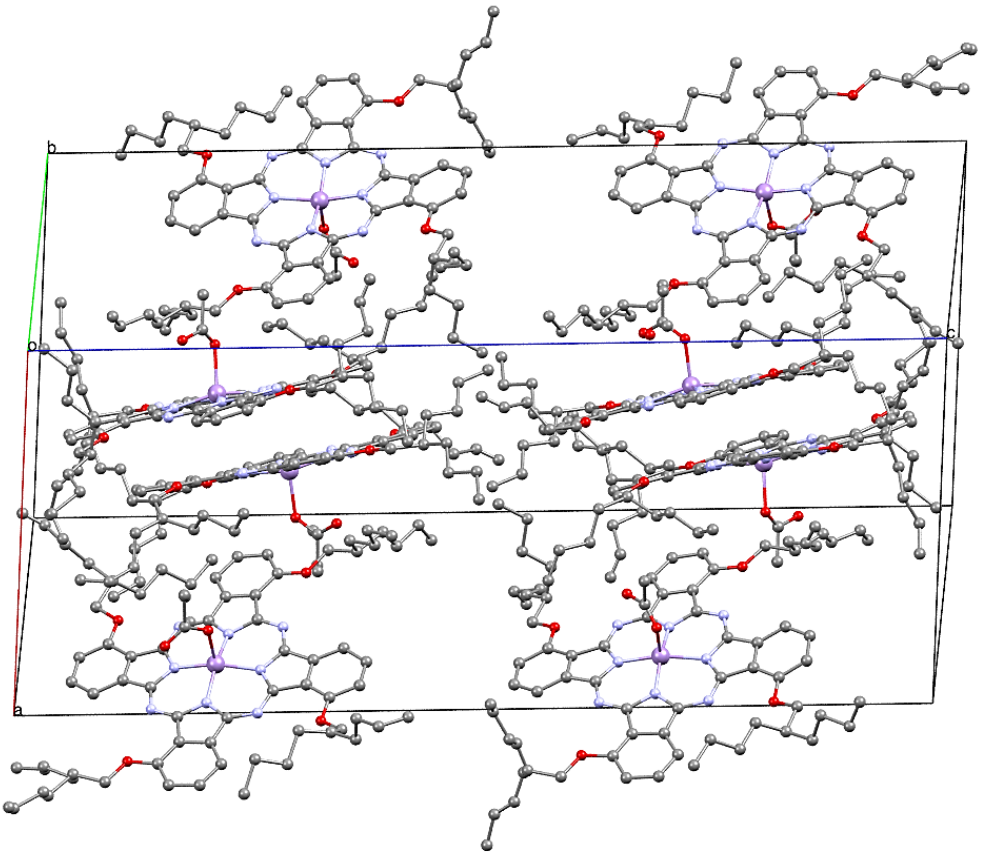

Figure IV.6. Perspective views of the crystal packing of **2** at 120 K along the crystallographic b^* axis illustrating intermolecular short contacts between molecules. Hydrogen atoms and solvent molecules are omitted for clarity.

IV.2.2. Magnetic Measurements

IV.2.2.1. $FMn^{III}Pc(OCH_2CH(Bu)_2)_4 \cdot DMF$

The temperature dependent magnetic properties of phase-pure crystalline samples of compounds **1** and **2** were measured in the range 270-1.8 K under an applied direct-current (*dc*) field of 1000 Oe (Figure **IV.6**). The value of χT at 270 K is 3.02 cm^3 K mol^{-1}, which is in good agreement with the presence of high-spin Mn^{III}

($S = 2$, $C = 3$ cm ^{3} K mol^{-1}, $g = 2$). This value remains approximately constant upon lowering of the temperature to 20 K where the χT product decreases to 2.20 cm^3 K mol^{-1} at 1.85 K. This thermal dependence reveals the presence of a second-order spin-orbit coupling, the so called zero-field splitting (ZFS). Moreover, the field dependence of the magnetization below 8 K (Figure **IV.7**, **right**) shows that the magnetization of **1** does not saturate even at 1.85 K and 7 T, consistent with the presence of magnetic anisotropy of the Mn (III) ion.

On the basis of the crystal structure where the Mn···Mn distances between paramagnetic metal centers (see crystal structure description) are too large to allow significant magnetic interactions, the magnetic data of **1** have been modeled with the following single spin Hamiltonian: $H = DS_z^2$, yielding a value for D of -2.64 cm^{-1} and $g = 2.0$. This $|D|$ value is significantly smaller than in other monometallic manganese (III) SMMs found in the literature, which display values of D ranging from -3 to -4 cm^{-1} [5].

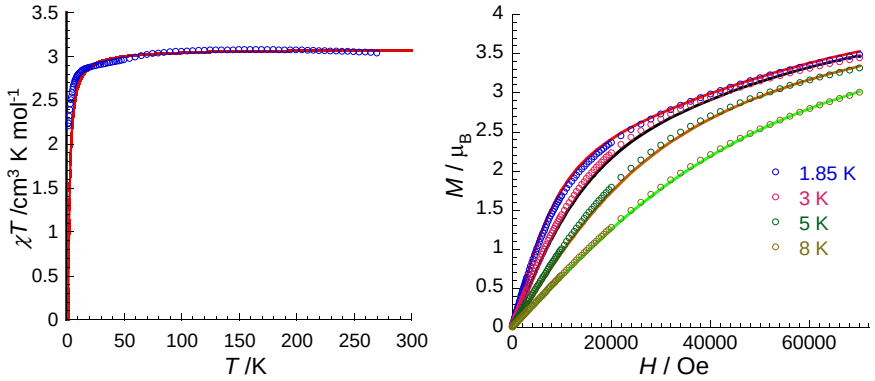

Figure IV.7. (left) Temperature dependence of the χT product at 1000 Oe and field dependence of magnetization for **1** (χ is defined as the molar magnetic susceptibility and equal to M/H; M = magnetization and H = external magnetic field). The lines are the fit discussed in the text.

The frequency-dependent out-of-phase *ac* signal (χ'') is considered as a signature for SMM properties (described in chapter I). For *ac* susceptibility measurements, an oscillating magnetic field is applied. When the magnetization vector of the molecule oscillates in phase with the *ac* field, no out-of-phase *ac* susceptibility signal is detected. The system is able to follow the ac field except when the magnetization relaxation becomes very slow. This is the case for SMMs when the temperature is lowered to a value at which the SMM or thermal barrier becomes significant compared to thermal energy (k_BT). A non-zero χ'' signal, which depends on the frequency, suggests a slow relaxation of the magnetization. Therefore, from *ac* susceptibility studies the effective energy barrier for the relaxation of magnetization can be estimated.

From the low-temperature alternating-current (*ac*) susceptibility data, **1** exhibits slow magnetic relaxation phenomena in the frequency range of 30-10000 Hz in a zero *dc* field, where in-phase (χ') and out-of-phase (χ'') components of the ac susceptibility of **1** show strong frequency dependence below 6 K (Figure **IV.8, right**). This phenomenon is suggestive of slow relaxation coming from the magnetic anisotropy of the HS Mn(III) ion of **1**.

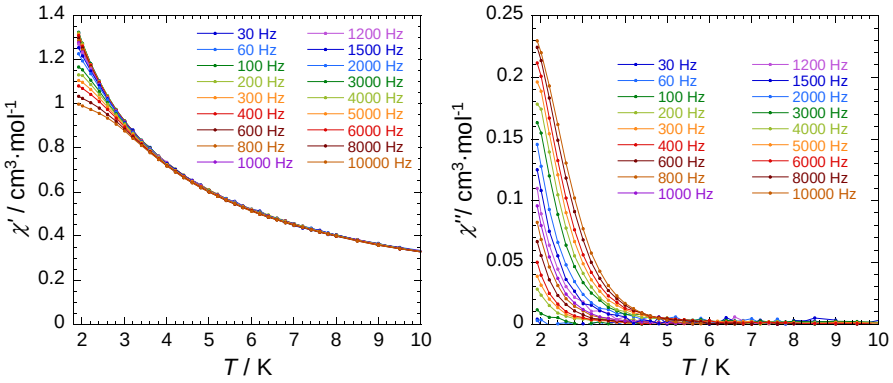

Figure IV.8. Temperature dependence of the real (χ', left) and imaginary (χ'', right) parts of the *ac* susceptibility for a polycrystalline sample of **1** at 0 Oe dc field at different frequencies between 1.85 and 10 K. Solid lines are guides.

In zero-dc field, the magnetization of complex **1** has a relaxation time that is faster than $1.6 \cdot 10^{-5}$ s at 1.9 K and its temperature dependence cannot be determined within our experimental limits (that is, with *ac* frequency up to 10 kHz and at temperatures higher than 1.9 K; Figure **S.IV.1**). To minimize the probability of magnetization relaxation by quantum tunneling pathways, the relaxation of magnetization was also studied by ac susceptibility under small *dc* fields (Figure **S.IV.2**). From the dependence of the out-of–phase χ'' component of the ac susceptibility at 1.9 K at different *dc*-field between 0 and 10000 Oe investigations, it is possible to determine the optimum field, (*i.e* 2500 Oe) where occurs a reduction of the probability of quantum tunneling relaxation (Figure **S.IV.3**). The frequency and temperature dependence of the *ac* susceptibility were measured at 2500 Oe *dc* field, as shown in Figure **IV.9.** Below 8 K, both the in-phase (χ') and out-of-phase (χ'') parts of the susceptibility (Figure **IV.9, right**) are strongly frequency dependent as typically observed in SMMs [12] under an applied field of 2500 Oe.

We were not able to see all the frequency maxima in the experimental window in order to extract the characteristic experimental time τ ($\tau_{exp} = (2\pi\nu_{exp})^{-1}$). In order to obtain τ_{exp}, we scaled the χ''/χ_0' curves (for temperatures from 1.9 to 3 K) to the χ''/χ_0' curve at 2.4 K, that exhibits a frequency maximum, by a factor of *a* (Figure **S.IV.4**). The frequency maximum at 2.4 K was multiplied by the corresponding factor *a* for each temperature (1.9 to 4 K) and the experimental time τ_{exp} was estimated.

Using *ac* frequency between 30 and 10000 Hz, the temperature dependence of the magnetization relaxation time τ was deduced from the maximum of the χ'' versus ν data ($\tau = 1/(2\pi\nu_{max})$ between 1.9 and 4 K. This is because at the frequency of the maximum of the plot, the *ac* field is in-step with the relaxation rate. Then the plot of τ versus T^{-1} was constructed and the experimental data are fitted to an Arrhenius law (Figure **IV.10**). Between 2.6 and 4 K, the $\tau(T)$ function is approximately linear as expected for a thermally activated process described by an Arrhenius law ($\tau = \tau_0 \cdot exp(\Delta_{eff}/k_B T)$ where τ is the relaxation time, k_B is the Boltzmann constant, Δ_{eff} is the energy barrier of the thermally activated regime and τ_0 a pre-exponential factor), allowing an estimation of the energy barrier of $\Delta_{eff} = 12.1$ cm^{-1} and $\tau_0 = 4.5\ 10^{-8}$ s. Obtained values are comparable with the values of the relaxation barrier and time extracted for previously reported Mn(III) mononuclear complexes [5].

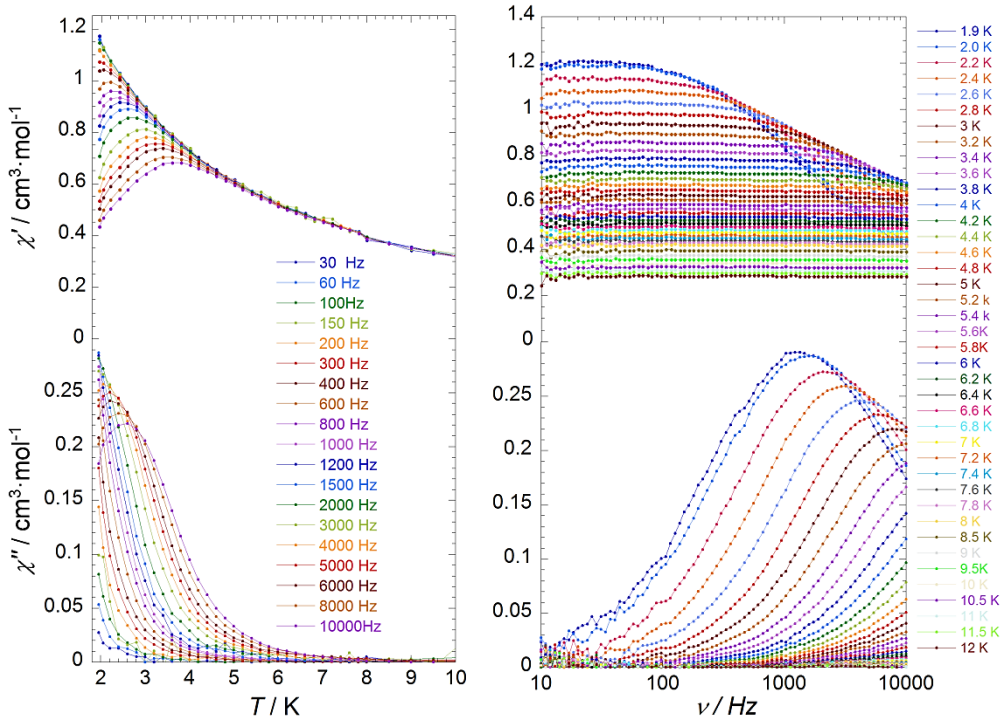

Figure IV.9. The temperature (left) and frequency (right) dependence of the in-phase (χ') and out-of phase (χ'') parts of the *ac* susceptibility, between 10 and 10000 Hz and between 1.9 and 12 K respectively, for **1** in a 2500 Oe dc field. Solid lines are visual guides.

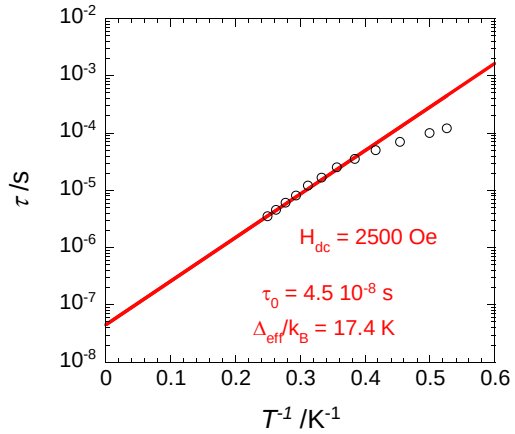

Figure IV.10. τ *vs* T^{-1} plot for **1** in 2500 Oe *dc* field. The solid line represents the best fit to the Arrhenius law.

On the basis of the Zero-Field Splitting (ZFS) values, the calculated thermal barrier is Δ_{cal} (~4|D|) ~ 10.6 cm^{-1} which is comparable slightly smaller than experimental energy barrier (Δ_{eff} = 12.1 cm^{-1}) obtained from the *ac* magnetic susceptibility measurements.

IV.2.2.2. $AcMn^{III}Pc(OCH_2CH(Bu)_2)_4$

The mononuclear complex $AcMn^{III}Pc(OCH_2CH(Bu)_2)_4$ (**2**) as well exhibits interesting magnetic properties with respect to Single-Molecule Magnet behavior. Direct current (*dc*) magnetic susceptibility data χ on polycrystalline **2** were collected in the 1.8-270 K range under an applied field of 1000 Oe and plotted as a function of temperature (*T*). A marked decrease of χ*T* is observed at low temperature. This thermal behavior could be associated with principally two phenomena: the zero field splitting (ZFS) arising from the Mn(III) ion

and/or possible intermolecular antiferromagnetic interactions between the neighboring dimer units. In comparison to *M* versus *H* data of the compound **1**, where a rapid increase in the magnetization at low magnetic fields is observed, the 'S-shaped' magnetization curves at low field for **2** could be attributed to the antiferromagetic interaction in pairs of **2**. This is also confirmed by the crystal structure, where short distances (the nearest intermolecular Mn···Mn distance is 5.215 Å) are observed. This separation is notably smaller than those observed in some dinuclear compounds (*i.e* 5.59-8.28 Å) [13]. Simultaneous fits of both the susceptibility and magnetization data were performed with the program *Phi* [14]. To model the magnetic data, the following Hamiltonian was used:

$$H = -2JS_{Mn1} \cdot S_{Mn2} + D_{Mn}(S^2_{z\,Mn1} + S^2_{z\,Mn2})$$

where *J* is the exchange interaction between Mn···Mn centers of neighboring paired molecules (Figure **IV.4**), *S* is the spin operator of the metal ion, and D_{Mn} is the uniaxial anisotropy for the Mn(III) complex.

In agreement with this, the magnetic susceptibility data (Figure **IV.11**) indicate that the Mn(III) in $AcMn^{III}Pc(OCH_2CH(Bu)_2)_4$ is in the high spin state and the best set of parameters obtained is $g = 2.0$, $D_{Mn} = -2.46$ cm $^{-1}$ and $J = -0.24$ cm $^{-1}$, where the *g* is the *g*-factor of the Mn ion and k_B is the Boltzmann constant. At room temperature, χT product of **2** reaches *ca.* 6 cm^3 K mol^{-1}, which is in good agreement with the presence of a contribution of two Mn^{III} sites ($S = 2$, $C = 6$ cm^3 K mol^{-1}, $g = 2$). Upon cooling, the χT value remains stable in the temperature range 270-110 K, and then slowly decreases to 5.6 cm^3 K mol^{-1} at around 20 K and, finally, sharply to 1.01 cm^3 K mol^{-1} at 1.85 K. This thermal behavior is typical for compounds that exhibit an antiferromagnetic interaction *J* between Mn(III) ions as well as a zero-field splitting effect induced by the uniaxial anisotropy D_{Mn} of each Mn(III) ion [15]. The field dependence of the magnetization and the *M* versus *H*/*T* plot confirm that **2** exhibits significant magnetic anisotropy below 8 K, due to the non-superimposable *M* versus *H*/*T* curves on a single master curve (Figure **IV.11, right**).

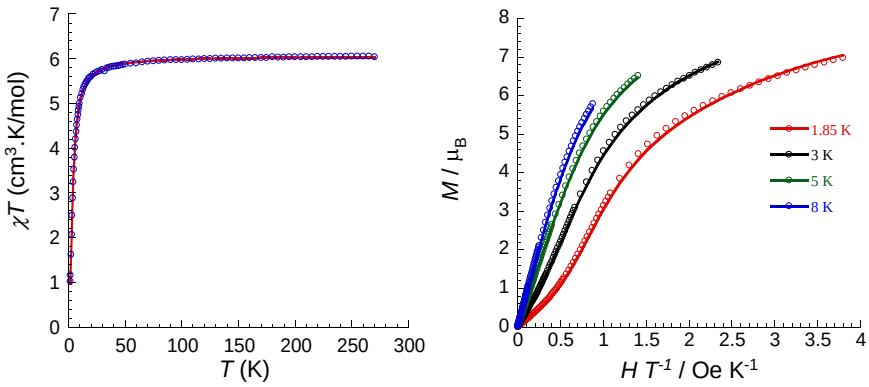

Figure IV.11. (left) Temperature dependence of the χT product at 1000 Oe and field dependence of magnetization for **2** (χ is defined as the molar magnetic susceptibility and equal to *M*/*H*; *M* = magnetization and *H* = external magnetic field). The lines are the fit discussed in the text.

To detect the slow relaxation of the magnetization, the temperature dependence of the in-phase (χ') and out-of-phase (χ'') *ac* magnetic measurements were carried out in the 1.9-10 K range at several oscillation frequencies from 30 to 10000 Hz. In contrast to compound **1**, where slow magnetic relaxation phenomena occur in the frequency range of 30-10000 Hz in a zero *dc* field, the maximum of the χ'' signals of compound **2** in zero *dc* magnetic field were observed almost at the limitation of the our experimental setup, even for the highest frequency used (ν=10000 Hz). Therefore, additional ac susceptibility measurements were performed under *dc* field (up to 2 T) at 1.9 K in order to probe the presence of fast quantum tunneling of the magnetization (Figure **IV.12**).

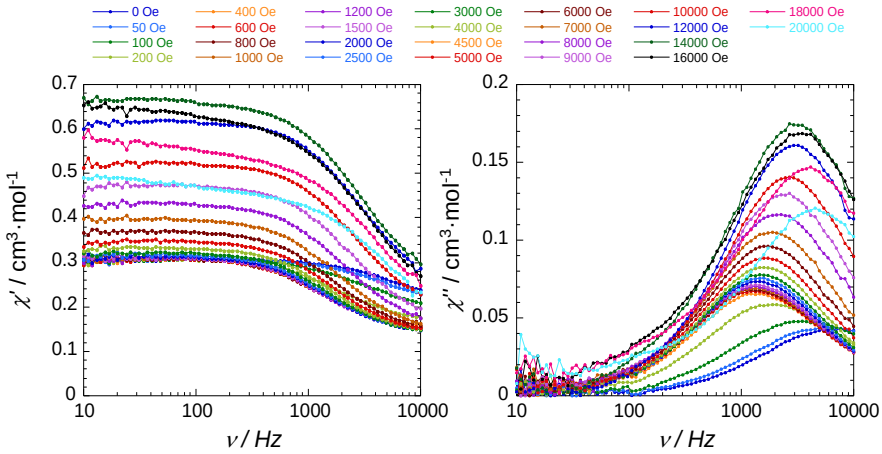

Figure IV.12. The frequency dependence of the in-phase (top), χ', and of the out–of–phase (bottom), χ'', components of the *ac* magnetic susceptibility of the compound **2** at 1.9 K in the presence of the indicated *dc* fields from 0 to 2 T.

Based on these measurements, the optimum field, for which the relaxation is the slowest, has been estimated as 1000 Oe (Figure **S.IV.5**). Indeed, in an applied field of 1000 Oe, as the temperature decreases, below 9 K the magnetic moment of the complex cannot stay in phase with the oscillating field for *ac* frequencies between 30 and 10000 Hz (strong frequency-dependent maxima occur in both χ' and χ''). In accordance, χ'' signals appeared at the corresponding temperatures, indicating SMM behavior of compound **2**. The maxima of the χ'' signal shift to higher temperature as the operating frequency increases (Figure **IV.13, left**). In order to estimate the relaxation time, τ, the maxima of the χ'' versus ν curves ($\tau = 1/2\pi\nu_{max}$) (Figure **IV.13, right**) were plotted as a function of $1/T$ (Figure **IV.14**). Between 2 and 4 K, a linear dependence of the relaxation time is observed, which obeys an Arrhenius law ($\tau = \tau_0 \cdot exp(\Delta_{eff}/k_BT)$ where τ is the relaxation time, k_B is the Boltzmann constant, Δ_{eff} is the energy barrier of the thermally activated regime and τ_0 a pre-exponential factor). From the analysis of the experimental data on the basis of an Arrhenius law, the experimental energy barrier and relaxation time were determined to be: Δ_{eff} = 7.9 cm^{-1} and τ_0 = 4.4 10^{-7} s. The extracted values of the pre-exponential factor and the activation energy (τ_0 = 4.4·10^{-7} s and Δ_{eff} = 7.9 cm^{-1}) are comparable with those previously reported for related Mn(III) SMMs [15].

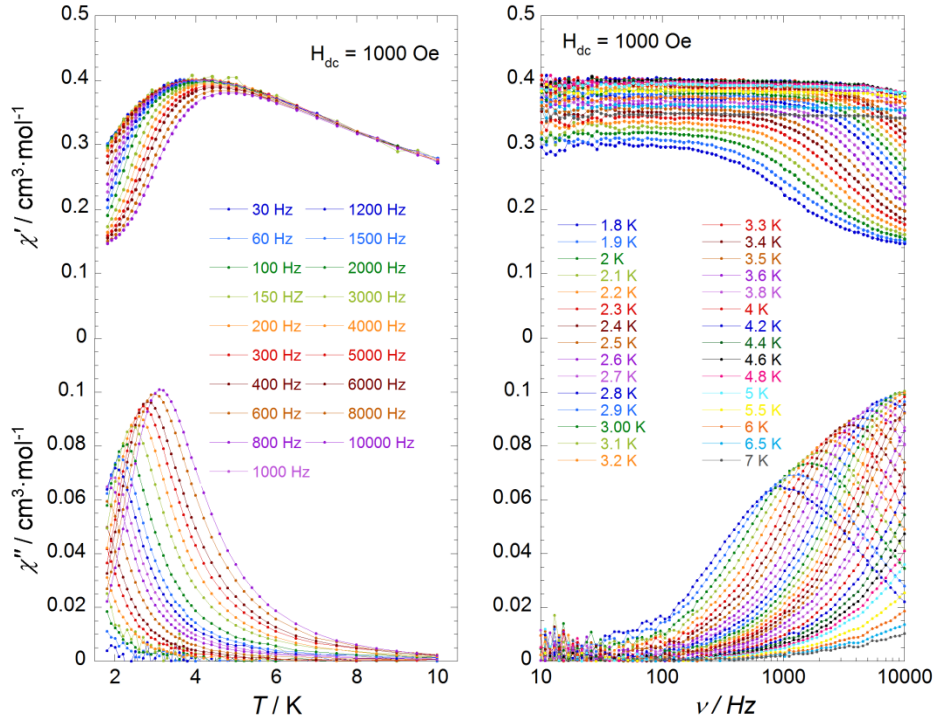

Figure IV.13. Left: The temperature dependence of the in-phase (top), χ' and of the out–of–phase (bottom), χ'', components of the *ac* magnetic susceptibility of the compound **2** at the frequency, *ν*, indicated under an external *dc* field of 1000 Oe. Right: The frequency dependence of the in-phase (top), χ' of the out–of–phase (bottom), χ'', components of the *ac* magnetic susceptibility of the compound **2** at the temperature indicated under an external *dc* field of 1000 Oe.

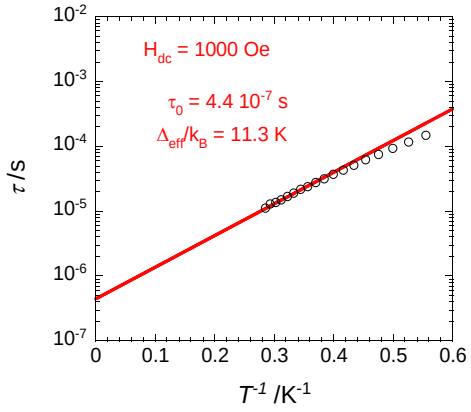

Figure IV.14. τ *vs* T^{-1} plot for **2** in 1000 Oe *dc* field. The solid line represents the best fit to the Arrhenius law.

The experimental energy barrier (Δ_{exp} = 7.9 cm^{-1}) is lower than the theoretical one (Δ_{cal} $(4|D|)$ ~ 9.84 cm^{-1}) indicating that the QTM is operative even at higher temperatures than seen in other SMM systems [5, 15, 16].

IV.3. Synthesis and Characterizations of $DyPc(OCH_2CH(Bu)_2)_4Ac(DMF)_2$ and $\{Bu_4N\}\{Dy[Pc(OCH_2CH(Bu)_2)_4]_2\}$

IV.3.1. Synthetic Strategy

In most cases, a template mechanism is used to obtain metalated monophthalocyanine derivatives, where cyclotetramerisation of the phthalonitrile (or other precursors such as phthalimide, phthalic anhydride or diiminiisoindoline) occurs in presence of a metal ion. This method has been used to prepare unsubstituted

complexes [17]. This synthetic approach is problematic in some cases, especially when avoiding of positional isomers (C_{4h}, C_{2v}, C_s, and D_{2h}) is a priority, for example when a mono-substituted phthalonitrile in 3- or 4-position is used (see Chapter II, section II.3). The synthesis of mono-phthalocyanine complexes from phthalonitrile and their derivatives suffer a number of drawbacks, the most substantial being the relatively low yields of some of the target products and/or difficulty of purification [18].

Therefore, the general synthetic approach adopted in the preparation of tetra-substituted mono-phthalocyanine lanthanide derivatives is a typical coordination reaction between a metal-free phthalocyanine and a lanthanide salt [19]. A distinctive feature of lanthanide mono-phthalocyanines compared to the complexes of most other elements is the unsaturation of the metal coordination sphere, which accounts for their existence as solvates $[Pc^{2-}Ln^{3+}X^{-}](Solv)_n$, where X^- is the counter-ion, and Solv are the external ligands (solvent or base molecules). The synthetic procedure consisted (Scheme **IV.1**) of the reaction of $H_2Pc(OCH_2CH(Bu)_2)_4$ (synthesis procedure is described in chapter II, section II.5) with a DMF solution of $Dy(CH_3CO_2)_3 \cdot 4H_2O$. The crystallizations were carried out by subjecting the filtered reaction mixtures to slow evaporation (see synthesis protocol in the Supporting Material).

Three different synthetic approaches are used for preparing the homoleptic double decker phthalocyanine complexes. I: The synthesis of Pc_2M synthons relies mostly on templating reactions, starting from the unsubstituted phthalonitrile precursor, in the presence of a strong base (e.g., DBU, alkoxides) and high-boiling solvents, such as pentan-1-ol, hexan-1-ol or octanol [20]. This template method has also been used for the synthesis of homoleptic tetra- or octa-β-substituted analogues $LnPc^{(\beta\text{-}R)4}$ and $LnPc^{(\beta,\beta'\text{-}R)8}$ [20 $^{f, g}$], and, with appreciable yields, of the protonated homoleptic α-α'-octa-substituted complexes $LnPc^{(\alpha,\alpha'\text{-}R)8}$ [20^{h}]. Microwave energy, as an alternative to conventional heating, [8] has also been used. In this way, side reactions and especially the formation of large amounts of empty phthalocyanine rings and resinification of the starting phthalogens is largely suppressed.

II. To avoid side processes typical of the template reaction, the synthesis of lanthanide bis(phthalocyanine) complexes can be accomplished by using the metal-free phthalocyanine. Synthesis of homoleptic bisphthalocyanine complexes from the ligand (H_2Pc) and lanthanide salt in high-boiling solvent is a method involving a one-pot reaction [21]. Controlling the selectivity of the reaction is often complicated in this case, because of steric factors arising in the complexation of the lanthanide mono phthalocyanine formed with the second free ligand.

III. Interaction of a free base phthalocyanine with a solvated lanthanide monophthalocyanine in high-boiling solvent in presence of base such as 1,8-diazabicyclo[5.4.0] undec-7-ene (DBU)) [22]. This method facilitates the reduction of the number of the byproducts and an increase of the yield of the target product. Following this method, it is possible to obtain good yields of heteroleptic double decker and triple decker phthalocyanine complexes simply by changing the ratio of metal-free phthalocyanine to solvated lanthanide mono-phthalocyanine [23]. Following to this approach, we synthesized the anionic double-decker complex salt

{TBA}{Dy[Pc(OCH$_2$CH(Bu)$_2$)$_4$]$_2$} (**4**) and its neutral radical form {Dy[Pc(OCH$_2$CH(Bu)$_2$)$_4$]$_2$}^{0} (**4***) by boiling the corresponding H$_2$Pc(OCH2CH(Bu)$_2$)$_4$ and DyPc(OCH$_2$CH(Bu)$_2$)$_4$Ac(DMF)$_2$ (**3**) in 1-octanol in the presence of DBU, followed by treatment with and without an small excess of tetrabutyl ammonium acetate ([TBA][OAc]) (see synthesis protocol in Supporting Material).

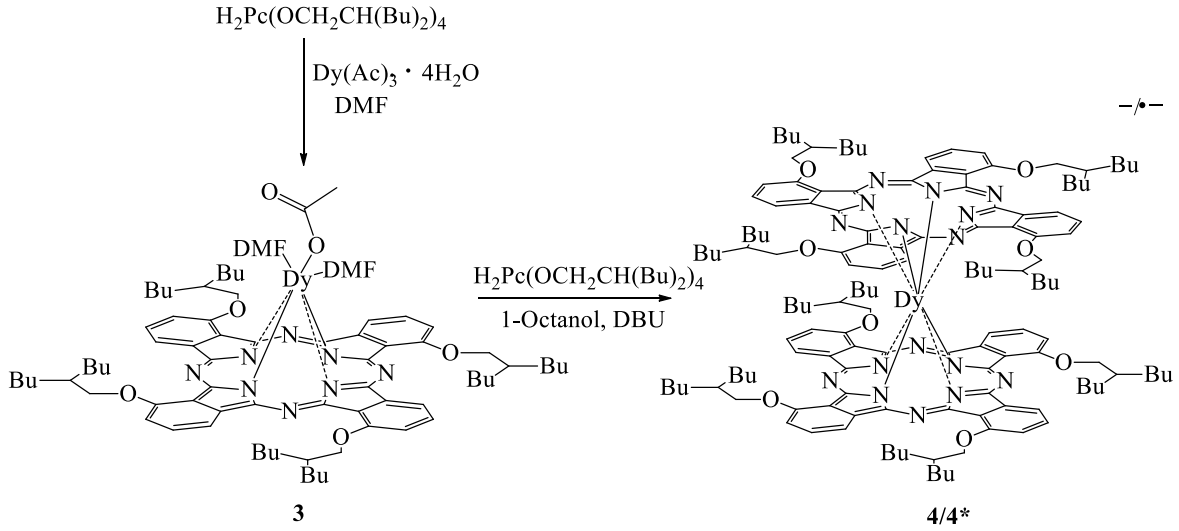

Scheme IV.1. Synthetic pathway for the preparation of solvated monophthalocyanine dysprosium acetate (**3**) and of the dysprosium phthalocyanine double decker in its anionic (**4**) and radical (**4***) forms.

Due to the four α-substituents in H$_2$Pc(OCH$_2$CH(Bu)$_2$)$_4$ in positions 1, 8, 15 and 22, the two possible cofacial orientations of the phthalocyanine rings gives rise to two diastereoisomers with C_{4h} and C_4 molecular symmetry. But because of the bulky branched alkoxy chains around the Pc core and their huge chemical hindrance in a sandwich type complex (short inter-planar Pc core-to-core distance), the most symmetrical isomer of C_{4h} symmetry is sterically favored. No isomeric by-product could be observed. By X-ray diffraction analysis, (see below), only the isomer of C_{4h} symmetry was observed. Despite several attempts to check the unit cell parameters of other crystals from the same sample, no variations in unit cell parameters could be detected. To the best of our knowledge, this is the first regiospecific formation of a rare-earth double decker complex of C_{4h} molecular symmetry.

IV.3.2. Spectroscopic Characterization

IV.3.2.1. FT-IR Spectroscopic Analyses of 4 and 4 *

The IR spectra of the sandwich-type rare-earth Ln(Pc)$_2$ complexes were studied in detail, as a helpful tool (in conjunction with other physicochemical measurements) to identify distinct forms of these compounds [33^c]. There are some identified distinctions in the IR spectra between different forms of double decker phthalocyanines (*i.e* anionic and π-radical forms). Careful analysis of the IR spectra of **4** and **4*** leads to the identification of some differences. An intense band at 1306 cm^{-1} together with an medium band at 1360 cm^{-1} was observed in the IR spectrum of **4***, suggesting the presence of a neutral compound in which one Pc ring is a mono anion π-radical Pc$^{\bullet -}$ (Figure **IV.15**). Depending on the lanthanide ion, the IR characteristic band for Pc$^{\bullet -}$ is located in the region of 1300 to 1320 cm^{-1}, and there is a less intense band around 1360-1380 cm^{-1} [21^e, 33].

These characteristic bands are clearly missing in case of the anionic form **4.** The characteristic IR bands of the TBA in **4** are hindered by the corresponding IR bands of the substituents on the Pc core.

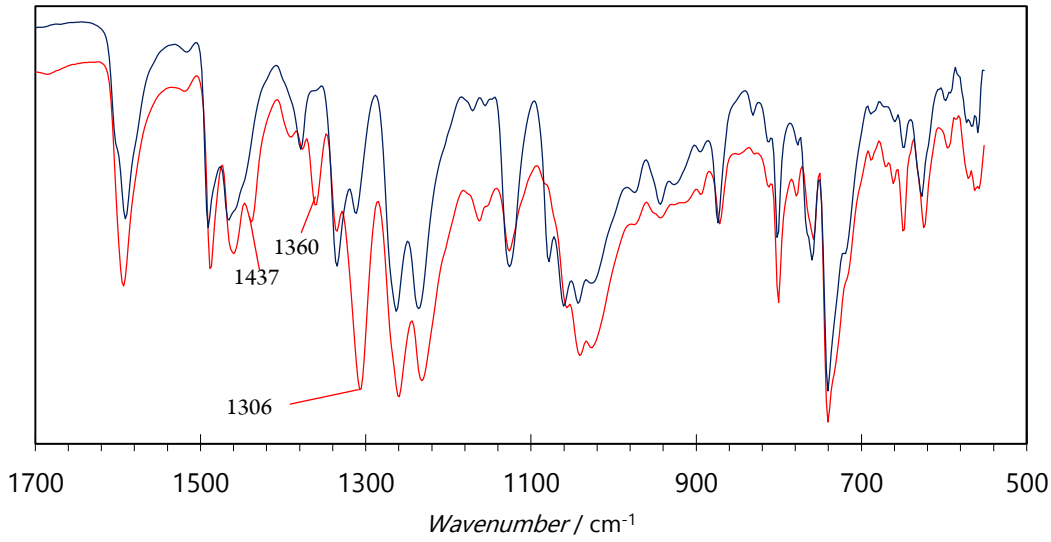

Figure IV.15. FT-IR spectrum of **4** (blue) and **4*** (red) at room temperature.

IV.3.2.2. Absorption Spectroscopy Analyses

The electronic absorption spectra of **3**, **4** ('blue form') and **4*** ('greenish-blue form') were measured in acetone and are presented in Figure **IV.16.** The spectrum of **3** presents characteristic B (Soret) and Q bands at 330 and 700 nm respectively, which are typical for the metalated phthalocyanines (see also chapter II). The Q-band of **3** is assigned to a pure single $(\pi)a_{1u} \rightarrow (\pi^*)e_g$ (HOMO→LUMO) transition Figure **IV.17.**

In contrast, the spectrum of **4** is characteristic of a double decker phthalocyanine, which shows a twin peak including a strong maximum absorption band around 648 nm and a medium one at 704 nm. The split of the Q band is common for the blue form $Ln(Pc)_2^-$ and it has been reported that the magnitude of the splitting significantly increases with decreasing ionic radius of the central metal ion [24], indicating that the π–π interaction between the macrocycles becomes stronger with decreasing interplanar distance. In fact, appearance of the split in the Q absorption band is also a result of the decrease of the molecular symmetry caused by a torsion angle between phthalocyanine cores. Therefore, the $\pi(a_{1u})$ HOMO in a **3** will be split into antibonding $\pi(a_2)$ and bonding $\pi(b_1)$ orbitals in the new molecular orbitals of **4**. Likewise, $\pi(a_{2u})$ and $\pi(e_g)$ in a monomer will be reorganized to a set of bonding $\pi(a_1)$ and antibonding $\pi^*(b_2)$ orbitals and a set of bonding $\pi(e_1)$ and antibonding $\pi(e_3)$ orbitals, respectively [25]. Accordingly, the Q-band for the monomer will be split into two bands, in the double-decker: of the four possible transitions derived from a_{1u}-to-e_g (Q-band) transitions, $a_2 \rightarrow e_1$ and $b_1 \rightarrow e_3$ transitions are dipole-allowed.

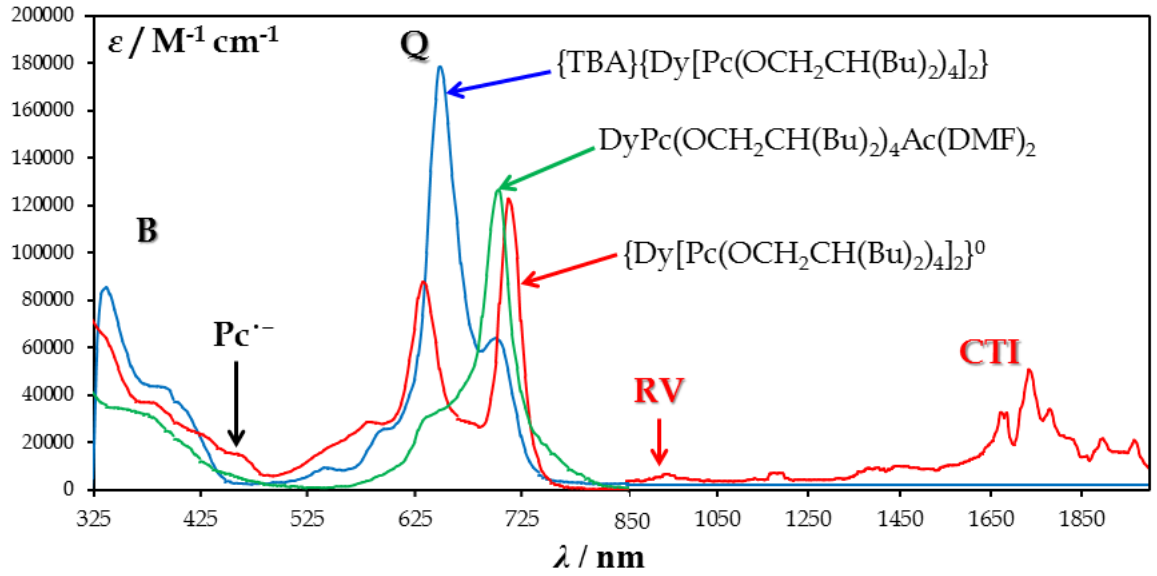

Figure IV.16. Electronic absorption spectra (5 μM in acetone) of **3** (green) **4** (blue) and **4*** (red).

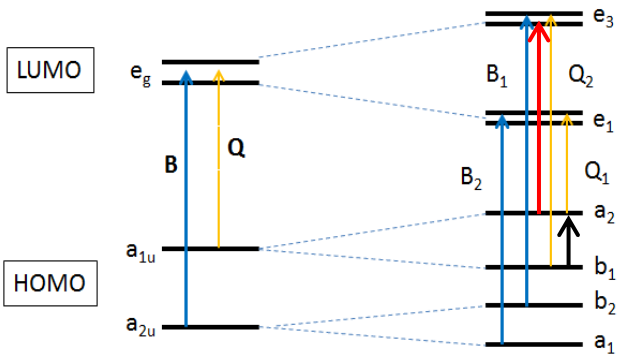

Figure IV.17. Schematic molecular orbital diagrams for **3** (left) and **4** (right).

In comparison with the **4** homolog, while the absorption bands at 460 and 910 nm and the CTI transitions (charge transfer inter-valence band, above 1400 nm) are clearly missing, the spectrum of **4*** includes a rich spectrum in the Uv-Vis and NIR. The longest wavelength band, previously assigned to an intramolecular charge transfer from one Pc ligand to another radical-containing Pc ligand, suggests that the hole is localized on one of the Pc rings [26]. However, since it was established that the hole is delocalized over both Pc rings [27], this band is now being assigned to an electronic transition from a bonding orbital constructed from the HOMO of each Pc ring to a semioccupied antibonding orbital (intervalence, $b_1(\pi) \rightarrow a_2(\pi^*)$, black arrow, Figure **IV.17**). The 460 and 944 nm bands correspond to the RV ('red valence', $a_2(\pi) \rightarrow e_3(\pi^*)$ transition red arrow in Figure **IV.17** and is characteristic of a π-radical-anion band for bis(phthalocyaninato) rare-earth (III) complexes [21a, b]. The Q band corresponds to the $e_1(\pi^*)1 \leftarrow a_2(\pi)$, $e_3(\pi^*) \leftarrow b_1(\pi)$ excitation.

IV.3.3. Cyclic Voltammetry Characterization

In order to characterize the electronic structure of metal-free Pc, **3, 4** and **4***, a cyclic voltammogram was recorded within the electrochemical window of CH_2Cl_2 with a platinum disk electrode in the potential range from –

2.4 to 1.5 V (vs. Fc^+/Fc). The electrochemical behavior of metal free phthalocyanines is characterized by three quasi-reversible oxidation waves and two reversible reduction waves in the cyclic voltammograms between −2.25 and 1.25 V vs. Fc^+/Fc. This redox behavior is very similar with those of the compound $H_2Pc(OCH_2CHBuHex)_4$ described in Chapter **3**, with no significant shift of the redox-potentials (Figure **IV.18**).

For compound **3**, three oxidations are observed, of which the last two are almost superposed on the CV. The rest potential of **3** has been identified at -0.33 V with respect to the Fc^+/Fc. They were observed at -0.08, + 0.38 and + 0.52 V versus Fc^+/Fc. Scanning cathodically, the complex **3** displays three reduction processes as well, a first at -1.11 V, a second (poorly defined) at around -1.54 V and a last (very well expressed) at -1.66 V. The full list of half-wave potentials is given in Table **IV.1**.

Table IV.1. Half-wave redox potentials for metal-free Pc, **3, 4** and **4*** in dichloromethane containing 0.1 M $TBAPF_6$

Compound	Ox_1	Ox_2	Ox_3	Red_1	Red_2	Red_3	E_{gap} (eV)
Metal free Pc	+0.12	+0.29	+0.77	-1.31	-1.71	-	1.43
3	-0.08	+0.38	+0.52	-1.11	-1.54[a]	-1.66	1.03
4	-0.33	+0.014	-	-1.57	-	-	1.24
4*	-0.23	+0.73	+0.98	-0.59	-	-	0.36

[a] These values are approximated since this redox process was poorly defined in the experimental conditions; $E_{1/2}$ values for quasi-reversible processes were determined using the relation $E_{1/2}= (E_p^a + E_p^c)/2$; $E_{gap} = E_{HOMO}-E_{LUMO}$; $E_{HOMO}=[(E_{ox} - E_{1/2(ferrocene)})+4.8]$ eV; $E_{LUMO}=[(E_{red} - E_{1/2(ferrocene)}) +4.8]$ eV;

While the cyclic voltammograms of all neutral double-decker compounds of tervalent rare earths $[LnPc_2]^0$ reveal two quasi-reversible one electron oxidations and up to five quasi-reversible one-electron reductions [28], in our case the electrochemical behavior of compound **4** (blue, or anionic form) consists of two quasi-reversible one electron oxidations and one quasi-reversible one electron reduction under the present conditions (Figure **IV.18**) and (see Scheme **IV.2**). The rest potential of **4** has been identified at -0.40 V with respect to the Fc^+/Fc. Since the oxidation state of the central trivalent rare earth ion does not change, these processes are due to successive removal or addition of electrons from or to the ligand-based orbitals. The first and second oxidation waves were found to be at -0.33 and +0.014 V versus Fc^+/Fc. These values are very close to previously reported oxidation potentials for $[TBA][Pc_2Tb]$ where the first and second oxidation is at −0.40 (O_{x1}) and +0.02 V (O_{x2}) respectively [29]. While the reduction process for similar anionic analogs displays two reduction waves in the range 1.5-2 V [29, 30], compound **4** shows only a single quasi-reversible one electron reduction process at -1.57 V, a value which is exactly the same as for $[TBA][Pc_2Tb]$ [29].

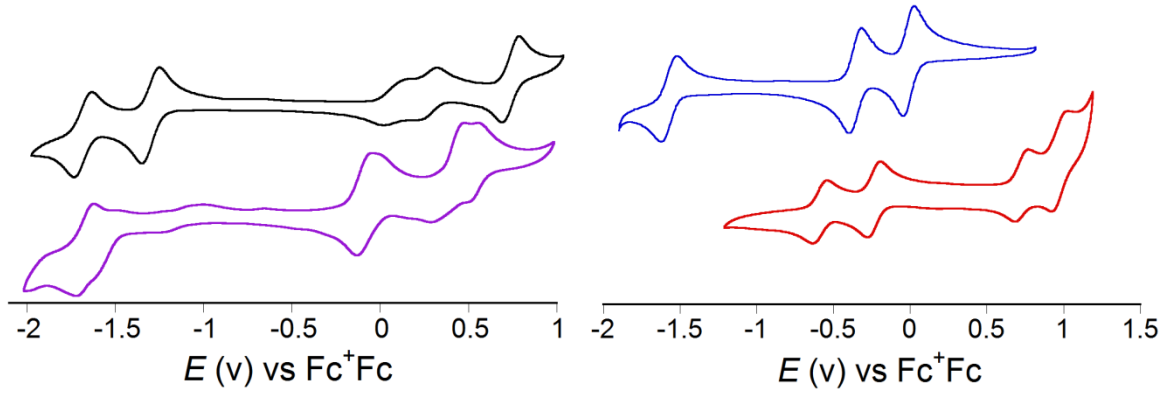

Figure IV.18. Cyclic voltammograms of free ligand (black), compound **3** (cyan), **4** (blue) and **4*** (red) in DCM containing 0.1 M $TBAPF_6$ at 0.1 V/s scan rate.

$$[Dy(Pc(OCH_2CH(Bu)_2)_4)_2]^{2-} \overset{R_1}{\rightleftharpoons} [Dy(Pc(OCH_2CH(Bu)_2)_4)_2]^{-} \overset{O_1}{\rightleftharpoons} [Dy(Pc(OCH_2CH(Bu)_2)_4)_2]^{0}$$

$$\Big\Updownarrow O_2$$

$$[Dy(Pc(OCH_2CH(Bu)_2)_4)_2]^{+}$$

Scheme IV.2. The one-electron redox processes of **4**

The first reduction potential is slightly cathodically-shifted from -1.11 V for **3** to -1.57 V for **4.** These redox potentials indicate a noticeable destabilization of complexes **4**, since less energy is required for the oxidation and more for the reduction processes. As the first oxidation step and first reduction step involve the HOMO and LUMO orbitals of the molecule, respectively, the energy difference between these two redox processes for **4** corresponds to its electrochemical molecular band gap. With $E_{1/2}(Fc^+/Fc)$ at 4.80 eV below vacuum, the first oxidation and reduction potentials correspond to E_{HOMO} and E_{LUMO} levels of - 4.26 and -3.02 eV, respectively, yielding an electrochemical band gap of 1.24 eV. This value its very close to earlier reported band gap values for the anionic form of the other unsubstituted lanthanide double decker phthalocyanines [28, 30], this suggests that the tetra α-substituents do not influence the redox properties of the molecules. The presented redox potential values reflect the energy necessary for the transition of the one electron from the HOMO to the LUMO of **4** and should correlate with the lowest energy optical transition in its electronic absorption spectrum.

The electrochemistry of **4***, in the same conditions, differs from its anionic form **4** and from previously investigated double decker lanthanide phthalocyanines [28]. While, as was mentioned above, the neutral double-decker compounds of tervalent rare earths exhibit up to five quasi-reversible one-electron reductions, the compound **4*** exhibits one quasi-reversible one electron reduction and tree quasi-reversible one electron oxidation processes. The rest potential of **4*** has been identified at -0.54 V with respect to the Fc^+/Fc. The half-wave potential for reduction is located at $E_{1/2}$ = -0.59 V, while the first oxidation wave is seen at $E_{1/2}$ = -0.24 V, and the second and third are located at 0.72 and 0.98 V *vs* Fc^+/Fc respectively. The measured potentials are listed in Table **IV.1**. The band gap is E_{gap} = 0.36 eV, much narrower than for the phthalocyanine complexes,

especially than its anionic homologue, E_{gap} = 1.24 eV, but accords well with previously reported results for bis(phthalocyaninato)rare-earth radical compounds [28c]. The narrow energy gap suggests that radical **4*** could have potential as molecular semi-conductor.

IV.3.4. Structural Characterization

IV.3.4.1. $DyPc(OCH_2CH(Bu)_2)_4Ac(DMF)_2$

Crystals of **3** suitable for X-ray characterization were grown by slow evaporation in their DMF solution, thereby allowing for the elucidation of the structure, which is illustrated in Figure **IV.19.** Compound **3** crystallizes in the monoclinic $P2_1/c$ space group with one molecule ($[PcDyAc](DMF)_2$) per asymmetric unit. In monophthalocyanine derivative **3**, the coordination geometry is a slightly distorted square antiprism. The donor atoms consist of the four isoindole nitrogens ($4N_{iso}$) of the phthalocyanine ring, two oxygen atoms of one acetate anion, and two oxygen atoms of two dimethylformamide molecules. The four Dy-N_{iso} bond distances range from 2.397(6) to 2.411(5) Å with a mean value of 2.399(7) Å. The Dy-$OAc_{1,2}$ bond lengths are 2.438(5) and 2.401(5) Å whereas the Dy-$ODMF_{1,2}$ separations equal 2.375(5) and 2.392(5) Å (Table **S.IV.3**)**.** The displacement of the dysprosium ion with respect to the $4N_{iso}$ mean plane is 1.36 Å. The phthalocyanine deviates strongly from planarity. It is convex in shape (Figure **IV.19, right**). With respect to the $4N_{iso}$ mean plane of the phthalocyanine ring, the following can be noted: the phenyl rings are bent away from the $4N_{iso}$ mean plane at angles that range from 3.05 to 9.71°. Despite the very large deviations from planarity, the average bond distances found within the four crystallographically independent isoindole moieties are not significantly different from those present in H_2Pc [31a] and other metallo-phthalocyanine complexes [31 b,c,d].

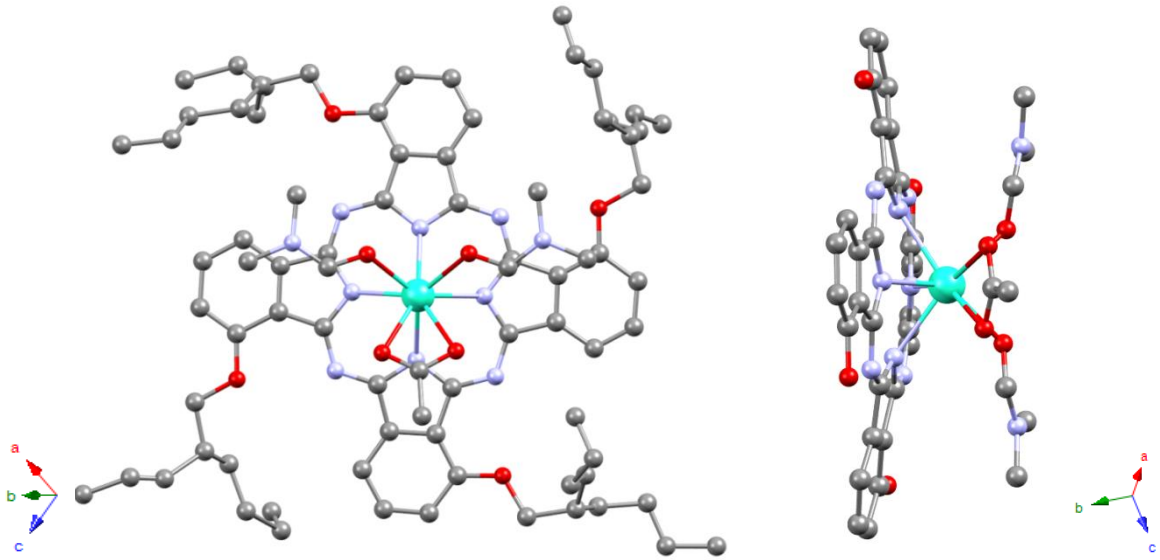

Figure IV.19. (left) The structure of the complex **3** at 120 K. (right) perspective side view of **3** illustrating the convex shape. Hydrogen atoms are omitted for clarity. Color scheme: C gray, Dy emerald, N blue, O red.

The molecules of **3** are organized in columns along the *b* axis in a slipped-stack arrangement (Figure **S.IV.6**) where the closest Pc-Pc distance is 6.515 Å. Additionally the tilted columnar stacks show a layered structure along the *a* axis, with a stack-to stack distance of 16.476 Å. No solvent molecule in the crystal structure

was found. Due to some thermal agitations at the end of the chains, a few carbon atoms of the chains with positional disorder were found. In order to fix those carbons in a definite position, some restrains were used.

IV.3.4.2. $\{Bu_4N\}\{Dy[Pc(OCH_2CH(Bu)_2)_4]_2\}$

One of the origins of the coordination variability of the double decker phthalocyanines is the stability of various valence states. It is known that some tetrapyrrole (mainly, Pc or porphyrin) based M^{III} double-decker complexes are stable with an unpaired electron in their ligand π-orbital. Because the complexes are composed of one Ln^{III} ion and two dianions of tetrapyrrole rings (total net charge -1), in the absence of an external cation, a one-electron oxidation of the ligand is required for neutrality. In order to obtain single crystals of the tetrabutylammonium salt $[TBA][Dy\{Pc(OCH_2CH(Bu)_2)_4\}_2]$ (**4**) suitable for X-ray measurements, several attempts of crystallization were done by changing the crystallization procedure (i.e. slow evaporation, liquid-liquid diffusion, vapor diffusion). Thus, we managed to obtain single crystal by slow evaporation of a 1:1 dichloromethane/acetone solution containing the tetrabutylammonium salt $\{Bu_4N\}\{Dy[Pc(OCH_2CH(Bu)_2)_4]_2\}$. The product **4** obtained by this procedure was identified to be the anionic form containing tetrabutylammonium as a cation, as revealed by means of a full set of physicochemical analyses: UV/vis/NIR spectroscopy, elemental analysis, magnetic susceptibility measurements and mass spectroscopy. Unfortunately, we could not get a crystal structure of compound **4** because of its weak diffraction at the work potential of our Bruker APEX II Quasar diffractometer. This setback made us do more attempts of crystallization involving different solvents.

IV.3.4.3. $[Dy\{Pc(OCH_2CH(Bu)_2)_4\}_2]^0$ (**4***)

By serendipity, we could crystallize a green-bluish form of the dysprosium double decker phthalocyanine starting from its tetrabutylammonium salt $\{Bu_4N\}\{Dy[Pc(OCH_2CH(Bu)_2)_4]_2\}$ (**4**). Suitable crystals for X-ray measurements were obtained by slow diffusion of methanol into a DMF solution of compound **4**. No counter anion could be found in the crystal structure; neither could we prove the protonated form of the Pc. This intriguing behavior is in line with other double decker phthalocyanine derivatives [18[b], 32]. Based on the UV-Vis measurements of compound **4** and this cation-free variant (**4***) it was possible to detect for **4*** that there is a weak characteristic absorption band attributed to $Pc^{\bullet-}$ at around 460 nm (Figure **IV.16**). In contrast to the IR spectrum of **4** (blue form), an additional strong band at 1306 cm^{-1} together with a medium band at approximately 1360 cm^{-1} were observed for this green-bluish form **4***, which, according to previous reports on double decker phthalocyanines, indicates the presence of an unpaired delocalized electron [33, 21[e]]. Thus the crystal structure of the green-bluish form **4*** is attributed to a one electron ligand-oxidized, non-protonated structure $[Dy\{Pc(OCH_2CH(Bu)_2)_4\}_2]^0$.

The compound **4*** crystallized in the triclinic space group P-1 with one molecule per asymmetric unit. The molecular structure of **4*** is shown in Figure **IV.20**.

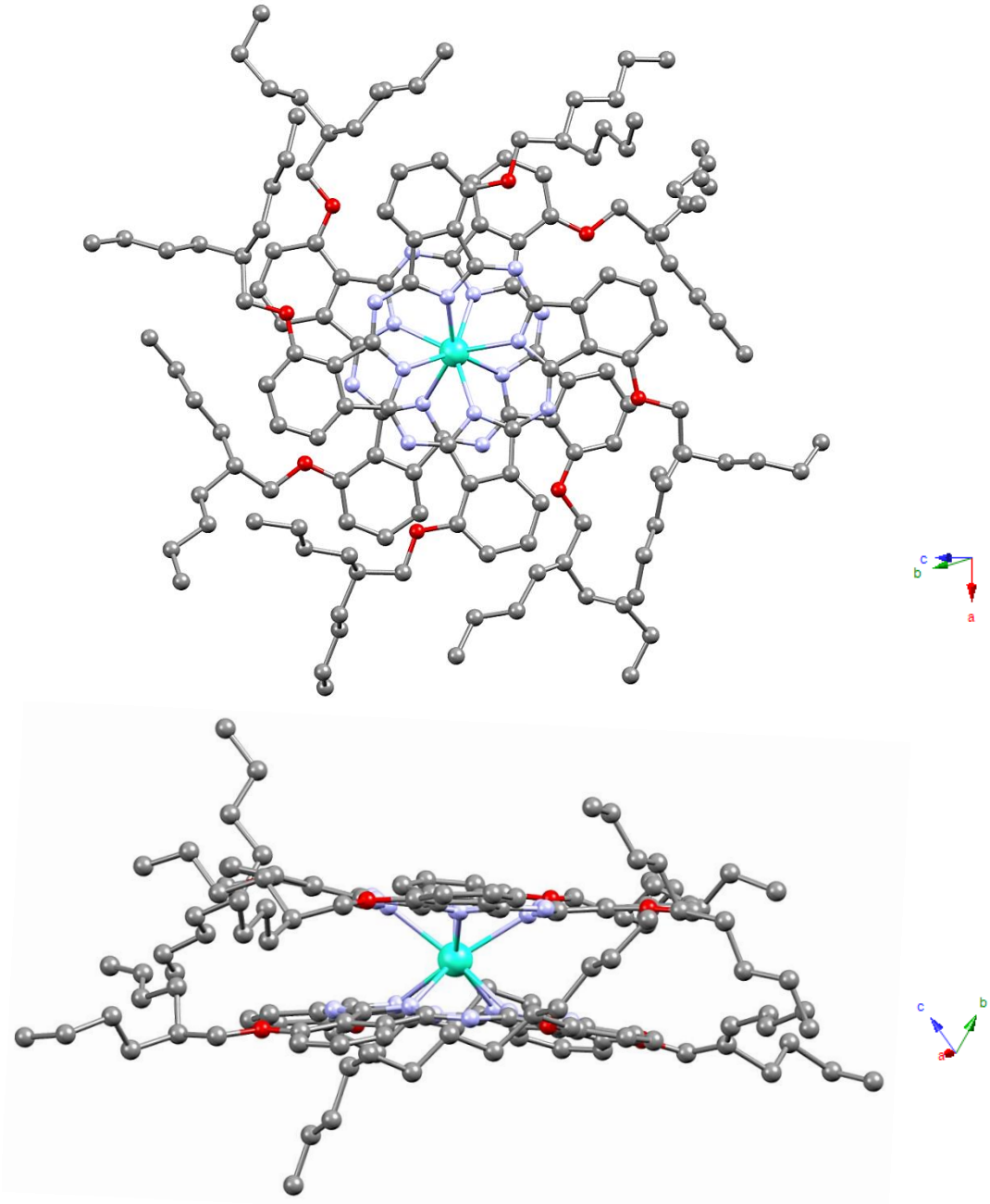

Figure IV.20. Molecular structure of the C_{4h} isomer of $[Dy\{Pc(OCH_2CH(Bu)_2)_4\}_2]^0$ (**4***) viewed along *a* axis (top) and viewed from the side (bottom). Color scheme: C gray, Dy emerald, N blue, O red.

The dysprosium center is eight-coordinated, bound to the four isoindole nitrogen atoms of the two tetra-α-substituted phthalocyaninato ligands (each of which has four 2-butylhexyloxy groups at the α positions) and adopts a slightly distorted square-antiprismatic structure around the metal center. The average twist angle, defined as the rotation angle of one macrocycle away from the eclipsed conformation of the two macrocycles, was found to be 39.4° (φ), very close to the value of 40.9° previous reported for a neutral Dy^{III} double decker [34[a]]. Like the structures of many tetrapyrrole double-decker complexes, [34[b,c,d,e]] the two ligands are not planar but saucer-shaped. The dysprosium ion lies almost in the center between two $4N_{iso}$ mean planes of the two $Pc(OCH_2CH(Bu)_2)_4$ rings (B) 1.377 *vs* (C) 1.365 Å (Figure **IV.21**). The ring-to-ring separation between the two phthalocyanine ligands, as defined by the two $4N_{iso}$ planes, thus amounts to 2.80 Å (A) (Figure **IV.21**).

It was reported that the inter-planar distances are linearly dependent on the ionic radii [20[a]]. Our values are in line with other values of the earlier reported double decker lanthanide complexes [20]. Due to the rotation angle between the macrocycles, the parallel-displaced π-π interaction distance between Pc core benzene rings is 3.3 Å.

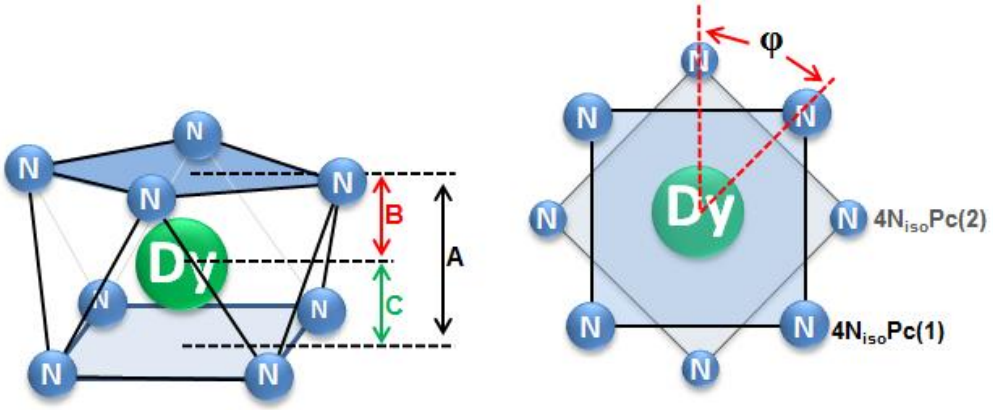

Figure IV.21. Schematic illustration of the square antiprism formed by the Dy complexes. A, B, and C represent the $4N_{iso}Pc(1)$– $4N_{iso}Pc(2)$, $4N_{iso}Pc$ (1)–Dy, and $4N_{iso}Pc(2)$–Dy distances, respectively. Stacking angle between $4N_{iso}Pc(1)$ and $4N_{iso}Pc$ (2) is expressed as φ.

The C-N bond length between the *meso*-nitrogen and neighboring carbon atoms is between 1.331-1.339 Å. No deviation from this length range was observed, as reported for the protonated form of a mixed Tb double decker complex, where a C-N distance of 1.36 Å was observed at a protonated *meso*-nitrogen [20[h]]. According to this, we could not identify something similar as above and this suggests that the compound **4*** is not protonated.

These data together with other structural parameters for **4*** are summarized in Table **S.IV.4**. The bulky four regularly disposed branched α-substituents (at the 1,8,15,22-positions), give rise to C_{4h} molecular symmetry. Indeed, as can be seen from Figure **IV.21,** the compound **4*** exhibits a pinwheel-like S_8 symmetry in the solid state. Such kind of symmetry has been reported earlier in a similar α-substituted double decker $[Y^{III}\{Pc(\alpha\text{-}OC_5H_{11})_4\}_2]$ [21[e]].

In the crystal, the molecules of $[Dy\{Pc(OCH_2CH(Bu)_2)_4\}_2^{\cdot-}]^0$ are stacked in tilted columns alternately along the 2-fold axes. The separation between the molecules in these columns is equal to 15.630 Å. A crystal-packing diagram of **4*** is shown in Figure **IV.22**. The shortest intermolecular Dy···Dy distance was determined to be 10.959 Å. Each dysprosium center of **4*** is rather well separated from neighboring molecules due to the four 2-butylhexyloxy groups of the Pc ligands.

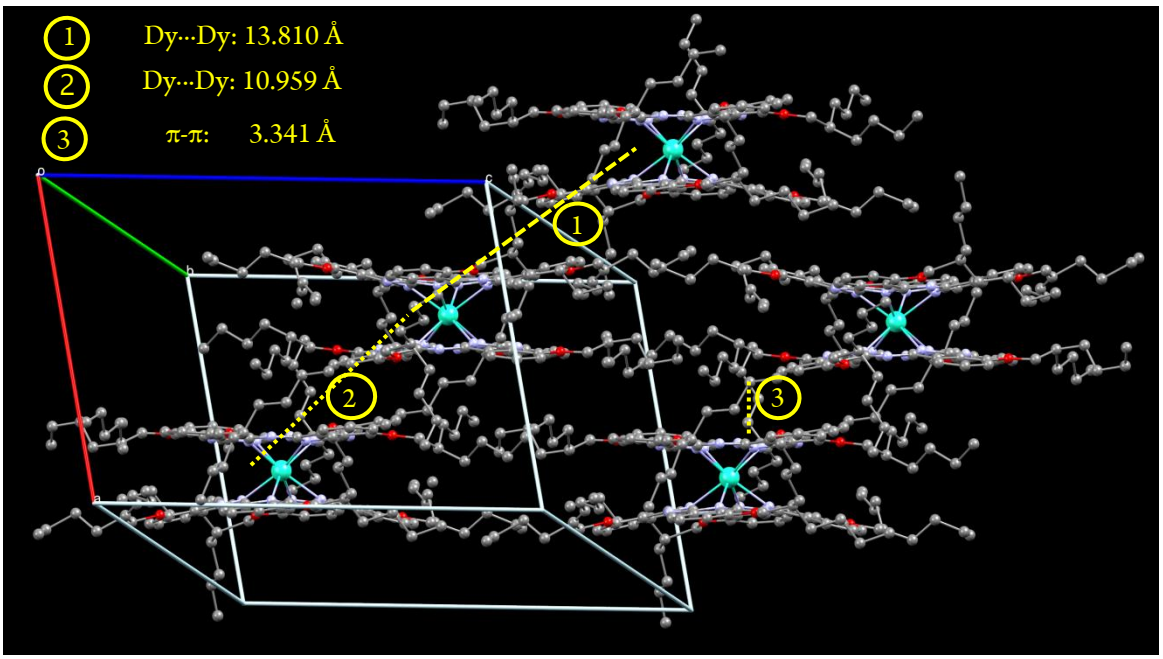

Figure IV.22. Packing diagram for $[Dy\{Pc(OCH_2CH(Bu)_2)_4\}_2^{\cdot-}]^0$.

IV.3.5. Magnetic Measurements

IV.3.5.1. $DyPc(OCH_2CH(Bu)_2)_4Ac(DMF)_2$ and $\{Bu_4N\}\{Dy[Pc(OCH_2CH(Bu)_2)_4]_2\}$

Magnetic data of $DyPc(OCH_2CH(Bu)_2)_4Ac(DMF)_2$ (**3**) and $\{Bu_4N\}\{Dy[Pc(OCH_2CH(Bu)_2)_4]_2\}$ (**4**) were collected on polycrystalline samples. The *dc* room-temperature χT product for **3** and **4** under applied direct current (*dc*) magnetic field at 1000 Oe is 13.7 and 14.00 cm^3 K mol^{-1}, respectively (Figure **IV.23**), in good agreement with the theoretically expected value for Dy^{III} (S= 5/2, L=5, $^6H_{15/2}$, g = 4/3, C = 14.09 cm^3 K mol^{-1}).

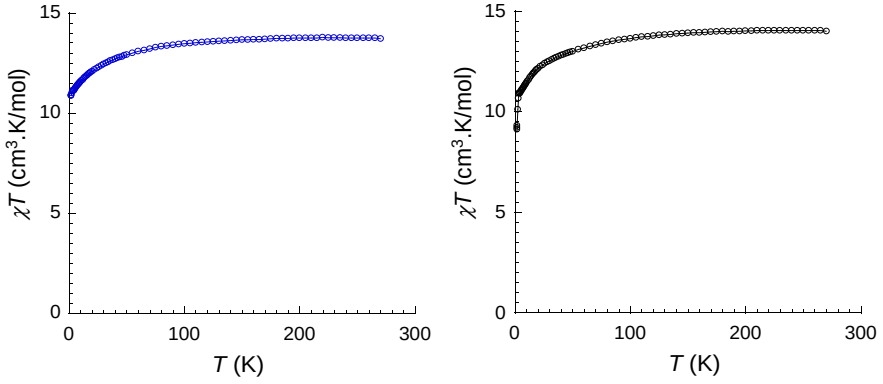

Figure IV.23. Temperature dependence of the product χT at 1000 Oe (where χ is the molar magnetic susceptibility, equal to the ratio between the magnetization and the applied magnetic field, M/H, per mole of Dy complexes) between 1.85 and 270 K for polycrystalline samples of **3** (left) and **4** (right).

For both complexes, the dc χT value gradually decreases upon lowering temperature, and reaches 10.85 and 9.11 cm^3 $Kmol^{-1}$ at 1.85 K for **3** and **4** respectively. This typical temperature dependence indicates that the magnetic excited states (Stark sublevels) of the $^6H_{15/2}$ ground state, split by the ligand field, are thermally depopulated at low temperature that is intrinsic to the individual Dy^{III} [35]. The non-superimposition of the M versus H/T data on a single master curve (Figure **IV.24, right**) suggests the presence of strong magnetic anisotropy. To estimate

their magnetization relaxation behaviors, the temperature dependence of the in-phase (χ') and out-of-phase (χ'') *ac* magnetic measurements were carried out at different frequencies in the range 1.9-20 for **3** and 1.9-50 K for **4** respectively. Figure **IV.25** (left and right) shows strong temperature and frequency dependences of the in–phase (χ') and out-of-phase (χ'') alternating current (ac) susceptibility signal under zero *dc* field for **3** and **4**. These are characteristic of SMM behavior. For compound **3**, the temperature dependences of the out-of-phase (χ'') part, at frequencies indicated, is apparent below 12 K, while for **4** this dependence is apparent below 40 K.

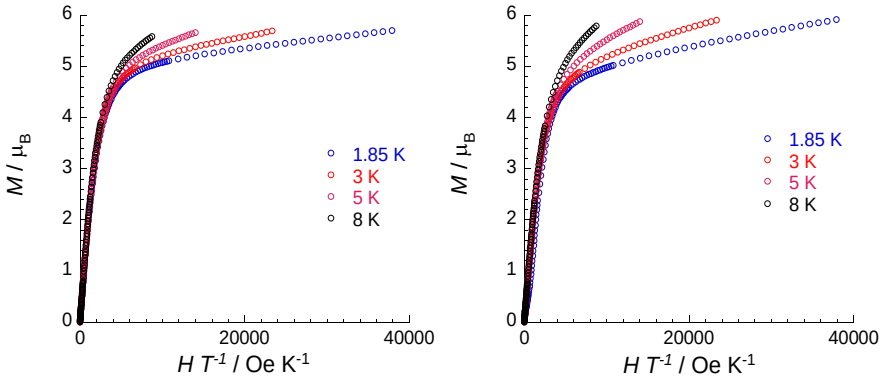

Figure IV.24. Field dependence of reduced magnetization for **3** (left) and **4** (right) at different temperatures.

The significant rise of the temperature is strongly related to different distributions of the sublevel structures of the ground-state multiplets of the complexes. In other words, the (*2J+1*)-fold degeneracy of the ground state of the Dy ion in the complexes (*J* is total angular momentum quantum number, Dy^{III}: J=15/2) is partly removed by the ligand field potential in **3** and **4**. Figure **IV.25, right** shows essentially the same temperature and frequency dependences as those of the unsubstituted $[Pc_2Dy]^-TBA^+$ [6]. This indicates that the alkoxy substituents in the Pc cores have little effect on the dynamical magnetism of the Dy complex as an SMM.

For compound **3**, the maximum peak of the out-of-phase χ'' signal could be not specified for any temperature (called blocking temperature, T_B), meaning that the ratio of the intensities of the out-of-phase and in-phase signals χ'' and χ' is far away from the ideal 1:1 at T_{max} of χ''. This also was previously observed in many lanthanide systems [36]. Additionally, the presence of severals frequency dependent maxima in the χ'' signal (Figure **IV.26**), (being at the limitation of our experimental setup, with ac frequencies up to 10 kHz and temperature higher than 1.85 K) suggests the presence of a fast zero field quantum regime. On the other hand, for compound **4** it is possible to read directly, from the temperature dependence of χ'', the blocking temperature (T_B) for a given frequency where χ'' is at maximum. For example at 100 Hz field the T_B is 7.3 K whereas at 400 Hz it is 9.1 K, but below 4.5 K (Figure **IV.25**) the χ'' values are increased. This suggests that at low temperature the QTM is persisting.

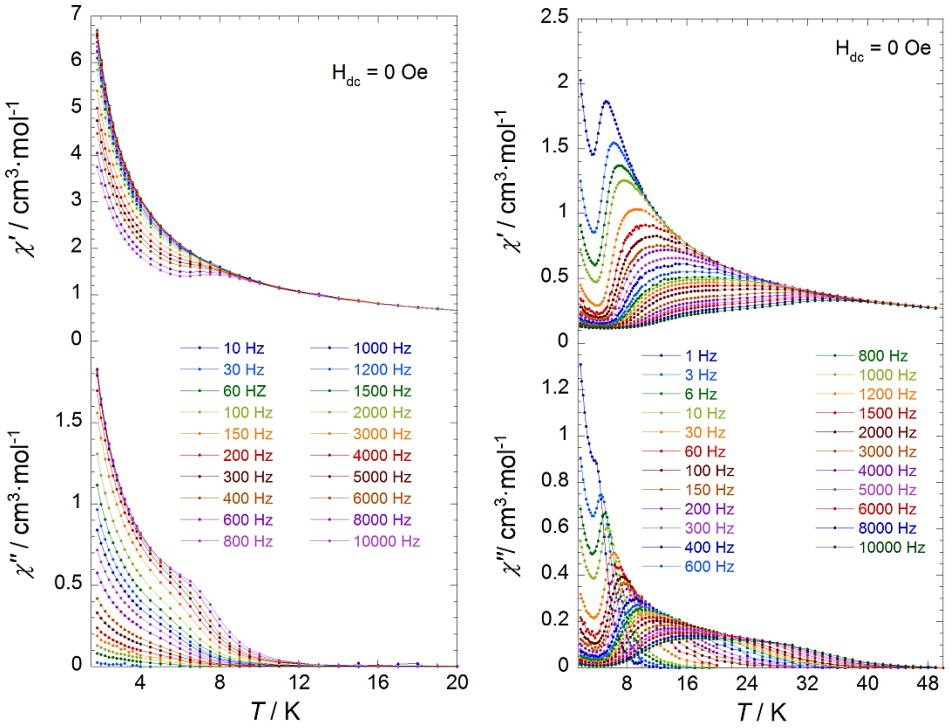

Figure IV.25. Temperature-dependence of *ac* susceptibility data for **3** (right) and **4** (left) collected under a zero *dc* field at various frequencies. Solid lines are guides for the eyes

To quantify the slow relaxation of magnetization, the frequency maxima from the frequency-dependence of the χ'' data between 1.8 and 8.5 K for **3** and from 1.8 to 26 K for **4** (Figure **IV.26, bottom**) were extracted and plotted as a function of T^{-1} in order to extract the characteristic experimental time (τ_{exp}(τ_{exp}= $(2\pi\nu_{exp})^{-1}$). Subsequently, the linear dependence of the experimental relaxation time, τ_{exp} *vs* T^{-1}, was fitted with an Arrhenius plot. Indeed, as was predicted above, below 6 K, the magnetization dynamics for **3** is clearly dominated by quantum tunneling processes with a constant relaxation time of about $1 \cdot 10^{-5}$ s. At higher temperature than 6.5 K, the relaxation may include thermal and quantum contributions, known as 'quantum-assisted thermal regime', yielding an energy barrier of 32.7 K ($9.81 \cdot 10^{-8}$ s) (Figure **IV.27**). Similarly to **3**, the relaxation time for **4** was estimated from the Arrhenius plot using the χ'' maximum (Figure **IV.26, bottom, right**). Linear data following an Arrhenius law were obtained in the temperature range 9-28 K (Figure **IV.27**) with an effective energy barrier of Δ_{eff}/k_B = 55.2 K and a pre-exponential factor $\tau_0 = 3.67 \cdot 10^{-6}$ s. These values are comparable with those previously reported for a Dy^{III} sandwich-type phthalocyanine with Δ_{eff}/k_B=58 K, and $\tau_0 = 1.3 \cdot 10^{-5}$ s [37].

In such cases, when two regimes are participating to the relaxation, the extracted energy barrier and relaxation time value are less accurate. The quantum tunneling of magnetization (QTM) at low temperature mainly originates from the hyperfine interaction of the Dy^{III} ion with the nuclear spin at low temperature so that the Kramer-ion nature of the Dy^{III} breaks down and the total quantum number in the ground state is split by the low symmetry [38].

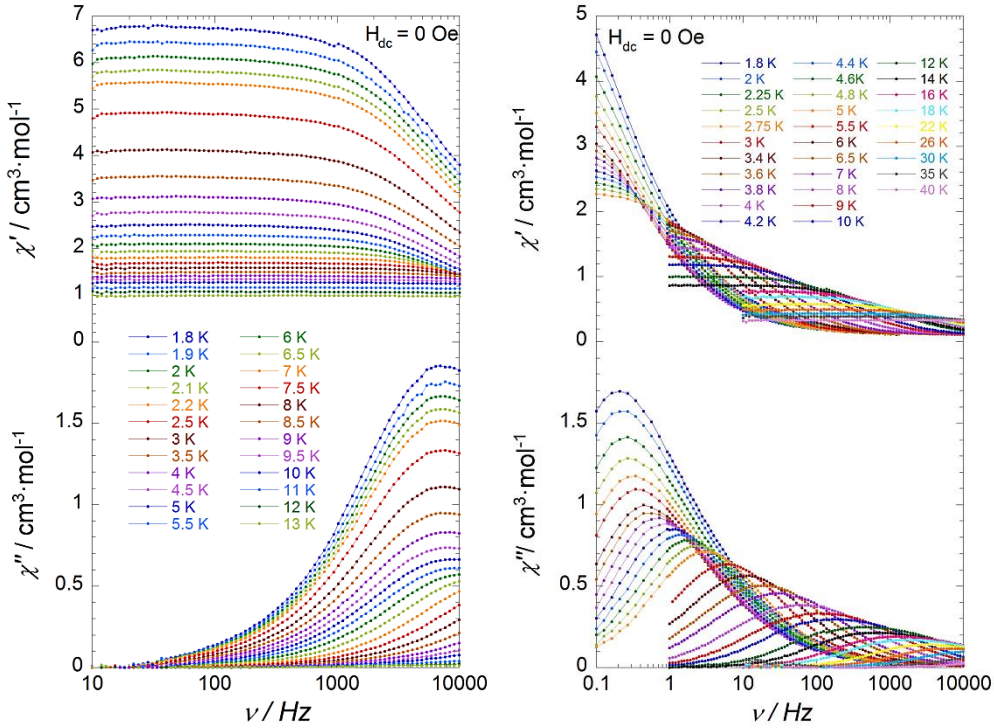

Figure IV.26. Frequency dependence of the real (χ', top) and imaginary (χ'', bottom) parts of the ac susceptibility for a polycrystalline sample of **3** (left) and **4** (right) at 0-Oe dc field at various temperatures. Solid lines are guides for the eyes.

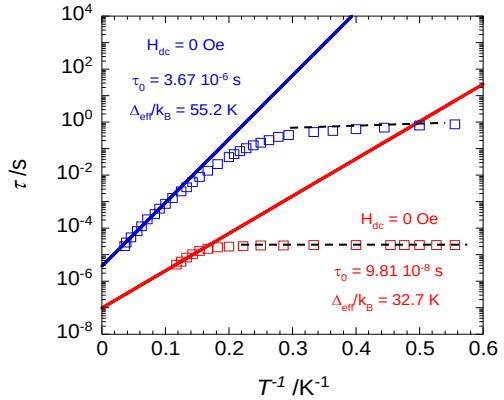

Figure IV.27. Magnetization relaxation time, τ, versus T^{-1} plotted for **3** (red square) and for 4 (blue square) under 0 dc field. The solid red and lines are an Arrhenius law fits.

In order to suppress the quantum tunneling of magnetization, *ac* data of **3** have been recorded under several *dc* fields (Figure **S.IV.7**). The optimum field was found to be 800 Oe (Figure **S.IV.8**). At 800 Oe, a strong frequency and temperature dependence of the *ac* susceptibility was observed (Figure **IV.28**). Relaxation times deduced from the maximum frequency (Figure **IV.28, bottom right**) between 5.8 and 7.6 K, where the thermal effect dominates, allowed the fitting to an Arrhenius law as shown in (Figure **IV.29**). The activation energy barriers Δ_{eff}/k_B and the pre-exponential factors τ_0 were estimated as Δ_{eff}/k_B= 75.6 K and τ_0= $1 \cdot 10^{-9}$s. At lower temperature, the curvature of the relaxation time becomes more temperature independent, suggesting the influence of the quantum relaxation pathway. The energy value for **3** obtained at applied dc field is higher than those reported for other mononuclear dysprosium(III) systems (for example Δ_{eff}/k_B= 60 K was found for a Dy/DOTA system [39], and Δ_{eff}/k_B= 23 K for a dysprosium macrocycle [40]) and lower than those recently published for square anti-prismatic Dy^{III} β-diketonate complexes (with energy barrier 130 K [41]).

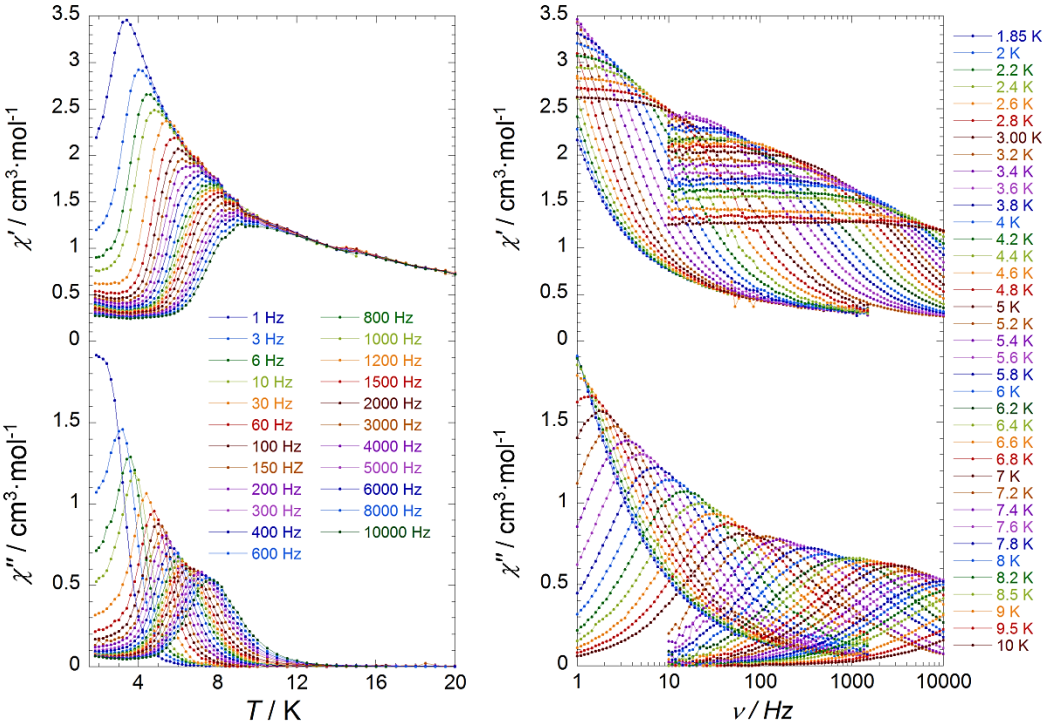

Figure IV.28. Dependence of temperature (left) and frequency (right) of the in phase (χ' top) and out of phase (χ'', bottom) parts of the ac susceptibility, between 1 and 10000 Hz and between 1.85 and 10 K respectively, for **3** under an 800 Oe applied *dc* field. Solid lines are visual guides.

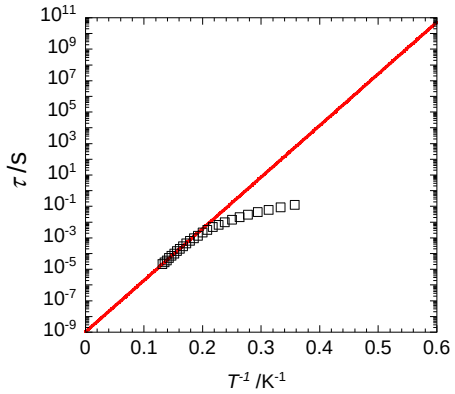

Figure IV.29. Magnetization relaxation time, τ, versus T^{-1} plotted for **3** under 800 Oe applied *dc* field, using χ'' vs *T* data from Figure **IV.28, right**. The solid red line is an Arrhenius law fit.

IV.4. Conclusions and Perspectives

In Chapter IV, five new mononuclear phthalocyanine complexes $FMnPc(OCH_2CH(Bu)_2)_4 \cdot DMF$ (**1**), $AcMnPc(OCH_2CH(Bu)_2)_4$(**2**), $Dy\{Pc(OCH_2CH(Bu)_2)_4Ac(DMF)_2$(**3**), $\{Bu_4N\}\{Dy[Pc(OCH_2CH(Bu)_2)_4]_2\}$ (**4**) and the radical $[Dy\{Pc(OCH_2CH(Bu)_2)_4\}_2]^0$ (**4***) were investigated in terms of synthesis, structural characterizations, and magnetic properties.

It is surprising that no report on a Mn(III) phthalocyanine based SMM has been appeared to date. The manganese (III) complexes **1** and **2** with square pyramidal geometry, in which the d_z^2 orbital contains an electron induced by the F and acetate ligands respectively, have a Jahn-Teller axis in the out–of plane direction corresponding with the site of the axial ligand. As a consequence, the ZFS parameter of the axial magnetic anisotropy is negative (for **1**: D = -2.64 cm^{-1}; for **2** D = -2.46 cm^{-1}). In particular, in zero-dc field, the magnetization of complexes **1** and **2** has a relaxation time that is faster than 1.6 10^{-5} s at 1.85 K and its temperature dependence cannot be determined with our experimental setup, suggesting quantum tunneling of magnetization. Alternating–current magnetic susceptibility measurements demonstrate that **1**, which contains isolated Mn^{III} centers; displays induced slow relaxation of its magnetization under external applied magnetic field. On the other hand, the compound **2**, which crystallizes in 'pairs' where the distance in-between molecules is 3.533 Å and 5.214 Å between Mn (III) centers, behaves as a binuclear complex from the magnetic point of view. The magnetic interaction between the Mn(III) ions was estimated as very weakly antiferromagnetic interaction with J= - 0.24 cm^{-1}. However, the determined energy barriers of both compounds are comparable, suggesting that the ligand fields of fluorine and acetate, as axial ligands, are comparable in these systems, or that their contribution is small, in agreement with the very close values of the ZFS parameters.

As magnetic proprieties are strongly dependent on the chemical structure (i.e. the environment of the metal ion), one of the perspectives, in order to enhance axial magnetic anisotropy of these compounds, is to synthesize new building blocks using bridging ligands or other complexes containing bridging groups (*i.e.* C≡N, halogens, hexacyanometalates and others). For a bridging ligand, the simplest conceivable geometry is to linearly connect two metal ions. Thus, this approach allows us to control not only the spatial arrangements, but also the electronic structure of complicated systems. A similar synthetic approach was involved in a recent report on several cyano-bridged single-chain magnets made of Mn(III) porphyrins [42].

For compounds **3** and **4,** we could show that the dynamic magnetism of the single Dy-ionic SMMs is greatly altered by the modification of the ligand field. At zero-*dc* field the magnetization dynamics for **3** is clearly dominated by quantum tunneling processes with a constant relaxation time of about $1 \cdot 10^{-5}$ s and consequently, the QTM was suppressed by performing the ac magnetic measurements in the presence of an external applied field. On the other hand, at lower temperature, the relaxation times for **4** indicate a more and more pronounced influence of quantum relaxation pathways. This leads us to infer that in **3** and **4** the disordered square-antiprismatic coordination environments of Dy(III) have a huge influence on the sublevel structures of the

ground-state multiplets of the complexes. To confirm that the slow magnetization relaxation behavior of **4** is an intrinsic molecular property, it is necessary to perform additional magnetic measurements on samples doped e.g. with its diamagnetic $\{Bu_4N\}\{Y[Pc(OCH_2CH(Bu)_2)_4]_2\}$ homolog. This will indicate whether the removal of intermolecular interactions could lead to a shift of χ'' at higher or lower temperatures. If such a shift is detected, then undoubtedly the magnetization relaxation is a single-molecular property of the compound.

Another aspect of compound **4** is that due of the presence of the bulky tetra α-alkoxy-substituents on the Pc ring we managed to promote the regiospecific formation of the C_{4h} symmetry isomer of the double decker phthalocyanine (**4** and **4***). Unfortunately, no crystal structure could be obtained for compound **4**. Instead, by serendipity, we could crystallize and determine the crystal structure of its radical form **4***. Since the SMM behavior of these complexes strongly depends on the energy gap between the lowest and second lowest sublevels in the ground state multiplet, the radical form of the **4*** remains to be further studied in terms of magnetic properties, expecting substantial altering of the dynamical magnetization of the Dy(III) sandwich type complex involving the unpaired π-electrons of the ligands. In some cases the energy barrier of the one-electron-oxidized-ligand form of the dysprosium double decker complexes is increased moderately or even doubled compared to the anionic form [43].

Linked to the lanthanide double decker family, a challenging perspective involving our phthalocyanine systems is the synthesis of new homoleptic and heteroleptic double deckers with lanthanide ions and one unsubstituted plus one tetra-alkyloxysubstituted Pc ligand as well as studying their different forms (i.e. anionic, radical, protonated and oxidized form). Since the anionic form of **4** requires a cation for neutralization, a protonation also can accomplish this process involving a modification of the properties of the double-decker complex as well. Preliminary investigations were done by UV-Vis spectroscopy upon addition of hydrochloric acid to a blue solution of **4** in acetone, followed by instantaneous change of color to green. The optical spectrum of such a solution is shown in Figure **IV.30**, where the blue curve is the pristine absorption spectrum of **4**, the red curve represents the absorption spectrum of the acidified solution **4** and the black curve is the absorption spectrum after deprotonation by adding base. This remarkable result demonstrates the reversibility of the protonation and deprotonation process in acid-base reactions:

$$[Dy\{Pc(OCH_2CH(Bu)_2)_4\}_2]^- \underset{OH^-}{\overset{H^+}{\rightleftharpoons}} \mathbf{H}[Dy\{Pc(OCH_2CH(Bu)_2)_4\}_2]$$

A similar acid-base reaction was done by Moskalev and Kirin on a lutetium double decker complex [44] and by Man Kay et al. on Gd diphthalocyanine [45]. In For further analysis, the green solution of the protonated form of **4** was subjected to crystallization by slow evaporation. Thereby, dark green needles were separated.

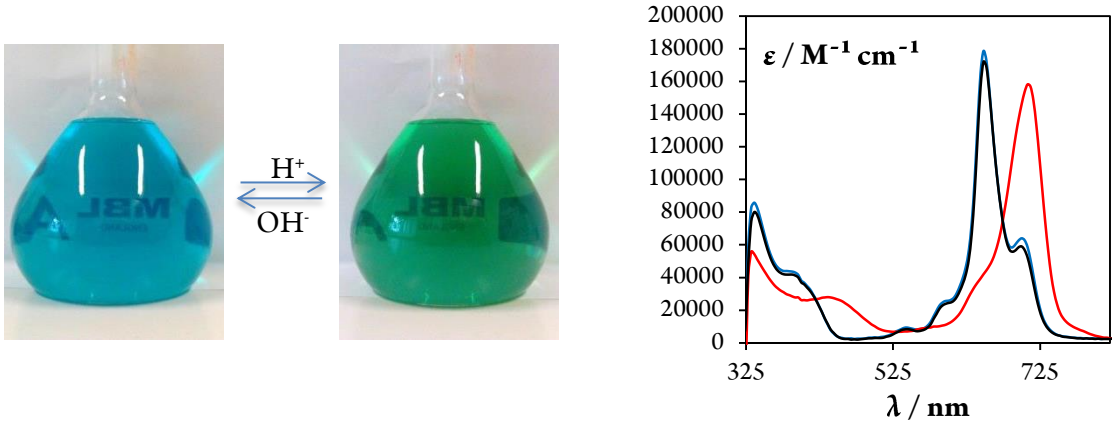

Figure IV.30. (left) Views of the solution during the acid base reactions. (right) Electronic absorption spectra (5 μM in acetone) of **4** (blue) its protonated form (red), and black curve is the absorption spectrum after deprotonation of **4** by adding base.

IR spectrometry has been proven to be reliable in determining the location of the proton. The IR spectrum shows $\nu_{N\text{-}H}$ absorbtions at 3323 cm^{-1} that are consistent with the presence of an N-H bond, most probably of a *meso-nitrogen*. The absorption resulting from the N-H vibration is different from that of free-base phthalocyanine ($H_2Pc(OCH_2CHBu_2)_4$ (3295 cm^{-1}) (Figure **IV.31**).

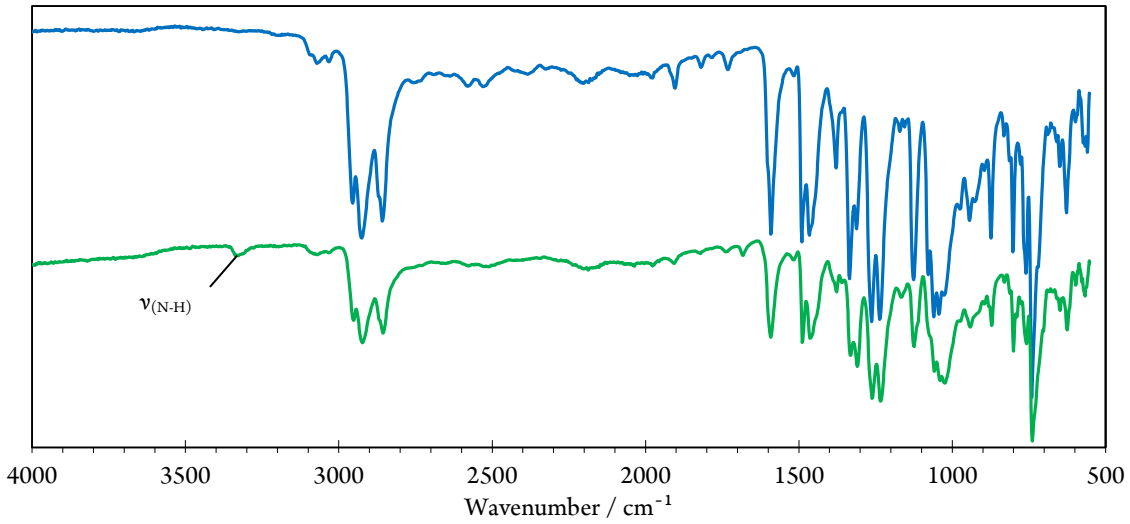

Figure IV.31. FT-IR spectra of compound **4** (blue) and its protonated form (green).

IV.5. Supporting Material

IV.5.1. Synthesis Protocols

Preparation of $FMn^{III}Pc(OCH_2CH(Bu)_2)_4$·DMF (1). Compound $H_2Pc(OCH_2CHBu_2)_4$ (0.1 g, 0.087 mmol) was refluxed with MnF_3 (15 mg, 0.134 mmol) in DMF (12 ml) for 12 h. The complex was separated by filtration after crystallization from the cold solution, washed with methanol and dried under ambient conditions. Yield: 0.085 g (77%), of greenish brown crystalline solid. IR (ATR, cm^{-1}): ῡ= 2952 (w), 2923 (vs), 2856 (s), 1619 (s), 1591 (s), 1491 (s), 1458 (m), 1335 (s), 1316 (s), 1269 (s), 1247 (s), 1138 (s), 1058 (s), 1041 (s), 950 (w), 886 (w), 798 (w), 750 (w), 738 (s), 647 (w); elemental analysis calcd (%) for $C_{75}H_{103}MnN_9O_5$: C 70.12, N 9.81, H 8.08; found C 70.20, N 9.65, H 8.10.

Preparation of $AcMn^{III}Pc(OCH_2CH(Bu)_2)_4$ (2). Compound $H_2Pc(OCH_2CHBu_2)_4$ (0.11 g, 0.09 mmol) was refluxed with $Mn(CH_3COO)_3 \cdot 2H_2O$ (15 mg, 0.13 mmol) in DMF (12 ml) for 6 h. The complex was separated by filtration after crystallization from the cold solution, washed with methanol and dried under ambient conditions. Yield: 0.085 g (77%), of greenish brown crystalline solid. Selected FT-IR data (ATR, cm^{-1}): ῡ= 2954 (w), 2920 (vs), 2852 (s), 2184 (w), 1727 (w), 1617(w), 1592 (s), 1493(s), 1491 (m), 1490 (s), 1458 (s), 1336 (s), 1316 (s), 1265 (s), 1246 (s), 1139 (s), 1057 (s), 1042(s), 948 (w), 886 (w), 798 (s), 749 (w), 737 (s), 648 (w); elemental analysis calcd (%) for $C_{74}H_{99}MnN_8O_6$: C 71.01, N 8.95, H 7.97; found C 71.09, N 8.80, H 8.01

Preparation of $DyPc(OCH_2CH(Bu)_2)_4$Ac 2DMF (3). Compound $H_2Pc(OCH_2CHBu_2)_4$ (0.14 g, 0.13 mmol) was refluxed with $Dy(CH_3COO)_3 \cdot 4H_2O$ (31 mg, 0.075 mmol) in DMF (15 ml) for 8 h. The emerald solution was cooled to room temperature, filtered (in order to remove unreacted metal-free ligand) and set for slow evaporation. After one week, the dark blue-green crystalline product was separated by filtration, washed with methanol and dried under ambient conditions. Yield: 0.11 g (57%), of blue-green crystalline solid. Selected FT-IR data (ATR, cm^{-1}): ῡ= 2954 (s), 2923 (vs), 2856 (s), 1639 (s), 1588 (s), 1546 (m), 1489 (s), 1464 (m), 1444 (s), 1375 (s), 1333 (s), 1313 (s), 1263 (s), 1235 (s), 1172 (s), 1078 (s), 1059 (s), 1038 (s), 1020 (s), 915 (w), 933 (s), 872 (w), 800 (w), 781 (s), 758 (s), 743 (s), 671 (s), 630 (w) UV-Vis (CH_2Cl_2): λ_{max} = 703(126200), 668(40500), 642(22000) nm(M^{-1} cm^{-1}); elemental analysis calcd (%) for $C_{80}H_{113}DyN_{10}O_8$: C 63.83, N 9.30, H 7.57; found C 63.70, N 9.25, H 7.48.

Preparation of $\{Bu_4N\}\{Dy[Pc(OCH_2CH(Bu)_2)_4]_2\}$ (4). Compound **3** (0.126 g, 0.083 mmol) was refluxed with $H_2Pc(OCH_2CHBu_2)_4$ (0.18 g, 0.16 mmol) in 1-octanol (10 ml) in the presence of 1,8-diazabicyclo[5.4.0]undec-7-ene (DBU) (0.75 ml, 5 mmol) for 20 h) under a slow stream of nitrogen. The solution was evaporated to dryness under reduced pressure which afforded an oily blue-green residue (the blue solution is changing to green when the flask is exposed to air, and the blue color of the solution reappears under vacuum). The residue was chromatographed with CH_2Cl_2 as eluent. Small amounts of unreacted $H_2Pc(OCH_2CHBu_2)_4$ were collected as a first fraction. Then, continued chromatography with THF as eluent

(as the second fraction) gave mixture of the target double decker product and some undetermined brown impurity. The solvent was removed under *vacuum*. The product was purified by two successive gel permeation chromatographies with Biorad S-X3 beads swelled with CH_2Cl_2. The stabilization of the anionic form ($\{\mathbf{Dy[Pc(OCH_2CH(Bu)_2)_4]_2}\}^-$) was obtained by excess addition a solution of n-tetrabutylammonium acetate in acetone (30 ml). The resulting deep-blue solution was then stirred vigorously 1 hour. Then, after adding 20 ml of water, the target product was crystallized and separated after evaporation of acetone under reduced pressure. Yield: 0.19 g (83%), of blue crystalline solid. Selected FT-IR data (ATR, cm^{-1}): ῡ= 2953 (s), 2923 (vs), 2855 (s), 1902 (w), 1729 (w), 1588 (s), 1488 (s), 1464 (s), 1376 (m), 1333 (s), 1310 (m), 1261 (s), 1234 (s), 1124 (s), 1076 (m), 1058 (m), 1040 (m), 941 (w), 871 (s), 799 (s), 757 (s), 738 (s), 647 (w), 625 (s); UV-Vis ((CH3)2CO): λ_{max} = 704(78600), 648(178600), 596(28000), 540(8200) nm(M^{-1} cm^{-1}); elemental analysis calcd (%) for $C_{160}H_{228}DyN_{17}O_8$: C 71.70, N 8.88, H 8.57; found C 71.45, N 8.63, H 8.65. FD-HRMS: m/z calcd. for $C_{144}H_{192}DyN_{16}O_8$ ($Dy(Pc)_2^-$) 2437.44; found 2438.14

Preparation of $\{\mathbf{Dy[Pc(OCH_2CH(Bu)_2)_4]_2}\}$ (4*). Compound **4*** was obtained following the procedure for compound **4**, except that the n-tetrabutylammonium acetate was not added. The product was purified by two successive gel permeation chromatographies with Biorad S-X3 beads swelled with CH_2Cl_2. The solvent was removed under *vacuum*. Then in order to crystallize this compound, the dark blue DMF solution of **4*** was exposed to methanol diffusion at room temperature. After one week, the bluish-green crystalline compound was filtered, washed with methanol and dried under ambient conditions. Yield: 0.14 g (63%), of bluish -green crystalline solid. Selected FT-IR data (ATR, cm^{-1}): ῡ= 2952 (s), 2923 (vs), 2855 (s), 2162 (w),1980 (w), 1909 (w), 1739 (w), 1593 (s), 1488 (s), 1459 (s), 1438 (s). 1360 (m), 1306 (s), 1259 (s), 1232 (s), 1162 (w), 1126 (s), 1041 (m), 943 (w), 871 (w), 800 (s), 757 (s), 778 (w), 758(w), 740(s), 661 (w), 624 (s); UV-Vis ($(CH_3)_2CO$): λ_{max} = 1736(49000), 1684(30892), 1452(8080), 1192(5190), 944(4080), 708(110600), 632(87800), 580(28400), 460(15000) nm(M^{-1} cm^{-1}); elemental analysis calcd (%) for $C_{160}H_{228}DyN_{17}O_8$: C 70.95, N 9.19, H 7.94; found C 71.00, N 9.10, H 8.0.

IV.5.2. Crystallographic Data for 1 and 2

Table S.IV.1. Crystallographic data for **1** at 120 K

Moiety formula	$C_{72}H_{96}FMnN_8O_4$, $C_3H_7N1O_1$
Empirical formula	$C_{75}H_{103}FN_9O_5$
Formula weight	1284.65
Crystal system	Triclinic
Space group	P-1
Wavelength, Å	0.71073
a, Å	12.9896(8)
b, Å	14.1216(9)
c, Å	20.0903(12)
α, °	100.579(3)
β, °	96.053(4)
γ, °	105.782(3)
V, Å^3	3438.69
Z	2
ρ_{calcd}, g/cm^3	1.241
μ, 1/mm	0.252
Reflections collected	60329
Independent reflections	11241
R_1[a]	0.0607
wR_2[a]	0.1748
GoF[a]	1.094

[a] $I > 2\sigma(I)$, $R_1 = \Sigma||F_o| - |F_c||/\Sigma|F_o|$. $wR_2 = \{\Sigma[w(F_o^2 - F_c^2)^2]/\Sigma[w(F_o^2)^2]\}^{1/2}$. GoF (goodness of fit on F^2) = $\{\Sigma[w(F_o^2 - F_c^2)^2]/(n-p)\}^{1/2}$, where n is the number of reflections and p is the total number of refined parameters.

Table S.IV.2. Crystallographic Data for **2** at 120 K

Moiety formula	$2(C_{75}H_{99}MnN_8O_6)$
Empirical formula	$C_{150}H_{198}Mn\ N_{16}O_{12}$
Formula weight	2503.14
Crystal system	Monoclinic
Space group	P $2_1/c$
Wavelength, Å	0.71073
a, Å	17.2049(5)
b, Å	20.0559(6)
c, Å	39.2961(11)
α, °	90
β, °	93.984(2)
γ, °	90
V, $Å^3$	13526.7
Z	4
ρ_{calcd}, g/cm^3	1.227
μ, 1/mm	0.254
Reflections collected	172798
Independent reflections	24933
R_1[a]	0.0947
wR_2[a]	0.2211
GoF[a]	1.018

[a] $I > 2\sigma(I)$, $R_1 = \Sigma(||F_o| - |F_c||)/\Sigma|F_o|$. $wR_2 = \{\Sigma[w(F_o^2 - F_c^2)^2]/\Sigma[w(F_o^2)^2]\}^{1/2}$.GoF (goodness of fit on F^2) = $\{\Sigma[w(F_o^2 - F_c^2)^2]/(n-p)\}^{1/2}$, where n is the number of reflections and p is the total number of refined parameters.

IV.5.3. Magnetic Properties of 1 and 2

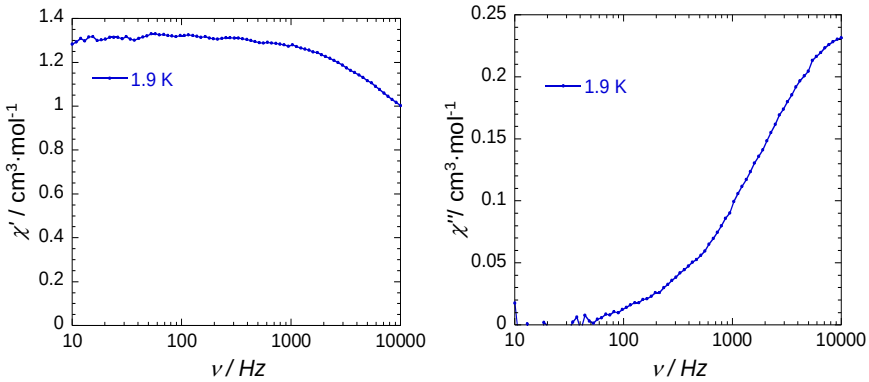

Figure S.IV.1. Frequency dependence of the real (χ', left) and imaginary (χ'', right) parts of the ac susceptibility for a polycrystalline sample of **1** at 0 Oe dc field at 1.9 K. Solid lines are guides.

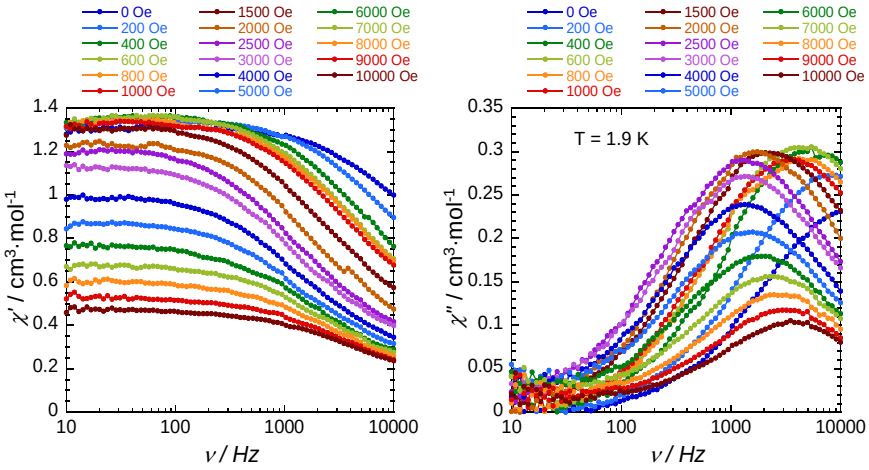

Figure S.IV.2. Plots of the in-phase (left), χ', and out-of-phase (right), χ", components of the *ac* magnetic susceptibility versus the frequency, *ν*, of the oscillating field at 1.9 K for compound **1** in the presence of the indicated *dc* fields from 0 to 10000 Oe

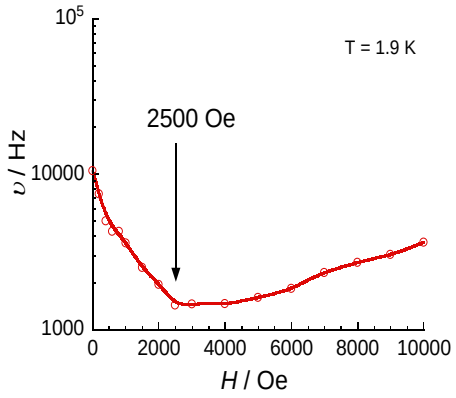

Figure S.IV.3. Field dependence of the characteristic frequency at 1.9 K for compound **1.**

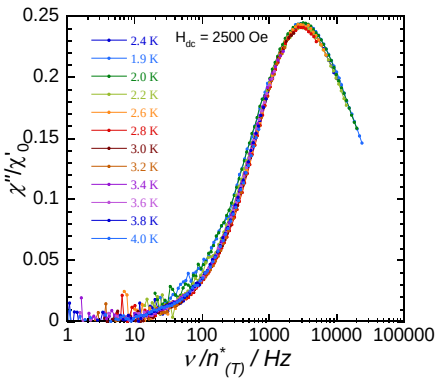

Figure S.IV.4. Plot of χ"/χ₀' versus the frequency, *ν*, under an external dc field of 2500 Oe at the indicated temperatures, showing the scaling of the curves (at 1.9 to 4 K) to the 2.4 K curve that exhibits a frequency maximum in the measurement window, for complex **1.**

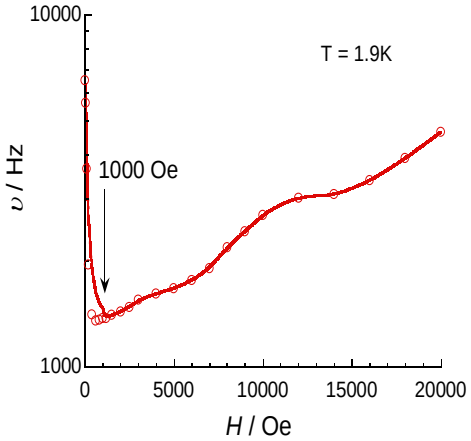

Figure S.IV.5. Field dependence of the characteristic relaxation frequency of the magnetization as a function of the applied field in **2** at 1.9 K. This plot is deduced from Figure IV.11.

IV.5.4. Crystallographic Data for 3 and 4*

Table S.IV.3. Crystallographic data for **3** at 120 K.

Moiety formula	$2(C_{80}H_{113}DyN_{10}O_8)$
Empirical formula	$C_{160}H_{226}Dy_2N_{20}O_{16}$
Formula weight	3010.56
Crystal system	Monoclinic
Space group	$P2_1/c$
Wavelength, Å	0.71073
a, Å	16.8910(11)
b, Å	13.1401(9)
c, Å	36.048(2)
α, °	90
β, °	101.118(3)
γ, °	90
V, Å^3	7850.6(9)
Z	2
ρ_{calcd}, g/cm^3	1.263
μ, 1/mm	1.011
Reflections collected	153514
Independent reflections	16032
R_1[a]	0.0663
wR_2[a]	0.1413
GoF[a]	1.066
Selected bond distances (Å)	
Dy1-N1	2.401(5)
Dy1-N2	2.394(6)
Dy1-N3	2.396(5)
Dy1-N4	2.395(7)
Dy1-O5	2.375(5)
Dy1-O6	2.397(5)
Dy1-O7	2.401(6)
Dy1-O8	2.438(5)
Selected bond angles (°)	
N3-N1-Dy1	34.71
N4-N2-Dy1	34.62
N1-N3-Dy1	34.88
N4-N1-Dy1	34.80
O6-Dy1-O8	109.48
O7-Dy1-O5	110.46

[a] $I > 2\sigma(I)$, $R_1 = \Sigma|(|F_o| - |F_c|)|/\Sigma|F_o|$. $wR_2 = \{\Sigma[w(F_o^2 - F_c^2)^2]/\Sigma[w(F_o^2)^2]\}^{1/2}$. GoF (goodness of fit on F^2) $= \{\Sigma[w(F_o^2 - F_c^2)^2]/(n-p)\}^{1/2}$, where n is the number of reflections and p is the total number of refined parameters.

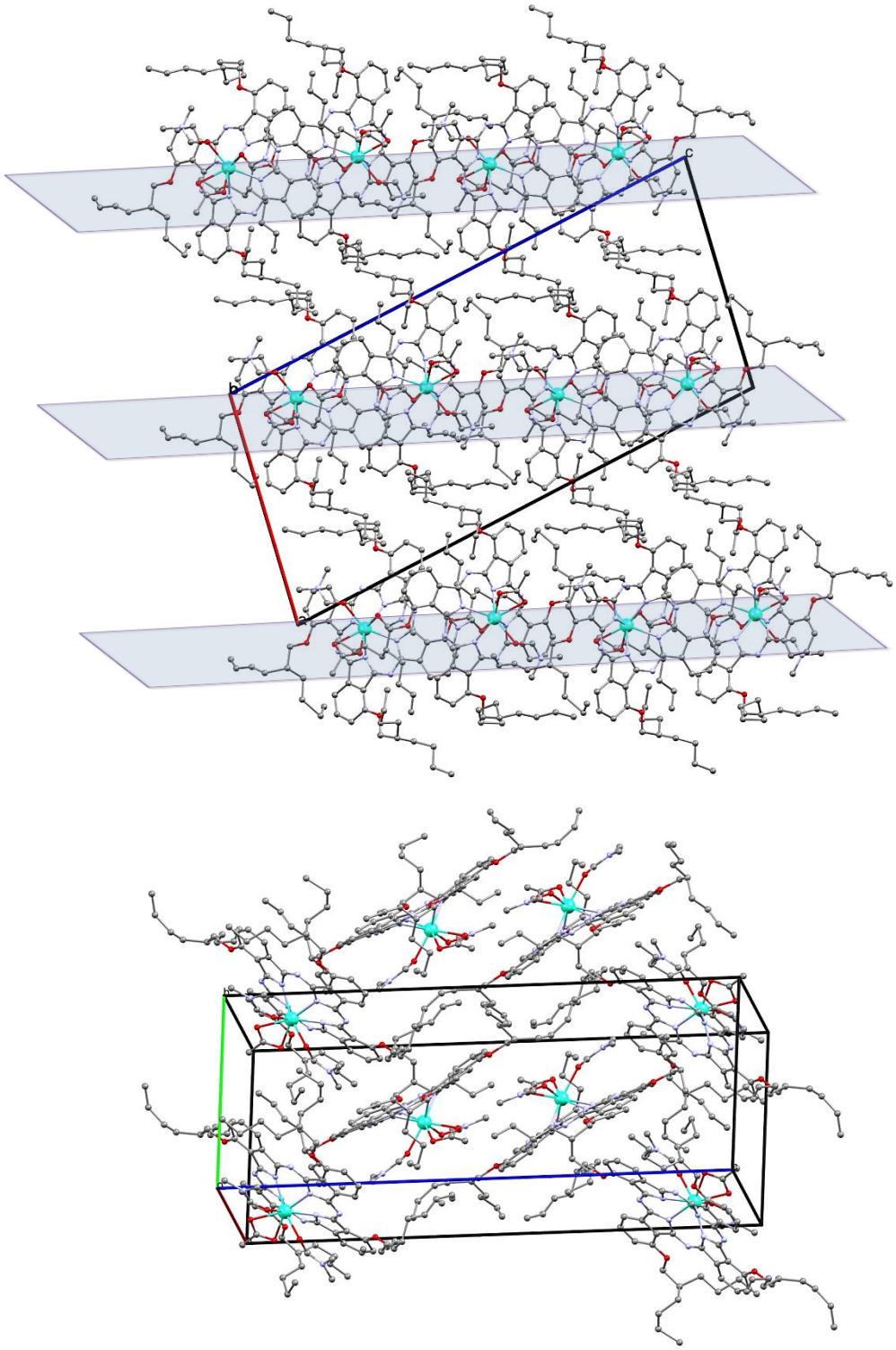

Figure S.IV.6. Perspective view of the crystal packing of **3** at 120 K, illustrating the tilted stacking into columns along the *b* axis. Hydrogen atoms are omitted for clarity.

Table S.IV.4. Crystallographic data for **4*** at 120 K

Moiety formula	$2(C_{144}H_{192}DyN_{16}O_8)$
Empirical formula	$C_{288}H_{384}Dy_2N_{32}O_{16}$
Formula weight	4868
Crystal system	Triclinic
Space group	P-1
Wavelength, Å	0.71073
a, Å	15.8207(13)
b, Å	21.4865(18)
c, Å	21.8282(17)
α, °	65.447(3)
β, °	80.173(4)
γ, °	84.500(4)
V, Å^3	6647.55
Z	2
ρ_{calcd}, g/cm^3	1.2262
μ, 1/mm	0.625
Reflections collected	356450
Independent reflections	24246
R_1[a]	0.0390
wR_2[a]	0.964
GoF[a]	1.072
Selected bond distances (Å)	
Dy1-N1	2.399(2)
Dy1-N2	2.412(3)
Dy1-N3	2.407(2)
Dy1-N4	2.410(2)
Dy1-N5	2.414(2)
Dy1-N6	2.408(3)
Dy1-N7	2.416(2)
Dy1-N8	2.412(2)
Selected bond angles (°)	
interplanar distance [Å]	2.804
dihedral angle between the two N_4 planes [°]	0.0
average twist angle [°][a]	39.4
average dihedral angle φ for the Pc_1 ring [°][b]	10.0
average dihedral angle φ for the Pc_2 ring [°][b]	8.7

[a] $I > 2\sigma(I)$, $R_1 = \Sigma||F_o| - |F_c||/\Sigma|F_o|$. $wR_2 = \{\Sigma[w(F_o^2 - F_c^2)^2]/\Sigma[w(F_o^2)^2]\}^{1/2}$.GoF (goodness of fit on F^2) = $\{\Sigma[w(F_o^2 - F_c^2)^2]/(n-p)\}^{1/2}$, where n is the number of reflections and p is the total number of refined parameters. [a] Defined as the rotation angle of one macrocycle away from the eclipsed conformation of the two macrocycles. [b] The average dihedral angle of the individual pyrrole or isoindole rings with respect to the corresponding N4 mean plane.

IV.5.5. Magnetic Properties of 3

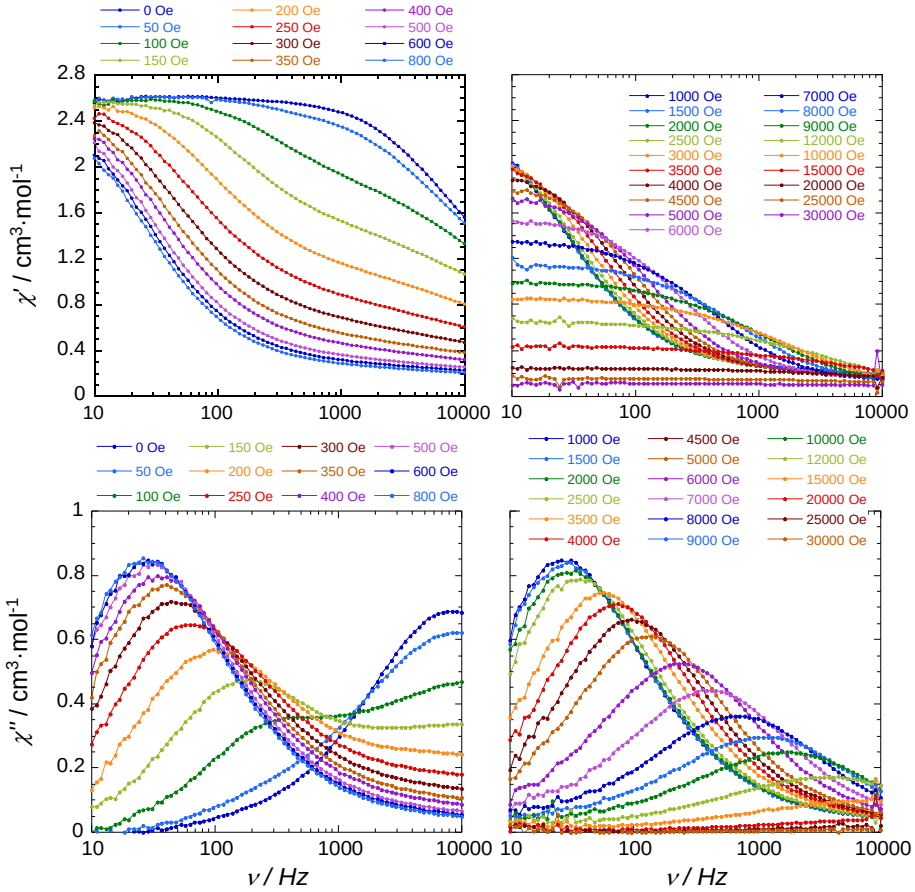

Figure S.IV.7. Frequency dependence of the real (χ', left) and imaginary (χ'', right) parts of the ac susceptibility for a polycrystalline sample of **3** at 4.5 K at different dc-field between 0 and 30000 Oe. Solid lines are guides.

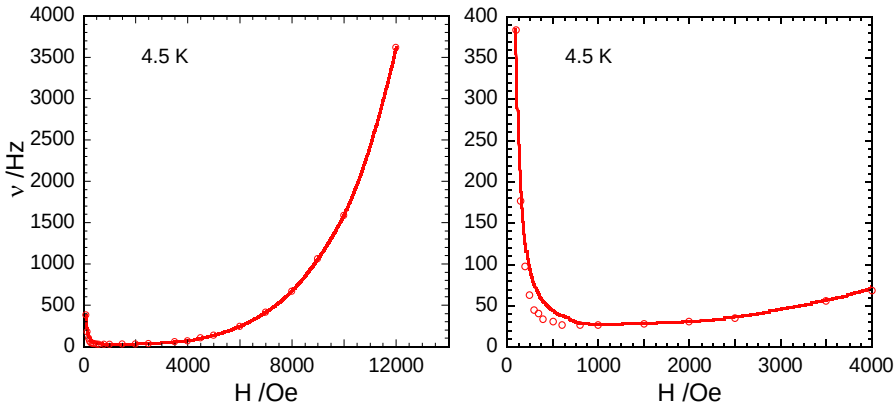

Figure. S.IV.8. Field dependence of the characteristic relaxation frequency of the magnetization as a function of the applied field in **3** at 4.5 K. This plot is deduced from **Figure S.IV.7.**

IV.6. References

[1] (a) R. Sessoli; L. Hui; A. R. Schake; S. Wang; J. B. Vincent; K. Folting; D. Gatteschi; G. Christou; *J. Am. Chem. Soc.* **1993**, 115, 1804-1816; (b) R. Sessoli; D. Gatteschi; A. Caneschi; M. A. Novak; *Nature* **1993**, 365, 141; c) R. Bagai; G. Christou; *Chem. Soc. Rev.*, **2009**, 38, 1011–1026. d) T. Lis *Acta Crystallogr., Sect. B: Struct. Crystallogr. Cryst. Chem.*, **1980**, 36, 2042–2046.

[2] C. J. Milios; A. Vinslava; W. Wernsdorfer; S. Moggach; S. Parsons; S. P. Perlepes; G. Christou; E. K Brechin; *J. Am. Chem. Soc.*, **2007**, 129, 2754.

[3] A. K. Ako; I. J. Hewitt; V. Mereacre; R. Clérac; W. Wernsdorfer; C. E. Anson; A. K. Powell; *Angew. Chem., Int. Ed.*, **2006**, 45, 4926.

[4] a) W. H. Harman; T. D. Harris; D. E. Freedman; H. Fong; A. Chang; J. D. Rinehart; A. Ozarowski; M. T. Sougrati; F. Grandjean; G. J. Long; J. R. Long; C. J. Chang; *J. Am. Chem. Soc.*, **2010**, 132, 18115–18126; b) J. M. Zadrozny; M. Atanasov; A. M. Bryan; C.-Y. Lin; B. D. Rekken; P. P. Power; F. Neese; J. R. Long; *Chem. Sci.*, **2013**, 4, 125–138; c) D. E. Freedman; W. H. Harman; T. D. Harris; G. J. Long; C. J. Chang; J. R. Long; *J. Am. Chem. Soc.*, **2010**, 132, 1224–1225; d) P.-H. Lin; N. C. Smythe; S. I. Gorelsky; S. Maguire; N. J. Henson; I. Korobkov; B. L. Scott; J. C. Gordon; R. T. Baker; M. Murugesu; *J. Am. Chem. Soc.*, **2011**, 133, 15806–15809; e) J. M. Zadrozny; J. R. Long; *J. Am. Chem. Soc.*, **2011**, 133, 20732–20734; f) S. Mossin; B. L. Tran; D. Adhikari; M. Pink; F. W. Heinemann; J. Sutter; R. K. Szilagyi; K. Meyer; D. J. Mindiola; *J. Am. Chem. Soc.*, **2012**, 134, 13651–13661; g) Y.-Y. Zhu; C. Cui; Y.-Q. Zhang; J.-H. Jia; X. Guo; C. Gao; K. Qian; S.-D. Jiang; B.-W. Wang; Z.-M. Wang; S. Gao; *Chem. Sci.*, **2013**, 4, 1802–1806; h) J. M. Zadrozny; D. J. Xiao; M. Atanasov; G. J. Long; F. Grandjean; F. Neese; J. R. Long; *Nat. Chem.*, **2013**, 5, 577–581; i) F. Habib; O. R. Luca; V. Vieru; M. Shiddiq; I. Korobkov; S. I. Gorelsky; M. K. Takase; L. F. Chibotaru; S. Hill; R. H. Crabtree; M. Murugesu; *Angew. Chem., Int. Ed.*, **2013**, 52, 11290–11293; j) J. M. Zadrozny; J. Telser; J. R. Long; *Polyhedron*, **2013**, 64, 209–217.

[5] a) J. Vallejo; A. Pascual-Alvarez; J. Cano; I. Castro; M. Julve; F. Lloret; J. Krzystek; G. De Munno; D. Armentano; W. Wernsdorfer; R. Ruiz-Garcia; E. Pardo; *Angew. Chem., Int. Ed.*, **2013**, 52, 14075−14079; (b) R. Ishikawa; R. Miyamoto; H. Nojiri; B. K. Breedlove; M. Yamashita; *Inorg. Chem.*, **2013**, 52, 8300−8302; (c) A. Grigoropoulos; M. Pissas; P. Papatolis; V. Psycharis; P. Kyritsis; Y. Sanakis; *Inorg. Chem.*, **2013**, 52, 12869−12871.

[6] N. Ishikawa; M. Sugita; T. Ishikawa; S-Y. Koshihara; Y. Kaizu; *J. Am. Chem. Soc.*, **2003**, 125, 8694.

[7] a) Y. Peng; V. Mereacre; A. Baniodeh; Y. Lan; M. Schlageter; G. E. Kostakis; A. K. Powell; *Inorg. Chem.* **2016**, 55, 68–74; b) N. Ishikawa; T. Iino; Y. Kaizu; *J. Phys. Chem.*, **2002**, 106, 9543-9550; c) N. Ishikawa; T. Iino; Y. Kaizu; *J. Am. Chem. Soc.*, **2002**, 124, 11440-11447.

[8] F. Branzoli; P. Carretta; M. Filibian; G. Zoppellaro; M. J. Graf; J. R. Galan-Mascaros; O. Fuhr; S. Brink; M. Ruben; *J. Am. Chem. Soc.*, **2009**, 131, 4387–4396, b) M. O. Liu; A. T. Hu; *J. Organomet. Chem.*, **2004**, 689 2450-2455.

[9] R. Weiss; J. Fischer; *The Porphyrin Handbook*, Vol. 16 (Eds.: K. M. Kadish, K. M. Smith, R. Guilard), Academic Press, San Diego, **2003**, 171–246.

[10] a) Y. Bian; R. Wang; J. Jiang; C.-H. Lee; J. Wang; D. K. P. Ng; *Chem. Commun.*, **2003**, 1194–1195; b) Y. Bian; R. Wang; D. Wang; P. Zhu; R. Li; J. Dou; W. Liu; C.-F. Choi; H.-S. Chan; C. Ma; D. K. P. Ng; J. Jiang; *Helv. Chim. Acta*, **2004**, 87, 2581–2596; c) R. Wang; Y. Li; R. Li; D. Y. Y. Cheng; P. Zhu; D. K. P. Ng; M. Bao; X. Cui; N. Kobayashi; J. Jiang; *Inorg. Chem.* **2005**, 44, 2114–2120.

[11] K. Yase; N. Yasuoka; T. Kobayashi; N. Uyeda; *Acta Cryst.*, **1988**, 44, 514-516.

[12] R. L. Carlin; *Magnetochemistry*, Springer-Verlag, Berlin Heidelberg, **1986.**

[13] H. Miyasaka; R. Clérac; T. Ishii; H.-C. Chang; S. Kitagawac; M. Yamashita; *J. Chem. Soc., Dalton Trans.*, **2002**, 1528–1534.

[14] N. F. Chilton; R. P. Anderson; L. D. Turner; A. Soncini; K. S. Murray; *J. Comput Chem.*, **2013**, 34, 1164-1174.

[15] G. A. Craig; J. J. Marbey; S. Hill; O. Roubeau; S. Parsons; M. Murrie; *Inorg. Chem.*, **2015**, *54* , 13–15.

[16] a) J. P. Costes; F. Dahan; W. Wernsdorfer; *Inorg. Chem.*, **2006**, 45, 5-7; b) Q. Wu; Y.-G. Li; Y.-H. Wang; R. Clérac; Y. Lua; E.-B. Wang; *Chem. Commun.*, **2009**, 5743–5745; c) Z. Lu; M. Yuan; F. Pan; S. Gao; D. Zhang; D. Zhu; *Inorg. Chem.*, **2006**, 45, 3538−3548.

[17] a) K. Kasuga; S. Takahashi; K. Tsukahara; T. Ohno; *Inorg. Chem.*. **1990**, 29, 354-356; b) K. Kasuga; M. Ando; H. Morimoto; *Inorg. Chim. Acta*, **1986**, 112 99-101; c) E. O. Tolkacheva; A. Y. Tsivadze; S. G. Bitiev; Y. G.

Gorbunova; V. I. Zhilov; V. V. Minin; *Zh. Neorg. Khim.*, **1995**, 40, 984; d) A. G. MacKay; J. F. Boas; G. J. Troup; *Aust. J. Chem.* **1974**, 27, 955-964.

[18] a) A. V. Ivanov; P. A. Svinareva; I. V. Zhukov; L. G. Tomilova; N. S. Zefirov; *Izv. Akad. Nauk., Ser. Khim*. **2003**, 1479; b) A. De Cian; M. Moussavi; J. Fisher; R. Weiss; *Inorg. Chem.*, **1985**, 24, 3162-3167.

[19] a) N. B. Subbotin; L. G. Tomilova; N. A. Kostromina; E. A. Luk'yanet; *Zh. Obshch. Khim.*, **1986**, 56, 397;b) V. N. Nemykin, A. Y. Tsivadze; N. B. Subbotin; N. A. Kostromina; S. V. Volkov; *Koord. Khim*. **1996**, 22, 315.

[20] a) N. Koike; H. Uekusa; Y. Ohashi; C. Harnoode; F. Kitamura; T. Ohsaka; K. Tokuda; *Inorg. Chem.*, **1996**, 35, 5798–5804; b) F. Nekelson; H. Monobe; Y. Shimizu; *Chem. Commun.*, **2006**, 3874–3876; c) C.-H. Lee; D. K. P. Ng; *Tetrahedron Lett.*, **2002**, 43, 4211–4214; d) S. Misumi; K. Kasuga; *Nippon Kagaku Zasshi,* **1971**, 92, 335; e) L. G. Tomilova; E. V. Chernykh; N. T. Ioffe; E. A. Luk'yanets. *Zh. Obshch. Khim*. **1983**, 53. 2594; g) K. L. Trojan; J. L. Kendall; K. D. Kepler; W. E. Hatfield; *Inorg. Chim. Acta,* **1992,** 795, 198-200; f) C. Clarisse; M. T. Riou; *Inorg. Chim. Acta,* **1987**, 130, 139; h) R. Wang; R. Li; Y. Bian; C.-F. Choi; D. K. P. Ng; J. Dou; D. Wang; P. Zhu; C. Ma; R. D. Hartnell; D. P. Arnold; J. Jiang; *Chem. Eur. J*. **2005**, 11, 7351 – 7357. i) G. Gümrükcü; M. Ü. Özgür; A. Altındal; A. R. Özkaya; B. Salih; Ö. Bekaroğlu; *Synthetic Metals,* **2011**, 161 112–123; j) Y. Gao; R. Li; S. Dong; Y. Bian; J. Jiang. *Dalton Trans.,* **2010**, 39, 1321–1327; h) D. Tanaka; N. Sumitani; T. Inose; H. Tanak; N. Ishikawa; T. Ogawa; *Chem. Lett.*, **2015**, 44, 668-670.

[21] a) J. Jiang; R. C. W. Liu; T. C. W. Mak; T. W. D. Chan; D K P Ng; *Polyhedron*, **1997**, 16, 515-520; b) J Jiang; J. Xie; M. T. M. Choi; Y. Yan; S. Sun; D. K. P. Ng; *J. Porphyrins Phthalocyanines*, **1999**, 3, 322-328; c) R. Aroca; R. E. Clavijo; C. A. Jennings; G. J. Kovacs; J. M. Duff; R. O. Loutfy; *Spectrochim. Acta, Part A*, **1989**, 45, 957-962; c) A. Iwase; C. Harnoode; Y. Kameda; *J. Alloys Compd*., **1993**, 192, 280-283; d) K. Takahashi; Y. Tomita; Y. Hada; K. Tsubota; M. Handa; K. Kasuga; K. Sogabe; T. Tokii; *Chem. Lett.*, **1992**, 21, 759-762. e) R. Wang; R. Li; Y. Bian; C. F. Choi; D. K. P. Ng; J. Dou; D. Wang; P. Zhu; C. Ma; R. D. Hartnell; D. P. Arnold; J. Jiang *Chem. Eur. J*. **2005**, 11 7351-7357.

[22] T. Gross; F. Chevalier; J. S. Lindsey; *Inorg. Chem*., **2001**, 40, 4762-4774.

[23] a) V. E. Pushkarev; E. V. Shulishov; Yu V. Tomilov; L. G. Tomilova; *Tetrahedron Lett*., **2007**, 48, 5269-5273; b) N. Ishikawa; Y. Kaizu; *Chem. Phys. Lett*., **1997**, 228, 625-632; b) R. Li. Wang; R. Li; Y. Zhang; X. Zhu; P. Lo; P.-C. Ng; D. K. P. Pan; N. Ma; C. Kobayashi; N. Jiang; J. *Chem. Eur. J*. **2006**, 12, 1475–1485.

[24] N. Kobayashi; *Coordination Chemistry Reviews*, **2002**, 227, 129-152.

[25] N. Ishikawa; O. Ohno; Y. Kaizu; H. Kobayashi; *J. Phys. Chem*., **1992**, 96, 8832–8839.

[26] D. Markovitsi; T.-H. Tran-Thi; R. Even; J. Simon; *Chem. Phys. Lett*., 137, **1987**, 107-202.

[27] N. Ishikawa; O. Ohno; Y. Kaizu, *Chem. Phys. Lett*., 180, **1991**, 51-56.

[28] a) P. Zhu; F. Lu; Na Pan; D. P. Arnold; S. Zhang; J. Jiang; *Eur. J. Inorg. Chem*., **2004**, 510-517; b) V. E. Pushkarev; A. Yu. Tolbin; N. E. Borisova; S. A. Trashin; L. G. Tomilova; *Eur. J. Inorg. Chem*., **2010**, 5254–5262; c) F. Guyon; A. Pondaven; P. Guenot; M. L'Her; *Inorg. Chem*. **1994**,3 3, 4787-4793.

[29] M. Gonidec; D. B. Amabilinoa; J. Veciana; *Dalton Trans*.**, 2012**, 41, 13632-13639.

[30] a) H. Konami; M. Hatano; *Chem. Phys. Lett*., **1990**, 165, 397-400; b) X. Li; D. Qi; C. Chen; L. Yang; J. Sun; H. Wang; X. Li; Y. Bian; *Dyes and Pigments* 101, **2014**, 179-185.

[31] a) L. E. Webb; E. B. Fleischer; *J. Chem. Phys*., **1965**, 43, 3100-3111; b) R. Mason; G. A. Williams; P. E. Fielding; *J. Chem. Soc., Dalton Trans*. **1978**, 676-683; c) M. K. Friedel; B. F Hoskins; R. L. Martin; S. A. Mason; *J. Chem. Soc., Chem. Commun*., **1970**, 400-401; d) L. H. Vogt; A. Zalkins; D. H. Templeton; *Inorg. Chem*., **1967**, 6, 1725-1730.

[32] a) A. T. Chang; J. C. Marchon; *Inorg. Chim. Acta,* **1981**, 53, 241-243; b) L. G. Tomilova; E. V. Chernykh; N. T Ioffe; , E. A Luk'yanets; *Zh. Obshch. Khim.,* **1983**, *53*, 2594.

[33] a) G. Ostendorp; H. Homborg; *Z. Anorg. Allg. Chem*., **1996**, vol. 622, 1222-1230; b) N. E. Galanin; L. A. Yakubov; G. P. Shaposhnikov; Russ. *J. Org. Chem*., **2008**, 44, 921-926; c) J. Jiang; D. P. Arnold; H. Yu; *Polyhedron*,**1999**, 18, 2129 –2139; d) F. Lu; M. Bao; C. Ma; X. Zhang; D. P. Arnold; J. Jiang; *Spectrochim. Acta* A **2003**, 59, 3273 – 3286; d) M. Bao; Y. Bian; L. Rintoul; R. Wang; D. P. Arnold; C. Ma, J. Jiang; *Vib. Spectrosc*., **2004**, 34, 283–291.

[34] a) K. Katoh; Y. Yoshida; M. Yamashita; H. Miyasaka; B. K. Breedlove; T. Kajiwara; S. Takaishi; N. Ishikawa; H. Isshiki; Y.- F. Zhang; T. Komeda; M. Yamagishi; J. Takeya; *J. Am. Chem. Soc*., **2009**, 131, 9967–9976; b) D. K. P. Ng; J. Jiang; *Chem. Soc. Rev*., **1997**, 26, 433 –442; c) J. W. Buchler; D. K. P. Ng; *The Porphyrin Handbook, Vol. 3* (Eds.: K. M. Kadish, K. M. Smith, R. Guilard), Academic Press, San Diego, **2000**, 245 –294; d) J. Jiang; K.

Kasuga; D. P. Arnold; *Supramolecular Photosensitive and Electroactive Materi*als (Ed.: H. S. Nalwa), Academic Press, New York, **2001**, 113 –210; e) W. R. Scheidt; Y. L. Lee; *Struct. Bonding*, **1987**, 64: 1-70.

[35] a) J. Tang; I. Hewitt; N. T. Madhu; G. Chastanet; W. Wernsdorfer; C. E. Anson; C. Benelli; R. Sessoli; A. K. Powell; *Angew. Chem. Int. Ed.*, **2006**, 45, 1729–1733; J. Tang; I. Hewitt; N. T. Madhu; G. Chastanet; W. Wernsdorfer; C. E. Anson; C. Benelli; R. Sessoli; A. K. Powell; *Angew. Chem.*, **2006**, 118, 1761–1765; b) S. Xue; X. H. Chen; L. Zhao; Y. N. Guo; J. Tang; *Inorg. Chem.*, **2012**, 51, 13264–13270; c) Y. X. Wang; W. Shi; H. Li; Y. Song; L. Fang; Y. Lan; A. K. Powell; W. Wernsdorfer; L. Ungur; L. F. Chibotaru; M. Shen; P. Cheng; *Chem. Sci.*, **2012**, 3, 3366 –3370; d) S. Y. Lin; Y. N. Guo; Y. Guo; L. Zhao; P. Zhang; H. Ke; J. Tang; *Chem. Commun.*, **2012**, 48, 6924–6926; e) I. J. Hewitt; Y. Lan; C. E. Anson; J. Luzon; R. Sessoli; A. K. Powell; *Chem. Commun.*, **2009**, 6765–6767; f) C. S. Liu; M. Du; C. E. Saçudo; J. Echeverria; M. Hu; Q. Zhang; L. M. Zhou; S. M. Fang; *Dalton Trans.*, **2011**, 40, 9366–9369; g) M. U. Anwar; S. S. Tandon; L. N. Dawe; F. Habib; M. Murugesu; L. K. Thompson; *Inorg. Chem.*, **2012**, 51, 1028–1034; h) Y. N. Guo; G. F. Xu; P. Gamez; L. Zhao; S. Y. Lin; R. Deng; J. Tang; H. J. Zhang; *J. Am. Chem. Soc.*, **2010**, 132, 8538–8539.

[36] a) P. H. Lin; T. J Burchell; R. Clérac; M. Murugesu; *Angew. Chem., Int. Ed.*, **2008**, 47, 8848–8851; b) H. L. C. Feltham; Y. Lan; F. Klöwer; L. Ungur; L. F. Chibotaru; A. K. Powell; S. Brooker; *Chem. Eur. J.*, **2011**, 17, 4362–4365; c) Y.-N. Guo; X.-H. Chen; S. Xue; J. Tang; *Inorg. Chem.*, **2012**, 51, 4035–4042; d) S. Xue, L. Zhao; Y.-N. Guo; J. Tang; *Dalton Trans.*, **2012**, 41, 351–353.

[37] a) K. Keiichi; U. Kaori; B. Brian K.; Y. Masahiro; *Science China Chemistry*; **2012**, 55, 918-925; b) M. Waters; F. Moro; I. Krivokapic; J; McMaster; J. van Slageren; *Dalton Trans.*, **2012**, **41**, 1128-1130.

[38] a) N. Ishikawa; M. Sugita; W. Wernsdorfer; *Angew. Chem., Int. Ed.*, **2005**, 44, 2931-2935.

[39] P.-E. Car; M. Perfetti; M. Mannini; A. Favre; A. Caneschi; R. Sessoli; *Chem. Commun.*, **2011**, 47, 3751–3753.

[40] H. L. C. Feltham; Y. Lan; F. Klower; L. Ungur; L. F. Chibotaru; A. K. Powell; S. Brooker; *Chem.-Eur. J.*, **2011**,17, 4362–4365.

[41] Y.-Z. Tong; C. Gao; Q.-L. Wang; B.-W. Wang; S. Gao; P. Chen; D.-Z. Liao; *Dalton Trans*. **2015**, 44, 9020–9026.

[42] a) X. Chen; S.-Q. Wu; A.-L. Cui; H.-Z. Kou; *Chem.Commun.*, **2014**, 50, 2120-2122; b) Z. Tomkowicz; M. Rams; M. Baanda; S. Foro; H. Nojiri; Y. Krupskaya; V. Kataev; B. Buchner S. K. Nayak; J. V. Yakhmi; W. Haase; *Inorg. Chem.*, **2012**, 51, 9983–9994; c) D. Zhang; L. Zhang; Y. Chen; H. Wang; Z.-H. Ni; W. Wernsdorfer; J. Jiang; *Chem. Commun.*, **2010**, **46**, 3550-3552; d) R. Ishikawa; K. Katoh; B. K. Breedlove; M. Yamashita; *Inorg. Chem.*, **2012**, 51, 9123–9131.

[43] a) S. Takamatsu; T Ishikawa; S. Koshihara; N. Ishikawa; *Inorg. Chem.*, **2007**, 46, 7250-7252; b) N. Ishikawa; Y. Mizuno; S. Takamatsu; T. Ishikawa; S. Koshihara; *Inorg. Chem.*, **2008**, 47, 10217–10219.

[44] P. N. Moskalev; I. S. Kirin; *Russ. J. Phys. Chem.*, **1972**, 46, 1019.

[45] A. G. Mac Kay; J. F. Boas; G. J. Troup; *Aust. J. Chem.*, **1974**, 27, 955.

General Conclusions

The subject of this thesis work has been the design and characterization of novel tetra-α-alkoxy substituted phthalocyanines and their metal (II/III) ion complexes with the aim of obtaining, on the one hand, novel discotic liquid crystals with enhanced mesogenic and optoelectonic behavior, and, on the other hand, novel SMMs.

After a conceptual introduction to liquid crystals, in particular columnar liquid crystals, and to single molecule magnets in **chapter I**, we show in **chapter II** that the fully regioselective synthesis of symmetric all-endo tetra-alkoxy-functionalized phthalocyanines and their metal ion complexes is possible under induction of columnar mesophases in convenient temperature ranges at moderate substituent sizes. The synthetic approach to follow is lithium-induced macrocyclization of 3-(2-alkylalkoxy)-phthalonitriles prior to transition metal ion insertion. Symmetrization of the aliphatic chains in the 3-alkoxy-phthalonitrile precursor from 2-butyloctyl to 2-pentylheptyl maintains both the regioselectivity and the mesomorphism, whereas shortening to 2-butylhexyl leads to the formation of a regioisomeric mixture during the cyclo-tetramerization and to a somewhat greater tendency to crystallization. $H_2Pc(OCH_2CHBuHex)_4$ and $H_2Pc(OCH_2CHPent_2)_4$, which clear at about 183 and 200°C respectively, show a liquid crystalline mesophase whose columnar order is maintained upon cooling to room temperature, whereas the shorter chain homolog $H_2Pc(OCH_2CHBu_2)_4$ (T_C = 209 °C) shows its hexagonal mesogenicity only at high temperature. In cases of $MPc(OCH_2CHBuHex)_4$, $MPc(OCH_2CHPent_2)_4$, the rectangular mesophase persists at room temperature, whereas for $MPc(OCH_2CHBu_2)_4$ the rectangular mesophase is maintained only at high temperature. All $MPc(OCH_2CHBuHex)_4$ homologues exhibit a small enthalpy liquid crystal to plastic crystal transition upon cooling to room temperature, which in the case of the metal-free homologue includes a transition from hexagonal to rectangular column lattice symmetry. In the case of $MPc(OCH_2CHPent_2)_4$, this transition could be inferred mainly from the appearance of additional peaks in the wide angle range of the powder X-ray pattern. But in $MPc(OCH_2CHBu_2)_4$, as revealed by DSC and SAXS analysis, a pronounced transition enthalpy from the columnar rectangular liquid crystal to the plastic crystal state could be detected. The nature of the metal ion exerts a strong influence on the thermal range of the columnar mesophase. The clearing temperature increases with the deviation from square-planarity coordination geometry of the metal ion, with passing from planar to octahedral or tetrahedral. The Zn homologs have the highest clearing temperatures of the three series of complexes presented in this chapter. The combination of attainable clearing temperatures with room temperature columnar stacking and a relatively high content of conjugated core within the molecular mass make the first two series of materials, i.e. ($MPc(OCH_2CHBuHex)_4$, and $MPc(OCH_2CHPent_2)_4$), potentially useful as uniformly orientable charge transporters in organic electronic devices.

In **chapter III** we establish that these tetra-α-alkoxy substituted phthalocyanine materials, as exemplified with $H_2Pc(OCH_2CHBuHex)_4$, $NiPc(OCH_2CHBuHex)_4$ and $CuPc(OCH_2CHBuHex)_4$, lead to original device performances when applied as an active organic layer in in simple ITO/PEDOT:PSS/PC/Al diode structures. A pronounced current rectification of the diodes is obtained despite the preponderantly planar alignment of the

columns in the films. The XRD, excited-state lifetime and optical absorption characterizations suggest that the π–π intermolecular interactions are stronger for $H_2Pc(OCH_2CHBuHex)_4$, whereas $CuPc(OCH_2CHBuHex)_4$ and $NiPc(OCH_2CHBuHex)_4$ presented better electrical responses, confirming that the metallic center plays an important role for the charge transport inside these materials.

In **chapter IV** we demonstrate with five new mononuclear phthalocyanine complexes – $FMnPc(OCH_2CH(Bu)_2)_4DMF$, $AcMnPc(OCH_2CH(Bu)_2)_4$, $Dy\{Pc(OCH_2CH(Bu)_2)_4Ac(DMF)_2$, $\{Bu_4N\}\{Dy[Pc(OCH_2CH(Bu)_2)_4]_2\}$ and the radical $[Dy\{Pc(OCH_2CH(Bu)_2)_4\}_2]^0$ – that well-defined single crystals of magnetically relevant metal (III) ions can be obtained using one of our symmetric tetra-endo-2-alkylalkoxy Pcs as ligand. Remarkably, regiospecific formation of the C_{4h} symmetric isomer of the double decker phthalocyanine is achieved due of the presence of the bulky tetra α-alkoxy-substituents on the Pc ring. The magnetic studies of $FMnPc(OCH_2CH(Bu)_2)_4$·DMF and $AcMnPc(OCH_2CH(Bu)_2)_4$ (Mn(III) high-spin, (S = 2)) reveal negative ZFS parameters: D_{Mn} = -2.64 cm^{-1} and D_{Mn}= -2.48 cm^{-1} respectively, and an intermolecular exchange interaction in $AcMnPc(OCH_2CH(Bu)_2)_4$ was found to be very weakly antiferromagnetic with J= -0.24 cm^{-1}. The observed uniaxial magnetic anisotropy leads to slow magnetic relaxation in the presence of an applied dc field. For compounds $Dy\{Pc(OCH_2CH(Bu)_2)_4$ Ac $(DMF)_2$ and $\{Bu_4N\}\{Dy[Pc(OCH_2CH(Bu)_2)_4]_2\}$ we could show that the dynamical magnetism of the single Dy-ionic SMMs is greatly altered by the modification of the ligand field. At zero-*dc* field the magnetization dynamics for $Dy\{Pc(OCH_2CH(Bu)_2)_4$ Ac $(DMF)_2$ is clearly dominated by QTM, whereas the relaxation times for $\{Bu_4N\}\{Dy[Pc(OCH_2CH(Bu)_2)_4]_2\}$ indicate an increasing influence of quantum relaxation pathways with decreasing temperature. Since double decker phthalocyanines can exist in a variety of different modifications such as anionic, radical, protonated and oxidized forms, a considerable leeway exists for the further elaboration and modification of the magnetic properties of such highy soluble regularly alkoxy-decorated sandwich type complexes.

Annex

A1: Physico-chemical methods

Elemental analysis (EA)

Elemental analyses (C, H and N) were performed following the classical Pregl–Dumas technique on a ThermoFischer Flash EA 1112 instrument at the Institut de Chimie de la Matière Condensée de Bordeaux (ICMCB). The results of this microanalysis are shown in mass fractions of each element in the compound.

Fourier transformed infrared (FT-IR) analysis

The FT-IR spectra were recorded between 4000 and 550 cm^{-1} on a Thermal Scientific Nicolet™ 6700 ATR (attenuated total reflectance) spectrometer equipped with a Smart iTR diamond window.

Nuclear magnetic resonance

^1H NMR spectra were collected with JEOL ECS 400 instrument at room temperature, using $CDCl_3$ or CD_2Cl_2 as solvent. Chemical shifts of ^1H NMR signals were quoted to internal standard TMS (δ = 0.00 ppm) and expressed as chemical shifts in ppm (δ), multiplicity, coupling constant (Hz), and relative intensity.

Single crystal X-ray analysis

The X-ray diffraction data for the single crystals of $FePc(OCH_2CHBuHex)_4(DMF)_2$, $ZnPc(OCH_2CH(Pent)_2)_4DMF$, $ZnPc(OCH_2CH(But)_2)_4DMF$, $FMn(III)Pc(OCH_2CH(Bu)_2$, $AcOMn(III)Pc(OCH_2CH(Bu)_2$, $DyPc(OCH_2CH(Bu)_2)_4Ac(DMF)_2$ and $DyPc(OCH_2CH(Bu)_2)_4$ were collected with a Bruker APEX II diffractometer, using graphite monochromated MoK_α radiation (λ = 0.71073 Å).

The data were collected using a routine to survey reciprocal space, and were indexed by the APEX II program [i].The structure was solved by direct methods and refined by least squares on F^2 with SHELXL-97 [ii]. All non-hydrogen atoms were refined anisotropically. Hydrogen atoms were assigned to ideal positions using the appropriate HFIX command in SHELXL-97.

Small and wide angle X-ray scattering (SAXS)

X-Ray scattering experiments at small and wide angles were collected on a home-made experimental set-up equipped with a Rigaku Nanoviewer (XRF microsource generator, MicroMax 007HF), with an 1200-W rotating anode (λ = 1.54180 Å) coupled to a confocal Max-FluxH Osmic mirror (Applied Rigaku Technologies) and a MAR345 image plate detector (Marresearch GmbH). The studied samples were mounted in glass capillaries of 1 mm diameter. Diffraction patterns were integrated with the FIT2D software [3].

Polarized optical microscopy

The thermal behavior and the optical textures of the compounds were studied with an Olympus BX51TRF polarizing microscope equipped with a Mettler Toledo FP82HT hot-stage.

Differential scanning calorimetry

The transition temperatures and enthalpies changes were measured by differential scanning calorimetry with a Q2000 TA instrument. DCS traces were recorded at different scanning rates, from 2 to 10 K/min in a nitrogen environment. Measurements were carried out using closed Tzero aluminium pans. Calibration of temperature and melting enthalpy was performed with an indium and tin sample. Transition enthalpies changes were deduced by integration of the DSC peaks after polynomial baseline corrections.

Spectroscopic techniques

UV/Vis spectra were recorded between 300 and 900 nm using a Unicam UV4 recording spectrophotometer and in the range 300-900 nm on a with PerkinElmer UV-Vis/NIR spectrometer, Lambda 950, Detectors: PMT/ PbS.

A SpectroVision UV-vis spectrophotometer, model DB-1880S, was used to record the absorption spectra of the PCs in solution and spin-coated films.

For emission measurements, a Hitachi fluorescence spectrophotometer, model F-7000, was used, with the samples excited at a wavelength of 636 nm. Time-resolved fluorescence decay curves were recorded using the technique of time-correlated single photon counting [4] on a FluoTime 200 (PicoQuant). Excitation was provided using a pulsed diode laser (instrument response function around 100 ps, 20 MHz repetition rate) at a wavelength of 636 nm. Fluorescence was collected perpendicular to excitation and passed through a polarizer set at the magic angle. The detection system consisted of a monochromator and a MCP-PMT photomultiplier (Hamamatsu R3809U-50). FluoFit software was used to analyze the decay curves, and the plots of weighted residuals and reduced chi-square (χ^2) were used to accurately determine the quality of the fittings during the analysis procedure.

Atomic Force Microscopy

The thickness and roughness of the spin-coated films were probed by atomic force microscopy (AFM), using the Nanosurf EasyScan2 apparatus in tapping mode with a scanning rate of 1.0 Hz covering a size of 20 μm × 20 μm with (512 × 512) pixels.

Electric measurements of diodes

The *J*/*V* curves were measured under ambient conditions and at room temperature (25 °C) using Keithley's Series 2400 Source Measure Unit (SMU) Instruments.

Magnetic measurements

Magnetic susceptibility measurements were carried out on a Quantum Design SQUID magnetometer MPMS-XL (CRPP) operating between 1.8 and 300 K for applied dc fields ranging from -7 to 7 T. Measurements in solid state were performed on microcrystalline samples. Magnetic data was corrected for the sample holder and diamagnetic contributions for all magnetic measurements..

Cyclic voltammetry

Cyclic voltammetry (CV) was performed in a three-electrode cell, utilizing an Autolab PGStat20 potentiostat, driven by GPES software (General Purpose Electrochemical System, Version 4.4, EcoChemie B.V., Utrecht, the Netherlands), a platinum wire counter-electrode, a 1.6 mm platinum disc working electrode, and a non-aqueous reference electrode that is comprised of a silver wire in a 0.01 M solution of $AgNO_3$ and 0.1 M tetrabutylammonium perchlorate in acetonitrile; the analytes (approximately 1 mM) were dissolved in DCM supplemented with 0.1 M tetrabutylammonium hexafluorophosphate and degassed by bubbling argon prior to measurement.

A2: List of abbreviations

1D	One-dimensional
2D	Two-dimensional
3D	Three-dimensional
μ_0	Charge mobility
ac	Alternating current
Col	Columnar
Col_h	Columnar hexagonal
Col_o	Columnar oblique
Col_r	Columnar rectangular
Cr	Crystal/crystalline phase
dc	Direct current
DMF	N,N-dimethylformamide
DSC	Differential scanning calorimetry
EA	Elemental analysis
FT-IR	Fourier transform infrared spectroscopy
HS	High spin
HT	High temperature
I	Isotropic phase
JT	Jahn-Teller
LCs	Liquid crystals
LED	Light emitting diode
LS	Low spin
LT	Low temperature
N_D	Discotic nematic
NMR	Nuclear magnetic resonance
Pc	Phthalocyanine
POM	Polarized optical microscopy
SAXS	Small angle X-ray scattering
Sm	Smectic phase
SMM	Single-molecule magnet
SIM	Single-ion magnet
S_T	Spin ground state
TBA	Tetrabutylammonium
THF	Tetrahydrofurane
XRD	X-ray diffraction
QTM	Quantum tunneling of magnetization

A3: Physical constants

	Symbol	Value	Units SI	CGS
Avogadro constant	N_A	6.02217	10^{23} mol^{-1}	
Boltzmann constant	k_B	1.38062	10^{-23} J·K^{-1}	10^{-21} erg·G^{-1}
Bohr magneton	μ_B	9.27410	10^{-24} J·T^{-1}	10^{-16} erg·K^{-1}
Electron volt	eV	1.60219	10^{-19} J	10^{-11} erg
Vacuum permeability	μ_0		$4\pi10^{-7}$ N·A^{-2}	1
Molar gas constant	R	8.31446	J·mol^{-1}·K^{-1}	10^{7} erg·mol^{-1}·K^{-1}

References:

[1] Bruker-AXS APEX2, SADABS, and SAINT Software Reference Manuals, Madison, Wisconsin, USA, 2009.

[2].G. M Sheldrick;. *Acta Cryst*. **2008**, *A64*, 112-122.

[3] a) A. P. Hammersley; *ESRF Internal Report, ESRF97HA02T*, **1997**; (b) www.esrf.eu/computing/scientific/FIT2D/

[4] D. V. O'Connor and D. Phillips, *Time-correlated single photon counting*, Academic, London, **1984**.

Résumé

Des systèmes cristallins liquides ne sont non seulement intéressants grâce à leur anisotropie et leur réorientabilité dans un champ électrique qui les rendent utiles dans les écrans plats [1], mais aussi grâce à leurs mobilités de charges élevées qui les rendent intéressants comme semi-conducteurs organiques anisotropes dans une variété de dispositifs électroniques. En particulier les cristaux liquides colonnaires constitués de molécules aromatiques en forme de disque se sont avérés être des transporteurs de charges unidimensionnels efficaces grâce aux fortes interactions π-π intermoléculaires [2], dans des dispositifs comme les cellules photovoltaïques, diodes électroluminescentes et transistors à effet de champ organiques. Un avantage spécifique des cristaux liquides colonnaires est que la mise en forme des colonnes est possible par des techniques variées (recuit thermique, dépôt de couches de Langmuir-Blodgett ou par étalement en zones, etc.) pour obtenir un alignement particulier souhaité (colonnes parallèles ou perpendiculaires à la surface du substrat). Dans ce contexte, les phtalocyanines sont une classe de matériaux particulièrement prometteurs. Depuis les premiers travaux de Piechocki et al. en 1982 [3], un nombre significatif de phtalocyanines mésogènes avec huit substituants linéaires alkyl [4], alkoxyméthyl [5] et alkoxy [6] en positions périphériques (β) a été décrit avec des transitions de l'état cristallin à l'état cristallin liquide à des températures élevées, et des températures de transition à l'état liquide à des températures extrêmement hautes, au-delà de 300°C. À coté des facteurs stériques, des fortes interactions électroniques semblent être déterminants pour la stabilité thermique de la mésophase. Les dispositifs optoélectroniques sont habituellement utilisés à température ambiante, donc il est souhaitable que la mésophase persiste à température ambiante. Les phtalocyanines tétra-substitués se distinguent de leurs homologues octa-β-substitués en ce qu'ils sont habituellement obtenus comme mélanges de quatre régio-isomères lors de la réaction de cyclo-tétramérisation du précurseur phtalique monosubstitué [7]. La présence d'un tel mélange de régio-isomères baisse la température de fusion par rapport aux homologues octa-substitués plus symétriques, car elle gène la cristallisation. Dans certains cas, la présence de chaînes latérales ramifiées volumineuses déstabilise l'empilement colonnaire et baisse ainsi la température de clarification, rendant ainsi possible des recuits thermiques proche de la température de clarification [8]. Les séries des phtalocyanines octa-β-alkoxy-substitués, abrégés MPc-$(OC_n)_8$, avec une variété de métaux centraux et avec une variété de longueurs de chaînes alkyl, se caractérisent par une très grande stabilité thermique de la mésophase, qui s'étend sur plus de 250°C. L'effet de la substitution périphérique ou non-périphérique a été étudié par Ahsen et al. [10], qui ont trouvé que tandis que des phtalocyanines tétra-β-substitués avec des chaînes ramifiées 13,17-dioxanonacosan-15-yloxy montrent une mésophase hexagonale colonnaire (Col_h) sur des larges plages thermiques incluant la température ambiante, leurs homologues α-substitués ne sont pas mésogènes et sont des huiles visqueuses à température ambiante. Ceci nous a laissé postuler qu'avec des α-substituants plus modérément ramifiés, une organisation mésomorphe colonnaire à température ambiante combinée avec une température de clarification modérée est atteignable.

La cyclo-tétramérisation de 3-alkoxy-phtalonitriles donne un mélange de quatre régioisomères, parmi lesquels l'isomère le plus symétrique, le 1,8,15,22-tétrasubstitué de symétrie C_{4h}, se forme statistiquement avec

un rendement de 12.5%, tandis que l'isomère le moins symétrique, le 1,8,15,25-tétrasubstitué de symétrie C_s, se forme avec un rendement de 50%, si les effects stériques et électroniques sont négligeables. Rager et al. [11] ont montré qu'en présence d'ions métalliques de transition comme le Ni(II) ou le Cu(II), les rendements réellement observés de ces isomères C_{4h} et C_s sont en effet proches des valeurs statistiquement attendus. Par contre, ils ont pu observer aussi que si le 3-(2-ethylhexyloxy)phtalonitrile est tétramérisé avec de l'alcoolate de lithium en absence d'ions métalliques de transition, l'isomère stériquement favorisé de symétrie C_{4h} se forme avec un rendement relatif de 87%, accompagné de 11% de l'isomère C_s statistiquement favorisé ainsi que de 2% de l'isomère C_{2v} (1,8,18,25-substitué), tandis que l'isomère D_{2h} (1,11,15,25-substitué), stériquement le moins favorisé, n'est pas observé. Comme la présence de plusieurs régioisomères est à éviter si on souhaite un matériau électroniquement homogène, l'observation de tels mélanges pose un défi synthétique. Ainsi un objectif majeur de ce travail de thèse a été la conception, la synthèse et l'étude des propriétés physico-chimiques de phtalocyanines tétra-α-substitués régioréguliers de métaux II et III. À coté de cela, la tétrasubstitution en positions α encombrants offre l'opportunité d'ajuster les plages thermiques des mésophases à fin d'obtenir des températures de clarification convenables et une persistance de l'ordre colonnaire à température ambiante en ajustant la gène stérique des substituants, sans devoir avoir recours à des substituants très volumineux qui dilueraient outre mesure la proportion massique du centre électroniquement intéressant de la molécule. En outre, nous nous sommes aussi intéressés au comportement électronique de ces phtalocyanines régioréguliers en diodes organiques assemblés depuis des solutions.

Cette thèse est constituée de quatre chapitres dédiés aux semi-conducteurs organiques cristallins liquides colonnaires à base de tétra-α-alkoxy-phtalocyanines et aux molécules-aimants à ions centraux Mn(III) et Dy(III) entourés de ligands tétra-α-alkoxy-phtalocyanines.

Les concepts de base des cristaux liquides et du magnétisme moléculaire sont exposés dans le chapitre I. Dans le chapitre II, nous présentons notre stratégie synthétique pour obtenir des tétra-α-alkoxy-phtalocyanines régioréguliers en utilisant trois chaînes alkoxy ramifiées différentes, une racémique et deux symétriques : rac-2-butyloctyloxy, 2-pentylheptyloxy et 2-butylhexyloxy. À coté des composés sans ion métallique central, nous traitons des complexes de Co(II), Ni(II), Cu(II) et Zn(II) en étudiant leur comportement mésogène. Notre approche synthétique est présentée dans le schéma **R.1**.

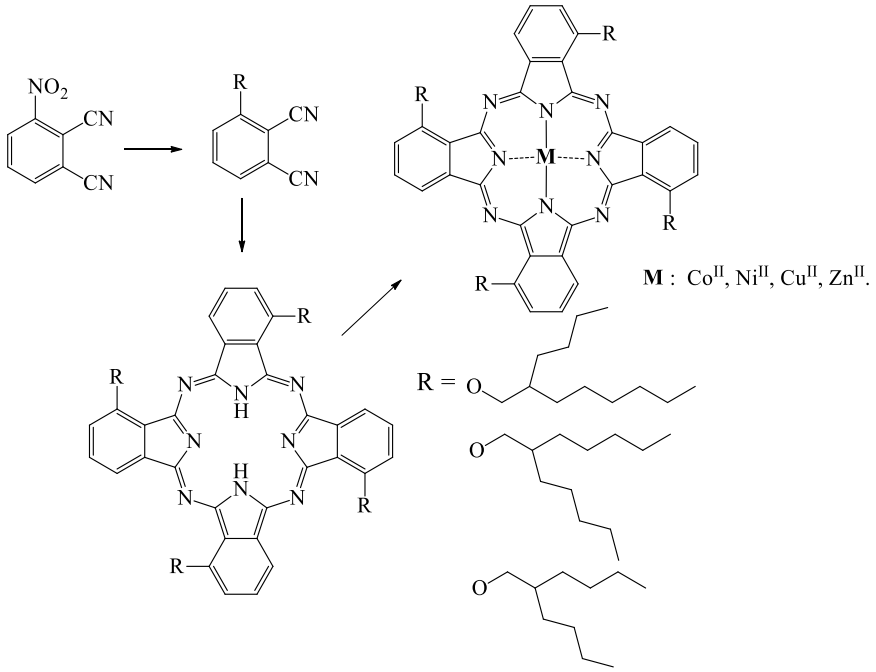

Schéma R.1. Synthèse de phtalocyanines 1,8,15,22,-tetra-alkoxy-substitués et de leurs complexes de métaux(II).

Après avoir trouvé que la chaîne rac-2-butyloctyloxy, légèrement plus volumineuse que la chaîne rac-2-ethylhexyloxy de Rager et al., induit une régiosélectivité totale et un bon comportement mésogène, nous avons choisi deux chaînes symétriques, avec une masse pareille ou légèrement inférieure que la chaîne rac-2-butyloctyloxy, pour les raisons suivantes : (i) pour trouver la taille minimale du substituant qui induit encore une régiosélectivité totale, et (ii) pour analyser l'influence du caractère racémique ou symétrique de la ramification, ainsi que de la taille du substituant, sur la plage thermique de la mésophase. Les alcools symétriquement ramifiés ont été synthétisés selon des procédures décrites pour des composés similaires [12] et représentées dans le schéma **R.2**.

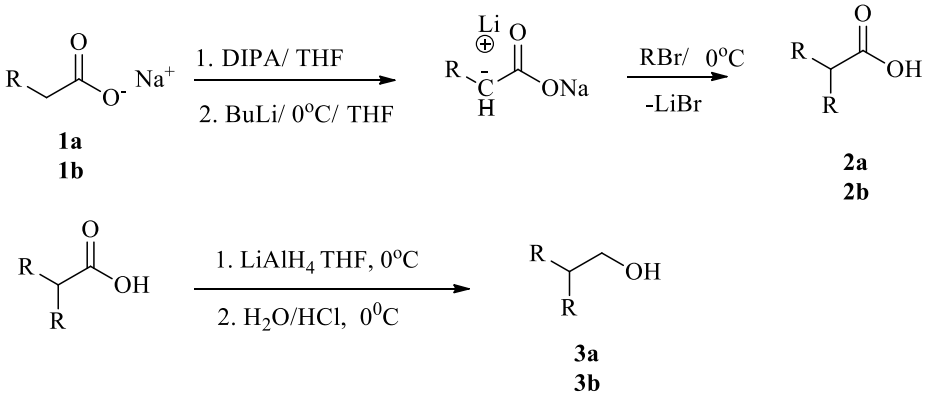

Schéma II.2. Synthèse d'alcools β-ramifiés

Ainsi quinze tetra-alkoxy-phtalocyanines ont été obtenus et caractérisés convenablement. Les températures de transition de la mésophase à la phase liquide isotrope montent légèrement dans l'ordre rac-2-butylhexyloxy – 2-pentylheptyloxy – 2-butylhexyloxy, p.ex. $H_2Pc(OCH_2CHBuHex)_4$: 192°C, $H_2Pc(OCH_2CHPent_2)_4$: 200°C et $H_2Pc(OCH_2CHBu_2)_4$: 209°C, tandis que la tendance à former un état cristallin à température ambiante augmente dans le même ordre. Tandis que les homologues sans ion métallique

montrent une mésophase colonnaire hexagonale, les homologues métallisés montrent tous une mésophase colonnaire rectangulaire, témoignant d'interactions métal-azote intermoléculaires qui induisent un empilement décalé et donc une inclinaison des normales aux disques moléculaires par rapport à l'axe de la colonne. Des textures observées par microscopie optique polarisante avec les dérivés non-métallisés à température ambiante après refroidissement du liquide isotrope, ainsi que leurs thermogrammes calorimétriques et leurs diffractogrammes de rayons X sur poudres sont représentés dans la Figure **R.1**.

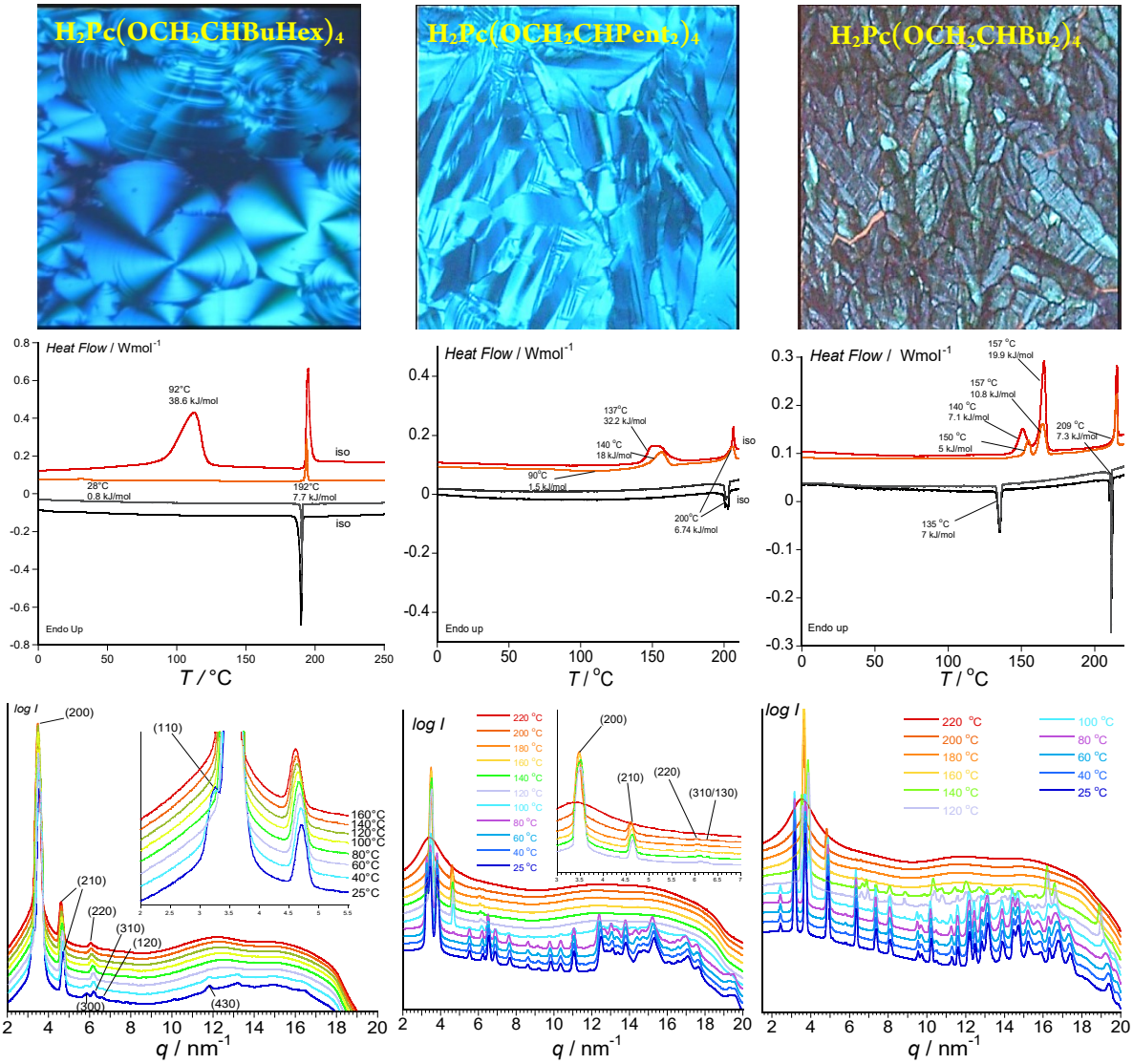

Figure R.1. Textures observées par microscopie polarisante à T ambiante, thermogrammes de calorimétrie différentielle et spectres de diffraction de rayons X sur poudres. De gauche à droite: $H_2Pc(OCH_2CHBuHex)_4$, $H_2Pc(OCH_2CHPent_2)_4$, $H_2Pc(OCH_2CHBu_2)_4$.

Tous les matériaux ont été caractérisés par calorimétrie différentielle entre 0 et 330°C ainsi que par diffraction des rayons X sur échantillons poudre; les résultats sont résumés dans le tableau **R.1.**

	Matériau	Séquence de phases (haut : premier chauffage d'un échantillon vierge, bas : deuxième chauffage) [°C]	Enthalpie de clarification $H_{col\text{-}iso}$ [Kj mol^{-1}]
MPc(OCH$_2$CHBuHex)$_4$	H_2Pc (3a)	cr-84-col_h-192-iso $col_{r,p}$-28-col_h-192-iso	7.7
	Fe (4a)	cr-36-col-280-iso col-280-iso	12.0
	Co (5a)	cr-54-col_r-294-iso $col_{r,p}$-42-col_r-294-iso	12.2
	Ni (6a)	cr-63-col_r-237-iso $col_{r,p}$-45-col_r-237-iso	9.2
	Cu (7a)	$col_{r,p}$-70-col_r-268-iso $col_{r,p}$-70-col_r-268-iso	12.7
	Zn (8a)	cr-96-col_r-297-iso cr-80-col_r-297-iso	14.8
MPc(OCH$_2$CHPent$_2$)$_4$	H_2Pc (3b)	cr-137-col_h-200-iso $col_{r,p}$-140-col_h-200-iso	6.7
	Co (4b)	cr-173-col_r-310-iso $col_{r,p}$-310-iso	12.0
	Ni (5b)	cr-160-col_r-255-iso $col_{r,p}$-255-iso	8.0
	Cu (6b)	cr-162-col_r-292-iso $col_{r,p}$-292-iso	11.3
	Zn(7b)	cr-75-col_r-312-iso $col_{r,p}$-312-iso	14.1
MPc(OCH$_2$CHBu$_2$)	H_2Pc (3c)	cr-140-col_h-209-iso cr-150-col_h-209-iso	7.0
	Co (4c)	cr-146-col_r-328-iso $col_{r,p}$-160-col_r-328-iso	14.2
	Ni (5c)	cr-168-col_r-270-iso $col_{r,p}$-153-col_r-270-iso	11.2
	Cu (6c)	cr-150-col_r-305-iso $col_{r,p}$ -190-col_r-305-iso	14.0
	Zn (7c)	cr-158-col_r-326-iso $col_{r,p}$ -187-col_r-326-iso	13.4

Table R.1. Propriétés thermiques des tetra-α-alkyloxy-phthalocyanines. cr = crystallin, col_h = cristal liquide colonnaire hexagonal; col_r = cristal liquide colonnaire rectangulaire; $col_{r,p}$ = cristal plastique colonnaire rectangulaire; iso = liquide isotrope.

La mésophase hexagonale observée avec les homologues non-métallisés est atypique car elle contient douze colonnes dans la maille hexagonale bidimensionnelle, tandis que la mésophase hexagonale de loin la plus répandue n'en contient que trois colonnes ; la mésophase rectangulaire observée avec les homologues métallisés par contre est conventionnelle, avec deux colonnes par maille rectangulaire (Figure **R.2**). Tous les homologues rac-2-butyloctyloxy montrent une transition de cristal liquide à cristal plastique de petite enthalpie en refroidissant à température ambiante, ce qui inclut dans le cas de l'homologue non-métallisé une transition de la symétrie du réseau de colonnes d'hexagonal à rectangulaire. Dans le cas des homologues 2-pentylheptyloxy, cette transition est déduite en premier lieu de l'apparence de pics supplémentaires à grands angles dans le

diffractogramme de rayons X, tandis que dans le cas des homologues 2-butylhexyloxy, une large enthalpie de transition est apparente dans le thermogramme calorimétrique. Les températures de clarification des homologues métallisés augmentent avec le changement de la géométrie de coordination préférée de l'ion métallique de plan-carré à octaédrique ou tétraédrique, en suivant l'ordre Ni < Cu < Co ≤ Zn.

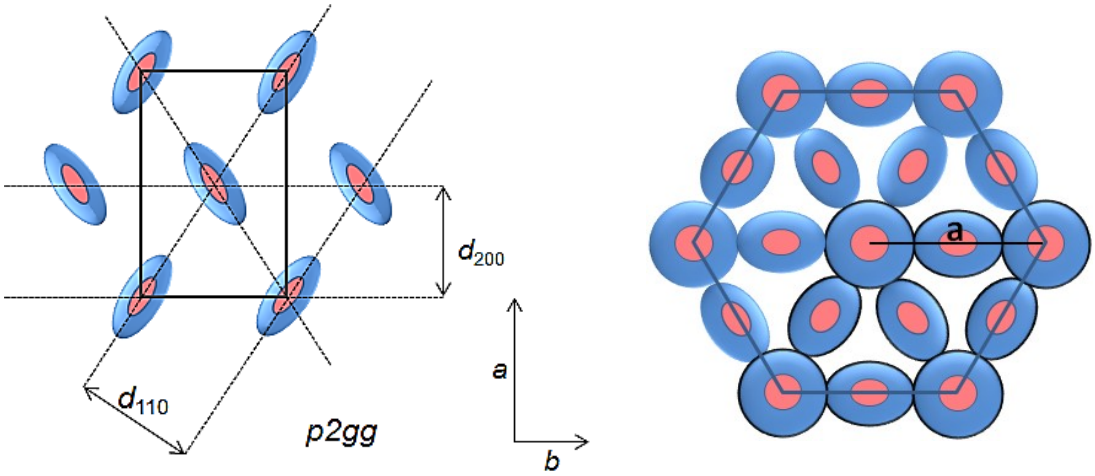

(a) (b)

Figure R.2. Illustrations des bissections des colonnes (a) dans un réseau colonnaire rectangulaire de symétrie *p2gg* ; (b) dans un réseau hexagonal à douze colonnes par maille hexagonale. Les colonnes à disques inclinés ont des bissections ovales, tandis que les colonnes à disques non-inclinés ont des bissections circulaires.

La présence d'une structure fortement ordonnée colonnaire à température ambiante qui se forme sans réorientation macroscopique depuis la mésophase à plus haute température prédestine ces matériaux à l'utilisation comme couche semi-conductrice dans des dispositifs électroniques organiques. Nous utilisons ainsi dans le chapitre III trois de ces matériaux, $H_2Pc(OCH_2CHBuHex)_4$ (**3a**), $NiPc(OCH_2CHBuHex)_4$ (**6a**) et $CuPc(OCH_2CHBuHex)_4$ (**7a**), comme couches actives dans des diodes de structure simple ITO/PEDOT:PSS/Pc/Al (Figure **R.3**).

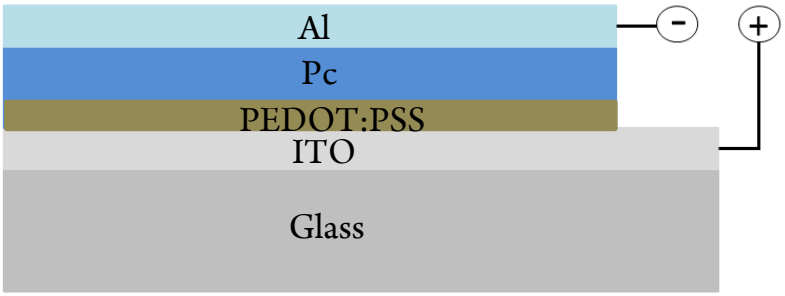

Figure R.3. Illustration schématique de la structure des diodes étudiées.

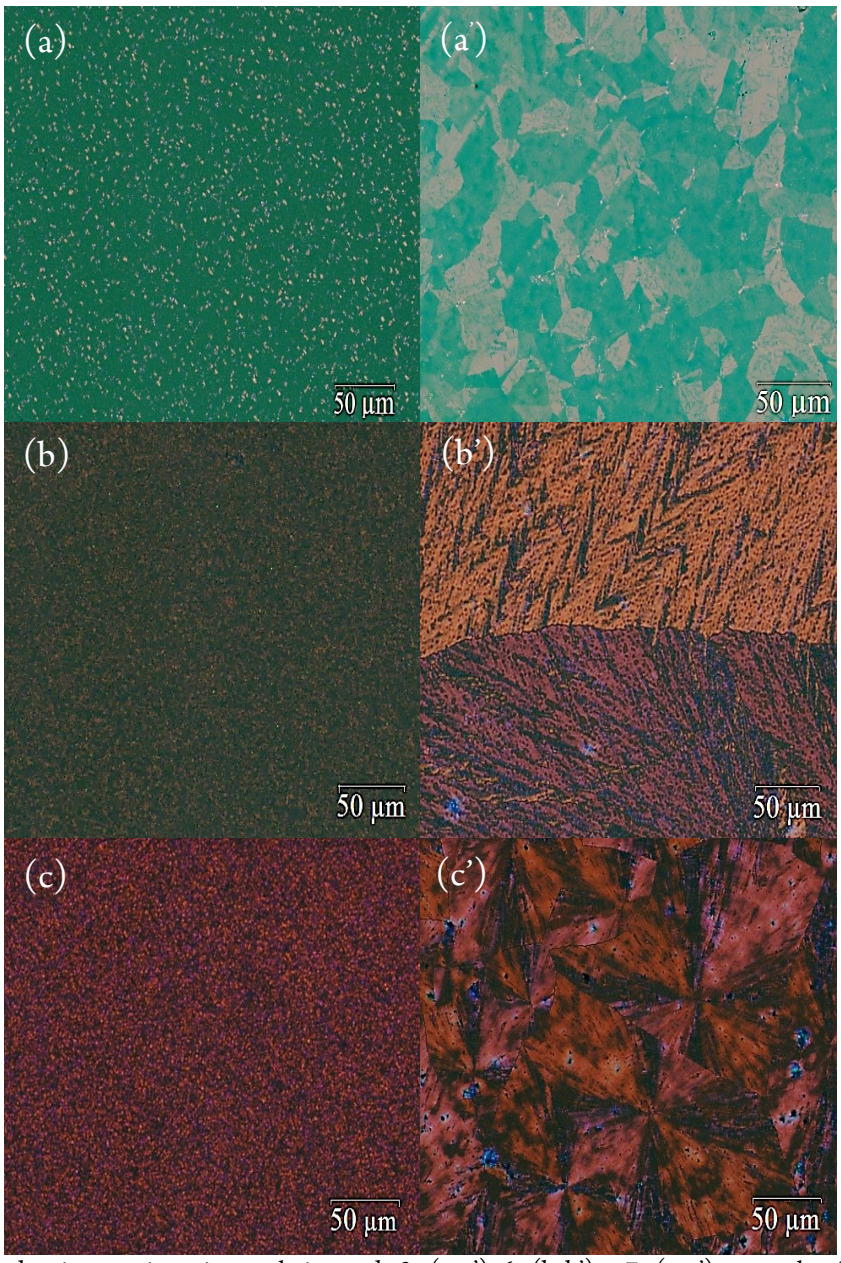

Figure R.4. Textures de microscopie optique polarisante de **3a** (a, a'), **6a** (b, b') et **7a** (c, c') en couches fraichement déposées (a, b, c) et après refroidissement rapide depuis la phase liquide isotrope (a', b', c').

Pour la fabrication des diodes, des verres à couche d'oxyde d'indium et d'étain (ITO) ont été utilisés comme substrats, sur lesquels une couche de polymère ionique conducteur PEDOT:PSS a été déposée par tournette, suivi du dépôt par tournette d'une couche de phtalocyanine (300 nm). Les électrodes supérieures en Al (80 nm) ont été déposées sous vide (10^{-7} mbar) avec une vitesse de dépôt de 1 Ås^{-1}. Des textures non-spécifiques consistantes de petits domaines biréfringents ont été observées dans les couches fraichement déposées (Figure **R.4**), et un traitement thermique en forme de refroidissement rapide depuis les températures de la phase liquide isotrope (**3a**: 192°C, **6a**: 237°C, and **7a**: 268 °C) induit des textures biréfringentes typiques pour un alignement planaire sur la surface (axes des colonnes parallèles au plan du substrat) (Figure **R.4(a', b', c')**). Les caractérisations électriques des diodes ont été faites à température et sous atmosphère ambiantes. Les caractéristiques courant-tension (J–V) sont représentés dans la Figure **R.5**. À notre surprise, les diodes faites de

chacune des trois homologues **3a, 6a** et **7a** montrent des ratios de redressement supérieurs à mille (Figure **R.5** (**a**)).

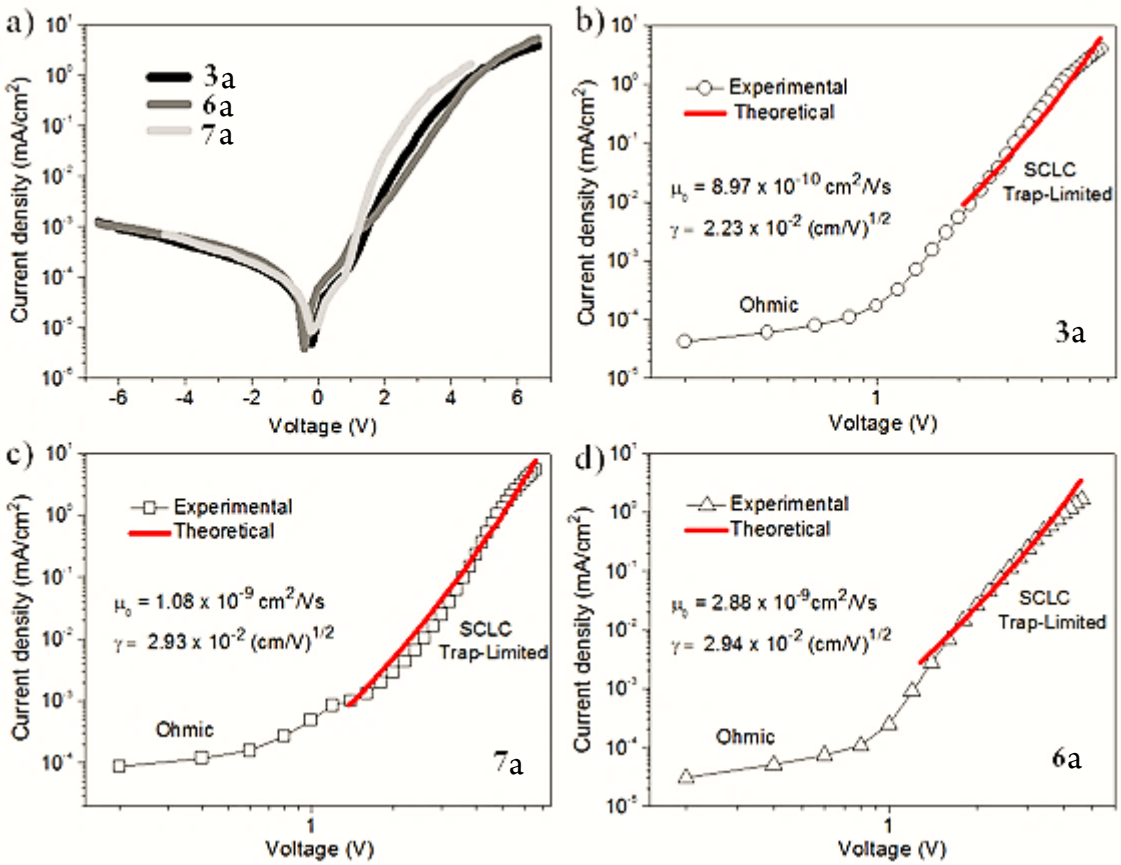

Figure R.5. Caractérisation électrique des diodes de structure ITO – PEDOT:PSS (80 nm) – PC (300 nm) – Al (80 nm); densité de courant sur tension. (a): représentation comparative semi-logarithmique; (b), (c) et (d): représentations doublement logarithmiques pour les composés **3a**, **7a** et **6a**. Les lignes rouges sont des modélisations dans le régime SCLC (courant limité par charge d'espace) limité par les pièges.

Ces ratios de redressement sont beaucoup plus élevées que celles préalablement observées pour une phtalocyanine de Zn colonnaire hexagonale moins régulièrement substituée avec une périphérie alkyl beaucoup plus volumineuse [13], qui montrait des ratios de redressement inférieurs à dix dans une configuration de dispositif très similaire avec des électrodes ITO/PEDOT:PSS et Ca/Al. Le redressement important pourrait résulter de l'empilement moléculaire proche et régulier dans les phases de cristal plastique colonnaire des matériaux **3a**, **6a** et **7a** [14], qui permet des interactions intimes intermoleculaires entre orbitales π ainsi qu'entre métaux et azotes, qui à leur tour favorisent une évacuation efficace des charges après injection, ce qui évite la formation d'un contre-champ qui anéantirait la géométrie intrinsèque de redresseur. Figure **R.5** (**b**)-(**d**) montre les courbes J-V doublement logarithmiques. Les densités de courant suivent un régime ohmique à basses tensions et un régime de courant limité par charge d'espace (SCLC) limité par les pièges à plus hautes tensions, dans lequel domine le courant qui résulte de l'injection des charges depuis les électrodes. Comme les courbes ne suivent pas la loi de Mott–Gurney ($J \propto V^2$), les mobilités de charges ont été obtenues directement des courbes *J*–*V* dans le régime SCLC limité par les pièges en appliquant un modèle théorique développé auparavant [15]. Ce modèle considère une mobilité dépendante du champ électrique, $\mu(E) = \mu_0 e^{\gamma\sqrt{E}}$, où μ_0 est la mobilité à

champ nul et γ la dépendance de la mobilité du champ. La dépendance de la mobilité du champ est représentée dans la figure **R.6.** La mobilité ainsi obtenue est plus grande pour les deux homologues métallisés, ce qui est cohérent avec le fait que le centre métallique et ses interactions avec les azotes des molécules voisins jouent un rôle important dans le transport des charges dans la couche organique. Des phtalocyanines non-mésogènes de Ni(II) et Cu(II) montrent généralement des mobilités supérieures à leurs homologues non-métallisés [16].

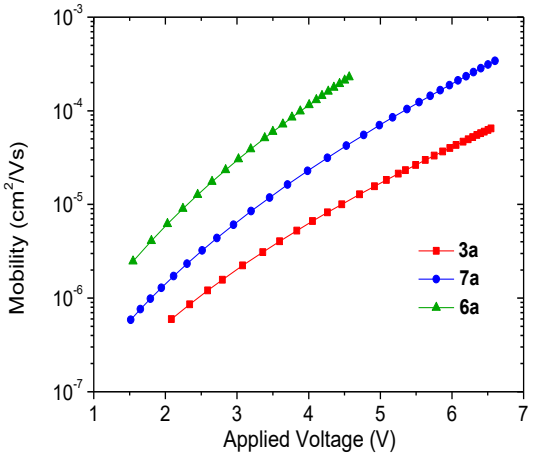

Figure R.6. Mobilité pour $H_2Pc(OCH_2CHBuHex)_4$ (**3a**), $NiPc(OCH_2CHBuHex)_4$ (**6a**) et $CuPc(OCH_2CHBuHex)_4$ (**7a**) dans le régime SCLC en fonction de la tension.

S'ils incluent un ion métallique paramagnétique, les phtalocyanines peuvent montrer des comportements magnétigues originaux tels que des propriétés de molécules-aimants (SMMs) [17]. La bonne solubilité de nos tetra-α-alkoxy-phtalocyanines peut permettre l'élaboration de tels matériaux. Ainsi, dans le chapitre IV, les cinq nouveaux complexes mononucléaire $FMnPc(OCH_2CH(Bu)_2)_4$·DMF (**1**), $AcMnPc(OCH_2CH(Bu)_2)_4$ (**2**), $Dy\{Pc(OCH_2CH(Bu)_2)_4Ac(DMF)_2$ (**3**), $\{Bu_4N\}\{Dy[Pc(OCH_2CH(Bu)_2)_4]_2\}$ (**4**) et le radical $[Dy\{Pc(OCH_2CH(Bu)_2)_4\}_2]^0$ (**4***) ont été synthétisés, structurellement caractérisés et leurs propriété magnétiques étudiés. Les complexes de manganèse **1** et **2** à géométrie pyramidale carrée, dans lesquels l'orbitale d_z^2 contient un électron induit par le fluor ou l'acétate, ont un axe de Jahn-Teller hors plan correspondant à la position du ligand axial. Par conséquent, le paramètre ZFS (levée de dégénérescence en champ nul) de l'anisotropie magnétique axiale est négative (**1**: D = -2.64 cm^{-1}; **2**: D = -2.48 cm^{-1}). En particulier, en champ nul, l'aimantation des complexes $FMnPc(OCH_2CH(Bu)_2)_4DMF$, et $AcMnPc(OCH_2CH(Bu)_2)_4$ a un temps de relaxation inférieur à 1.6 10^{-5} s à 1.85 K et sa dépendance de la température ne peut donc pas être déterminé par notre dispositif expérimental, ce qui suggère la présence d'un régime quantique de la relaxation de l'aimantation par effet tunnel (QTM) (Figures **R.7** et **8).**

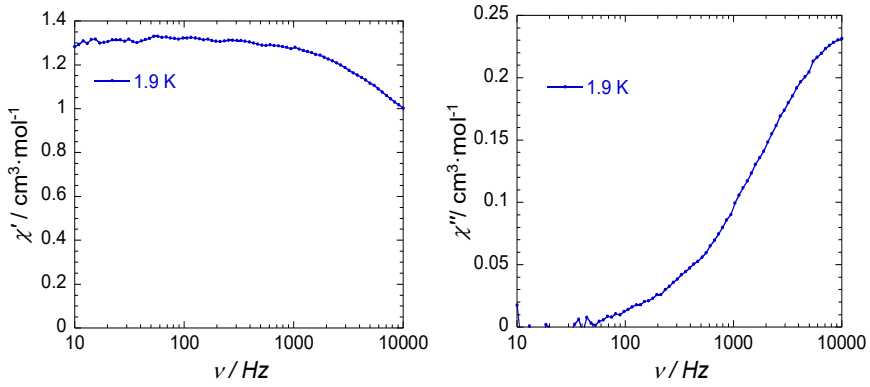

Figure R.7. Dépendance de la fréquence des parties réelle (χ', à gauche) et imaginaire (χ'', droite) de la susceptibilité en courant alternatif d'un échantillon polycristallin de FMnPc$(OCH_2CH(Bu)_2)_4$DMF en champ statique nul à 1.9 K.

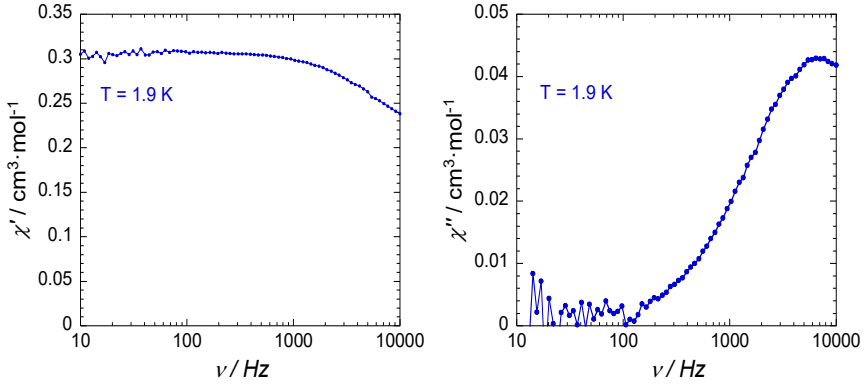

Figure R.8. Dépendance de la fréquence des parties réelle (χ', à gauche) et imaginaire (χ'', droite) de la susceptibilité en courant alternatif d'un échantillon polycristallin de AcMnPc$(OCH_2CH(Bu)_2)_4$ en champ statique nul à 1.9 K.

Des mesures de susceptibilité ac montrent que FMnPc$(OCH_2CH(Bu)_2)_4$·DMF, qui contient des centres Mn^{III} isolés, présente une relaxation lente de son aimantation sous champ magnétique statique (2500 Oe) (**Figure R.9**). Entre 2.6 et 4 K, la fonction τ(T) quasi linéaire, comme attendu pour un processus thermiquement activé suivant une loi d'Arrhenius ($\tau = \tau_0 \cdot exp(\Delta_{eff}/k_BT)$ où τ est le temps de relaxation, k_B la constante de Boltzmann, Δ_{eff} la barrière d'énergie du régime thermiquement activé et τ_0 un facteur pré-exponentiel), ce qui permet d'estimer la barrière d'énergie Δ_{eff} = 12.1 cm^{-1} et τ_0 = 4.5 10^{-8} s (**Figure R.10).** En revanche, le complexe AcMnPc$(OCH_2CH(Bu)_2)_4$, se comporte d'un pont de vue magnétique gamme une paire moléculaire, on sison des effets cristallographique (interaction intermoléculaires entre deux complexes). Le couplage magnétique entre les ions Mn(III) ions dent être estimé comme très faiblement antiferromagnétique, avec J= - 0.24 cm^{-1}. Contrairement au composé FMnPc$(OCH_2CH(Bu)_2)_4$DMF, qui montre des phénomènes de relaxation lente de l'aimantation dans la gamme de fréquences de 30 à 10000 Hz en champ nul, le maximum des signaux χ'' du composé AcMnPc$(OCH_2CH(Bu)_2)_4$ en champ nul sont proche de la limite de la fenêtre d'acquisition de notre dispositif expérimental, même pour les plus hautes fréquences utilisées (ν=10000 Hz) (Figure **R.8**). Dans un champ de 1000 Oe, quand la température passe en-dessous de 9 K le moment magnétique de AcMnPc$(OCH_2CH(Bu)_2)_4$ ne peut plus rester en phase avec un champ oscillant à des fréquences entre 30 et 10000 Hz (de forts maxima dépendants de la fréquence apparaissent en χ' et χ'').

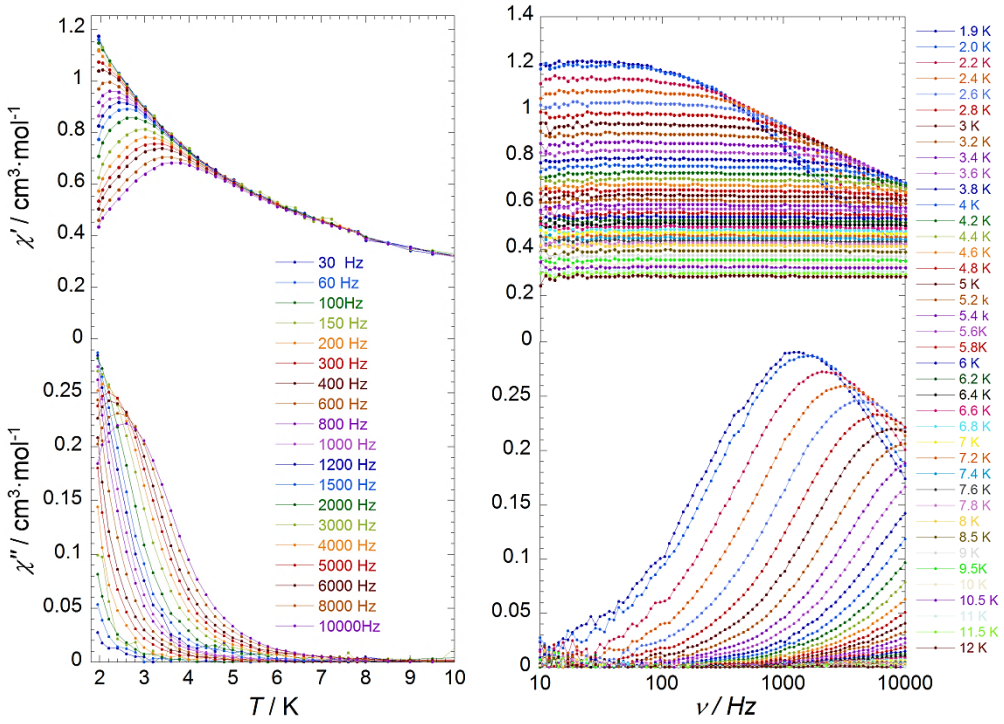

Figure R.9. Dépendance de la température (à gauche) et de la fréquence (à droite) des parties en phase (χ') et déphasées (χ'') de la susceptibilité, entre 30 et 10000 Hz et entre 1.9 et 12 K, pour **1** dans un champ de 2500 Oe.

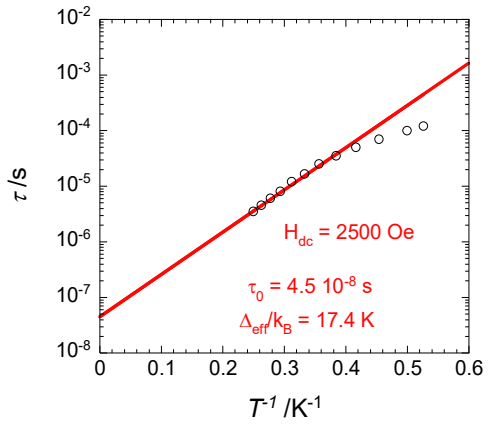

Figure R.10. τ sur T^{-1} pour **1** dans un champ de 2500 Oe. La ligne rouge représente le meilleur ajustement de la loi d'Arrhenius.

Les maxima de χ'' se déplacent vers plus haute température quand la fréquence augmente (Figure **R.11, gauche**). Pour estimer le temps de relaxation τ, les maxima des courbes de χ'' sur ν ($\tau = 1/2\pi\nu_{max}$) (Figure **R.11, droite**) ont été reportés comme fonction de $1/T$ (Figure **R.12**). Entre 2 et 4 K, une dépendance linéaire du temps de relaxation est observée, qui suit une loi d'Arrhenius $\tau = \tau_0 exp(\Delta_{eff}/k_B T)$, qui nous permet d'obtenir une barrière d'énergie et un temps de relaxation de $\Delta_{eff} = 7.9$ cm^{-1} et $\tau_0 = 4.4\ 10^{-7}$ s.

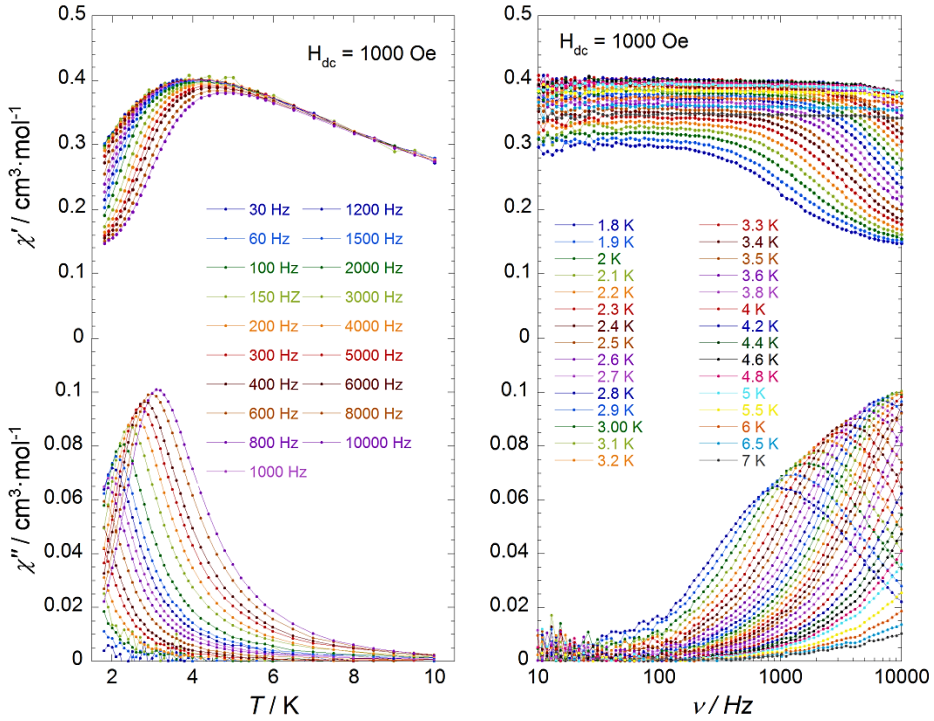

Figure R.11. Dépendance de la température (à gauche) et de la fréquence (à droite) des parties en phase (χ') et déphasées (χ") de la susceptibilité, entre 30 et 10000 Hz et entre 1.8 et 7 K, pour $AcMnPc(OCH_2CH(Bu)_2)_4$ dans un champ de 1000 Oe.

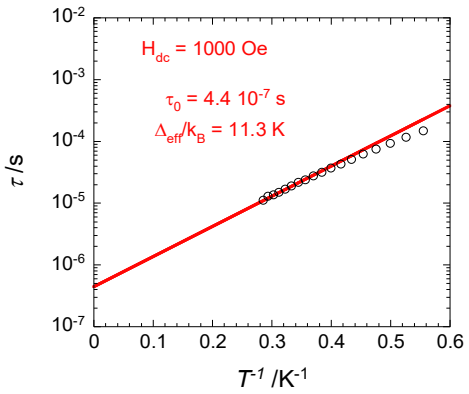

Figure R.12. τ sur T^{-1} pour $AcMnPc(OCH_2CH(Bu)_2)_4$ dans un champ de 1000 Oe. La ligne rouge représente le meilleur ajustement de la loi d'Arrhenius.

Les barrières d'énergie déterminées pour les deux composés sont comparables, ce qui suggère que les champs des ligands axiaux du fluor et de l'acétate sont comparables dans ces systèmes ou que leur contribution est petite, en accord avec les valeurs très proches des paramètres ZFS.

Pour les composés $Dy\{Pc(OCH_2CH(Bu)_2)_4Ac(DMF)_2$ et $\{Bu_4N\}\{Dy[Pc(OCH_2CH(Bu)_2)_4]_2\}$, nous avons pu montrer que la dynamique d'aimantation des SMMs mono-Dy est fortement modifié par le changement du champ de ligands. À champ nul, la dynamique d'aimantation pour de $Dy\{Pc(OCH_2CH(Bu)_2)_4Ac(DMF)_2$ est clairement dominée par un QTM avec un temps de relaxation constant d'environ 10^{-5} s et par conséquent, le QTM a été supprimé en mesurant l'aimantation en présence d'un champ externe. D'un autre côté, les temps de relaxation pour $\{Bu_4N\}\{Dy[Pc(OCH_2CH(Bu)_2)_4]_2\}$, à plus basse température indiquent un accroissement prononcé du procédé de relaxation pur voie quantiques. Ceci nous

laisse postuler que dans $Dy\{Pc(OCH_2CH(Bu)_2)_4Ac(DMF)_2$ et $\{Bu_4N\}\{Dy[Pc(OCH_2CH(Bu)_2)_4]_2\}$, les environnements désordonnés antiprismatiques-carrés du Dy(III) ont une forte influence sur les structures des sous-niveaux des multiplets de l'état fondamental. Pour confirmer que la relaxation lente de l'aimantation du $\{Bu_4N\}\{Dy[Pc(OCH_2CH(Bu)_2)_4]_2\}$ est une propriété moléculaire intrinsèque, il est nécessaire de conduire des mesures additionnelles d'aimantation sur des échantillons dopés par exemple avec l'homologue diamagnétique $\{Bu_4N\}\{Y[Pc(OCH_2CH(Bu)_2)_4]_2\}$. Ceci indiquera si l'annulation des interactions intermoléculaires induira un déplacement de χ'' à des températures plus élevées ou plus basses.

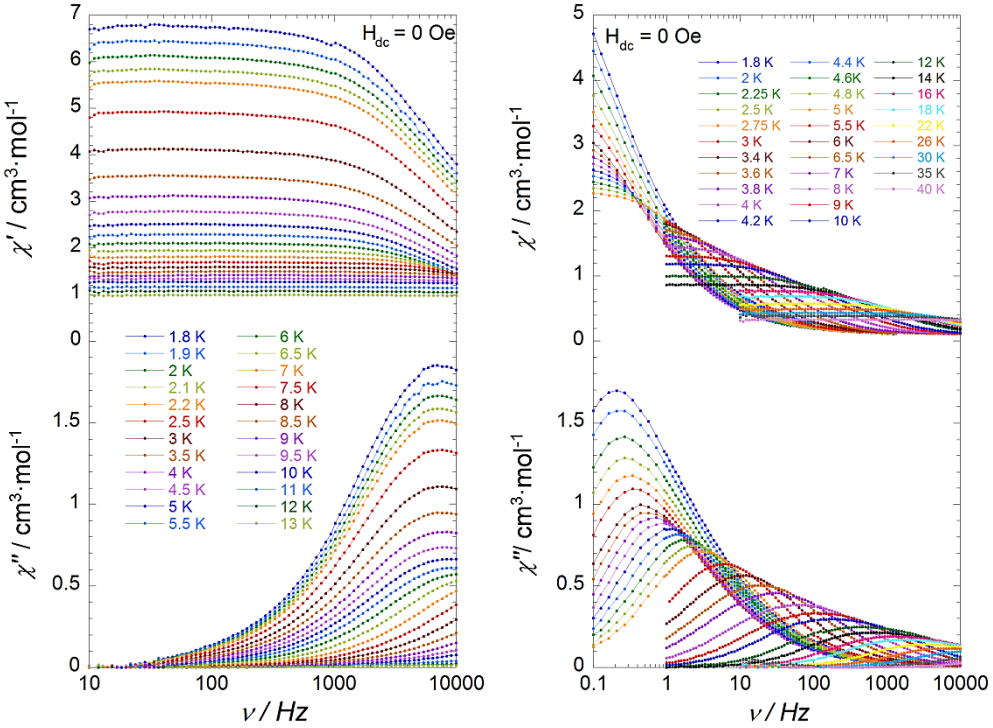

Figure R.13. Dépendance de la fréquence des parties réelle (χ', en haut) et imaginaire (χ'', en bas) de la susceptibilité d'échantillons polycristallins de $Dy\{Pc(OCH_2CH(Bu)_2)_4Ac(DMF)_2$ (à gauche) et de $\{Bu_4N\}\{Dy[Pc(OCH_2CH(Bu)_2)_4]_2\}$ (à droite) en champ statique nul.

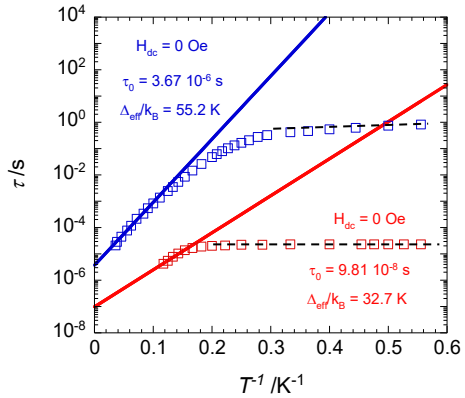

Figure R.14. τ sur T^{-1} pour $Dy\{Pc(OCH_2CH(Bu)_2)_4Ac(DMF)_2$ (rouge) et $\{Bu_4N\}\{Dy[Pc(OCH_2CH(Bu)_2)_4]_2\}$ (bleu) en champ nul. Les lignes représentent des ajustements de la loi d'Arrhenius.

Pour supprimer le QTM, des données en courant alternatif ont été enregistrées avec $Dy\{Pc(OCH_2CH(Bu)_2)_4Ac(DMF)_2$ sous un champ statique de 800 Oe. Dans ces conditions, une forte dépendance de la température et de la fréquence a été observée sur la susceptibilité (Figure **R.15**). Des temps de relaxations obtenus par la fréquence maximale des courbes de χ'' mesurées entre 5.8 et 7.6 K (Figure **R.15**, **en**

bas à droite), où l'effet thermique domine, suivant une loi d'Arrhenius (Figure **R.13**). La barrière d'énergie d'activation Δ_{eff}/k_B et le facteur pré-exponentiel τ_0 ont été estimés à Δ_{eff}/k_B= 75.6 K et τ_0= $1 \cdot 10^{-9}$s. A température plus basse, le temps de relaxation devient plus indépendant de la température, ce qui suggère une contribution plus importante des procédés relaxation par effet tunnel.

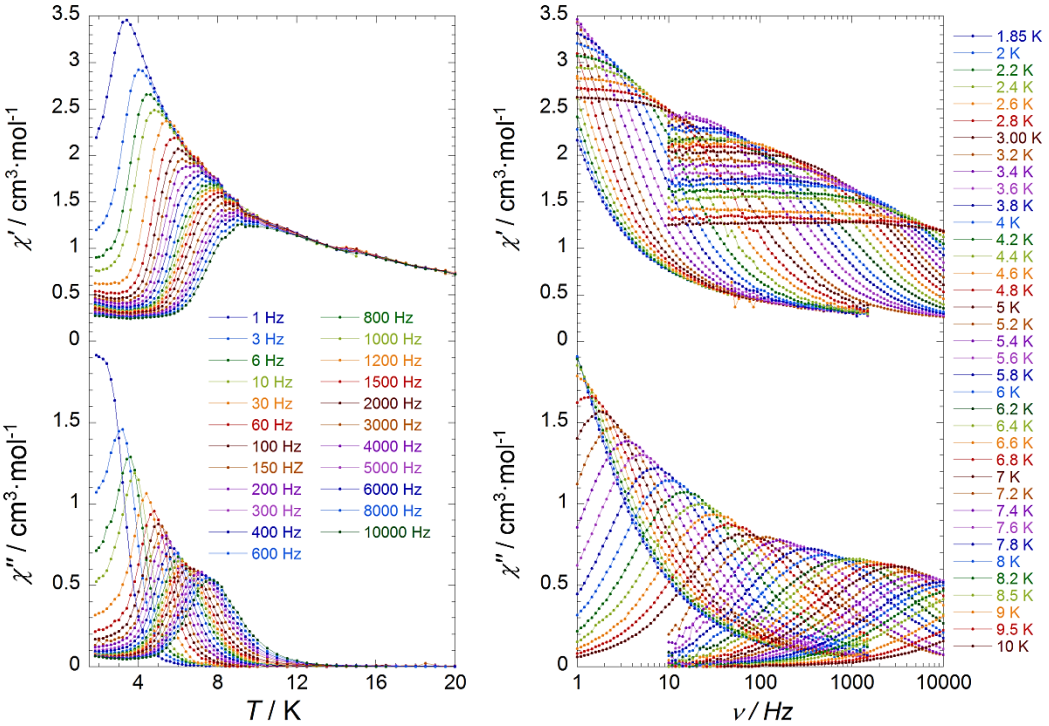

Figure R.15. Dépendance de la température (à gauche) et de la fréquence (à droite) des parties en phase (χ') et déphasées (χ'') de la susceptibilité, entre 1 et 10000 Hz et entre 1.85 et 10 K, pour **3** par un champ statique de 800 Oe.

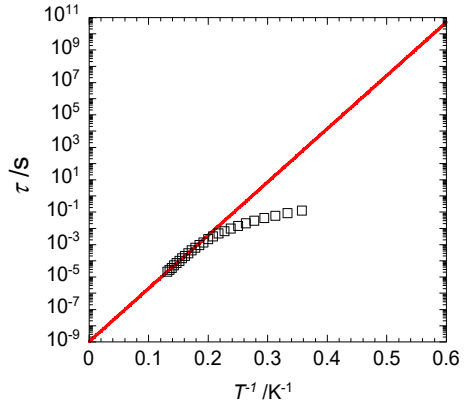

Figure R.16. τ sur T^{-1} pour **3** dans un champ de 800 Oe utilisant des données χ'' sur T de la figure **R.15, (droite)**. La ligne représente un ajustement de la loi d'Arrhenius.

Comme le comportement SMM de ces complexes dépend fortement de la différence en énergie entre les deux sous-niveaux les plus bas du multiplet de l'état fondamental, la forme radicalaire $[Dy\{Pc(OCH_2CH(Bu)_2)_4\}_2]^0$ reste à étudié davantage en termes de propriétés magnétique, en vue d'évaluer l'impact sur l'aimantation dynamique de électrons π non-appariés des ligands. Dans certains cas, la barrière d'énergie de la forme mono-oxidé du complexe sandwich de dysprosium est aussi sois plus grande comparé à la forme anionique [18]. Comme les complexes phtalocyanines sandwich peuvent exister sous une variété de

formes (anionique, radicalaire, protoné ou oxydé), ouvre des perspectives considérable par moduler les propriétés magnétiques pour le design de ces solubles complexes régulièrement alkoxy-décorés.

Références:

[1] a) G. H. Heilmeier; L. A. Zanonii; L. A. Barton; *Appl. Phys. Lett.*, 1968, 13, 46; b) M. Schadt; W. Helfrich; *Appl. Phys Lett.*, 1971, 18, 127.

[2] a) A. Bayer; S. Zimmermann; J. H. Wendorff; *Mol. Cryst. Liq. Cryst.*, **2003**, 396, 1; b) K. Kohary; H. Cordes; S. D. Baranovskii; P. Thomas; J.-H. Wendorff; *Phys. Status Solidi B* ,**2004**, 241, 76; c) S. Laschat; A. Baro; N. Steinke; F. Giesselmann; C. Hägele; G. Scalia; R. Judele; E. Kapatsina; S, Sauer; A. Schreivogel; M. Tosoni; *Angew Chem Int Ed Engl.,* **2007**; 46, 4832-4887.

[3] C. Piechocki; J. Simon; A. Skoulios; D. Guillon; P. Weber; *J. Am. Chem. Soc.*, **1982**, 104, 5119-5123.

[4] M. K. Engel; P. Bassoul; L. Bosio; H. Lehmann; M. Hanack; J. Simon*; Liq. Cryst.*, 1993, 15, 709–722.

[5] a) M. Hanack, A. Beck, H. Lehmann, *Synthesis* 8, **1987**, 703–705; b) I. Cho; Y. Lim; *Mol. Cryst. Liq. Cryst.,***1998,** 154, 9–26.

[6]] a) J. F. van der Pol; E. Neeleman; J. W. Zwikker; R. J. M. Nolte; W. Drenth; J. Aerts; R. Visser; S. J. Picken; *Liq. Cryst,* **1989**, 6, 577–592; b) W. T. Ford; L. Sumner; W. Zhu; Y. H. Chang; P.-J. Um; K. H. Choi; P. A. Heiney; N. C. Maliszewskyj; *New J. Chem.*, **1994**, 18, 495–505.

[7] a) C. Rager; G. Schmid; M. Hanack; *Chem. Eur. J,* **1999**, 5, 280–288; b) B. Görlach; M. Dachtler; T. Glaser; K. Albert; M. Hanack; *Chem. Eur. J.*, **2001**, 7, 2459–2465.

[8] J. Tant; Y. H. Geerts; M. Lehmann; V. De Cupere; G. Zucchi; B. W. Laursen; T. Bjørnholm; V. Lemaur; V. Marcq; A. Burquel; E. Hennebic; F. Gardebien; P. Viville; D. Beljonne; R. Lazzaroni; J. Cornil; *J. Phys. Chem., B,* **2005**, 109, 20315–20323.

[9] a) J. Sleven; T. Cardinaels; C. Görller-Walrand; K. Binnemans; *Arkivoc,* **2003**, 4, 68–82. b) J. Hoogboom; P. M. L. Garcia; M. B. J. Otten; J. A. A. W. Elemans; J. Sly; S. V. Lazarenko; T. Rasing; A. E. Rowan; R. J. M. Nolte; *J. Am. Chem. Soc.*, **2005**, 127, 11047–11052.

[10] M. Durmus; C. Lebrun; V. Ahsen; *J. Porphyr. Phthalocyanines,* **2004**, 8, 1175–1186.

[11] C. Rager; G. Schmid; M. Hanack; *Chem. – Eur. J.*, **1999**, **5**, 280.

[12] P. L. Creger*; J. Am. Chem. Soc.,* **1970**, 92, 5, 1397–1398.

[13] P. Bertoncello and M. Peruffo, *Colloids Surf., A*, **2008**, 321, 106–112.

[14] B. R. Kaafarani; *Chem. Mater.*, **2011**, 23, 378–396.

[15] G. Valduga; E. Reddi; G. Jori; R. Cubeddu; P. Taroni; G. Valentini; *J. Photochem. Photobiol., B*, **1992**, 16, 331–340.

[16] L. Q. Li; Q. X. Tang; H. X. Li; W. Hu; X. O. Yang; Z. Shuai; Y. Q. Liu; D. Zhu; *Pure Appl. Chem.*, **2008**, 80, 2231–2240.

[17] a)M. Gonidec; F. Luis; A. Vilchez; J. Esquena; D. B. Amabilino; J. Veciana; *Angew. Chem. Int. Ed.* **2010**, 49, 1623-1626; b) S. Sakaue; A. Fuyuhiro; T. Fukuda; N. Ishikawa; *Chem. Commun.*, **2012**, 48, 53375339; c) F. Branzoli; P. Carretta; M. Filibian; G. Zoppellaro; M. J. Graf; J. R. Galan-Mascaros; O. Fuhr; S. Brink; M. Ruben; *J. Am. Chem. Soc.* **2009**, 131, 4387-4396; d) N. Ishikawa; M. Sugita; T. Ishikawa; S.-Y. Koshihara; Y. Kaizu; *J. Am. Chem. Soc.* **2003**, 125, 8694; e) N. Ishikawa; M. Sugita; W. Wernsdorfer; *J. Am. Chem. Soc.*, **2005**, 127, 3650-3651; f) M. Gonidec; D. B. Amabilinoa; J. Veciana; *Dalton Trans.***, 2012**, 41, 13632-13639.

[18] a) S. Takamatsu; T. Ishikawa; S. Koshihara; N. Ishikawa; *Inorg. Chem.*, **2007**, 46, 7250-7252; b) N. Ishikawa; Y. Mizuno; S. Takamatsu; T. Ishikawa; S. Koshihara; *Inorg. Chem.*, **2008**, 47, 10217–10219.

List of Publications:

1. **Petru Apostol**, Ahmed Bentaleb, Mbolotiana Rajaoarivelo, Rodolphe Clérac and Harald Bock; "Regiospecific synthesis of tetrasubstituted phthalocyanines and their liquid crystalline order" *Dalton Trans.*, **2015**, 44, 5569-5576.

2. **Petru Apostol**, Juliana Eccher, Marta Elisa Rosso Dotto, Cassiano Batesttin Costa, Thiago Cazati, Elizabeth A. Hillard, Harald Bock and Ivan H. Bechtold; "High rectification in organic diodes based on liquid crystalline phthalocyanines" *Phys. Chem. Chem. Phys.*, **2015**, 17, 32390-32397.

Synthèse et propriétés de cristaux liquides et magnétiques de 1,8,15,22-tétraalkoxy–phtalocyanines de métaux (II) et (III)

Cette these décrit dans un premier temps la synthèse entièrement régiosélective de phtalocyanines tétra-(endo-alcoxy)-fonctionnalisées puis la formation de leurs complexes avec des ions métalliques. Dans un second temps sont étudiées leurs propriétés magnétiques, l'induction de mésophases colonnaires dans des gammes de températures convenables et avec des tailles modérées de substituants, ainsi que leur utilisation dans des diodes organiques. L'approche synthétique à suivre est la cyclo-tétramérisation de 3-(2-alkylalcoxy)-phtalonitriles suivie de la coordination d'un ion métallique. La symétrisation des chaînes aliphatiques dans le précurseur 3-alcoxy-phtalonitrile, en allant de 2-butyloctyl à 2-pentylheptyl, maintient la régiosélectivité et le mésomorphisme, tandis que les courtes chaînes 2-butylhexyl mènent à la formation d'un mélange de phtalocyanines régioisomères et à une plus grande tendance à la crystallisation. La combinaison de températures de clarification raisonnables avec un empilement colonnaire à température ambiante et avec une proportion assez importante de centres conjugués au sein de la masse moléculaire rend les deux premières séries de matériaux, c'est-à-dire $MPc(OCH_2CHBuHex)_4$, and $MPc(OCH_2CHPent_2)_4$, potentiellement utiles comme transporteurs de charges uniformément orientables dans des dispositifs électroniques organiques. Nous démontrons que ces matériaux phtalocyanines tétra-α-alcoxy-substitués, représentés par $H_2Pc(OCH_2CHBuHex)_4$, $NiPc(OCH_2CHBuHex)_4$ et $CuPc(OCH_2CHBuHex)_4$, mènent à des performances originales des dispositifs quand ils sont utilisés comme couche active organique dans des structures simples de diode ITO/PEDOT:PSS/PC/Al. Un redressement prononcé du courant est obtenu dans les diodes malgré l'alignement planaire prépondérant des colonnes dans les couches. Le ligand Pc tétra-α-alcoxy-substitué très soluble donne des molécules-aimants mononucléaires originales par coordination avec Mn^{III} et Dy^{III}. Remarquablement, l'isomère de symétrie C_{4h} du complexe sandwich octa-alcoxy se forme sélectivement grâce aux subsistants encombrants sur les deux cycles Pc.

Mots-clés: cristal liquide, régiosélectivité, diode organique, molécule-aimant

Synthesis and liquid crystal and magnetic properties of 1,8,15,22-tetraalkoxy-metal(II/III)-phthalocyanines

This thesis describes the fully regioselective synthesis of symmetric all-endo tetra-alkoxy-functionalized phthalocyanines and their metal ion complexes accompanied by induction of columnar mesophases in convenient temperature ranges at moderate substituent sizes, as well as their use in organic diodes and the study of their magnetic properties. The synthetic approach to follow is lithium-induced macrocyclization of 3-(2-alkylalkoxy)-phthalonitriles prior to transition metal ion insertion. Symmetrization of the aliphatic chains in the 3-alkoxy-phthalonitrile precursor from 2-butyloctyl to 2-pentylheptyl maintains both the regioselectivity and the mesomorphism, whereas shortening to 2-butylhexyl leads to the formation of a regioisomeric mixture during the cyclo-tetramerization and to a somewhat greater tendency to crystallization. The combination of attainable clearing temperatures with room temperature columnar stacking and with a relatively high content of conjugated core within the molecular mass makes the first two series of materials, i.e. $MPc(OCH_2CHBuHex)_4$, and $MPc(OCH_2CHPent_2)_4$, potentially useful as uniformly orientable charge transporters in organic electronic devices. We establish that these tetra-α-alkoxy substituted phthalocyanine materials, as exemplified with $H_2Pc(OCH_2CHBuHex)_4$, $NiPc(OCH_2CHBuHex)_4$ and $CuPc(OCH_2CHBuHex)_4$, lead to original device performances when applied as an active organic layer in simple ITO/PEDOT:PSS/PC/Al diode structures. A pronounced current rectification of the diodes is obtained despite the preponderantly planar alignment of the columns in the films. The highly soluble tetra-α-alkoxy-substituted Pc ligand, when combined with Mn^{III} and Dy^{III}, gives rise to original mononuclear single molecule magnets. Remarkably, the C_{4h}-symmetric isomer of the octa-alkoxy double decker complex is formed selectively due of presence of the bulky substituents on both Pc rings.

Keywords: liquid crystal, regioselectivity, organic diode, single-molecule magnet

Thèse préparée au Centre de Recherche Paul Pascal UPR 8641 / CNRS - Université de Bordeaux
115 av. Albert Schweitzer, 33600 PESSAC (France) http://www.crpp-bordeaux.cnrs.fr/